Research in Optoelectronics (A)

Reprints published in 2007

by

Professor Larry A. Coldren

and Collaborators

Published as

Technical Report # ECE 08-01

of

The Department of Electrical & Computer Engineering

The University of California

Santa Barbara, CA 93106

Phone: (805) 893-4486

Fax: (805) 893-4500

E-mail: coldren@ece.ucsb.edu

www.ece.ucsb.edu/Faculty/Coldren

Introduction:

Conference and Journal papers published by Prof. Coldren, together with his students, post docs, and other collaborators in 2007, are contained in this edition of Research in Optoelectornics (A). These generally focus on III-V semiconductor lasers and related photonic integrated circuits. The work spans efforts from basic materials and processing technology, through device physics and design, to device formation, characterization, and insertion into systems demonstrations.

The reprints have been grouped into three areas: **I. Photonic IC Technology & Devices; II. Vertical-Cavity Surface-Emitting Lasers; and III. Cavity QED, Single-Photon Emitters, and Spin Physics.** The majority of the work is in the first area, which has been further subdivided into *A. PIC Transmitters, Receivers, and Sensor Technology; B. Analog PICs and RF-Photonics, and C. Photocurrent-Driven Wavelength Converter PICs.* All of the epitaxial wafers for this work except for the MBE group is grown on InP by MOCVD. The epitaxial growth activity is strongly supported by Prof. DenBaars (MOCVD) and Prof. Gossard (MBE), who co-advise the students involved in these areas. Thus, their contributions have been invaluable to the research, even when they do not appear as co-authors on the device oriented papers.

The work was performed with funding from several grants from industry and government, some gifts funds from industry, and support from the Kavli Endowed Chair in Optoelectronics and Sensors. Specific projects included one on wavelength converters and photonic networks under the DARPA DoDN program (Prof. Blumenthal, PI); an analog receiver project sponsored by DARPA Phorfront (Prof. Bowers, PI); two projects to create very high-efficiency optical interconnects for ICs using either edge-emitting short-cavity laser-modulators (supported by the DARPA C2OI program) or directly-modulated vertical-cavity surface-emitting lasers (supported by a UC-MICRO with IBM).

The first group of reprints (*IA.*) summarizes efforts to make highly-functional and efficient widely-tunable transmitters, receivers and sensors using the integration platforms developed at UCSB over the past several years. Figure 1 illustrates an integrated widely-tunable transmitter that incorporates a sampled-grating distributed-Bragg-reflector (SG-DBR) laser with a traveling-wave electro-absorption modulator (TW-EAM) on InP. In this case the both the load resistor and the rf-bypass capacitor are also integrated on the PIC. The traveling-wave effect is illustrated by the wider bandwidth observed for co-propagating optical and electrical waves. This work provides a prototype universal (any wavelength) transmitter for 40 Gb/s wavelength-division multiplexed (WDM) optical communication systems. It was also integrated with a SOA-PIN receiver for a single-chip wavelength converter, but only the transmitter stage is reviewed here. The current work was done in support of all-optical networking experiments.

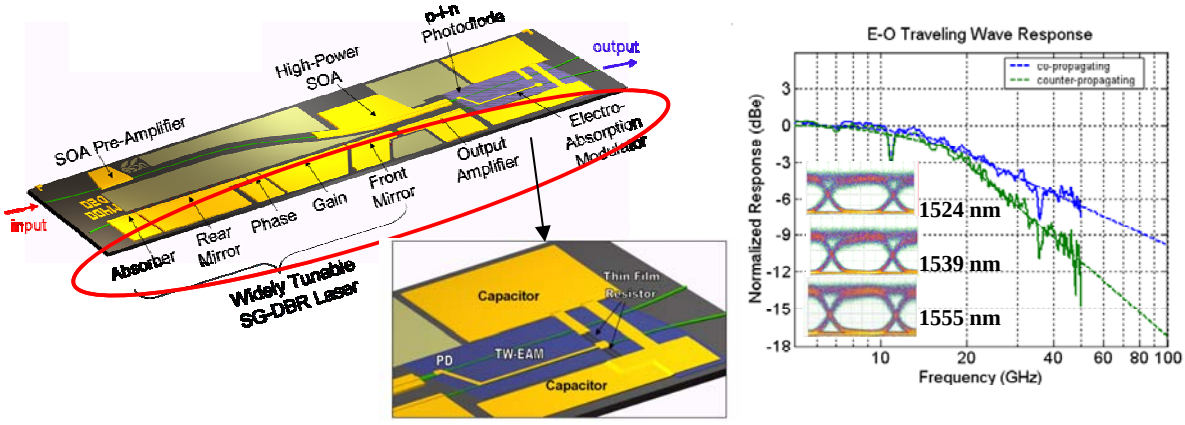

Figure 1. Widely-tunable transmitter incorporating a traveling wave EAM following an SGDBR laser. Inset shows integrated loads and by-pass capacitors. Frequency response verifies traveling wave effect. Transmitter shown integrated with SOA-PIN receiver for wavelength conversion.

Figure 2 shows an integrated short-cavity DBR laser with an EAM on GaAs. Error-free data links were demonstrated at 35 Gb/s. With a wider bandwidth receiver it is anticipated that data rates up to 40 Gb/s would be viable. The overall length of the DBR-EAM was < 300 μm, but additional absorber and output coupling regions were included for testing convenience. Strained-layer InGaAs quantum-wells provide for very high efficiency operation. These were partially intermixed for the modulator and passive regions. The objective of this work was to provide a small-footprint, highly-efficient, and high-data-rate transmitter for short-reach data communications, perhaps for board-to-board or chip-to-chip optical links within computers. Higher output powers and data rates than the alternative directly-modulated VCSELs should be possible.

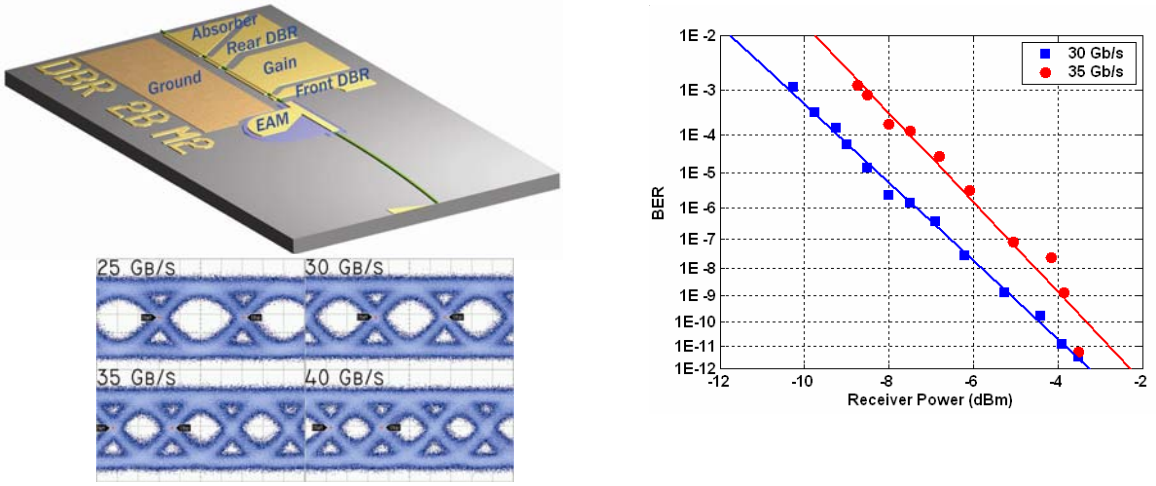

Figure 2. Small footprint GaAs-based DBR laser-EAM PIC schematic, BER and eye-diagrams @ 980 nm.

Work in the Analog PICs and RF-Photonics area (*IB*) has continued to focus on an integrated phase demodulator that consists of closely integrated PIC and EIC chips as illustrated in Fig. 3. The close integration is necessary to limit loop delay and increase

the stable bandwidth of the feedback loop from the balanced photodetector pair to the tracking balanced phase modulator pair. The feedback loop limits the magnitude of the detector output to avoid nonlinearities, even with phase modulation depths of many radians in the input signal. For good balance the MMI coupler should have a 50 : 50 splitting ratio, so it was desirable to incorporate a tuning electrode to trim the coupling to precisely this level. Photodetector saturation currents > 60 mA, and an output third-order intercept point (OIP3) of about 35 dBm was observed at 40 mA, very good results for such waveguide photodetectors.

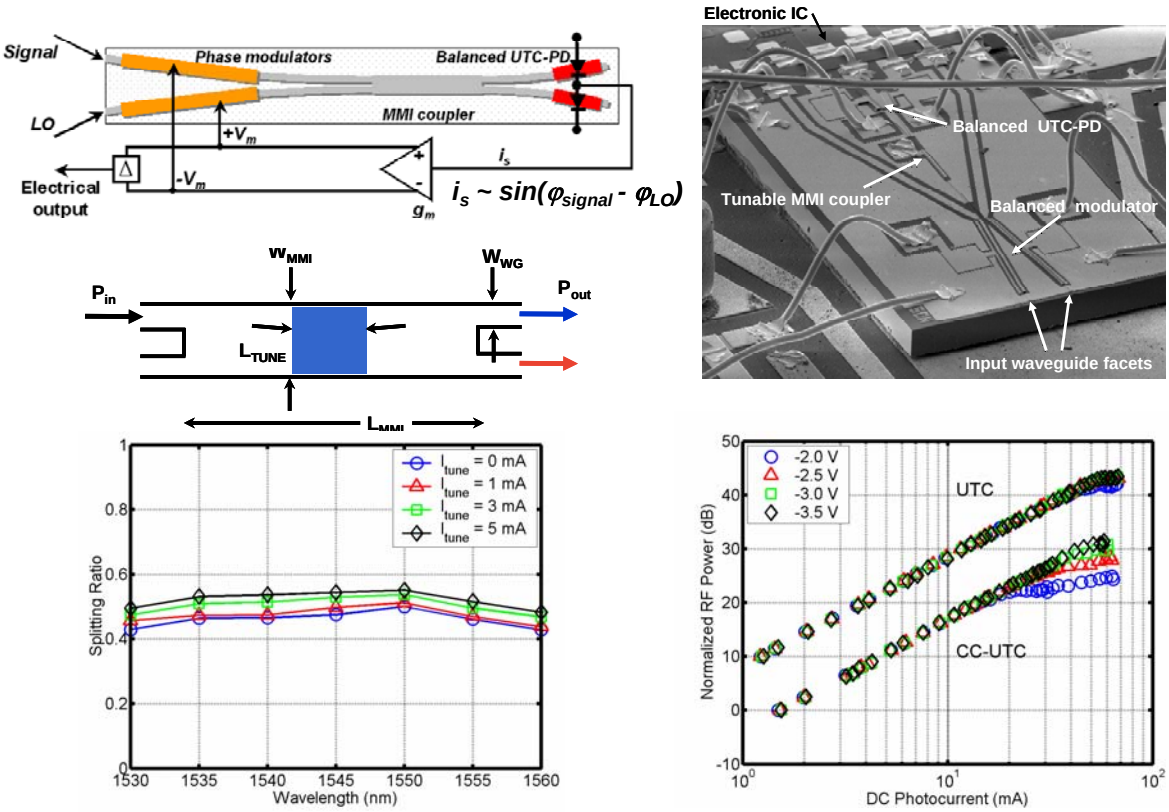

Figure 3. Coherent receiver for phase modulated signals. (top) Schematic and SEM of EIC-PIC combination; (bottom-left) schematic of current-controlled MMI and results; (bottom-right) photodetector saturation characteristics for unitraveling-carrier (UTC) and charge-compensated UTC designs.

To further reduce loop delay in the phase demodulators introduced above, we have explored the use of optical beam splitters in place of the 350 μm long MMI directional coupler. Figure 4 shows a schematic of a phase demodulator with a grating beam splitter in which the grating is etched entirely through the waveguide. As illustrated, splitting ratios ~ 50 : 50 result for grating lengths a little longer than 10 μm.

Recent efforts on photocurrent-driven wavelength-converter PICs are described in Section *IC*. Figure 5 gives an example of a design that incorporates a high-gain, high-saturation-power SOA pre-amplifier before a PIN detector in a receiver section that directly drives the EAM of an SGDBR-EAM transmitter, all integrated on the same InP chip without any additional regrowths beyond the one 'blanket' growth necessary for the SGDBR gratings. Overall wavelength-conversion gain was demonstrated at 10 Gb/s in a

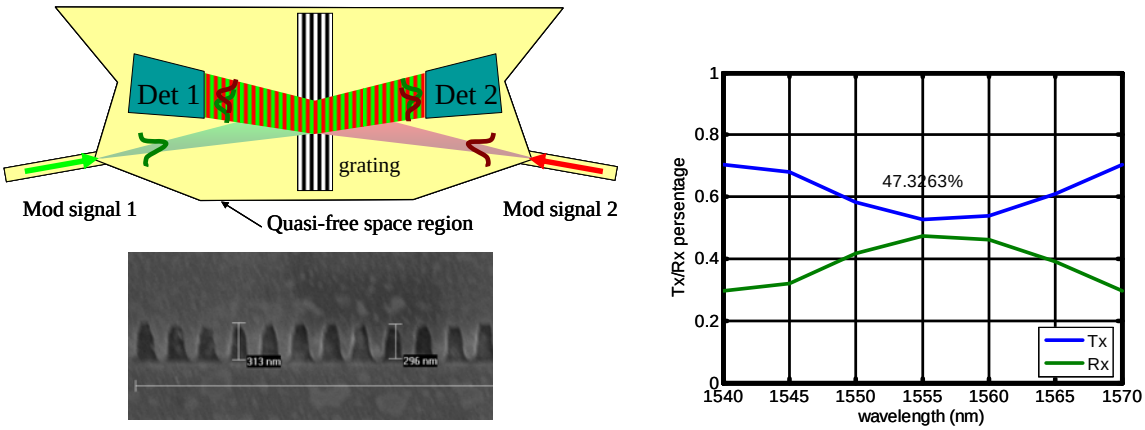

Figure 4. Heterodyne receiver using a grating beam splitter to combine two input signals on a pair of detectors. SEM show deep grating etch; transmitted & reflected power for 10 μm long grating.

relatively low-power dissipation, small footprint PIC. Typical wavelength converters, which use cross-phase modulation in saturated SOAs for wavelength conversion together with a widely tunable SGDBR and pre-amp SOAs, require about twice the power and footprint. Also, conversion losses > 10 dB are typical and a filter is needed to remove the input at its original wavelength. Such is not the case here.

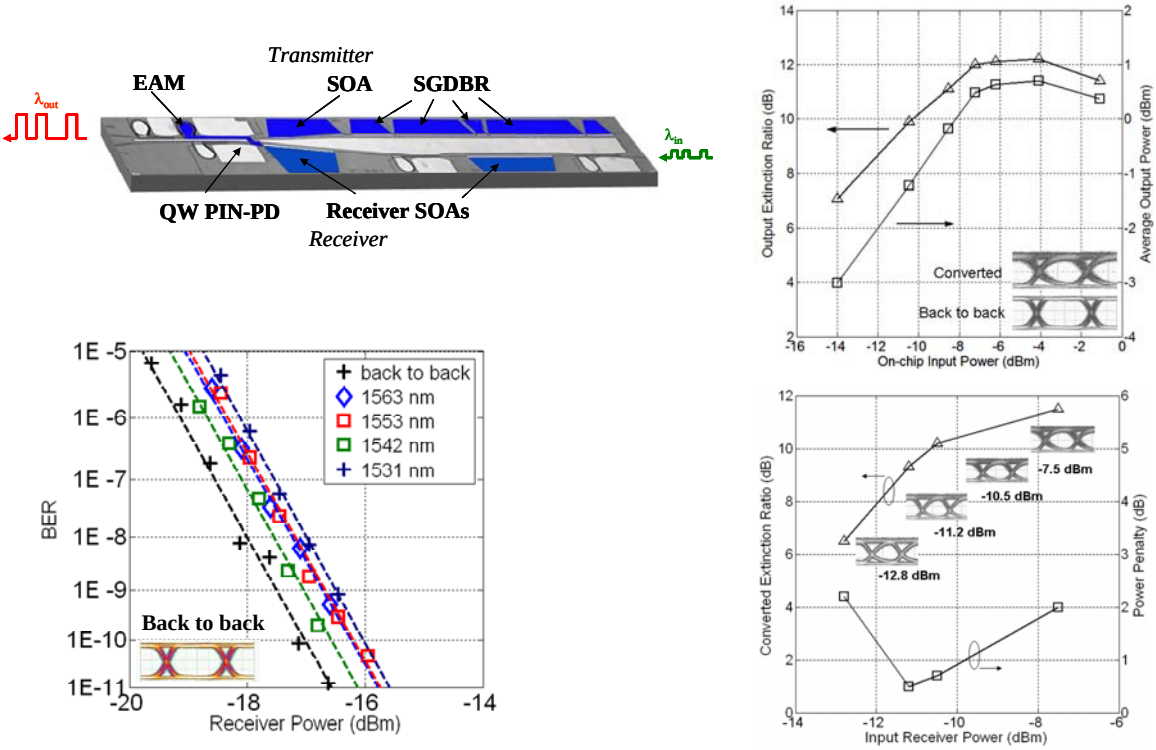

Figure 5. Photocurrent-driven wavelength converter schematic (top-left); fiber-coupled output and extinction ratio vs. input power showing conversion gain (top-right); filterless BER (bottom-left); and extinction ratio and power penality for BER data without any AGC (bottom-right).

Work on vertical-cavity surface-emitting lasers (VCSELs) during this year has led to a new record in the data-rate/power dissipation figure-of-merit as reported in Section **II**. Figure 6 summarizes our recent GaAs-based 980 nm VCSEL results. Error-free data transmission at 35 Gb/s was obtained with a power dissipation of 10 mW. The data rate of 35 Gb/s was also a new record for directly modulated VCSELs when it was first published. Work continues to improve upon these record performance levels.

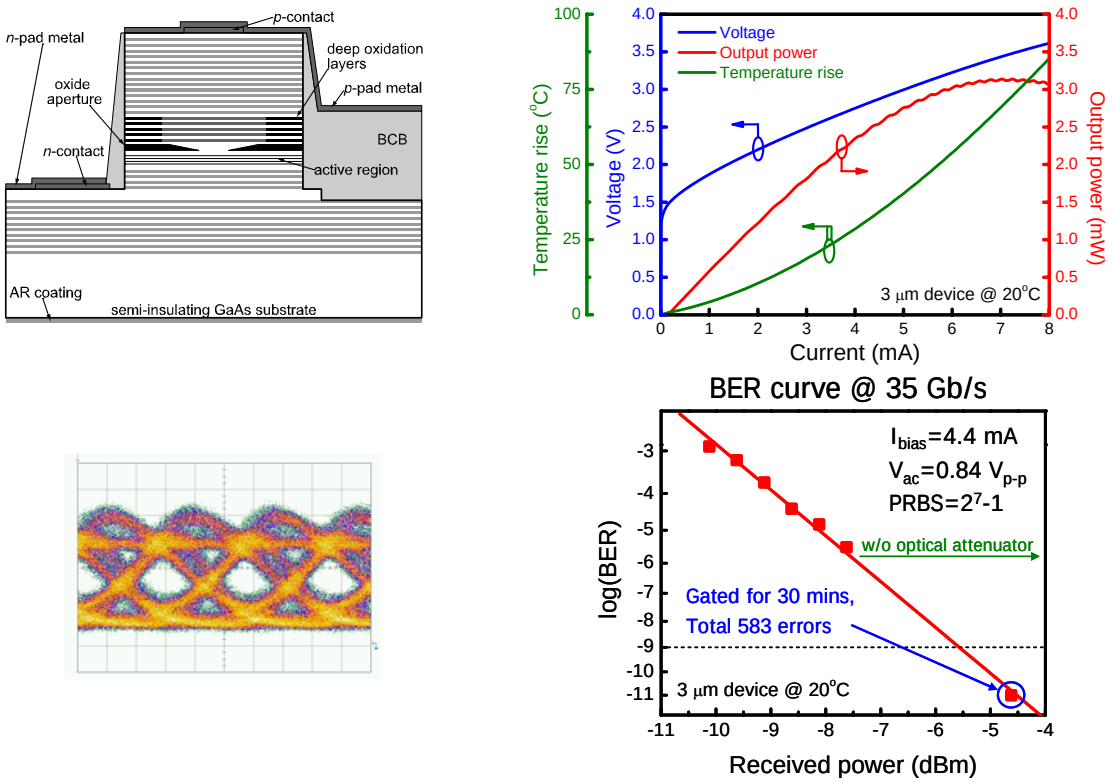

Figure 6. 980 nm VCSEL results. (top-left) Schematic; (top-right) Power-out, temperature rise, and voltage vs dc current; (bottom-left) Eye-diagram @ 35 Gb/s; (bottom-right) BER @ 35 Gb/s.

The final group of papers on Cavity QED, Single-Photon Emitters, and Spin Physics is reported in Section **III.** It lists four papers that utilized GaAs-based MBE material and devices formed in our group. This work was led by other faculty members both at UCSB and elsewhere. Thus, we will not highlight it to a larger extent in this reprint collection. We continue to be receptive to outside collaborations that can use our expertise to some advantage.

Back Row: Jon Klamkin, Uppili Krishnamachari, Sasa Ristic, Chad Wang, Steve Nicholes, John Parker, Chin-Han Lin and Leif Johansson.
Front Row: Joseph Chang, Janet Chen, Rob Guzzon, Larry Coldren, Matt Dummer, Jeannine Roson, and Yan Zheng.

Professor Coldren's Group

I. *Researchers*

L. Johansson	Post Doctoral Researcher, UCSB
S. Ristic	Post Doctoral Researcher, UCSB

II. *Students*

Y. Chang	Ph.D. Program
C. Chen	Ph.D. Program
M. Dummer	Ph.D. Program
R. Guzzon	Ph.D. Program
J. Klamkin	Ph.D. Program
U. Krishnamachari	Ph.D. Program
C. Lin	Ph.D. Program
S. Nicholes	Ph.D. Program
J. Parker	Ph.D. Program
N. Stoltz	Ph.D. Program, now at UCLA
A. Tauke-Pedretti	Ph.D. Program, now at Air Force Research Labs
C. Wang	Ph.D. Program, now at Aerius Photonics, LLC
Y. Zheng	Ph.D. Program

III. *Staff*

D. Cohen	Principal Development Engineer
J. Roson	Center Assistant, OTC

Collaborators

I. *Faculty*

D. Blumenthal	UCSB
D. Bouwmeester	UCSB
J. Bowers	UCSB

S. DenBaars	UCSB
E. Hu	UCSB
P. Petroff	UCSB
M. Rodwell	UCSB
S. Strauf	Stevens Institute of Technology

II. *Researchers*

Y. Akulova	JDSU
J. Barton	Post Doctoral Researcher, UCSB (Blumenthal)
Y. Choi	Post Doctoral Researcher, UCSB (Hu)
H. Chou	Post Doctoral Researcher, UCSB (Bowers), now at Luminent
K. Hennessy	Post Doctoral Researcher, UCSB (Hu)
D. Lofgreen	Raytheon
G. Morrison	Apogee Photonics
J. Nolde	Naval Research Labs
H. Poulsen	Post Doctoral Researcher, UCSB (Blumenthal)
J. Raring	Sandia National Labs
E. Skogen	Sandia National Laboratories
M. Sysak	Post Doctoral Researcher UCSB (Bowers)
D. Zibar	Post Doctoral Researcher UCSB (Bowers), now at Com-DTU, Institute for Communication, Optics and Materials; Denmark

Collaborating Students

A. Badolato	UCSB (Petroff)
N. Parthasarathy	UCSB (Rodwell)
M. Rakher	UCSB (Bouwmeester)
A. Ramaswamy	UCSB (Bowers)
C. Sheldon	UCSB (Rodwell)

Table of Contents:

I. Photonic IC Technology and Devices Page

IA. PIC Transmitters, Receivers, and Sensor Technology

IB. Analog PICs and RF-Photonics

J. Klamkin, A. Ramaswamy, L.A. Johansson, H.-F. Chou, M.N. Sysak, J.W. Raring, N. Parthasarathy, S. P. DenBaars, J.E. Bowers, and L.A. Coldren, "High Output Saturation and High Linearity Uni-Traveling-Carrier Waveguide Photodiodes," *Photonics Technology Letters,* **19**, (3), pp.149-151 (February 1, 2007)

M. N. Sysak, L.A. Johansson, J.S. Klamkin, L.A. Coldren, and J. E. Bowers, "A Dynamic Measurement Technique for Third Order Distortion in Optical Phase Modulators," *Photonics Technology Letters,* **19**, (3), pp.170-172 (February 1, 2007)

A. Ramaswamy, L.A. Johansson, J. Klamkin, C. Sheldon, H.F. Chou, M.J. Rodwell, L.A. Coldren, and J.E. Bowers, "Coherent Receiver Based on a Broadband Optical Phase-Lock Loop," *Proc. Optical Fiber Communications Conference*, paper no. PDP3, Anaheim, CA (March 25-29, 2007)

H.-F. Chou, A. Ramaswamy, D. Zibar, L.A. Johansson, J.E. Bowers, M. Rodwell, and L.A. Coldren, "Highly Linear Coherent Receiver with Feedback," *Photonics Technology Letters,* **19**, (12), pp.940-942 (June 15, 2007)

L.A. Johansson, H.-F. Chou, A. Ramaswamy, L.A. Coldren and J.E. Bowers, "Coherent Optical Receiver for Linear Optical Phase Demodulation," *Proc. IEEE MTT-S International Microwave Symposim*, paper no. TU3D-01, Honolulu, Hawaii (June 2007) INVITED PAPER

L.A. Johansson, D. Zibar, A. Ramaswamy, and L.A. Coldren, "Analysis of Sampled Optical Phase-Lock Loops," *Proc. IEEE International Topical Meeting on Microwave Photonics*, paper no Th-4.32, Victoria, BC Canada (October 2007)

J.E. Bowers, A. Ramaswamy, L.A. Johansson, J. Klamkin, M.N. Sysak, D. Zibar, L.A. Coldren, M.J. Rodwell, L. Lembo, R. Yoshimitsu, D. Scott, R. Davis, and P. Ly, "Linear Coherent Receiver based on a Broadband and Sampling Optical Phase-Locked Loop," *Proc. IEEE International Topical Meeting on Microwave Photonics*, paper no. F-1.2, Victoria, BC Canada (October 2007) INVITED PAPER

J. Klamkin, A. Ramaswamy, Y-C. Chang, L.A. Johansson, M.M. Dummer, J.E. Bowers, S. P DenBaars, and L.A. Coldren, "Uni-Traveling-Carrier Photodiodes with Increased Output Response and Low Intermodulation Distortion," *Proc. IEEE International Topical Meeting on Microwave Photonics*, paper no. W-1.4, Victoria, BC Canada (October 3, 2007)

J. Klamkin, L.A. Johansson, A. Ramaswamy, J.E. Bowers, S.P. DenBaars, and L.A. Coldren, "Monolithically Integrated Coherent Receiver for Highly Linear Microwave Photonic Links," *Proc. 20th Annual Lasers and Electro Optics Society Meeting*, paper no. ME 2, Lake Buena Vista, FL (October 21 – 25, 2007)

C.-H. Chen, M.N. Sysak, J. Klamkin, and L.A. Coldren, "Ultra-Compact Grating-Based 2x2 Beam Splitter for Miniature Photonic Integrated Circuits," *Proc. 20th Annual Lasers and Electro Optics Society Meeting*, paper no. ThM4, Lake Buena Vista, FL (October 21 – 25, 2007)

A. Ramaswamy, L.A. Johansson, J. Klamkin, M.J. Rodwell, J.E. Bowers, and L.A. Coldren, "Integrated All-Photonic Coherent Receiver," *Proc. 20th Annual Lasers and Electro Optics Society Meeting*, paper no. TuM1, Lake Buena Vista, FL (October 21-25, 2007)

IC. Photocurrent-Driven Wavelength Converter PICs

M.N. Sysak, J.W. Raring, M. M. Dummer, H.N. Poulsen, D.J. Blumenthal, and L.A. Coldren, "Analysis of Digital System Performance in EAM-Based Photocurrent Driven Wavelength Converter," *Photonics Technology Letters,* **19**, (4), pp. 215-217 (February 15, 2007)

A. Tauke-Pedretti, M.M. Dummer, M.N. Sysak, J.S. Barton, J.W. Raring, J. Klamkin, and L.A. Coldren, "Monolithic 40 Gbps Separate Absorption and Modulation Mach-Zehnder Wavelength Converter," *Proc. Optical Fiber Communications Conference*, paper no. PDP36, Anaheim, CA (March 25-29, 2007)

A. Tauke-Pedretti, M.M. Dummer, J.S. Barton, M.N. Sysak, J.W. Raring, J. Klamkin, and L.A. Coldren, "Widely Tunable 10 Gbps Separate Absorption and Modulation Mach-Zehnder Wavelength Converter," *Electronics Letters*, **43**, (10), pp.584-585 (May 10, 2007)

M.N. Sysak, J.W. Raring, J.S. Barton, H.N. Poulsen, D.J. Blumenthal, and L.A. Coldren, "A 10 Gb/s Monolithically Integrated, Filterless, InGaAsP/InP Widely Tunable Wavelength Converter with Conversion Gain," *Journal of Lightwave Technology,* **25**, (12), pp. 3748-3759 (December 2007)

II. Vertical-Cavity Surface-Emitting Lasers

D.D. Lofgreen, Y.-C. Chang, and L.A. Coldren, "Vertical-Cavity Surface-Emitting Lasers with Lateral Carrier Confinement," *Electronics Letters*, **43**, (3), pp. 163-164 (February 1, 2007)

Y.-C. C hang, C.S. Wang, and L.A. Coldren, "Small-Dimension Power-Efficient High-Speed Vertical-Cavity Surface-Emitting Lasers," *Electronics Letters*, **43**, (7), pp. 396-397 (March 29, 2007)

Y.-C. Chang, C.S. Wang, and L.A. Coldren, "High-Efficiency, High-Speed VCSELs with 35 Gb/s Error-Free Operation," *Electronics Letters*, **43**, (9), 1022-1023. (September 2007)

Y-C. Chang, C.S. Wang, and L.A. Coldren, "High-Speed Tapered-Oxide-Apertured 980 nm VCSELs Supporting Data Rates up to 30 Gb/s," *Proc. 20th Annual Lasers and Electro Optics Society Meeting*, paper no. WR 3, Lake Buena Vista, FL (October 21 – 25, 2007)

L.A. Coldren, "High-Speed Datacom VCSELs at 1310 and 980 nm," *Proc. International Symposium on VCSELs and Integrated Photonics*, paper no. A2, Tokyo, Japan (December 18-19, 2007) INVITED PAPER

III. Cavity QED, Single-Photon Emitters, and Spin Physics

M.T. Rakher, S.Strauf, Y. Choi, N.G. Stoltz, K.J. Hennessy, H. Kim, A. Badolato, L.A. Coldren, E.L. Hu, P.M. Petroff, and D. Bouwmeester, "Cavity QED with QD in Semiconductor Microcavities," *Proc. SPIE Photonics West*, vol. 6481, 648109, San Jose, CA (January 23-25, 2007)

M.T. Rakher, S. Strauf, N.G. Stolz, L.A. Coldren, P.M. Petroff, and D. Bouwmeester, "Efficient Source of Single Photons From Charge-Tunable Quantum Dots in a Micropillar Cavity," *Proc. CLEO/QELS*, paper no. QThH1, Baltimore, MD (May 6-11, 2007)

S. Strauf, N.G. Stoltz, M.T. Rakher, L.A. Coldren, P.M. Petroff, and D. Bouwmeester, "High-frequency Single Photon Source With Polarization Control," *Nature Photonics*, **1**, pp. 704-708 (October 2007)

M.H. Mikkelsen, J. Berezovsky, N.G. Stoltz, L.A. Coldren, and D.D. Awschalom, "Optically Detected Coherent Spin Dynamics of a Single Electron in a Quantum Dot," *Nature Physics*, **3**, pp. 770-773 (November 2007)

I. Photonic IC Technology and Devices

A. PIC Transmitters, Receivers, and Sensor Technology

Available online at www.sciencedirect.com
ScienceDirect
Solid-State Electronics 51 (2007) 16–25
SOLID-STATE ELECTRONICS
www.elsevier.com/locate/sse

Electroabsorption modulator performance predicted from band-edge absorption spectra of bulk, quantum-well, and quantum-well-intermixed InGaAsP structures

Gordon B. Morrison [a,*], James W. Raring [c], Chad S. Wang [b], Erik J. Skogen [c], Yu-Chia Chang [b], Matt Sysak [b], L.A. Coldren [b]

[a] Apogee Photonics, 6580 Snow Drift Road, Suite 100, Allentown, PA 18106, USA
[b] Department of Electrical and Computer Engineering, University of California, Santa Barbara, CA 93106, USA
[c] Sandia National Labs, Albuquerque, NM, 87123, USA

Received 20 December 2005; accepted 26 October 2006
Available online 12 December 2006

The review of this paper was arranged by Prof. Y. Arakawa

Abstract

Band-edge absorption spectra from bulk, quantum-well, and quantum-well-intermixed InGaAsP material are collected and compared using photocurrent spectroscopy. The expected performances of ideal electroabsorption modulators fabricated from these materials are predicted and compared using the band-edge absorption data. A graphical method for simultaneously considering chirp, insertion-loss, extinction-ratio, and tuning range is presented, and is used to compare the suitability of the various materials for electroabsorption modulator applications. The quantum-well material is shown to be superior to bulk material for most EAM applications. Quantum wells with 85 meV conduction band depth and 80 Å width are shown to be superior to quantum wells with 120 meV conduction band depth and 65 Å width. Both well designs exhibit strong excitons. Finally, the effect of quantum-well intermixing is considered, and the expected performances of quantum-well-intermixed electroabsorption modulators are presented.

Keywords: Photocurrent spectroscopy; Electroabsorption; Modulator; Quantum confined Stark effect; Franz–Keldysh effect; Chirp; Exciton; Bandwidth; Quantum well; Bulk material; Tunable

1. Introduction

Electroabsorption modulators (EAM) are key components in modern fiber-optic communication systems. Discrete EAMs can be co-packaged with lasers to form integrated transmitter modules, but EAMs monolithically integrated with semiconductor lasers are now commercially available at both 1550 nm and 1310 nm. A wide variety of methods have been used for monolithic integration of lasers with EAMs on InP, including asymmetric twin waveguides (ATG) [1,2], quantum well intermixing (QWI) [3,4], identical active layers [5], offset quantum wells [6], dual quantum wells [7,8], butt-coupling regrowth [9,10] and selective area regrowth (SAG) [11]. With growing demand for bandwidth, increasingly complex photonic integrated circuits (PICs) that include EAMs are under development [6].

Regardless of the integration platform, the optimal performance of the modulator is ultimately limited by the band-edge absorption characteristics of the material from which it is fabricated. Therefore, a comprehensive knowledge of the band-edge absorption characteristics of various

* Corresponding author. Tel.: +1 610 706-0282.
E-mail address: gordon.morrison@apogeephotonics.com (G.B. Morrison).

0038-1101/$ - see front matter © 2006 Elsevier Ltd. All rights reserved.
doi:10.1016/j.sse.2006.10.013

EAM materials is mandatory. Insights into the relationship between band-edge absorption spectra and EAM performance are also vital for optimal EAM design.

The fundamental property requisite in an EAM material is that an applied bias will change the band-edge absorption spectrum. This property can be induced in InGaAsP by two distinct mechanisms. One of these mechanisms is the Franz–Keldysh effect, and occurs in bulk material. An electric field is applied to the bulk material so that the electron and valence energy bands are tilted. The carrier wavefunctions can tunnel into the tilted bands so that lower energy photons can excite an electron into the conduction band [12]. Thus, under a reverse bias, the absorption spectrum of the bulk material shifts to longer wavelengths. The electroabsorption coefficient of this Franz–Keldysh mechanism can be approximated for weak fields using Airy functions [13]. The other mechanism commonly used for InP EAM modulators is the quantum confined Stark effect (QCSE), which occurs in quantum well structures. Carriers are confined to the quantum wells, and the electron–hole pairs form excitons at room temperature, even in the presence of electric fields. The exciton binding energy manifests itself in the QW band-edge absorption spectrum as an absorption-peak (exciton peak). When an electric field is applied, the conduction and valence bands are tilted, altering the shape of the potential well. The altered well potential results in a reduced overlap of electron and hole wavefunctions, and the magnitude of the exciton peak is reduced. The energy levels of the electron and hole are also reduced, and lower energy photons can be absorbed [14]. Therefore, under a reverse bias, the absorption spectrum of the QW structure shifts to longer wavelengths.

In this work, the band-edge absorption spectra of bulk, quantum-well (QW), and QWI InGaAsP materials grown on InP are obtained by a photocurrent spectroscopy technique [15–19]. The band-edge absorption characteristics of these structures are compared and contrasted, and are related to the predicted performances of ideal EAMs fabricated from similar epitaxial structures. An ideal EAM is assumed to operate without undesirable second order effects such as saturation, or heating. Photocurrent spectroscopy data does not yield insight into the effects of heating or saturation because the photodiodes are characterized using very low light intensity. The photocurrent is less than 1 μA, and neither heating nor saturation is present. In general, small amounts of heating are expected to red-shift the modulator band-edge. Saturation is undesirable in EAMs because the build up of carriers reduces both extinction and RF performance. A well-designed EAM should be free from saturation in its operating regime (carriers are easily swept out of the active region by the electic field), and therefore predictions made from band-edge absorption data are expected to be accurate.

The validity of using photocurrent spectroscopy data to predict modulator characteristics such as extinction and chirp has been demonstrated previously [18,19]. Kim et. al. have also demonstrated the use of electroabsorption spectroscopy for accurate prediction of various modulator characteristics [20].

To correctly describe EAM performance, many characteristics must be simultaneously examined. The insertion-loss of an EAM should be as low as possible to avoid optical power attenuation. The extinction-ratio should be large, to keep the bit-error-rate (BER) low, and to reduce power penalty. For many telecommunications applications, the large signal chirp should be low, or preferably negative, to compensate for the dispersive properties of the optical fiber. A large wavelength tuning range is also desirable for applications such as uncooled (i.e., wavelength variable) transmitters [21], or broadly tunable transmitters [22]. In this paper, we combine photocurrent spectroscopy predictions with novel graphical analysis to simultaneously consider EAM tuning range, chirp, extinction, and insertion-loss. A comprehensive comparison of the suitability of various different materials to EAM applications is thereby enabled. Although the data presented in this paper are for a finite number of epitaxial structures, the results and trends from these structures offer insights into a wider range of possible designs.

2. Experiment

2.1. Photocurrent spectroscopy

In this work we employ a Varian Cary 500 spectrophotometer as the wavelength-tunable light source. The Cary 500 has a wide UV/Vis/NIR bandwidth ranging from 175 nm to 3000 nm. The photodiode is connected to a Keithly 2400 L–V source meter that scans across a range of reverse biases. A 3 kHz chopper samples the spectrophotometer optical source and an EG&G 5210 lock-in amplifier is used to reject leakage current and other noise. A 1 mm diameter aperture samples light from the spectrophotometer beam, and input light is calibrated using a Newport1835 C optical power meter. The entire system is automated. A basic diagram of the apparatus is shown in Fig. 1.

The photocurrent data is converted to a measure of electrons per second or equivalently the number of photons absorbed per second. The incident optical power is known,

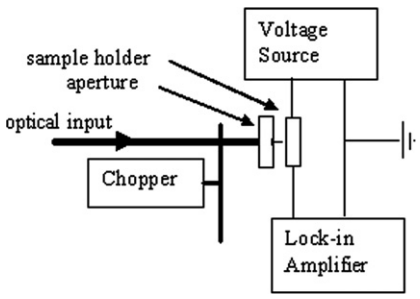

Fig. 1. Block diagram of the photocurrent spectroscopy test bench.

and is scaled down appropriately to account for absorption in the contact layer and reflection from the air/semiconductor surface. Weak optical interference between the contact layer and underlying semiconductor was noted during transmission and reflection measurements using the Cary 500 spectrophotometer, and these weak interference effects were taken into consideration during calibration of the optical input. Calculation of absorption is performed using

$$\alpha_{abs} = -\ln\left(\frac{P_{in} - P_c}{P_{in}}\right)\Big/ L \quad (1)$$

where α_{abs} is the power absorption per unit length of material, P_{in} is the number of photons entering the photodiode per second, P_c is the number of photons per second absorbed and measured as photocurrent, and L is the length of the absorbing material.

2.2. Epitaxial structures

The band-edge absorption spectra of three distinct epitaxy layer structures are considered in this paper. Each structure contains a slab-waveguide suitable for fabrication of ridge-waveguide components. The first structure employs a 3500 Å (i.e., bulk) InGaAsP absorbing layer with a band-edge of 1.395 μm (1.395Q). Due to the thick nature of the absorbing material, this structure exhibits the Franz–Keldysh effect, and is therefore useful for EAM applications.

The second structure considered in this paper consists of 15 compressively strained 80 Å wells and 16, 80 Å barriers centered in a 1.1Q waveguide. The conduction band depth in the wells is approximately 85 meV. These wells exhibit a photoluminescence peak (λ-PL) of 1554 nm. There are 650 Å of unintentionally doped material on either side of the wells. Quantum well structures exhibit the Quantum Confined Stark Effect and are therefore useful for EAM applications.

The final distinct structure contains 10 compressively strained 65 Å wells and 11, 80 Å barriers all centered within a 1.3Q waveguide. The conduction band depth in these wells is approximately 120 meV. These wells exhibit a λ-PL of 1556 nm. There are 1050 Å of unintentionally doped material on either side of these wells. The net width of unintentionally doped material in each QW structure is similar, thus the two structures exhibit similar electric fields across their wells.

Each of the QW structures has been subjected to various degrees of QWI. The characteristics of these QWI structures are also considered in this paper.

2.3. Photodiode fabrication

Prior to the fabrication process, parts of the QW samples are blue-shifted by QWI. Initially, each structure consists of the waveguide beneath a 15 nm InP layer, 20 nm 1.3Q etch stop, and a 450 nm InP implant buffer layer. A 5000 Å SixNy mask layer is deposited on the samples, and is selectively removed to define areas for QWI. A 100 keV, 5e14 cm-2 dose of P+ is implanted into the buffer layer. Regions protected by the 5000 Å of SixNy remain implant-free, and therefore do not experience QWI. Rapid thermal annealing at 675 °C is performed to drive point defects from the implant buffer layer through the quantum wells [3]. The magnitude of the blue-shift is controlled by the anneal time. Multiple band-edges are obtained on a single sample by annealing to the desired blue-shift, selectively removing the ion implant buffer layer, and then further annealing the sample. Areas that have had the buffer layer removed remain at a fixed wavelength throughout subsequent annealing, whereas areas retaining the implant buffer layer are blue-shifted further.

The fabrication process for each material is identical. Circular photodiodes ranging from 50 μm to 400 μm in radius are patterned on each sample (the data presented in this paper were obtained using 250 μm photodiodes). A reactive-ion etch process is used to etch through the waveguide and active region of the material. A 2000 Å SixNy layer is deposited over the sample, and circular vias are etched into the SixNy to expose the mesa contact layers. Ti/Pt/Au ring contacts are deposited on top of the mesas. The photodiodes are designed for operation with very small (often less than 1 μA) photocurrent, therefore resistance caused by the ring contact does not constitute a significant voltage drop. Finally, the samples are thinned and back-side metalized. A 30 s contact anneal at 420 °C is performed to reduce ohmic resistance and avoid schottky barriers. The photodiodes are mounted and wire bonded on AlN carriers. The fabrication process for these absorption-edge spectroscopy photodiodes can be completed very rapidly with minimal effort, making absorption-edge spectroscopy a useful and realistic tool for assisting in the design of optimized photonic integrated circuits. Fig. 2 shows a side-view of a typical photodiode for photocurrent spectroscopy.

Some samples were grown on Fe-doped substrates rather than n-type substrates. For samples on Fe-doped substrates, vias are opened on the top side for the n-contacts. These Fe-doped samples do not require back-side metallization for the n-contact, and heating is not an issue

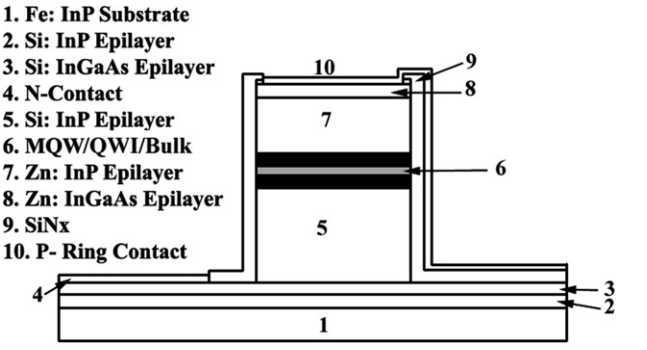

Fig. 2. Cross sectional view of a simple photodiode used for photocurrent spectroscopy.

with such very small photocurrents. Interestingly, samples without back-side metallization produce about 35% more photocurrent than their back-side metalized counterparts, and did not result in predictions consistent with modulators fabricated from the same material. Furthermore, back-side metal deposition reduces the photocurrent in previously unmetalized devices by 35%. The explanation for this phenomenon is that without back-side metallization, a fraction of light is scattered from the back-side of the sample and is able to pass through the absorbing region of the photodiode a second time. The back-side metallization and annealing process eliminates the back-scattering effect, and the subsequent photocurrent data has been shown to agree well with actual modulator performance [18,19].

2.4. Data and observations

Figs. 3–5 show the band-edge absorption spectra for bulk material, 80 Å wells, and 65 Å wells, respectively. In Figs. 4 and 5, the band-edge absorption spectra of the QWI materials are also presented. An exciton peak is clearly visible in QW structures. In contrast, there is no exciton peak in the bulk absorption-edge. The Stark shift in the 80 Å wells is much larger than that in the 65 Å wells, and the excitons in the 80 Å wells decay much faster than the excitons in the 65 Å wells. These simple observations are in excellent agreement with previous experiments and well-known absorption-edge theory [23].

The blue-shift associated with QWI occurs when group V atoms diffuse across the as-grown QW compositional boundaries, causing the QWs to develop rounded edges and become wider, shallower, and more parabolic. The exciton peaks in Figs. 4 and 5 decay more rapidly in the intermixed QWs than in the as-grown QWs. This weakening of the exciton is consistent with decreased carrier confinement in the intermixed wells.

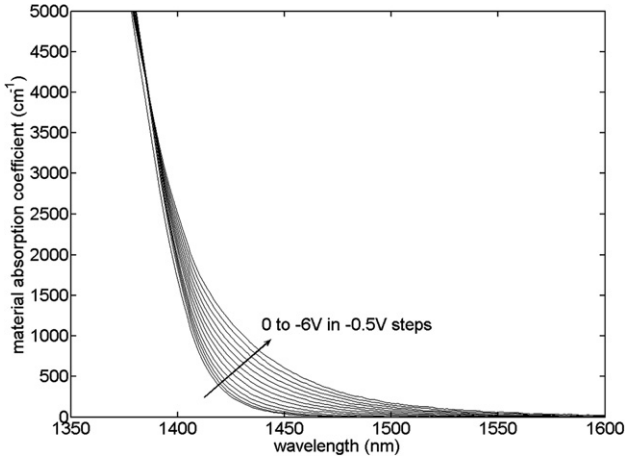

Fig. 3. Absorption-edge in bulk material. Data is shown ranging from 0 to −6 V in −0.5 V steps.

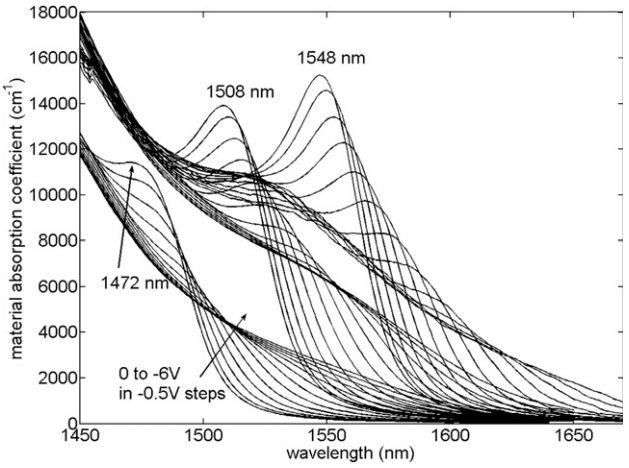

Fig. 4. Band-edge absorption spectra for the 80 Å QW structure at various applied biases. Also shown are the blue-shifted band-edge absorption spectra obtained from the same structure after different amounts of QWI. Each absorption-edge has been measured with biases ranging from 0 V to −6 V in −0.5 V steps.

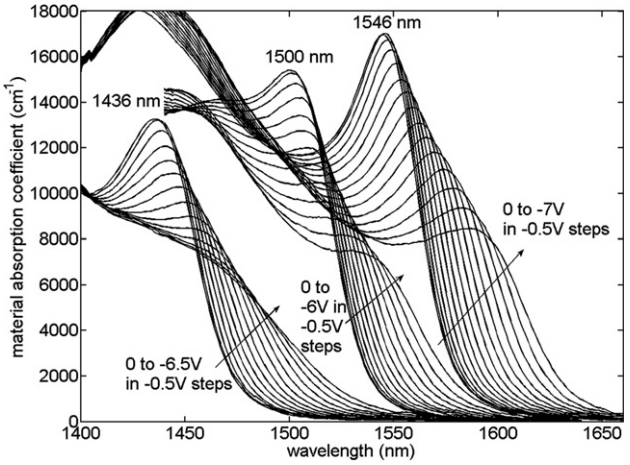

Fig. 5. Band-edge absorption spectra in the 65 Å quantum-well structure at various applied biases. Also shown are the blue-shifted band-edge absorption spectra obtained from the same structure after different amounts of QWI. Each absorption-edge is shown for a range of different bias voltages separated by 0.5 V steps.

The data in Figs. 4 and 5 provide a unique opportunity for simple observations comparing the effect of QWI on the band-edge absorption spectra of different QW structures. The maximum QWI blue-shift that was obtainable in the shallower 80 Å wells of Fig. 4 was only 70 nm, compared to the 108 nm shift of the narrower, deeper wells in Fig. 5. It is evident that the structure and eigenenergies of the deeper, narrower wells of Fig. 5 are more susceptible to QWI than the shallower, wider wells of Fig. 4. This difference in response to the intermixing process occurs for two reasons. First, the deeper wells have a larger compositional difference at the well boundary, which enhances diffusion of group V atoms between the well and the barrier, resulting in a larger perturbation to the well structure. Secondly, the diffusion process originates from the material

composition interface at the edges of the well, so that the diffusion process has greater influence throughout the narrow well. The center of the wider well is further from the material interface, and thus less susceptible to the diffusion process.

The optical loss in intermixed material has been shown previously [24] to depend exponentially on how far the material is intermixed from operation wavelength. This phenomenon is clearly observable in Figs. 4 and 5. The degree of absorption at 1550 nm for the passive (1436 nm) material in Fig. 5 will be less than the absorption of the passive (1472 nm) material in Fig. 4. Furthermore, the 0 V absorption for the deeper, narrower well approaches zero as a function of wavelength faster than the 0 V absorption of the wider, shallower well. Thus, from a passive material insertion-loss perspective, the deeper wells of Fig. 5 may have a significant advantage.

3. Analysis and results

3.1. Calculations

In this paper, scattering losses and other process-dependent insertion-losses are not included in the analysis. The insertion-loss considered in this paper is simply the loss due to absorption when the modulator is at its smallest bias (i.e., the optical power "on" state). The extinction is the ratio, in dB, between the "off" state and "on" state of the modulator. The chirp parameter measures the relationship between change in signal amplitude and change in carrier frequency. Low or negative chirp values are desirable as they are necessary to counter the dispersion inherent to optical fiber [25].

The absorption-edge data in Figs. 3–5, are easily manipulated to predict EAM extinction. The low input optical power used in the photocurrent spectroscopy experiments makes the predictions valid for optimally designed, ideal devices, in which second order effects such as heating, contact resistance, saturation and optical scattering are presumed negligible. The extinction (dB) as a function of wavelength and voltage is determined by

$$z = 10\log(e^{\alpha_{abs}\Gamma L_{eff}}) \tag{2}$$

where Γ is the overlap integral between the optical mode and the absorbing material, L is the effective length of the device, and α_{abs} is the material absorption, which is a function of wavelength and voltage. In previous work [18,20], DC extinction predictions have been shown to agree well with data from real EAM devices fabricated from the same material. Any wavelength-independent errors (e.g., scattering, measurement of optical input) in determination of α in Eq. (1) would simply mean that predictions from Eq. (2). are correct but for a slightly different modulator length. For example, a 10% overestimation of α_{abs} would mean that extinction predictions are actually for a modulator 10% shorter in length than the one considered. Similarly, errors in estimation of optical confinement (Γ) would result only in an inversely proportional error in the stated modulator length. The sum of measurement errors and errors in estimation of optical confinement are estimated to be less than 10%.

Starting with a change in absorption as a function of bias and wavelength, changes in index of refraction as a function of bias and wavelength are easily obtained using the Kramers–Kronig transform,

$$\Delta n(\lambda_0, \Delta V) = \frac{\lambda_0^2}{2\pi^2} P \int_0^\infty \frac{\Delta\alpha_{abs}(\lambda, \Delta V)}{\lambda_0^2 - \lambda^2} d\lambda \tag{3}$$

where Δn is the change in index of refraction at wavelength λ_0 due to a bias change ΔV, and P indicates the principle value of the integral. Of course, Eq. (2). is also a function of V_0, the bias point at which ΔV is centered. The singularity at $\lambda = \lambda_0$ is avoided using the transformation described by Henry et al. in [26]. Note that the denominator in the Kramers–Kronig transform acts somewhat as a filter, so that the absorption near λ_0 make the greatest contribution to the index of refraction near λ_0, whereas the absorption values further from λ_0 make much smaller contributions. Data used in Eq. (3) covered the entire range over which significant changes in absorption were measured as a function of voltage (i.e., $\Delta\alpha \approx 0$ outside the data range). With knowledge of Δn and $\Delta\alpha_{abs}$ the large signal chirp is calculated as

$$\beta_c = \frac{4\pi}{\lambda}\frac{\Delta n}{\Delta\alpha_{abs}} \tag{4}$$

where it is understood that the change in absorption and index are a function of wavelength, bias voltage, and magnitude of voltage change. The absolute magnitude of absorption, as obtained in Eq. (1) is not necessary to accurately determine the chirp using Eq. (4); thus any wavelength and voltage independent errors in determining α have no effect on calculated β_c. In previous work [19], we have demonstrated that chirp predicted from photocurrent spectroscopy measurements agrees with measured chirp in devices fabricated from identical material.

3.2. Presentation of EAM characteristics

In order to compare the suitability of various materials for EAM device performance, one must simultaneously consider chirp parameter, insertion-loss, and extinction, as well as the wavelength range over which these parameters are satisfactory. Figs. 6–8 present large signal ($\Delta V = 2V$) chirp (β_c) as a function of bias (V_0) for four different wavelengths (λ_0) spanning a range of 30 nm. In Figs. 6–8, two separate low or negative chirp operating points are clearly marked for each wavelength (e.g., in Fig. 6, for each wavelength (λ_0), $\beta_c = 0.4$ and $\beta_c = 0.85$ operating points are marked with stars on the chirp (β_c) vs. voltage (V_0) line). The insertion-losses and extinction-ratios, in dB, at each of the marked operating points, are plotted against a secondary y-axis on the same graph. The extinction and

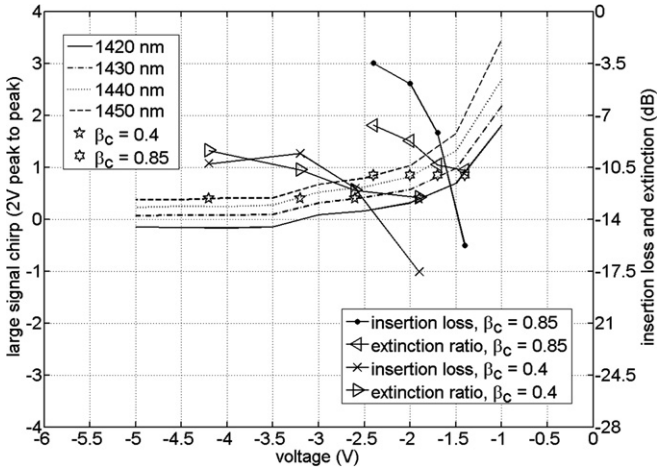

Fig. 6. Projected large signal chirp for a 125 μm modulator using 1.385Q bulk material having a 60% overlap with the optical mode. The lines curving downwards to the left are chirp as a function of voltage for four different wavelengths spanning 30 nm. Operating points for $\beta_c = 0.85$ and $\beta_c = 0.4$ are marked on each of these wavelength lines. Insertion-losses and extinction-ratios at these same operating points of $\beta_c = 0.85$ and $\beta_c = 0.4$ are also marked. Operation with negative chirp and acceptable insertion-loss and extinction is clearly not possible with this device.

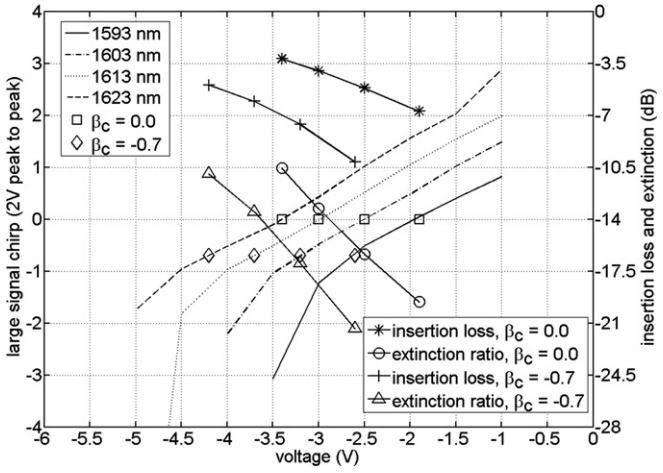

Fig. 7. Projected large signal chirp for a 125 μm modulator using 80 Å 85 meV wells having a 9% overlap with the optical mode. The lines curving downwards to the left are chirp as a function of voltage for four different wavelengths spanning 30 nm. Operating points for $\beta_c = 0.0$ and $\beta_c = -0.7$ are marked on each wavelength line. Insertion-losses and extinction-ratios at the $\beta_c = 0.0$ and $\beta_c = -0.7$ operating points are also marked. Clearly, negative chirp is readily available over a full 30 nm tuning range.

insertion-loss markers are connected by lines to highlight the trend in extinction and insertion-loss as a function of wavelength for a given chirp. With these graphs, one can simultaneously examine chirp, extinction, and insertion-loss as a function of wavelength and voltage. These novel figures simplify the evaluation of predicted EAM device performance.

Fig. 6 shows the predicted performance of the 1.385Q bulk material. Fig. 7 shows the predicted performance of the as-grown (i.e., not intermixed) 80 Å wells, and Fig. 8

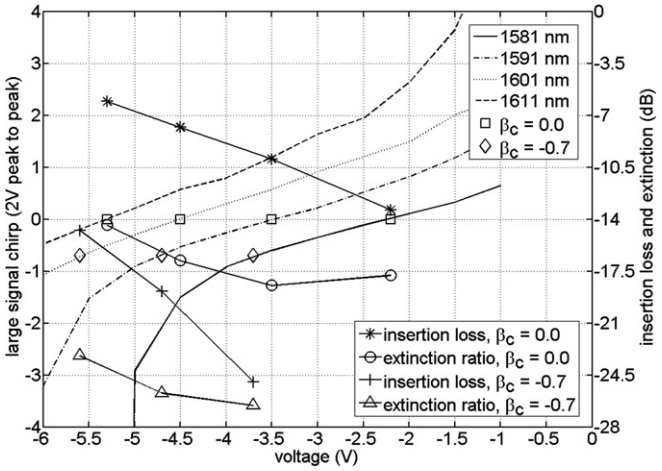

Fig. 8. Projected large signal chirp for a 125 μm modulator using 65 Å 120 meV wells having a 9% overlap with the optical mode. The lines curving downwards to the left are chirp as a function of voltage for four different wavelengths spanning 30 nm. Operating points for $\beta_c = 0.0$ and $\beta_c = -0.7$ are marked on each wavelength line. Insertion-loss and extinction-ratios at the $\beta_c = 0.0$ and $\beta_c = -0.7$ operating points are also marked. This device suffers from larger insertion-loss, smaller wavelength tuning range, and higher operating biases than the device in Fig. 7.

shows predicted performance for the as-grown 65 Å wells. The calculations for each of Figs. 6–8 assumed a modulator length of 125 μm. The confinement factor Γ was set at 9% for the QW structures, whereas Γ for the bulk material (Fig. 6) was set at 60%. These parameters reflect realistic values of actual devices, i.e., bulk materials have much larger overlaps [6] with the optical mode than QW material [27]. The overlap integral, Γ, scales the insertion-loss and extinction (Eq. (2)), but it does not affect the chirp parameter. Thus, for a given material, larger values of Γ will allow design of shorter EAMs. Shorter devices are preferable for high speed modulation in lumped element designs. Bulk material, however, has much lower absorption than QW material, so the higher value of Γ in bulk EAMs does not automatically allow shorter device length or higher extinction than in QW EAMs.

In each of Figs. 6–8, the detuning of the operating wavelengths from the modulator absorption-edge was chosen to allow maximum wavelength range with low or negative chirp. In Figs. 7 and 8, trends of insertion-loss and extinction as a function of wavelength clearly infer that moving to longer or shorter wavelengths will not improve performance. Longer wavelengths require much higher bias voltages, and shorter wavelengths introduce prohibitive insertion-loss. The wavelengths examined in Fig. 6 are unusually close to the modulator absorption-edge compared to bulk EAMs that are integrated with lasers using offset quantum-well technology [28]. The operating wavelengths in Fig. 6, do, however, highlight the difficulty of obtaining low chirp in a bulk device, regardless of integration platform (chirp is lower nearer the absorption-edge).

When interpreting Figs. 6–8, it is important to recall that for consistency and ease of comparison, all three

simulated devices have lengths of 125 μm. Naturally, different epitaxy layer structures will be better suited to longer or shorter modulator lengths. Insertion-loss, for instance, can be greatly reduced by shortening the length of the device. Unfortunately, shortening the device also scales the extinction-ratio by the same amount as the insertion-loss. It is therefore important to consider the ratio between insertion-loss and extinction. Ideally, the insertion-loss should be much smaller than the extinction.

Figs. 6–8 compare values assuming a 2 V p–p drive signal. Depending on the application, larger or smaller drive signals could be used; the intent here is to demonstrate trends that offer insight into a broader spectrum of possible modulator designs and operating points.

The QW structures discussed in this paper were grown for use in integrated laser/EAMs, where the EAM portion is blue shifted by QWI. Thus the wavelengths considered for modulators fabricated from the as-grown wells are relatively long. Similar wells with the same characteristics could easily be grown for operation at shorter wavelengths. The effects of QWI on modulator performance are considered later in this paper.

3.3. Analysis and explanation of EAM performance

Comparison of Figs. 6–8 highlight the importance of choosing a suitable material structure when designing an EAM. The device fabricated from bulk material, shown in Fig. 6, exhibits relatively high (~10 dB) insertion-losses, even at a positive chirp of 0.4. The insertion-losses for $\beta_c = 0.4$ operating points in Fig. 6. are as large, or larger, than the available extinction-ratios, making operation at $\beta_c = 0.4$ difficult. At a chirp of $\beta_c = 0.85$, operation with extinction that is significantly larger than insertion-loss is possible, but only at the longer wavelengths. Operation at even longer wavelengths would decrease insertion-loss, but would increase chirp and decrease extinction (although the decreased extinction can be countered with greater modulator length). The wavelength range in Fig. 6 was chosen to demonstrate the futility of trying to obtain negative chirp in a simple bulk device. Larger extinction with lower insertion-loss is obtainable with bulk material in longer devices operated at wavelengths that are further from the modulator absorption-edge [6,28]. These longer devices suffer from large positive chirp parameters. Negative chirp with acceptable insertion-loss and extinction is unattainable with bulk material in a simple EAM. A relatively complex dual modulator configuration has been proposed to reduce chirp in bulk EAMs [29].

Fig. 7 demonstrates that an 80 Å QW structure will outperform bulk material. Chirp of 0 to −0.7 is available across a full 30 nm range, with much higher extinction-ratios and acceptable insertion-losses (<10 dB). Operating points for 0 to −0.7 chirp exhibit much larger extinction ratios than insertion-losses for the full 30 nm range. Excellent performance similar to that predicted in Fig. 7 has recently been reported in an EAM modulator designed using the same QWs [19].

Given that the 80 Å QWs of Figs. 4 and 7 are more suitable for EAM design than the bulk material of Figs. 3 and 6, one might assume that higher confinement and stronger excitons (i.e., more "quantum-well like" quantum wells) would lead to even better performance. Such an assumption is shown to be false in Fig. 8. The operating points in Fig. 8 have unacceptably high insertion-losses, especially for the $\beta_c = -0.7$ operating points. A shorter device would reduce insertion-loss, but would also reduce extinction. A reduced extinction is unacceptable because the ratios of insertion-loss to extinction in Fig. 8 are much less favorable than those in Fig. 7. In Fig. 8, much higher bias voltages, V_0, are required for low or negative chirp operation. As demonstrated by the wide spread of operation points relative to the x-axis, larger biases are also necessary to operate at longer wavelengths. Operation with −0.7 chirp is not possible at the longest (1611 nm) wavelength, even with a bias of −6 V. High voltages cause power inefficiency and heating and should be avoided.

Although modulator of Fig. 8 is difficult to operate at negative chirp, the 65 Å QW material from which it is fabricated exhibits a very pronounced exciton peak (Fig. 5). Thus, for applications tolerating positive chirp at a fixed wavelength, high extinction efficiencies in a relatively short device are feasible with large drive signals.

For the bulk material modulator of Fig. 6, increased voltages do not lower chirp beyond a certain bias point. In contrast, higher bias voltages, V_0, always result in lower, or more negative chirp for the QW materials of Figs. 7 and 8. The change in absorption-edge in these materials is actually a function of electric field rather than applied voltage. The electric field across the bulk material or quantum wells depends on the doping scheme in and around the waveguide. It is therefore highly desirable to design a structure that allows strong electric fields across the wells as a function of voltage, provided that the fields are less than breakdown strength. By increasing the available range of electric field in the wells, the bias voltage is reduced, and extinction efficiency is increased. Furthermore, negative chirp at longer wavelengths becomes attainable with more acceptable bias. In overly wide or shallow wells, however, high fields will destroy the exciton, and the structure will begin to exhibit less desirable properties similar to that of bulk material [30].

Our experimental results, which indicate that an 80 Å well has better negative chirp characteristics than a 65 Å well, are in keeping with purely theoretical calculations [31]. Slightly wider wells could further improve performance, but as demonstrated in Figs. 4 and 5, excitons are more easily quenched in wider wells, and in a well that is too wide the material properties will become bulk-like.

Deeper wells will have greater exciton strength, and might allow for shorter devices, but deeper wells are also more likely to suffer from saturation or poor RF perfor-

mance due to increased carrier escape times. The times for carrier escape by thermionic and tunneling mechanisms increase with increased well depth. Various mechanisms [5,32] have been proposed in order to maximize carrier sweep out time with minimal electric field, but such design considerations are beyond the scope of this paper.

The fact that negative chirp can be obtained in QW modulators, but not in bulk material modulators, stems from the presence of an exciton peak in the QW band-edge absorption spectra. The Kramers–Kronig integral (Eq. (3)) can be broken into a sum of two parts [31,33]: wavelengths longer than the operating wavelength (λ_0), and wavelengths shorter than the operating wavelength (λ_0). The part that is longer than the operating wavelength has a negative numerator and contributes negative values to the calculated change in index (ideal for negative chirp). The part that is at wavelengths shorter than the operating wavelength has a positive numerator, and contributes to positive index change (for positive absorption change). The numerator in the Kramers–Kronig transform of Eq. (3) also acts as a sampling window so that $\Delta\alpha$ near the wavelength in question make the most significant contributions to Δn. In bulk material, the large positive contribution from the short wavelength part of the Kramers–Kronig integral generally results in an overall net positive index change and hence a positive chirp, even in regions very close to the band-edge where insertion-loss is prohibitively high. In contrast, the QW band-edge absorption spectra have exciton peaks governed by the QCSE so that $\Delta\alpha_{abs}$ of Eq. (3) changes sign as a function of wavelength. This change in sign results in a short wavelength part of the Kramers–Kronig integral for Δn that is relatively small in magnitude compared to the negative, long wavelength part of the integral. Thus, with proper design, negative chirp is attainable with low insertion-loss, at lower voltages (V_0) [5], and over broad tuning ranges [34].

3.4. Quantum-well-intermixed material performance

The QWs discussed in this paper were also blue-shifted by QWI, as shown in Figs. 4 and 5. The QWI process is an ideal approach for monolithically integrated laser-EAM modulators [24,35]. The effect of QWI on modulator characteristics such as chirp, extinction, and insertion-loss, has not previously been investigated in depth. In Figs. 3 and 4, QWI reduces the magnitude of the exciton peak, and increases the decay of the exciton as a function of applied bias. It is therefore important to consider the effect that QWI will have on the performance of a QWI modulator.

In the case of both the 65 Å and 80 Å wells, the effect of QWI on modulator performance was detrimental, but in no way prohibitive. Figs. 9 and 10 show chirp, extinction, and insertion-loss for the 80 Å wells intermixed by 40 and 76 nm, respectively. The range of biases (V_0) necessary to obtain negative chirp across a 30 nm range do not significantly change in the QWI wells. Intermixing by an amount

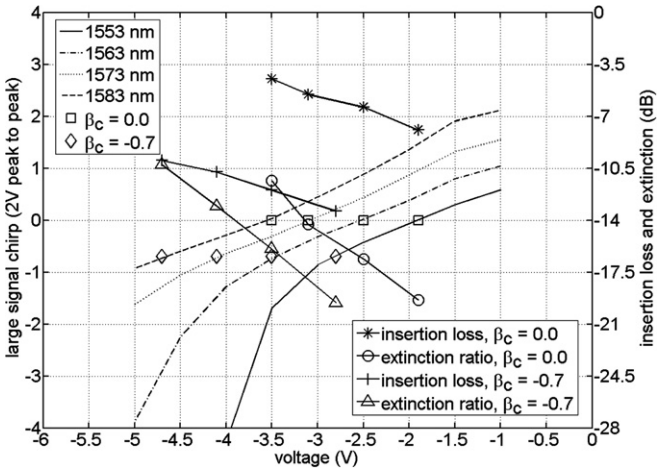

Fig. 9. Projected large signal chirp on a 2 V p–p signal for the 80 Å material after intermixing by 40 nm from 1548 nm to 1508 nm. The performance at 0 chirp is not significantly different from the as-grown material. Chirp of −0.7 is also available across the full range of wavelengths but the extinction vs insertion-loss ratio for $\beta_c = -0.7$ is not as favorable as it was for the as-grown material (Fig. 7).

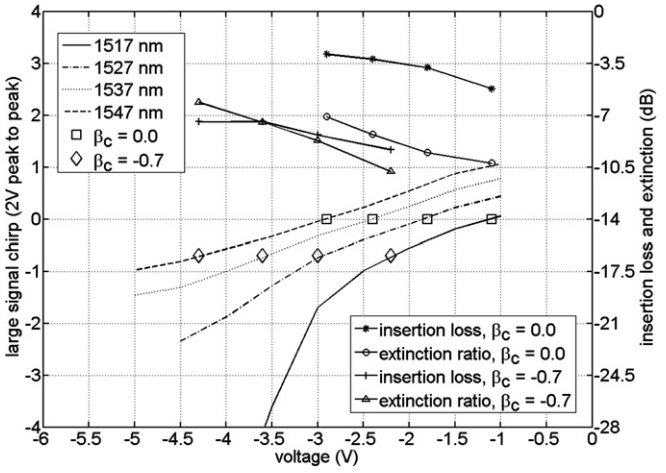

Fig. 10. Projected large signal chirp on a 2 V p–p signal for the 80 Å material after intermixing by 76 nm from 1548 nm to 1472 nm. The $\beta_c = -0.7$ ratio of extinction to insertion-loss is poor for the entire range of wavelengths, and both the extinction-ratio and insertion-loss have significantly decreased.

suitable for a modulator, e.g., 40 nm, results in no real change in expected modulator performance at 0 chirp. For $\beta_c = -0.7$, however, the insertion-loss increases noticeably, and the ratio of extinction to insertion-loss is less favorable, especially at longer wavelengths. Intermixing to the maximum extent possible (76 nm) results in very significant reduction of the exciton peak (Fig. 4) and as a result both the extinction and insertion-loss are significantly reduced. In the highly intermixed material, (Fig. 10) the $\beta_c = -0.7$ insertion-loss is approximately equal to the extinction-ratio across the entire range of wavelengths. This degradation in performance is due to the weakening of the exciton peak by the QWI process.

One possible method for improving the characteristics of the intermixed material would be to slightly increase the depth of the 80 Å wells. A deeper well would have better carrier confinement, and the intermixed material should then have an absorption-edge more similar to the as-grown material of Fig. 5.

4. Conclusion

The band-edge absorption spectra intrinsic to several different epitaxial layer structures have been collected by photocurrent spectroscopy. These band-edge absorption spectra have been used to predict the optimal conceivable performance of modulators fabricated from similar materials. Negative chirp appears unattainable in bulk EAMs that rely on the Franz–Keldysh effect. Negative chirp is attainable in QW structures, but 80 Å wells exhibit negative chirp over a wider tuning range and at lower biases than 65 Å wells, which is in keeping with theoretical predictions. The wider 80 Å wells were also shallower than the 65 Å wells, but the exciton peak was nonetheless resolvable at high biases, so that operation with negative chirp is attainable over a wide range (30 nm) of wavelengths. Wells that are much wider than 80 Å, or wells that are too shallow, will become increasingly ''bulk-like'', and will be poor candidates for EAM design. The optimum band-edge absorption spectra for an EAM modulator has maximum Stark shift with minimum exciton decay, thereby enabling high extinction as well as negative chirp over a wide tuning range. For optimal performance, the material should be incorporated into an EAM waveguide so as to maximize overlap with the optical mode and maximize the bias induced electric field.

QWI lowers carrier confinement and reduces the exciton peak, and therefore reduces modulator performance. The degree of quantum QWI necessary for optimal modulator absorption-edge placement, however, is small enough that the performance of QWI EAMs is acceptable. For QWI applications requiring passive material, the shallower 80 Å wells discussed in this paper may be less suitable than the 65 Å wells because the band-edge of the 85 Å wells cannot be blue-shifted as far as the narrower, deeper, 65 Å wells.

For fabrication of PICs in which passive waveguide regions are necessary, QWI has one significant advantage over other integration platforms. QWI PICs can be designed with EAMs having band-edges with relatively small blue-shifting from the lasing wavelength. The passive regions of the PIC can then be intermixed further [3] to minimize loss outside the modulator. In contrast, integration platforms that allow only two band-edges may need to compromise with EAM material that is detuned further from the lasing wavelength, thereby minimizing loss in ''passive'' waveguide regions. A modulator with larger detuning will, in general, result in higher biases, lower extinction, and larger chirp.

Acknowledgements

This work was supported in part by ARMY Grant DAAD19-03-1-0058. G.B. Morrison was supported in part by an NSERC Canada PDF.

References

[1] Studenkov PV, Xia F, Forest SR. Photonic integration using asymmetric twin-waveguide (atg) technology: Part II-Devices. IEEE J Sel Topics Quant Electron 2005;11(12):30–42.
[2] Studenkov PV, Xia F, Forest SR. Photonic integration using asymmetric twin-waveguide (ATG) technology: Part-I: concepts and theory. IEEE J Sel Topics Quant Electron 2005;11(1):15–29.
[3] Skogen EJ, Raring JW, Barton J, DenBaars S, Coldren LA. Post-growth control of the quantum-well band edge for the monolithic integration of widely-tunable lasers and electroabsorption modulators. IEEE J Sel Topics Quant Electron 2003;9(5):1183–90.
[4] Ramdane A, Krauz P, Rao EVK, Hamoudi A, Ougazzaden A, Robein D, et al. Monolithic integration of InGaAsP-InP strained layer distributed feedback laser and external modulator by selective quantum-well interdiffusion. IEEE Photon Technol Lett 1995;7(9):1016–8.
[5] Delprat D, Ramdane A, Ougazzaden A, Nakajima H, Carré M. Integrated multiquantum well distributed feedback laser-electroabsorption modulator with a negative chirp for zero bias voltage. Electron Lett 1997;33(1):853–5.
[6] Sysak MN, Barton JS, Johansson LA, Raring JW, Skogen EJ, Mašanović ML, et al. Single-chip wavelength conversion using a photocurrent-driven EAM integrated with a widely tunable sampled-grating DBR laser. IEEE Photon Technol Lett 2004;16(9):2093–5.
[7] Steinmann P, Borchert B, Stegmüller B. Improved behavior of monolithically integrated laser/modulator by modified identical active layer structure. IEEE Photon Technol Lett 1997;9(12):1561–3.
[8] Sysak MN, Barton JS, Raring JW, Dummer M, Tauke-Pedretti A, Blumenthal DJ, et al. 10 Gb/s photocurrent driven, widely tunable electroabsorption based wavelength converter. In: Optical fiber communication conference and exposition. Anaheim, CA, 2005, OtuM4.
[9] Nam ES, Lee SW, Jang DH, Lee JG, Pyun KE. Monolithis integration of a 1.55-μm strained multiple-quantum-well distributed feedback laser and quantum-confined stark-effect modulator by metal organic vapor-phase epitaxy using an InP-buffer-layer incorporated butt coupling scheme. J Korean Phys Soc 2000;36(4):228–32.
[10] Takeuchi H, Tsuzuki K, Sato K, Yamamoto M, Itaya Y, Sano A, et al. Very high-speed light-source module up to 40 Gb/s containing an MQW electroabsorption modulator integrated with a DFB laser. IEEE J Sel Topics Quant Electron 1997;3(3):336–43.
[11] Aoki M, Suzuki M, Sano H, Kawano T, Ido T, Taniwatari T, et al. InGaAs/InGaAsP MQW electroabsorption modulator integrated with a DFB laser fabricated by band-gap energy control selective area MOCVD. IEEE J Quantum Electron 1993;29(6):2088–96.
[12] Coldren LA, Corzine SW. Diode lasers and photonic integrated circuits. New York: John Wiley and Sons; 1995, p. 355–9.
[13] Alping A, Coldren LA. Electrorefraction in GaAs and InGaAsP and its application to phase modulators. J Appl Phys 1987;61(7):2430–3.
[14] Chuang SL. Physics of optoelectronic devices. New York: John Wiley and Sons; 1995, p. 557–72.
[15] Moseley AJ, Robbins DJ, Marshall AC, Kearley MQ, Davies JI. Quantum confined Stark effect in InGaAs/InP single quantum wells investigated by photocurrent spectroscopy. Semicond Sci Technol 1989;4(3):184–90.
[16] Wood TH. Direct measurement of the electric-field-dependent absorption coefficient in GaAs/AlGaAs multiple quantum wells. Appl Phys Lett 1986;48(21):1413–5.

[17] Charbonneau S, Koteles ES, Poole PJ, He JJ, Aers GC, Haysom J, et al. Photonic integrated circuits fabricated using ion implantation. IEEE J Sel Topics Quantum Electron 1998;4(4):772–93.
[18] Morrison GB, Skogen EJ, Wang CS, Raring JW, Chang Y, Sysak MN, et al. Photocurrent spectroscopy for quantum well intermixed photonic integrated circuit design. IEEE Photon Technol Lett 2005; 17(7):1414–6.
[19] Morrison GB, Raring JW, Skogen EJ, Wang CS, Coldren LA. Photocurrent spectroscopy analysis of widely tunable negative-chirp quantum-well intermixed laser-modulator transmitters. Appl Phys Lett 2005;86(71118):1–3.
[20] Kim I, Jang DH. Electroabsorption spectroscopy analysis of quantum-well modulator extinction and chirp. IEEE Photon Technol Lett 2004;6(11):2463–5.
[21] Gokhale MR, Studenkov PV, Ueng-McHale J, Thomson J, Yao J, van Saders J. Uncooled, 10 Gb/s 1310 nm electroabsorption modulated laser. In: Optical fiber communication conference 2003, PD-42.
[22] Raring JW, Skogen EJ, Johansson LA, Sysak MN, DenBaars SP, Coldren LA. Widely tunable negative-chirp SG-DBR laser/EA-modulated transmitter. IEEE J Lightwave Technol 2005;23(1):80–6.
[23] Miller DAB, Chemla DS, Damen TC, Gossard AC, Wiegmann W, Wood TH, et al. Electric field dependence of optical absorption near the band gap of quantum-well structures. Phys Rev B 1985;32(2): 1043–60.
[24] Skogen EJ, Raring JW, Morrison GB, Wang CS, Lal V, Masanovic ML, et al. Monolithically integrated active components: a quantum-well intermixing approach. IEEE J Sel Topics Quant Electron 2005; 11(2):343–55.
[25] Agrawal GP. Fiber-optic communications systems. New York: John Wiley and Sons; 1997, p. 425–431.
[26] Henry CH, Logan RA, Bertness KA. Spectral dependence of the change in refractive index due to carrier injection in GaAs lasers. J Appl Phys 1981;52(7):4457–61.
[27] Skogen EJ, Wang CS, Raring JW, Morrison GB, Coldren LA. Small footprint, high-efficiency, integrated transmitters for high-speed optical interconnect applications. Integrated photonics research, San Francisco 2004, ITHD2.
[28] Mason B, Fish GA, DenBaars SP, Coldren LA. Widely tunable sampled grating DBR laser with integrated electroabsorption modulator. IEEE Photon Technol Lett 1999;11(6):638–40.
[29] Johansson LA, Akulova YA, Fish GA, Coldren LA. Sampled-grating DBR laser integrated with SOA and tandem electroabsorption modulator for chirp-control. IEE Electon Lett 2004;40(1):70–1.
[30] Miller DAB, Chemla DS, Schmitt-Rink S. Relation between electroabsorption in bulk semiconductors and in quantum wells: the quantum-confined Franz–Keldysh effect. Phys Rev B 1986;33(10): 6976–82.
[31] Yamanaka T, Wakita K, Yokoyama K. Potential chirp-free characteristics (negative chirp parameter) in electroabsorption modulation using a wide tensile strained quantum well structure. Appl Phys Lett 1996;68(22):3114–6.
[32] Sahara R, Morito K, Sato K, Kotaki Y, Soda H, Okazaki N. Strongly improved frequency response at high-optical input powers from InGaAsP compensated strain MQW electroabsorption modulators. IEEE Photon Technol Lett 1995;7(9):1004–6.
[33] Matsuda M, Morito K, Yamaji K, Fujii T, Kotaki Y. A novel method for designing chirp characteristics in electroabsorption MQW optical modulators. IEEE Photon Technol Lett 1998;10(3):364–6.
[34] Raring JW, Skogen EJ, DenBaars SP, Coldren LA. Demonstration of negative chirp characteristics over wide wavelength range using monolithically integrated SG-DBR laser/electroabsorption modulator. IEE Electron Lett 2004;40(25):1599–600.
[35] Qiu BC, Liu XF, Ke ML, Lee HK, Bryce AC, Aitchinson JS, et al. Monolithic fabrication of 2×2 crosspoint switches in InGaas-InAlGaAs multiple quantum wells using quantum well intermixing. IEEE Photon Technol Lett 2001;13(12):1292–4.

40-Gb/s Widely Tunable Low-Drive-Voltage Electroabsorption-Modulated Transmitters

James W. Raring, *Member, IEEE,* Leif A. Johansson, *Member, IEEE,* Erik J. Skogen, *Member, IEEE,* Matthew N. Sysak, *Member, IEEE,* Henrik N. Poulsen, Steven P. DenBaars, *Fellow, IEEE,* and Larry A. Coldren, *Fellow, IEEE*

Invited Paper

***Abstract*—We present the first 40-Gb/s widely tunable electroabsorption modulator (EAM)-based transmitters. The sampled-grating Distributed Bragg Reflector (SG-DBR) laser/EAM devices were fabricated using a multiple-band-edge-quantum-well-intermixing (QWI) technique, which requires only simple blanket regrowth and avoids disruption of the axial waveguide. Devices were fabricated from two different multiple quantum well (MQW) active-region designs for direct comparison. The SG-DBR lasers demonstrated 30 nm of tuning with output powers up to 35 mW. The integrated QW EAMs provided 3-dB optical modulation bandwidths in the 35–39 GHz range, low-drive voltage (1.0–1.5 V_{PtoP}), and low/negative-chirp operation. Bit-error-rate measurements at 40 Gb/s demonstrated 0.2–1.1 dB of power penalty for transmission through 2.3 km of standard fiber.**

***Index Terms*—Chirp, electroabsorption modulators (EAMs), laser tuning, optical-fiber communication, quantum-well-intermixing (QWI), semiconductor lasers, wavelength-division multiplexing (WDM).**

I. Introduction

ELECTROABSORPTION-MODULATED lasers are candidate sources for 40-Gb/s very-short-reach (VSR) router-to-router interconnect applications, as they are compact, potentially low-cost, and can facilitate low-drive voltages with high-modulation bandwidth [1]. The monolithic integration of electroabsorption modulators (EAMs) with widely tunable lasers allows for inventory reduction and wavelength agile functionality in communication systems based on wavelength-division multiplexing (WDM). An EAM making use of a quantum-well (QW) absorber region exploits the quantum-confined Stark effect offering increased efficiency over bulk Franz–Kelydsh-type EAMs [2]. Additionally, QW-EAMs can enable negative-chirp operation for efficient transmission at high bit-rates, where fiber dispersion is increasingly important.

Manuscript received June 14, 2006; revised September 28, 2006.

J. W. Raring, L. A. Johansson, E. J. Skogen, M. N. Sysak, H. N. Poulsen, and L. A. Coldren are with the Electrical and Computer Engineering Department, University of California, Santa Barbara, CA 93106-2030 USA (e-mail: jraring@engineering.ucsb.edu; leif@ece.ucsb.edu; skogen@engineering.ucsb.edu; mnsysak@engineering.ucsb.edu; henrik@ece.ucsb.edu; coldren@ece.ucsb.edu).

S. P. DenBaars is with the Materials Department, University of California, Santa Barbara, CA 93106-2030 USA (e-mail: denbaars@engineering.ucsb.edu).

Digital Object Identifier 10.1109/JLT.2006.886722

We present the first QW-EAM-based 40-Gb/s widely tunable transmitter devices. Previous reports of 40-Gb/s QW-EAMs either did not include an integrated laser or included a single-frequency distributed-feedback laser [1], [3], [4]. In this paper, we demonstrate widely tunable transmitters fabricated using a simple and robust quantum-well-intermixing (QWI) processing platform to avoid the traditional fabrication complexity necessary for the integration of negative-chirp EAMs with diode lasers.

The conventional method for the realization of a single-chip-diode laser/QW-EAM transmitter involves the selective removal of the as-grown multiple quantum well (MQW) for use in laser gain regions followed by the regrowth of an MQW with a higher band edge for use in the EAMs. This method is commonly referred to as butt-joint regrowth [1], [5]. Although the butt-joint regrowth process does facilitate high flexibility, it requires etching and defining a regrowth interface in the core of the optical waveguide. The difficulty associated with matching the thickness and achieving the desired composition to avoid reflection and loss at the interface is great [5]. Another technique used to realize multiple band edges across a wafer is selective-area growth. However, the abruptness of the transition region is limited by the surface diffusion of the growth constituents, which may be on the order of tens of micrometers. Additionally, the optical mode overlap with the MQW may not be ideal in all sections due to the thickness variation. The relatively simple QWI process employed in this work enables the precise placement of the band edge of each component within the device, allowing for blue-shifted QWs to remain in the modulator while leaving the axial waveguide undisturbed.

The widely tunable transmitters presented in this paper consists of an EAM with partially intermixed QWs and a sampled-grating DBR (SG-DBR) laser with as-grown QWs in the gain region and severely intermixed QWs in the passive and tuning sections. We explore two different centered-multiple QW (c-MQW) active-region designs. The first design uses ten 6.5-nm wells to yield a confinement factor of 12.6% while the second design makes used of fifteen 8.0-nm wells to yield a confinement factor of 25.0%. The increased number of wells in the 15 MQW is expected to result in improved EAM efficiency at the expense of somewhat degraded laser performance.

The 10- and 15-MQW transmitters exhibit 30 nm of tuning with high output power. The 10-MQW EAMs demonstrated

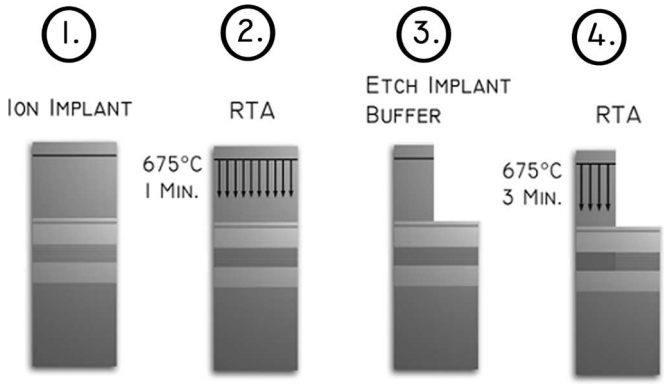

Fig. 1. Step-by-step schematic of the intermixing process. From left to right: ion implantation; RTA; buffer-layer removal; and further annealing.

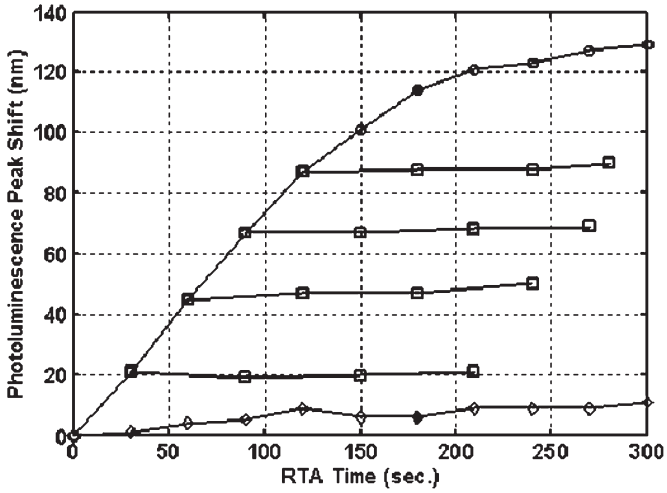

Fig. 2. PL peak shift as a function of anneal time, showing the initial linear increase in the peak shift and the complete halting of the peak shift for samples for which the implant buffer layer has been etched. Symbols indicate nonimplanted (triangles), implanted (circles), and samples with partial anneal followed by the removal of the implant buffer layer (squares).

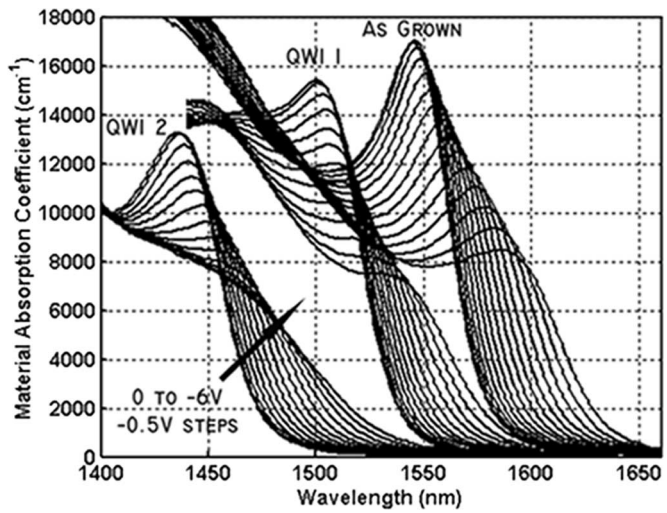

Fig. 3. Material-absorption coefficient versus wavelength for photodiodes fabricated from as-grown material and material intermixed to two different levels.

3-dB optical modulation bandwidths of up to 39 GHz, 1.5-V_{PtoP} drive voltages, power penalties of 0.2–0.5 dB for 40-Gb/s transmission through 2.3 km of fiber across the tuning range of the laser. The 15-MQW EAMs demonstrated 3-dB optical modulation bandwidths of up to 35 GHz, 1.0-V_{PtoP} drive voltages, power penalties of 0.7–1.1 dB for 40-Gb/s transmission through 2.3 km of fiber across the tuning range of the laser.

II. Background

A. QWI Integration Platform

QW intermixing allows for the strategic postgrowth tuning of the QW band edge using a relatively simple procedure. Since this technique enables the employment of c-MQW active regions for maximized modal gain lasers and blue-shifted QWs for use in EAMs, QWI breaks the complexity tradeoff associated with the flexible butt-joint regrowth and SAG integration schemes. QWI makes use of the metastable nature of the compositional gradient found at heterointerfaces. The natural tendency for materials to interdiffuse is the basis for the intermixing process. Since QWI does not change the average composition but only slightly changes the compositional profile, there is a negligible index discontinuity at the interface between adjacent sections. This eliminates parasitic reflections that can degrade performance.

In this paper, we employ the implant-enhanced interdiffusion QWI technique illustrated in the step-by-step diagram of Fig. 1. This method has been shown to have good spatial resolution and is controllable using anneal time, temperature, and implant dose [6]. Furthermore, we can achieve any number of QW band edges in the structure using selective removal of the catalyst. In the first step of Fig. 1, a selective P^+ implantation is performed to introduce point defects in an unintentionally doped sacrificial InP implant buffer layer grown above the MQW active region. Next, a rapid-thermal-anneal (RTA) step is performed to shift the MQW band edge to that desired in the EAM regions. Once the EAM band edge is reached, the point defects are removed in the EAM region by selective removal of the InP implant buffer layer. The anneal is then continued until the desired band edge is reached for the passive and tuning sections. Once all the desired band edges have been defined, the remaining buffer layer is removed and the p-cladding regrowth is performed. The buffer-layer etch and RTA sequence can be repeated to achieve any number of band edges across the wafer. This capability is demonstrated in Fig. 2 with a plot of photoluminescence (PL) peak versus anneal time for samples with and without implantation and samples with the implant buffer layer removed at intermediate anneal steps.

To realize an optimized QW-EAM, it is crucial that the QWI process does not significantly degrade the absorption characteristics of the as-grown MQW. This effect was studied using photocurrent spectroscopy on photodiodes fabricated with as-grown material ($\lambda_{PL} = 1545$ nm) and material intermixed to two different levels, QWI 1 ($\lambda_{PL} = 1500$ nm) and QWI 2 ($\lambda_{PL} = 1430$ nm). The absorption coefficient contours versus wavelength for photodiodes biased from 0 to -6 V in -0.5-V increments are shown in Fig. 3. The photodiode

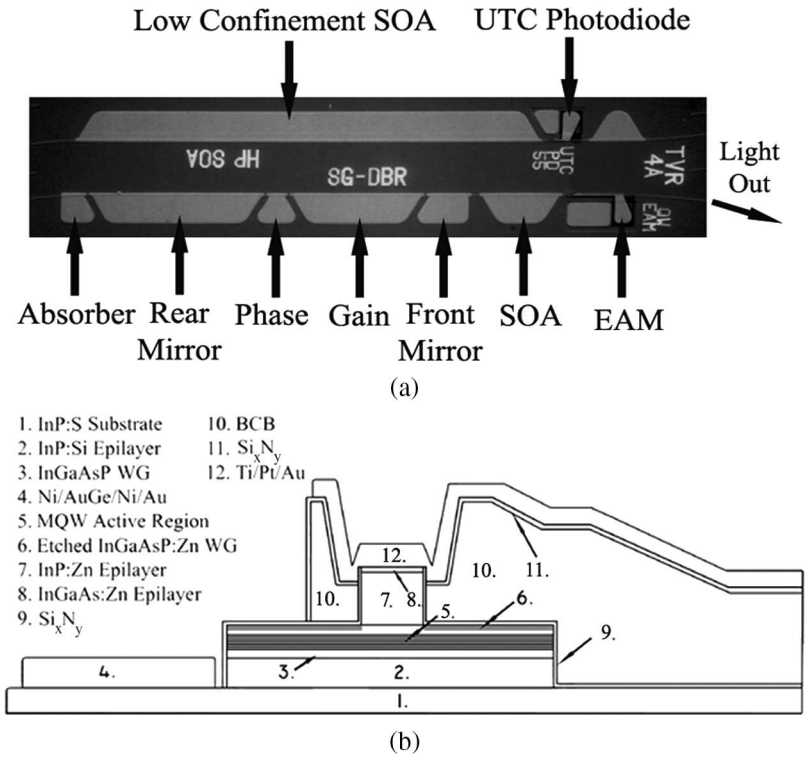

Fig. 4. (a) Top-view SEM of the device architecture, where the SG-DBR/EAM transmitter device is positioned on the lower ridge. (b) Cross-sectional schematic of modulator sections.

devices contained seven 6.5-nm compressively strained QWs and eight 8.0-nm barriers sandwiched between two 120-nm waveguide layers. As expected, the exciton peak shifts to shorter wavelengths as the degree of intermixing is increased and the quantized energy levels are separated. The exciton strength is somewhat decreased with intermixing due to the wider/shallower nature of the intermixed well, which reduces the exciton confinement. However, the exciton remains as a dominant characteristic in the absorption spectra, especially in the material shifted by only $\sim$45 nm (QWI 1), which represents a band-edge detuning in the vicinity required for optimal EAM performance.

B. Device Architecture

The transmitters reported here were part of integrated-transceiver devices. A top-view scanning-electron-micrograph (SEM) image of the parallel-surface-ridge waveguide architecture is shown in Fig. 4(a). The optical receiver [upper ridge in Fig. 4(a)] consists of a low-confinement factor semiconductor optical amplifier (SOA) followed by a unitraveling-carrier (UTC) photodiode. In this paper, we focus on the optical transmitter [lower ridge in Fig. 4(a)] consisting of a five-section SG-DBR laser followed by a 250-μm-long output SOA and a 125-μm-long EAM. The five sections of the SG-DBR laser are, from left to right in Fig. 4(a): backside absorber; rear mirror; phase; gain; and front mirror. The output waveguide is simultaneously flared from 3 to 5.5 μm in width and curved to reach a final facet angle of 6.5° to minimize reflections.

C. SG-DBR Laser

The SG-DBR mirror is a special form of the DBR mirror, where the gratings are periodically blanked in order to create a comblike reflectivity spectrum [7]. The lithographically defined SG mirrors make this laser ideal for monolithic integration. By differing the sampling periods in the front and back mirrors, the peak reflectivity spacing of the mirrors will differ so that only one set of reflectivity peaks is aligned within the desired tuning range. By differentially tuning the front and back mirrors, a small amount adjacent reflectivity peaks can be aligned and the laser will operate at this new widely spaced wavelength. The simultaneous tuning of front and back mirrors allows wavelength coverage between mirror reflectivity peaks. The phase section provides cavity-mode tuning, which ensures that the laser cavity mode is aligned with the mirror reflectivity peaks. The tuning in the mirrors and phase sections is based on carrier injection, producing a negative change in refractive index.

D. EAM

In an EAM, a reverse bias is used to shift the band edge of the modulator section to a lower energy, thereby increasing the absorption of that region. In our case, QWI only smears the interfaces between the QWs and barriers, such that the QWs still remain intact after the intermixing, although slightly shallower and rounded. To achieve high-speed operation, we minimize the capacitance associated with the EAM. The low-k dielectric benzocyclobutene (BCB) is defined underneath the p-electrode, a short dry etch is performed adjacent to the ridge to eliminate a thin diffused Zn layer, and the diode length and

p-electrode area are minimized. A cross-sectional schematic of the EAM is shown in Fig. 4(b).

III. Process

Two different epitaxial-base-structure MQW designs were explored in this paper. The first consisted of 10 InGaAsP 6.5-nm compressively strained (0.9%) QWs and 11 8.0-nm tensile-strained (0.3%) InGaAsP barriers yielding a conduction-band offset of 115 meV. The 10 MQW was centered within two 105-nm 1.3Q waveguide layers designed for maximum modal confinement (12.6%). The second MQW design consisted of 15 InGaAsP 8.0-nm compressively strained (0.6%) QWs and 16 8.0-nm tensile-strained (0.3%) InGaAsP barriers yielding a conduction-band offset of 85 meV. The lower band offset of the 15-MQW design was intended to promote the uniform filling of carriers in the wells under forward bias. The 15 wells were centered within two 60-nm 1.3Q waveguide layers designed for maximum modal confinement (25.0%). The metal-organic chemical-vapor-deposition grown epitaxial base structures initiated on a conducting InP substrate. The growth sequence began with 1.8 μm of InP:Si, followed by the c-MQW active region, a 25-nm InP regrowth layer, a 20-nm 1.3Q stop etch, and a 450-nm InP implant buffer layer.

A 500-nm Si_xN_y mask layer was deposited using plasma-enhanced chemical vapor deposition and lithographically patterned such that it remained only over the active regions of the samples. Next, ion implantation was performed using P^+ at an energy of 100 keV, with a dose of 5E14 cm^{-2}, yielding a damage range of 90 nm, at a substrate temperature of 200 °C. The point defects created during the P^+ implant were then partially diffused through the structure using a 675-°C RTA step to shift the as-grown MQW band edge ($\lambda_{\rm PL} = 1540$ nm) to the desired EAM band edge ($\lambda_{\rm PL} = 1505$ nm). The implant buffer layer above the EAM sections was removed using a wet-etching process designed to terminate on the 1.3Q stop-etch layer. The samples were then subjected to an additional RTA step to severely blue-shift the passive and tuning sections, where the implant buffer layer remained. The resulting peak PL wavelength of these passive sections was 1440 nm in the 10-MQW sample and 1460 nm in the 15-MQW sample. Upon completion of the QWI process, the PL spectra of the three different bandgap regions was characterized from the actual 10-MQW and 15-MQW device samples. As shown in Fig. 5(a) and (b), the as-grown and EAM PL peaks are nearly identical in the 10- and 15-MQW devices.

Following the QWI process, two blanket regrowth and etch sequences were performed for the definition of the low-confinement SOA and UTC photodiode-receiver structures. Details of these structures can be found elsewhere [8], [9]. Finally, the InP:Zn cladding and the InGaAs:Zn contact layers were grown. Standard lithography and etch techniques were carried out for the definition 3-μm-wide surface-ridge devices. The wafers were thinned; the devices were cleaved into bars and antireflection coated. The die were separated, soldered to aluminum-nitride carriers, and wire bonded for characterization. A scanning electron micrograph (SEM) image of the completed devices mounted on a carrier is shown in Fig. 6.

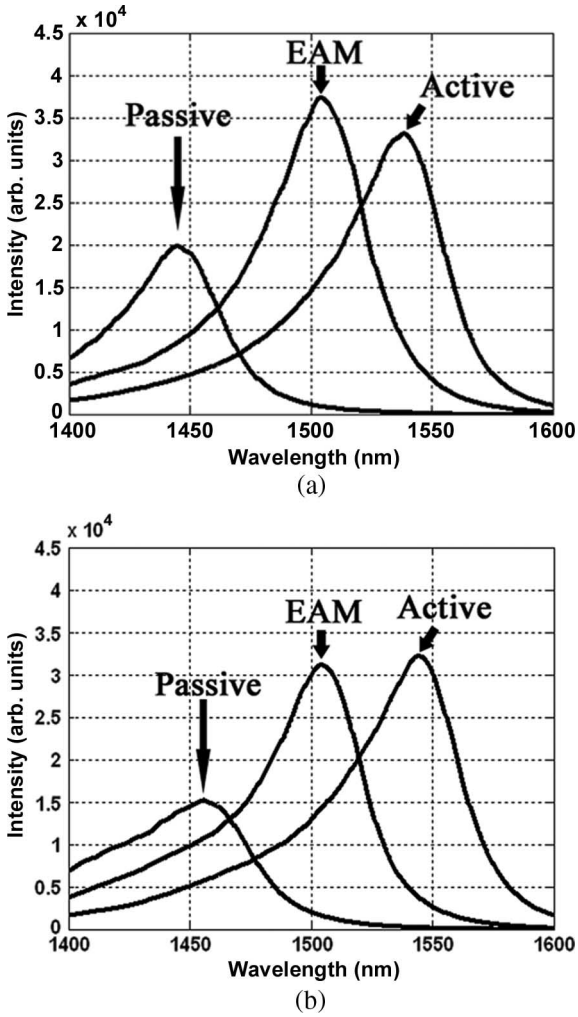

Fig. 5. PL spectra of active, EAM, and passive sections rendered using QWI for the (a) 10-MQW and (b) 15-MQW devices. Data taken from actual device chips previous to regrowth steps.

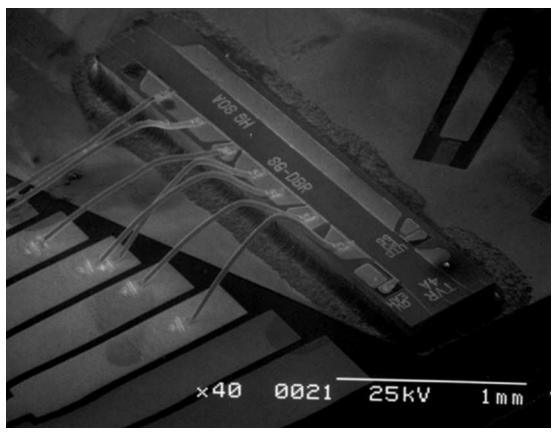

Fig. 6. SEM image of transmitter device mounted on a carrier.

IV. Device Results

To extract the laser parameters and determine the material/processing quality, 3-μm-wide Fabry–Pérot (FP) active and active/passive ridge lasers were fabricated on the same chip as the transmitters and subjected to pulsed testing. The inverse

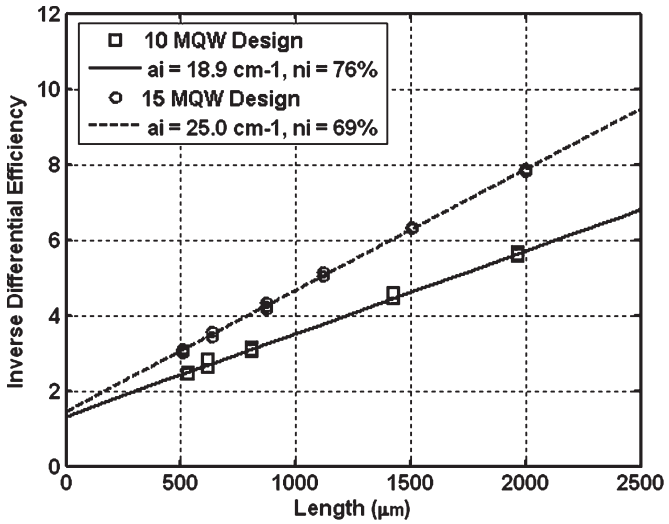

Fig. 7. Plot of inverse differential efficiency versus active FP laser length for lasers fabricated from 10- and 15-MQW base structures.

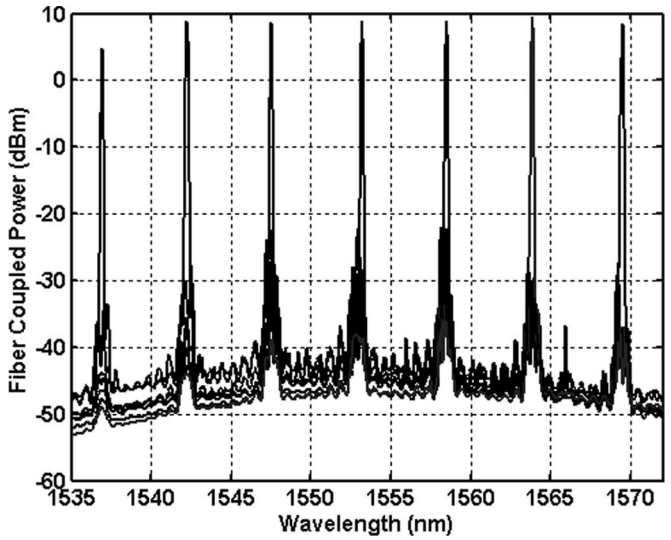

Fig. 8. Superimposed output spectrums tuned to different lasing wavelengths for SG-DBR lasers fabricated from 10-MQW base structure.

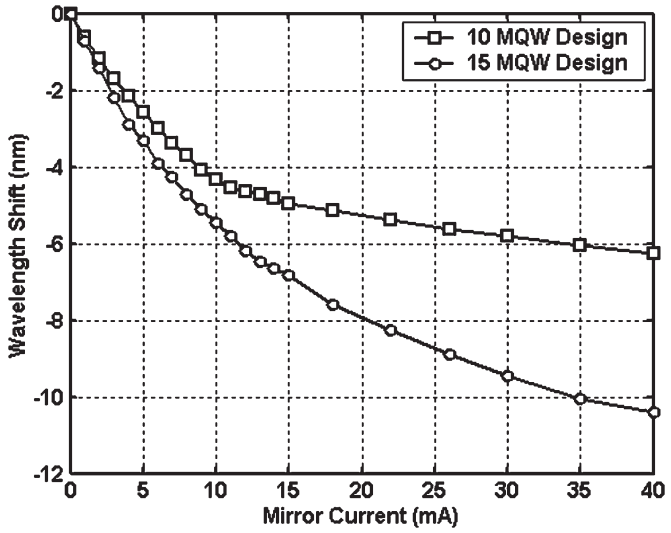

Fig. 9. Wavelength shift versus applied current to front mirror in SG-DBR laser fabricated from 10-MQW and 15-MQW base-structure designs.

differential efficiency is plotted versus active FP laser length in Fig. 7. As shown in the figure, the 10-MQW device demonstrated an injection efficiency (ni) of 76% with a modal loss (ai) of 18.9 cm^{-1} while the 15-MQW device demonstrated an injection efficiency of 69% with a modal loss of 25.0 cm^{-1}. The higher confinement factor of the 15 MQW will lead to an increased modal loss and the greater number of wells will likely reduce the injection efficiency. However, the higher confinement factor of the 15-MQW device will increase the modal gain and somewhat compensate the degraded loss and injection efficiency.

The cleave-back method described in [10] was used to characterize the passive and EAM loss in both MQW designs at a wavelength of 1550 nm. The passive loss was extracted to be 1.8 cm^{-1} and the EAM loss was found to be 13 cm^{-1} in the 10-MQW design. This corresponds to a passive propagation loss of under 1 dB/mm and an unbiased insertion loss of under 1 dB for a 125-μm-long EAM at 1550 nm. The passive propagation loss can largely be attributed to the free-carrier absorption in the p-cladding and waveguide scattering. However, the stated loss value is very acceptable in these devices as the total passive waveguide length is less than 0.5 mm. In the 15-MQW design, the passive loss was extracted to be 4.0 cm^{-1} and the EAM loss was found to be 24.5 cm^{-1}. This corresponds to a passive propagation loss of under 2 dB/mm and an unbiased insertion loss of under 1.5 dB for a 125-μm-long EAM. The increased losses associated with the 15-MQW design is likely caused by the increased band-tail absorption, which results from the $\sim 2\times$ higher confinement within the wells and the slightly lower band-gap energy in the passive sections.

The continuous wave performance of the transmitters was characterized at a stage temperature of 18 °C. The surface-ridge SG-DBR lasers fabricated from the 10-MQW and 15-MQW active-region designs both demonstrated over 30 nm of continuous tuning from wavelengths of 1536–1569 nm. Superimposed output spectrums for lasing wavelengths across the SG-DBR tuning band are shown in Fig. 8 for a 10-MQW device with the laser-gain section and a 250-μm-long output SOA biased at 100 mA. The laser/SOA output light passed through the unbiased EAM and curved/flared waveguide before being coupled into a conical-tipped lensed fiber, with an estimated coupling loss of 4.5 dB. As shown in Fig. 8, the device demonstrated fiber-coupled output powers of up to 10 dBm with a side-mode suppression ratio of over 35 dB for wavelengths from 1542 to 1569 nm. By design, a wavelength shift of over 5.4 nm must be achieved through current injection to tune between the adjacent reflectivity peaks for continuous tuning across the entire supermode spectrum. To characterize the tuning efficiency of both active-region types, the wavelength shift was characterized as a function of current injected into the front mirror. As shown in Fig. 9, both MQW designs easily provide the required 5.4 nm of shift for continuous tuning. However, the 15-MQW design facilitates increased efficiency requiring only $\sim$10 mA to achieve such a value while the 10-MQW design requires $\sim$20 mA for an equivalent shift. The increased tuning efficiency of the 15-MQW device can be explained by the $\sim 2\times$ greater modal

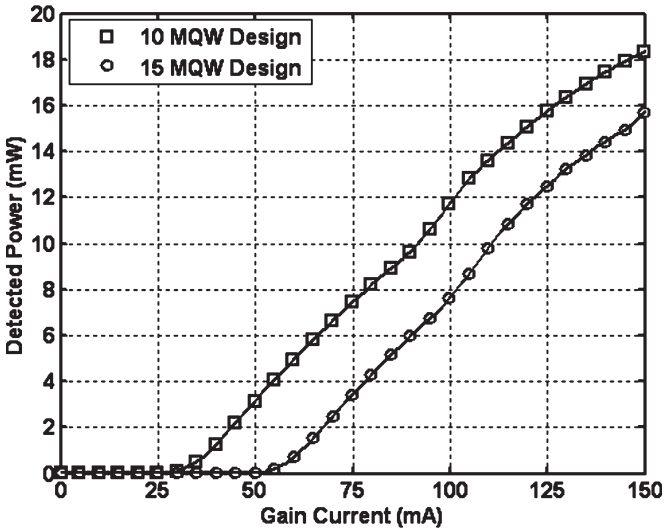

Fig. 10. On-chip laser output power versus gain current for SG-DBR lasers fabricated from the 10-MQW and 15-MQW base-structures designs.

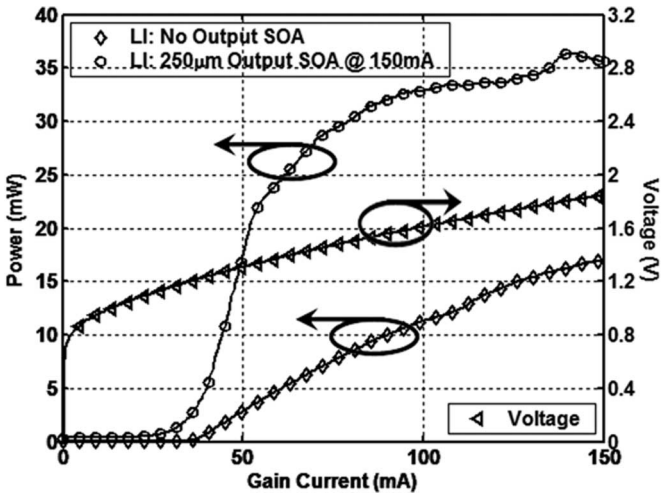

Fig. 11. Output power of 10-MQW SG-DBR laser captured in an integrating sphere for the case with no output SOA and with a 250-μm-long SOA. The voltage is depicted on the right-hand y-axis.

overlap with the lower bandgap QW material than that of the 10-MQW device [11].

By reverse biasing the SOA placed directly after the front mirror of the SG-DBR laser, the on-chip light out versus applied gain current can be measured. This is an excellent means to evaluate the SG-DBR laser performance without the influence of the EAM insertion loss, passive propagation loss, or fiber-coupling loss, since the SOA is positioned immediately following the laser in a continuous waveguide. In Fig. 10, the on-chip light versus current is plotted for SG-DBR lasers fabricated from the 10- and 15-MQW base structures. The 10-MQW device demonstrated a threshold current of $\sim$30 mA while the 15-MQW SG-DBR laser required $\sim$55 mA to reach threshold. The increased threshold current in the 15-MQW device scales closely with the increase in active-region volume over the 10-MQW device indicating that nonuniform pumping of the 15 wells is not significantly degrading the device performance.

The on-chip light versus current measurement does not account for the EAM insertion loss or passive waveguide loss that occurs before the light exits the chip and becomes useful to the external world. To determine the net device output power, the light is detected in an integrating sphere. In this configuration, the light exits the laser or laser/SOA and is then passed through the unbiased EAM, curved/flared output waveguide, and captured into an integrating sphere. Fig. 11 plots the output power and voltage versus gain current (LIV) for SG-DBR lasers fabricated from the 10-MQW active-region design for a device with no output SOA and for a laser with a 250-μm-long SOA positioned after the front mirror. At a gain current of 150 mA, the 10-MQW device demonstrates over 16 mW of output power with no output SOA and over 35 mW of output power with an output SOA biased at 150 mA. At the same gain current, the 15-MQW device produces 12 mW with no output SOA and over 18 mW with an output SOA biased at 150 mA. The lower output power of the 15-MQW device with no SOA is a result of higher modal loss, reduced injection efficiency, and the increased threshold current coupled with the increased passive waveguide loss and EAM insertion loss. The $\sim 2\times$ greater confinement factor of the 15-MQW active-region design results in a reduced SOA saturation power, and hence, further limits the output power of the 15-MQW SG-DBR/SOA device. Thus, the 10-MQW device employing an output SOA demonstrates a significantly higher output power than the 15-MQW device.

The dc extinction from 125-μm-long EAMs in both the 10- and 15-MQW transmitters are shown in Fig. 12(a) and (b), respectively. The 10-MQW device provides 20–30 dB of total extinction with slope efficiencies of 14–16 dB/V for wavelengths from 1536 to 1560 nm. The 15-MQW device provides 25–33 dB of total extinction with slope efficiencies of 19–23 dB/V for wavelengths from 1542 to 1565 nm. The efficient EAM extinction properties are due to the combination of the high confinement factors associated with the c-MQW designs and the intermixing process that allows for precise placement of the modulator band edge.

The small signal-frequency response of the EAMs was measured using a 50-GHz network analyzer. The EAM electrodes were directly probed using ground-signal probes with a 50-Ω termination load. The stage temperature was again maintained at 18 °C. The electrical to optical response of the 10- and 15-MQW 125-μm-long modulators is shown in Fig. 13. The optical 3-dB modulation bandwidth was measured to be 39 GHz in the 10-MQW EAM and 35 GHz in the 15-MQW EAM. The slightly higher modulation bandwidth of the 10-MQW device is a result of a thicker BCB layer used underneath the p-electrode.

The large signal chirp was measured for both device types at 10 Gb/s for wavelengths from 1541 to 1564 nm using Agilent's Time Resolved Chirp software. The chirp parameter was measured as a function of the dc bias applied to the EAM with a 1.5-V_{PtoP} drive applied to the 10-MQW device and 1.0-V_{PtoP} drive applied to the 15-MQW device. As shown in Fig. 14, the chirp parameter is reduced with increasing reverse bias and decreasing wavelength. The measurement demonstrates negative-chirp values for the 15-MQW device at reverse-bias levels ranging from 1.5 to 2.8 V. An issue with the test set limited the measurement range in the 10-MQW device such

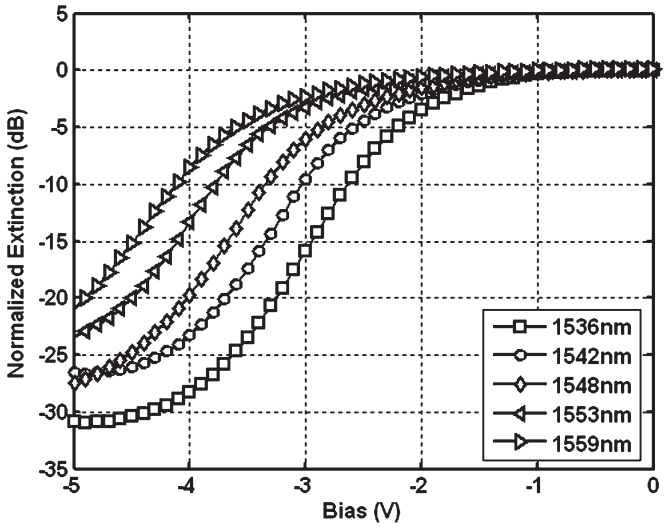

(a)

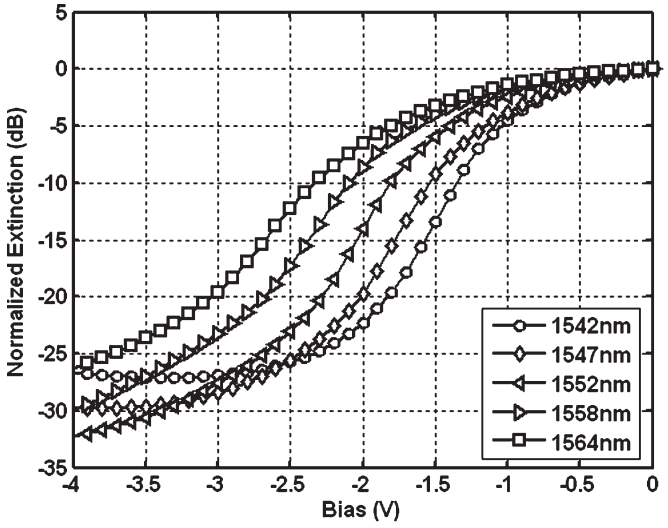

(b)

Fig. 12. Broadband dc extinction of a 125-μm modulator fabricated from the (a) 10-MQW base-structure and (b) 15-MQW base-structure design.

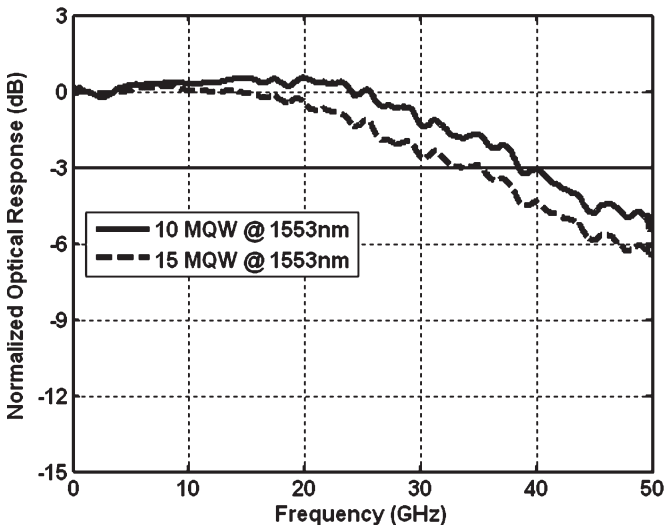

Fig. 13. Electrical-to-optical small signal response of 125-μm EAMs using 10- and 15-MQW designs.

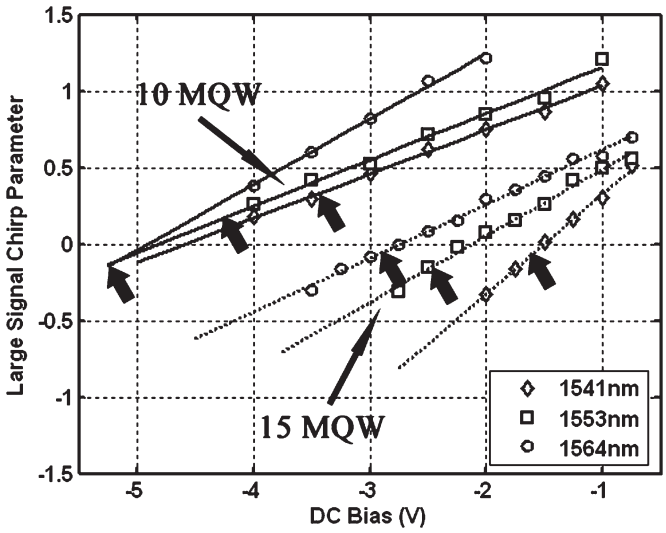

Fig. 14. Broadband large signal chirp parameter of EAMs using the 10-MQW ($1.5\ \mathrm{V_{PtoP}}$) and 15-MQW ($1.0\ \mathrm{V_{PtoP}}$) designs with arrows indicating dc bias used for 40-Gb/s eye diagrams shown in Fig. 15.

that the lowest measured chirp value was 0.15. However, the chirp parameter approaches negative values in the reverse bias range of 4.5–5.0 V. The lower required bias for negative chirp in the 15-MQW design is a result of the wider/shallower wells allowing for a greater Stark shift. The increased required reverse bias with increasing wavelength correlates with that reported in [12] and is perfectly reasonable when considering the proximity of the modulator band edge to the laser-operating wavelength. While the general shape of the absorption curves remain the same, the onset of absorption with reverse voltage increases and the absorption efficiency decreases somewhat with increasing wavelength.

Nonreturn-to-zero eye diagrams were taken at 40 Gb/s with a pseudorandom bit sequence (PRBS) of $2^{31}-1$ over the tuning range of the SG-DBR lasers for both MQW designs. In Fig. 15(a), the back-to-back input eye along with device output eyes are shown for the 10-MQW EAM with a 1.5-$\mathrm{V_{PtoP}}$ drive. As depicted in the figure, extinction ratios (ER) greater than 8.7 dB are demonstrated for wavelengths up to 1560 nm with dc-bias levels ranging from 3.4 to 5.2 V. The average fiber-coupled output power of this device ranged from -5 to 0 dBm. In Fig. 15(b), the back-to-back input eye along with device output eyes are shown for the 15-MQW EAM. Due to the increased efficiency offered by the 15-MQW device, a 1.0-$\mathrm{V_{PtoP}}$ drive was used. As depicted in the figure, the ERs ranged from 6.8 to 7.8 dB for wavelengths from 1542 to 1559 nm with dc-bias levels ranging from 1.6 to 2.6 V. The average fiber-coupled output power of this device ranged from -10 to -5 dBm. The dc bias points for the eye diagrams from both the 10- and 15-MQW EAMs in Fig. 15 are indicated with arrows in Fig. 14 to demonstrate the expected chirp at these operating points. As shown, the predicted chirp for the 10-MQW EAMs range from -0.1 to 0.3, and for the 15 MQW, the chirp parameter is negative in all cases. The discrepancy between the RF ERs shown in Fig. 15 and the dc-extinction-efficiency data of Fig. 12 predicting 14–16 dB/V for the 10-MQW device and 19–23 dB/V for the 15-MQW device indicates the presence of RF losses.

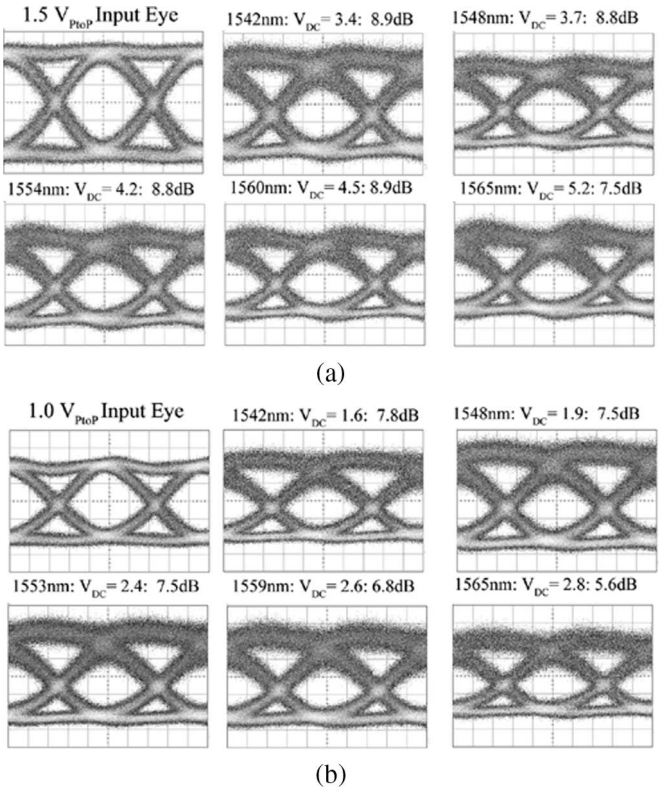

Fig. 15. 40-Gb/s eye diagrams from the (a) 10-MQW device with a 1.5-V_{PtoP} drive and (b) the 15-MQW device with a 1.0-V_{PtoP} drive.

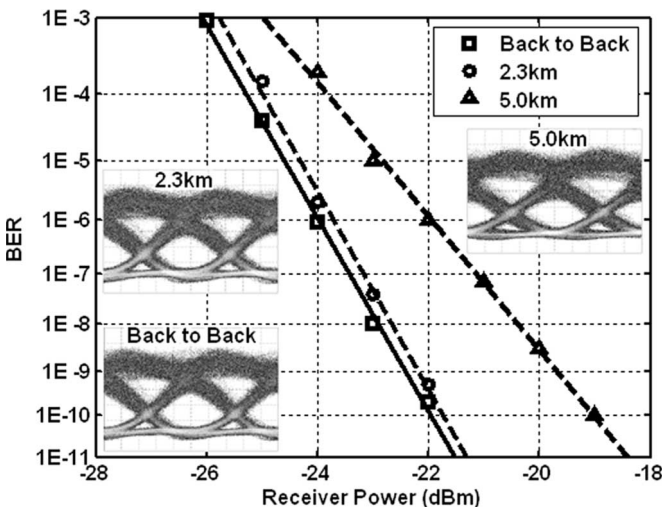

Fig. 16. BER measurements from 10-MQW device at 40 Gb/s with a 1.5-V_{PtoP} drive and a wavelength of 1553 nm. The back-to-back eye diagram along with the eye diagrams after transmission shown as insets.

This is most likely a result of the impedance mismatch between the source and device causing significant electrical reflections. This problem could be corrected with an impedance-matched-electrode design to yield improved RF efficiency.

Bit-error-rate (BER) measurements were made for 40-Gb/s transmission through 2.3 and 5 km of standard Corning SMF-28 fiber. A PRBS of $2^7 - 1$ was used due to a noise floor in the BER test setup that manifested itself at longer word lengths. In Fig. 16, the BER results and the respective eye diagrams are shown for the 10-MQW device at a wavelength of 1553 nm

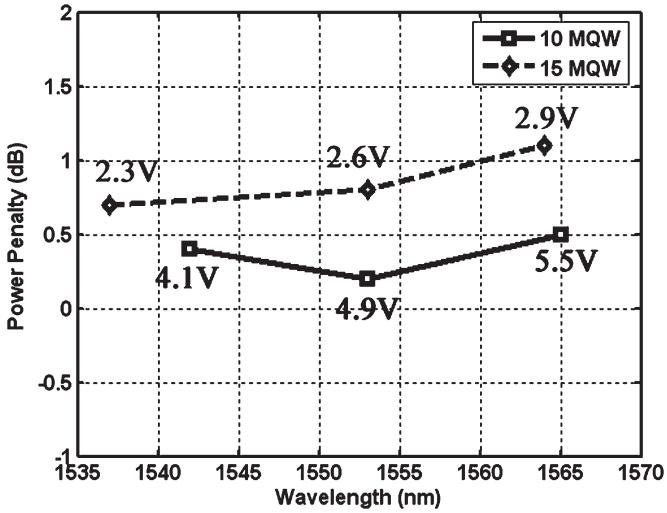

Fig. 17. Broadband 1E-9 BER power penalty for 40-Gb/s transmission through 2.3 km of fiber for both the standard 10-MQW base structure and the modified 15-MQW base-structure design.

using a 1.5-V_{PtoP} drive and a dc bias of 4.9 V. As shown in the figure, the transmitter demonstrated only 0.2 dB of power penalty through 2.3 km and 2.3 dB of penalty through 5.0 km at a BER of 1E-9. Fig. 17 plots the 40-Gb/s power penalty at a BER of 1E-9 for transmission through 2.3 km of fiber across the tuning band of both the 10- and 15-MQW transmitters. The dc operating points are depicted in the figure. The 10-MQW device demonstrates between 0.2 and 0.5 dB of power penalty for transmission through 2.3 km of fiber at wavelengths spanning from 1543 to 1565 nm, while the 15-MQW device demonstrates between 0.7 and 1.1 dB of penalty. According to Fig. 14, the dc operating points are expected to provide slightly negative chirp.

V. Conclusion

We have demonstrated the first widely tunable EAM-based transmitters operating at 40 Gb/s. This paper was made possible by a robust QWI technique for the precise placement of multiple band edges to achieve high-modulation efficiency from relatively short EAMs. Two different active-region designs were explored. The 10-MQW SG-DBR lasers demonstrated threshold currents of $\sim$30 mA, output powers up to 35 mW, and over 30 nm of tuning. The 15-MQW SG-DBR laser demonstrated threshold currents of $\sim$55 mA, output powers up to 18 mW, and over 30 nm of tuning. The 3-dB optical modulation bandwidth of the 125-μm-long EAMs was 39 and 35 GHz for the 10- and 15-MQW devices, respectively. Although the additional wells of the 15-MQW design slightly degraded the laser performance, the dc extinction efficiency was increased from 16 dB/V in the 10-MQW EAM to 23 dB/V in the 15-MQW EAM. This allowed for slightly lower drive voltage at 40 Gb/s with the 10-MQW EAM requiring 1.5 V to achieve a $\sim$9-dB ER and 1.0 V for the 15-MQW EAM to achieve an $\sim$8-dB ER. Both EAMs demonstrated low- to negative-chirp operation. Fiber-transmission experiments demonstrated low-power penalties of 0.2–1.1 dB for 40-Gb/s transmission through 2.3 km of fiber across the tuning range of the lasers.

REFERENCES

[1] M. Okayasu *et al.*, "A 1550-nm 40-Gb/s electro-absorption DFB laser diode module for transponders with very short reach (< 2 km) applications," in *LEOS Tech. Dig.*, 2004, pp. 513–514, Paper WG2.

[2] M. K. Chin, "Comparative analysis of the performance limits of Franz–Keldysh effect and quantum confined Stark effect electroabsorption waveguide modulators," *Proc. Inst. Electr. Eng.—Optoelectron.*, vol. 142, no. 2, pp. 109–114, Apr. 1995.

[3] H. Fukano, T. Yamanaka, M. Tamura, Y. Kondo, and T. Saitoh, "Very low driving voltage InGaAlAs/InAlAs electroabsorption modulators operating at 40 Gb/s," *Electron. Lett.*, vol. 41, no. 4, pp. 211–212, Feb. 2005.

[4] P. Gerlach *et al.*, "40-Gb/s operation of laser-integrated electroabsorption modulator using identical InGaAlAs quantum," in *Proc. Int. Conf. Indium Phosphide and Rel. Mater. Tech. Dig.*, 2005, pp. 554–557.

[5] J. Binsma, P. Thijs, T. VanDongen, E. Jansen, A. Staring, G. VanDenHoven, and L. Tiemeijer, "Characterization of butt-joint InGaAsP waveguides and their application to 1310 nm DBR-type MQW Ganin-Clamped semiconductor optical amplifiers," *IEICE Trans. Electron.*, vol. E80-C, no. 5, pp. 675–681, May 1997.

[6] S. Charbonneau, E. Kotels, P. Poole, J. He, G. Aers, J. Haysom, M. Buchanan, Y. Feng, A. Delage, F. Yang, M. Davies, R. Goldberg, P. Piva, and I. Mitchell, "Photonic integrated circuits fabricated using ion implantation," *IEEE J. Sel. Topics Quantum Electron.*, vol. 4, no. 4, pp. 772–793, Jul./Aug. 1998.

[7] V. Jayaraman, Z. Chuang, and L. Coldren, "Theory, design, and performance of extended tuning range semiconductor lasers with sampled gratings," *IEEE J. Quantum Electron.*, vol. 29, no. 6, pp. 1824–1834, Jun. 1993.

[8] J. Raring, E. Skogen, M. Mašanović, S. DenBaars, and L. Coldren, "Demonstration of high saturation power/high gain SOAs using quantum well intermixing and MOCVD regrowth," *Electron. Lett.*, vol. 41, no. 24, pp. 1345–1346, Nov. 2005.

[9] J. W. Raring, E. J. Skogen, C. S. Wang, J. S. Barton, G. B. Morrison, S. Demiguel, S. P. DenBaars, and L. A. Coldren, "Design and demonstration of novel quantum well intermixing scheme for the integration of UTC-Type photodiodes with QW-based components," *IEEE J. Quantum Electron.*, vol. 42, no. 2, pp. 171–181, Feb. 2005.

[10] E. Skogen, J. Barton, S. DenBaars, and L. Coldren, "A quantum-well-intermixing process for wavelength-agile photonic integrated circuits," *IEEE J. Sel. Topics Quantum Electron.*, vol. 8, no. 4, pp. 863–869, Jul./Aug. 2002.

[11] J. Shim, M. Yamaguchi, P. Delansay, and M. Kitamura, "Refractive index and loss changes produced by current injection in InGaAs(P)–InGaAsP multiple quantum-well (MQW) waveguides," *IEEE J. Sel. Topics Quantum Electron.*, vol. 1, no. 2, pp. 408–415, Jun. 1995.

[12] G. B. Morrison, J. W. Raring, E. J. Skogen, C. S. Wang, and L. A. Coldren, "Photocurrent spectroscopy analysis of widely tunable negative-chirp quantum well intermixed laser-modulator transmitters," *Appl. Phys. Lett.*, vol. 86, no. 7, pp. 1–3, Feb. 2005.

James W. Raring (M'06) was born in Ramsey, NJ, in 1978. He received the B.S. degree from the Materials Engineering Department, California Polytechnic State University, San Luis Obispo, in 2001 and the Ph.D. degree in materials science from the University of California, Santa Barbara, in 2006. His dissertation focuses on the design, growth, and fabrication of high-functionality wavelength-agile photonic integrated circuits operating at 10 and 40 Gb/s. The photonic circuits are based on sampled-grating DBR lasers, electroabsorption modulators, semiconductor optical amplifiers, and photodiodes.

He is currently with the Electrical and Computer Engineering Department, University of California, Santa Barbara. His work explores novel integration methods coupling quantum-well intermixing with straightforward metal–organic chemical-vapor-deposition regrowth steps. He has authored or coauthored more than 70 technical papers.

Dr. Raring is a member of IEEE Lasers and Electro-Optics Society, the Optical Society of America, and the International Society for Optical Engineers.

Leif A. Johansson (M'04) received the Ph.D. degree in engineering from University College London (UCL), London, U.K., in 2002.

He took up a postdoctoral position with the University of California, Santa Barbara, in 2002. His current research interests include design and characterization of integrated photonic devices for analog and digital applications.

Erik J. Skogen (M'04) was born in Minneapolis, MN, in 1975. He received the B.S. degree from Iowa State University, Ames, in 1997 and the M.S. and Ph.D. degrees from the University of California, Santa Barbara, in 1999 and 2003, respectively.

He is currently with the Electrical and Computer Engineering Department, University of California, Santa Barbara. His current research interests include widely tunable semiconductor lasers, monolithic integration for photonic integrated circuits, growth aspects in the InGaAsP material system using metal-organic chemical vapor deposition, and quantum-well intermixing.

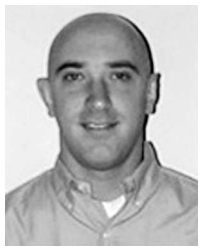

Mathew N. Sysak (M'06) was born in Smithtown, NY, in 1976. He received the B.S. degree in chemical engineering from Pennsylvania State University, State College, in 1998.

He is currently with the Electrical and Computer Engineering Department, University of California, Santa Barbara. His current research interests include the monolithic integration of widely tunable semiconductor lasers with semiconductor optical amplifiers, electroabsorption modulators, and photodetectors in the InGaAsP material system.

Henrik N. Poulsen received the B.S. degree materials and metallurgical engineering from University of Arizona, Tucson, in 1984, the M.S. and Ph.D. degrees from the Department of Materials Science, University of Southern California, Los Angeles, in 1986 and 1988, respectively, and the M.Sc.E.E. from the Technical University of Denmark, Lyngby, Denmark, in 1995.

From 1995 to 2001, he worked first as a Research Associate and later as an Associate Research Professor in the field of high-speed wavelength-division multiplexing and optical time-division multiplexing. In 2001, he moved from Copenhagen, Denmark, to Santa Barbara, CA to join Calient Networks, where he worked on optical amplification and performance monitoring for all-optical microelectromechanical-based switches. He is currently working as an Associate Project Scientist in the Optical Communications and Photonics Network Group with Prof. D. J. Blumenthal with the Department of Electrical and Computer Engineering at the University of California, Santa Barbara. His main research area is all-optical packet switching using all-optical interferometric structures. His main interests were ultrahigh-speed optical-signal processing using nonlinear fiber and semiconductor material, mainly semiconductor optical amplifiers, interferometric structures, and electroabsorption modulators.

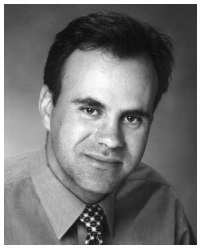

Steven P. DenBaars (M'91–SM'03–F'05) received the B.S. degree in materials and metallurgical engineering from the University of Arizona, Tucson, in 1984 and the M.S. and Ph.D. degrees from the University of Southern California, Los Angeles, in 1986 and 1988, respectively.

He was a member of the technical staff at Hewlett-Packard from 1988 to 1991, where he was involved in the fabrication of high-brightness light-emitting diodes. In 1991, he joined the faculty of the University of California, Santa Barbara (UCSB) where he is developing new solid-state optoelectronic devices. He is currently a Professor of materials and electrical engineering with the Materials Department, UCSB. Currently, he is an Associate Director of the Solid-State Lighting and Display Center at UCSB, which is developing new more energy-efficient light sources. His research also involves metal–organic chemical-vapor-deposition growth of GaN and InP-based tunable lasers and detectors. Special interests include the effect of materials' properties on device performance, blue VCSEL lasers, and microwave power transistors. He has authored over 200 technical publications, three book chapters, and 100 conference presentations, and is the holder of seven patents.

Prof. DenBaars received an NSF Young Scientist Award in 1995 and the Young Scientist Award from the International Symposium on Compound Semiconductors in 1998.

Larry A. Coldren (S'67–M'72–SM'77–F'82) received the Ph.D. degree in electrical engineering from Stanford University, Stanford, CA, in 1972.

After 13 years in the research area at Bell Laboratories, he joined the University of California, Santa Barbara, in 1984, where he currently holds appointments in materials and electrical and computer engineering, and is Director of the Optoelectronics Technology Center. In 1990, he cofounded Optical Concepts, later acquired as Gore Photonics, to develop novel vertical-cavity surface-emitting laser (VCSEL) technology. In 1998, he cofounded Agility Communications to develop widely tunable integrated transmitters. He is currently the Fred Kavli Professor of Optoelectronics and Sensors at the University of California, Santa Barbara. At Bell Laboratories, he initially worked on waveguided surface-acoustic-wave signal-processing devices and coupled-resonator filters. He later developed tunable coupled-cavity lasers using novel reactive-ion etching technology that he created for the then new InP-based materials. At the University of California, Santa Barbara, he continued work on multiple-section tunable lasers, inventing the widely tunable multielement-mirror concept in 1988. During the late 1980s, he also developed efficient vertical-cavity multiple-quantum-well modulators, which led to novel VCSEL designs that provided unparalleled levels of performance. He continues to be active in developing new photonic integrated circuit (PIC) and VCSEL technology, including the underlying materials growth and fabrication techniques. In recent years, for example, he has been involved in the creation of vertical and in-plane GaN-based emitters, efficient all-epitaxial InP-based VCSELs, and a variety of PICs incorporating numerous optical elements for widely tunable integrated transmitters, receivers, and wavelength converters. He has authored or coauthored over 700 papers, five book chapters, and one textbook, and has been issued 36 patents.

Prof. Coldren has presented dozens of invited and plenary talks at major conferences, he is a Fellow of Optical Society of America and of the Institute of Electrical Engineers, received the 2004 John Tyndall Award, and is a member of the National Academy of Engineering.

40-Gb/s Widely Tunable Transceivers

James W. Raring and Larry A. Coldren

(Invited Paper)

***Abstract*—We present the first monolithic widely tunable 40-Gb/s transceivers. The devices integrate sampled grating distributed Bragg reflector (SG-DBR) lasers, quantum-well electroabsorption modulators (EAM), low-confinement semiconductor optical amplifiers (SOA), and uni-traveling carrier (UTC) photodiodes for state-of-the-art light generation, modulation, amplification, and detection. A relatively simple high-flexibility fabrication scheme combining quantum-well intermixing (QWI) and blanket metal-organic chemical vapor deposition (MOCVD) regrowth was used to integrate components with performance rivaling optimized discrete devices. The SG-DBR/EAM transmitters demonstrate 30 nm of tuning, 39-GHz bandwidth, low-drive voltage, and low power penalty 40-Gb/s transmission through 2.3 km of fiber. The SOA/UTC photodetector receivers provide 23–28 dB of gain, saturation powers up to 18.6 dBm, and −20.2 dBm of chip-coupled sensitivity at 40 Gb/s. By connecting the transmitters and receivers off-chip, we demonstrate 40-Gb/s wavelength conversion.**

***Index Terms*—Electroabsorption modulators, photodetectors, semiconductor lasers, semiconductor optical amplifiers, transceivers, wavelength converters.**

I. Introduction and Motivation

THE monolithic integration of highly optimized photonic devices onto a single chip could revolutionize lightwave communications as it is perhaps the only way to truly revitalize the optical component industry. The generation, detection, modulation, amplification, switching, and transport of light on a single chip allows for a new generation of high-functionality photonic integrated circuits (PICs) with reduced cost, size, and power dissipation. Since fiber is not required for light transfer between components, PICs do not suffer from the device-to-device coupling problem of systems comprised of discrete components. The removal of the coupling loss allows for a reduction in power dissipation because lower drive currents will be required to achieve equivalent power levels to and from the device. Fewer packages are necessary since multiple components can be housed within a single enclosure. Device reliability is improved from the elimination of possible mechanical movements among the optical elements and from the reduced drive current requirements.

The potential benefits of monolithic integration fueled the pioneering efforts of the late 1980s and early 1990s to develop increased functionality chips [1]. During this time, researchers made great advances with the demonstration of distributed feedback (DFB) laser/modulators, highly functional balanced heterodyne receivers, and integrated mode converters [2]–[4]. Despite this early progress, the PIC has failed to scale at the same Moore's Law rate of the integrated circuit (IC) [5]. This can be largely attributed to the difficulty associated with optimizing the diverse components required in high-functionality photonic chips. Ever-increasing bit rate demands amplify this challenge since the individual components will necessitate more exotic structures for efficient, high-speed operation.

Low-threshold current, high-output power diode lasers benefit from maximized modal gain within the active section. By placing quantum wells (QWs) in the center of a symmetric waveguide, the optical confinement factor and hence the modal gain can be maximized within the laser [6]. The electroabsorption modulator (EAM) is an attractive modulator due to its compact size, simple fabrication, high modulation bandwidth, and high efficiency. To achieve negative chirp along with high modulation efficiency from relatively short devices for 40-Gb/s operation, QW absorber regions are required to exploit the quantum confined Stark effect (QCSE) [7]. Low optical confinement QW active regions are a popular choice for use in semiconductor optical amplifiers (SOAs) requiring high-saturation powers since the photon density within the QWs can be kept relatively low. Using this scheme, impressive saturation powers of $+23$ dBm have been demonstrated [8]. The uni-traveling carrier (UTC) photodiode has been developed specifically to eliminate the influence of hole transport on the operation of the photodetector such that the classic space charge effect plaguing the performance of conventional p-i-n detectors can be avoided. Since the carrier transport properties are dominated by electrons, saturation current densities, 4–6 times higher than that in p-i-n photodiodes, are theoretically possible, enabling high-power, high-speed operation [9].

Defining these unique components on a single chip to realize a high-performance transceiver is a demanding task due to the common two-dimensional (2-D) growth and processing platforms used for device fabrication. Simple integration schemes limit design flexibility, imposing a performance penalty within the PIC. Complex schemes with increased flexibility can lead to decreased yield, driving the device cost upwards. For the potential benefits of PICs to win out over discrete devices, the integration must be accomplished in a manner as to provide high device yield and repeatability at low cost.

II. Background: Methods of Monolithic Integration

In Fig. 1, we present several integration platforms used for high-functionality PIC fabrication. The butt-joint regrowth

Manuscript received June 22, 2006; revised September 13, 2006. This work was supported in part by Defense Advanced Research Projects Agency/Microsystems Technology Office (DARPA/MTO) CS-WDM under Grant N66001-02-C-8026 and in part by Intel Corporation under Grant TXA001630000.

The authors are with the Department of Electrical Engineering, University of California, Santa Barbara, CA 93106 USA (e-mail: jraring@engineering.ucsb.edu).

Digital Object Identifier 10.1109/JSTQE.2006.885329

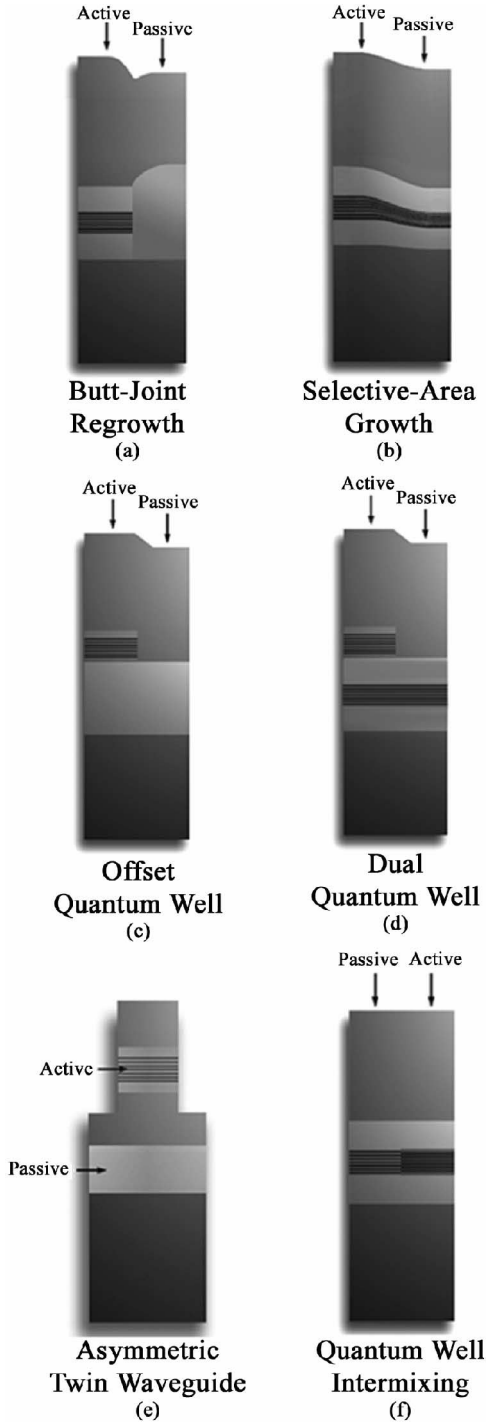

Fig. 1. Various techniques for achieving active and passive sections orthogonal to the growth direction.

(BJR) method in Fig. 1(a) offers a high degree of versatility. This method involves the selective removal of the base structure, as-grown multiple-quantum-well (MQW) active region followed by the nonplanar selective regrowth of an alternative material structure with the desired band-edge in the core of the waveguide. The BJR process enables the use of a centered MQW (c-MQW) active region for maximized modal gain in the laser, and allows each integrated component to possess a unique band-edge and/or epitaxial structure. The drawback to this method is the difficulty associated with achieving high-quality butt-joint interfaces across the chip to avoid reflections and losses in the core of the optical waveguide [10], [11]. Furthermore, this method relies on a dielectric mask to prevent deposition in specified areas during growth. As the PIC functionality is increased to the transceiver level where more active architectures are required, the complexity of BJR process is compounded with additional BJR steps.

Selective area growth (SAG), as shown in Fig. 1(b), has proven to be useful in providing multiple band-edges across a single wafer in one growth step [12]. In this method a dielectric mask is patterned on the wafer, which is then subjected to metal-organic chemical vapor deposition (MOCVD) growth. Growth is limited to regions between the dielectric mask, where the thickness and the composition of the growing layers are modified based on the mask pattern. This technique allows for the definition of c-MQW active regions on the same chip as blue-shifted MQW regions for use in EAMs and passive sections. Beyond this, SAG does not afford much flexibility since the epitaxial architecture is fixed in all components. The SOA and photodetector are forced to employ the same high-confinement MQW structure as used in the laser, resulting in low-saturation power in both receiver components. Since SAG exploits the contrast in surface kinetics of the growth constituents on the semiconductor and dielectric, a high degree of calibration/optimization must be performed to tightly control the MOCVD reactor conditions.

An established and simple integration platform is based on the use of offset QWs, where the MQW active region is grown above a passive bulk waveguide. The MQW is selectively etched in regions where gain is not required, leaving the nonabsorbing waveguide as shown in Fig. 1(c). Although this process only requires a single, blanket-type regrowth, it allows for only two band-edges on a single-chip. The modal gain in the offset QW design is less than optimal since the peak of the optical mode is offset from the MQW. This scheme forces the use of bulk Franz–Keldysh (FK) type EAMs, which are not as efficient as QW-EAMs utilizing the QCSE [7], [13].

In the dual QW platform, as shown in Fig. 1(d), an MQW is grown in the center of the bulk waveguide below the offset MQW, such that a second QW band-edge is defined on the single-chip [14]. The dual QW platform does not provide optimal modal gain to the laser active region since the peak of the mode is offset from the wells. Additionally, this scheme imposes a passive loss versus EAM efficiency tradeoff. The EAM efficiency will increase as the waveguide MQW bandgap energy is decreased, however, this will also increase the passive loss since the waveguide wells are present throughout the device. To manage this tradeoff, longer EAM lengths are used at the expense of bandwidth [14]. In the dual QW and offset QW platforms, SOAs are forced to employ the same MQW structure as the laser, and the photodetector must use either the MQW or the waveguide material as the absorber [15]. The relatively high confinement factor in the active MQW will result in low-SOA saturation power. The high-confinement factor p-i-n structure is not an optimal architecture for high-power, high-speed photodiodes [9].

In the asymmetric twin waveguide (ATG) integration scheme shown in Fig. 1(e), multiple waveguides are grown on top of each other with a transparent InP layer separating them. Active/passive integration is realized by selective removal of the upper "active" waveguide such that only the lower "passive" waveguide remains in regions where active functions are not required. The optical power is coupled between the even and odd modes supported by the waveguide using carefully designed taper couplers [16]. This technique eliminates the need for regrowth only in applications where vertical current injection is not required in grating regions for high-efficiency tuning, which are not applicable to wavelength-agile PICs. Although this platform can enable multiple functions on a single chip, the nature of the vertical coupling into different epitaxial layers would create great difficulty when defining additional active component architectures beyond the two found in the laser/modulator transmitters or the SOA/photodetector receivers devices reported in [17]. That is, the ATG platform does not appear fit for the simultaneous integration of high-confinement MQW active regions for high-gain, low-confinement MQW active regions for high-saturation power, a high-confinement blue-shifted MQW for high-efficiency EAMs, and high-saturation current photodetector structures such as the UTC.

Quantum-well intermixing (QWI), as shown in Fig. 1(f), allows for the strategic, post-growth tuning of multiple QW band-edges without introducing difficult growth steps or discontinuities in the axial waveguide. QWI has been used in the past to fabricate a multitude of devices and there are a number of techniques that have evolved over the years to accomplish selective intermixing, such as impurity-induced disordering (IID) [18], impurity-free vacancy-enhanced disordering (IFVD) [19], photoabsorption-induced disordering (PAID) [20], and implantation-enhanced interdiffusion [21].

QWI enables the use of a c-MQW active region for maximized modal gain in lasers and blue-shifted QWs in the EAMs, and thus breaks the tradeoff of the simplicity offered by the offset QW method and the flexibility offered by BJR and SAG. Since multiple QW band-edges can be defined on a single chip, the passive and EAM band-edges can be independently optimized to avoid the passive loss versus EAM efficiency tradeoff of the dual QW platform. QWI does not change the average composition of the MQW such that there is a negligible index discontinuity at the interface between adjacent sections. This eliminates parasitic reflections that can degrade performance.

III. Novel High-Flexibility Integration Platform

Here, we employ a high-flexibility integration method combining an impurity-free implant-enhanced QWI technique with simple blanket MOCVD regrowth. The QWI process uses a single implant to introduce point defects in an undoped InP buffer layer grown above the QWs [22], [23]. Thermal propagation steps are used to diffuse the point defects through the MQW to shift the band-edge. Selective removal of the buffer layer is used to halt the intermixing process in regions where the desired band-edge has been achieved. This process allows for the realization of any number of band-edges on a single-chip, as the number is determined only by the number of times the thermal processing is interrupted such that the buffer layer can be selectively removed in specified regions. In Fig. 2, the characteristic band-edge shift versus anneal time is shown for implanted regions with and without the buffer layer and for regions not subjected to the implant. A thorough description of the QWI process along with an overview of the PICs fabricated using this technique can be found in [23].

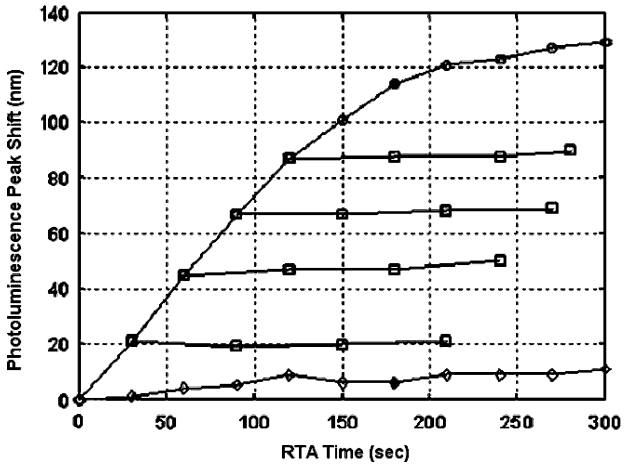

Fig. 2. Peak PL peak shift as a function of anneal time, showing the initial linear increase in the peak shift and the complete halting of the peak shift for samples for which the implant buffer layer has been etched. Symbols indicate nonimplanted (*diamonds*), implanted (*circles*), and samples with partial anneal followed by the removal of the implant buffer layer (*squares*).

Although QWI provides a simple method to achieve multiple QW band-edges on a single chip for high-performance lasers and QW-EAMs, alone it does not provide the capability to integrate optimal architectures for high-saturation power SOAs and specialized photodetectors. By combining blanket MOCVD regrowth steps with the multiple band-edge QWI process, we present a method to define state-of-the-art lasers, modulators, SOAs, and photodetectors on a single chip without BJR or SAG. The PIC designer is not only free to control the MQW band-edge in the growth plane, but now has the flexibility to control the MQW band-edge in the direction normal to the growth plane and to define unique architectures in the SOAs and photodetectors.

First, QWI is used to define three unique QW bandgaps in the high-confinement base structure c-MQW for use in the laser, EAM, and passive sections. Next, simple blanket MOCVD regrowth and wet etch steps are carried out to define a low-confinement offset MQW (o-MQW) for use in SOAs and UTC photodiode structures. A side-view schematic of a single-chip possessing the four state-of-the-art architectures is shown in Fig. 3.

The key attribute of this high-flexibility scheme is that it requires only simple blanket regrowth steps for the added functionality. The platform does not require the disruption of the waveguide core with regrowth interfaces as does the butt-joint method. The slight discontinuities created in this scheme reside above the intermixed c-MQW waveguide core such that only the tail of the propagating mode encounters them. Furthermore, our process requires no complicating dielectric patterns to remain on

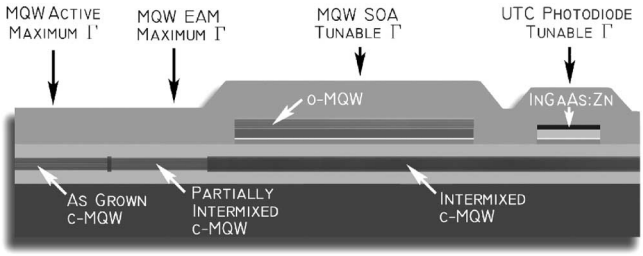

Fig. 3. Schematic side-view of various component architectures that can be defined on a single chip using the QWI and MOCVD regrowth high-flexibility integration scheme.

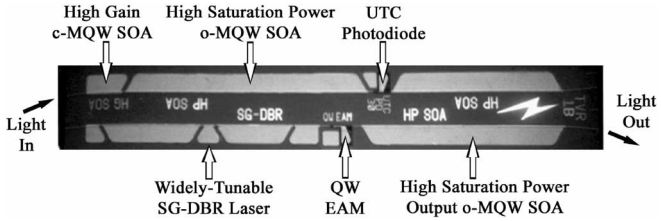

Fig. 4. Top-view SEM image of single-chip 40-Gb/s transceiver with a 0.5 by 3.5 mm footprint.

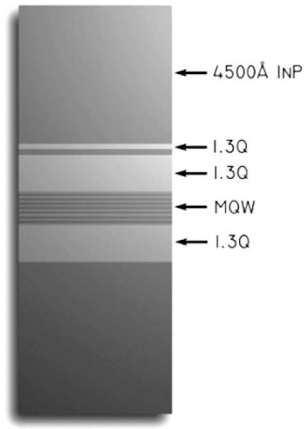

Fig. 5. Epitaxial base structure employing c-MQW active region.

the semiconductor surface to prevent deposition during growth as in the BJR or SAG methods.

Using the high-flexibility integration scheme, we demonstrate single-chip widely tunable 40-Gb/s transceivers. The widely tunable transmitters demonstrate over 30 nm of tuning with 3-dB optical bandwidths up to 39 GHz and low-drive voltages at 40 Gb/s. The power penalty for 40-Gb/s transmission through 2.3 km of fiber was less than 0.5 dB across the device tuning range. These transmitters represent the first widely tunable EAM-based 40-Gb/s devices and achieve performance levels rivaling state-of-the-art single frequency transmitters requiring BJR [24]. The receiver SOAs provide 23–28 dB of gain with saturation powers in the 18.5-dBm range while the UTC photodiodes exhibit 40-Gb/s operation under high photocurrent conditions. The 40-Gb/s chip-coupled sensitivity of better than -20 dBm is competitive with discrete SOA/photodiode receivers requiring BJR [25]. By connecting the receiver and the transmitter off-chip, we demonstrate low power-penalty widely tunable 40-Gb/s wavelength conversion.

IV. 40-Gb/s Transceiver Architecture

The 40-Gb/s transceiver devices employed a parallel surface ridge waveguide architecture with one ridge functioning as the transmitter and the adjacent ridge functioning as the receiver. The 3-μm-wide surface ridge transmitter consisted of a five-section widely tunable sampled grating distributed Bragg reflector (SG-DBR) laser as described in [26] and a QW-EAM with a length of 125 or 175 μm. Select transmitters made use of a high-gain c-MQW output SOA positioned before the EAM or a high-saturation power o-MQW output SOA positioned after the EAM. Two different receiver designs were explored, both consisted of a 5-μm-wide dual section SOA and a 3 by 30 μm or 3 by 40-μm UTC photodiode. The SOAs contained a short high-gain c-MQW front-end followed by a long high-saturation power o-MQW section. Curved and flared input/output waveguides were used to reduce the demands on the antireflection coating. A labeled top-view scanning electron micrograph (SEM) image of a transceiver containing the high-saturation power output SOA with a footprint of 0.5 by 3.5 mm is shown in Fig. 4.

V. 40-Gb/s Transceiver Fabrication Sequence

Device fabrication begins with the MOCVD growth of a c-MQW base structure (Fig. 5) on a sulfur doped InP substrate. The base structure consists of ten 6.5-nm quantum wells and eight 8.0-nm barriers sandwiched between two 105-nm-thick 1.3Q waveguide layers designed for a maximized optical confinement of 12.6%. The as-grown c-MQW had a peak photoluminescence (PL) emission wavelength of 1540 nm. A 25-nm InP regrowth layer, a 20-nm 1.3Q stop etch layer, and a 450-nm InP layer were grown above the upper waveguide. The top most InP layer, called the implant buffer layer, was designed to capture a low-energy ion implant.

A complete step-by-step schematic illustrating the high-flexibility integration scheme is presented in Fig. 6. After growth of the base structure, a 500-nm Si_xN_y, mask layer is deposited using plasma enhanced chemical vapor deposition and lithographically patterned such that it remains only in regions where high-gain c-MQW active regions are desired on the chip. In step 2, an ion implantation is performed using P^+ at an energy of 100 keV, with a dose of 5E14 cm^{-2}, and a substrate temperature of 200 °C to yield a damage range of 90 nm [22]. The point defects created during the P^+ implant are then partially diffused through the c-MQW structure during a $\sim$30-s rapid thermal anneal (RTA) at 675 °C, yielding the desired peak PL wavelength of 1505 nm in the EAM sections. The point defects promote the interdiffusion of the well/barrier constituents, reshaping the MQW profile by distorting the well/barrier interface. The result is a shift in the quantized energy levels in the well, and hence a shift in the band-edge energy.

In step 4, the implant buffer layer above the EAM sections is removed using a wet etching process, terminating on the 1.3Q stop etch layer. The sample is then subjected to an additional $\sim$180-s RTA step to further blue-shift the regions where the implant buffer layer remains. In step 5, the remaining buffer

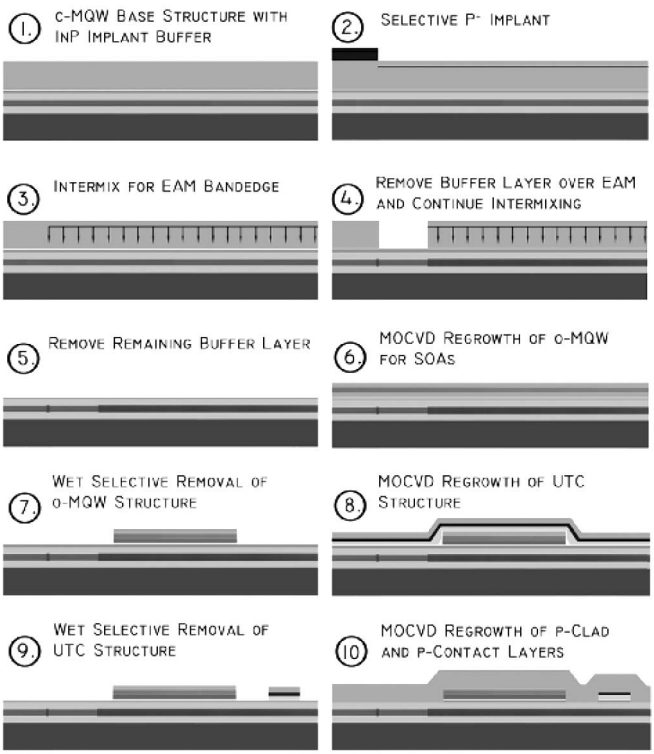

Fig. 6. Step-by-step illustration of high-flexibility integration scheme.

layer and the 1.3Q stop etch layers are removed using wet etching.

A blanket MOCVD regrowth is performed in step 6 for the growth of a thin InP:Si layer, followed by a 1.3Q:Si stop etch layer, an InP:Si confinement tuning layer (CTL), a low-confinement o-MQW active region with similar compositions and thicknesses to that of the base structure c-MQW design, 50 nm of InP, and a 200-nm InP:Zn cap layer. The CTL layer functions to offset the active wells from the peak of the optical mode influencing the confinement factor. Therefore, the choice of the CTL thickness is a key aspect in the SOA design. In this paper, we use five offset wells and choose the CTL thickness to yield a confinement factor of $\sim 1.4\%$. Further details of the regrowth aspects and the influence of the CTL thickness can be found in [27].

Following the regrowth, the sample is patterned with Si_xN_y and a wet chemical selective etch sequence is carried out such that the o-MQW structures remain in regions where low confinement SOAs are desired, as shown in step 7. In step 8, a second blanket MOCVD regrowth is performed for the definition of the UTC photodiode structure. Again, the regrowth initiates with a thin InP:Si regrowth layer and a 1.3Q:Si stop etch layer, but is then followed by the growth of a thin InP:Si layer, a 200-nm unintentionally doped InP collector layer, conduction band smoothing layers based on those given in [9], a 50-nm InGaAs:Zn absorber layer, and a 150-nm InP:Zn cap layer. The thickness and doping of both the collector and absorber layers have a great impact on the expected device performance. Further details of the offset UTC structure can be found in [28]. The sample is patterned with Si_xN_y and a wet etch is performed to define the UTC structure only where detectors are desired as shown in step 9.

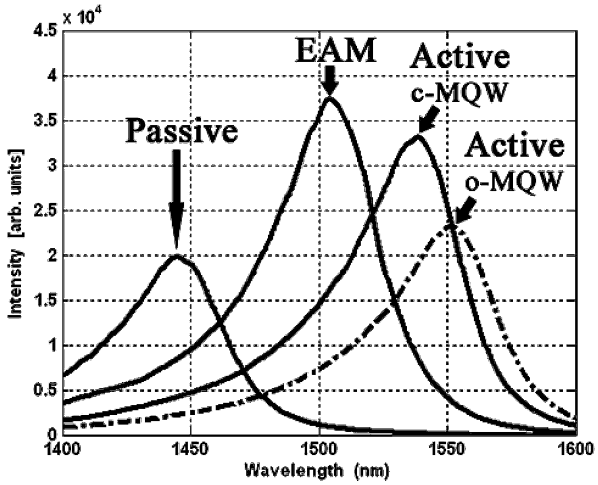

Fig. 7. PL spectra of c-MQW active, EAM, and passive sections along with the regrown o-MQW gain region (*dashed*).

In step 10, a final blanket MOCVD regrowth is performed to grow the p-type InP:Zn cladding and p-contact InGaAs:Zn layers such that four distinct regions remain on a single chip: the as-grown c-MQW active regions to be used for high-gain lasers and SOA sections, the partially intermixed c-MQW regions for use in high-efficiency QW-EAMs, low-confinement o-MQW regions grown above intermixed wells for high-saturation power SOAs, and finally UTC structures grown over intermixed wells for high-saturation power high-bandwidth photodiodes. The PL spectra from the four unique QW band-edges on the single-chip are shown in Fig. 7.

Following the growth sequence, standard lithography and etch techniques were carried out for the definition surface ridge devices. The wafers were thinned, the devices were cleaved into bars and anti-reflection coated. The die were separated, soldered to aluminum nitride carriers, and wire bonded for characterization.

VI. Device Results

A. Material Efficiency and Loss Characterization

It is good practice to test diagnostic structures to determine the basic quality of the epitaxial material before examining the high-level PICs. The cleave-back method was used to measure the differential efficiency versus length of 3-μm-wide c-MQW and 5-μm-wide o-MQW surface ridge Fabry–Perot (FP) active lasers identical to the gain region of the lasers and SOAs. With this data, the injection efficiency and modal loss within the gain regions of the PICs was extracted.

A plot of inverse differential efficiency versus FP laser length is presented in Fig. 8 for both the c-MQW and o-MQW devices. The injection efficiency was extracted to be 76% and 74% and the modal loss was extracted to be 18.9 and 3.0 cm^{-1} in the c-MQW and o-MQW gain regions, respectively. The low modal loss in the o-MQW gain region is essential for high-performance SOA operation since the low optical confinement will result in low incremental modal gain. Therefore, small

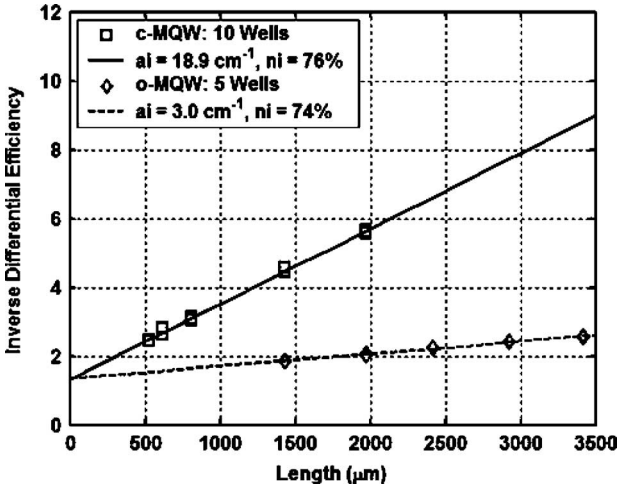

Fig. 8. Plot of inverse differential efficiency versus active FP laser length for lasers fabricated from c-MQW and o-MQW gain sections.

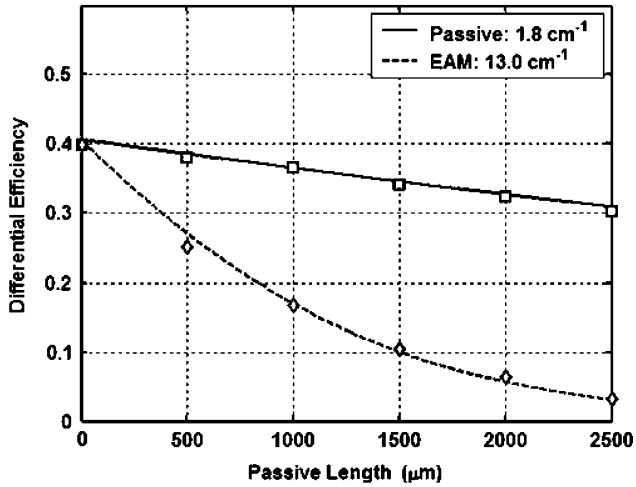

Fig. 9. Differential efficiency of active/passive lasers versus passive length used to extract modal propagation loss for passive and EAM regions at a wavelength of 1550 nm.

changes in the propagation losses will greatly influence the large signal gain. Future work could focus on reducing this loss value for improved performance.

It is important that the propagation loss in the passive waveguide, mirror, phase, and EAM sections of the device are kept low such that high output powers can be achieved. To study this characteristic we fabricated active/passive FP lasers, where the passive regions are composed of an intermixed MQW. The propagation loss in the passive and EAM sections was extracted at a wavelength of 1550 nm by successively cleaving back the passive/EAM portions of the active/passive lasers and then measuring the differential efficiency when subjecting the active region to pulsed current injection. By constructing a plot of the differential efficiency versus passive/EAM region length, theoretical curves can be fit to the experimental data to extract the loss as described in [6].

Fig. 9 plots the experimental differential efficiency versus passive region length along with theoretical fits for the passive and EAM c-MQW regions on the chip. The passive loss was extracted to be 1.8 cm^{-1} and the EAM loss was found to be 13 cm^{-1} at a wavelength of 1550 nm. This corresponds to a passive propagation loss of 1 dB/mm and an unbiased insertion loss of $\sim$1 dB for a 175-μm-long EAM.

B. 40-Gb/s SG-DBR/EAM Transmitter Performance

The continuous wave performance of the transmitters was characterized at a stage temperature of 18 °C. The surface ridge SG-DBR lasers demonstrated over 30 nm of continuous tuning from wavelengths of 1536–1569 nm. In Fig. 10, we present superimposed output spectrums for lasing wavelengths across the SG-DBR tuning band using front mirror bias currents up to 25 mA (5 kA/cm^2) with a back mirror current of 5 mA (0.3 kA/cm^2). The lasers achieved threshold currents of $\sim$35 mA, fiber-coupled powers up to 10 dBm, and a side-mode suppression ratio (SMSR) of over 35 dB for wavelengths from 1542 to 1569 nm.

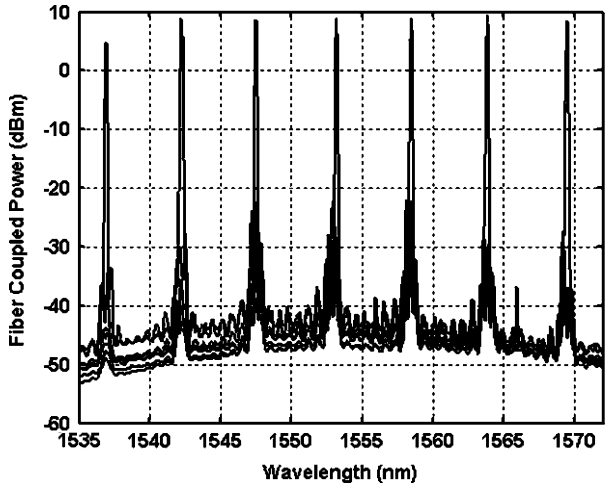

Fig. 10. Superimposed output spectrums tuned to different lasing wavelengths from SG-DBR laser with high gain output SOA.

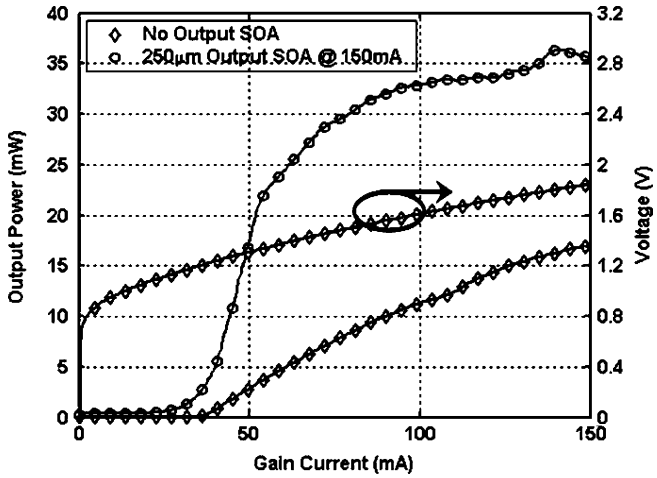

Fig. 11. Output power of SG-DBR laser captured in an integrating sphere for the case with no output SOA and with a 250-μm-long SOA. The gain section voltage is indicated with the right-hand y-axis.

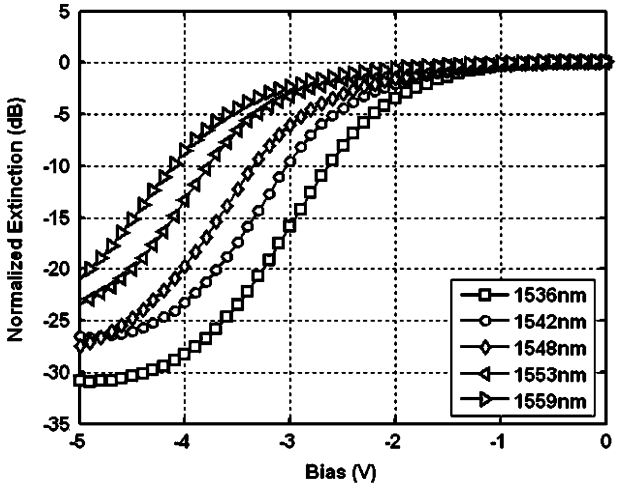

Fig. 12. Broadband DC extinction of a 125-μm-long EAM.

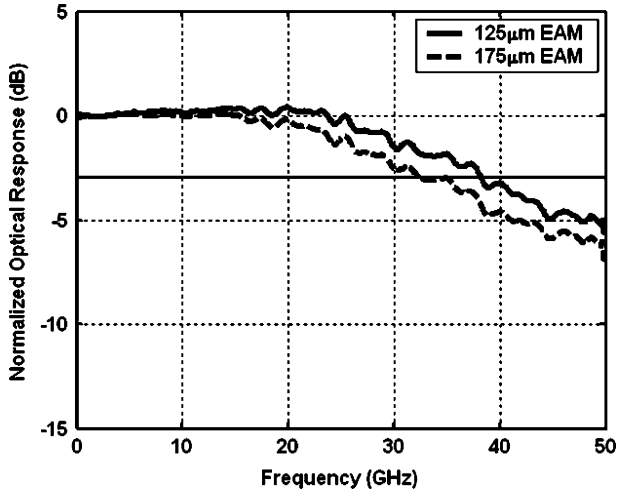

Fig. 13. Electrical-to-optical small signal response of EAMs.

The output power captured into an integrating sphere and voltage versus gain current (LIV) for SG-DBR lasers with no output SOA and for a device with a 250-μm-long c-MQW SOA positioned after the front mirror are shown in Fig. 11. At a gain current of 150 mA, the device demonstrates over 16 mW of output power with no output SOA and over 35 mW of output power with an output SOA biased at 150 mA.

The broadband dc extinction characteristics from a 125-μm-long EAM are shown in Fig. 12. The EAM provides 20–30 dB of total extinction with slope efficiencies of 14–16 dB/V for wavelengths from 1536 to 1560 nm. The 175-μm-long EAMs provide 34–38 dB of total extinction with efficiencies over 20 dB/V. The efficient dc extinction properties are due to the combination of the high confinement factor provided by the c-MQW and the intermixing process that allows for precise placement of the modulator band-edge.

The small signal electrical to optical frequency response characteristics of 125-and 175-μm-long EAMs were measured using a 50-GHz network analyzer and are shown in Fig. 13. The EAM electrodes were directly probed using ground-signal probes with a 50-Ω termination load. The stage temperature was again maintained at 18 °C. The optical 3-dB bandwidth was measured to be 39 GHz in the 125-μm-long EAM and 32 GHz in the 175-μm-long EAM.

Nonreturn to zero (NRZ) eye diagrams were taken at 40 Gb/s with a pseudorandom bit sequence (PRBS) of $2^{31}-1$ over the tuning range of a transmitter with a 125-μm-long modulator. Fig. 14, presents the back-to-back input eye along with the output eyes from the device with a 1.5-V_{PtoP} drive applied to the EAM. The eye diagrams are open and clear with extinction ratios (ER) over 8.7 dB for wavelengths up to 1560 nm at dc bias levels from 3.4 to 5.2 V. The average fiber-coupled output power under these conditions ranged from -5 to 0 dBm. The 1.5-V_{PtoP} drive required in these devices approach the state-of-the-art discrete EAMs reported in [29], which required 0.79 V_{PtoP} to drive over 10-dB ER.

The large signal chirp of the EAMs was measured at 10 Gb/s for wavelengths from 1541 to 1564 nm using Agilent's time

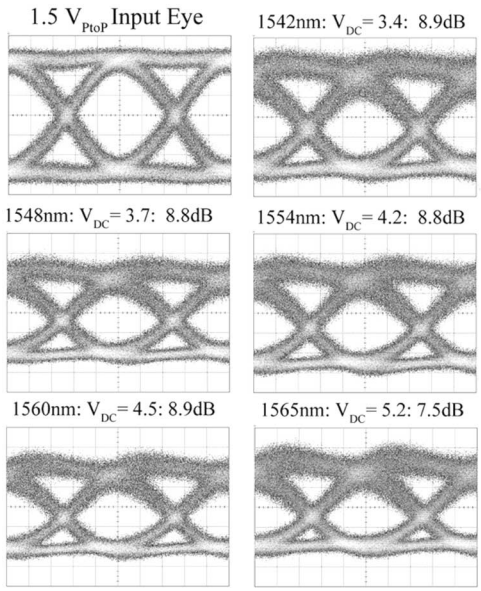

Fig. 14. 40 Gb/s eye diagrams from 125-μm-long EAM.

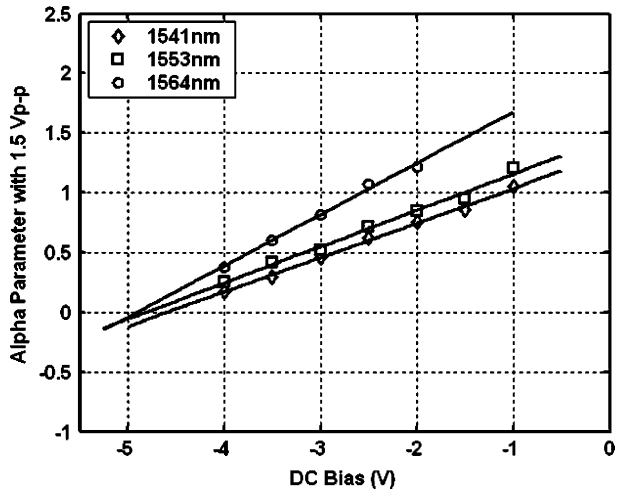

Fig. 15. Large signal chirp parameter of EAM with a 1.5-V_{PtoP} drive.

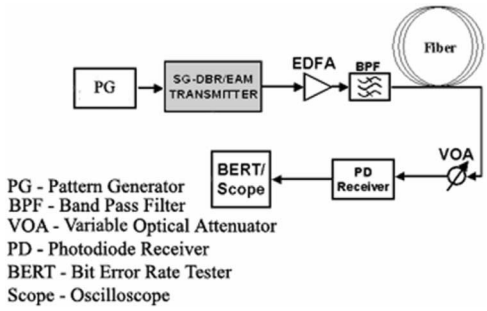

Fig. 16. Test set used for 40-Gb/s transmission measurements.

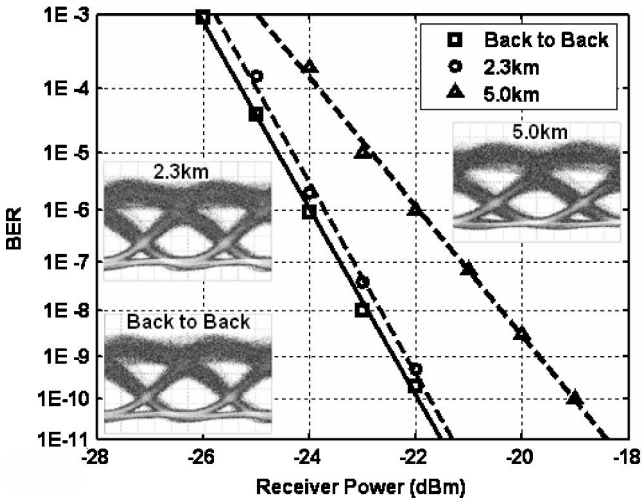

Fig. 17. BER measurements from 125-μm-long EAM at 40 Gb/s with a 1.5-V_{PtoP} drive and a wavelength of 1553 nm. The corresponding eye diagrams before and after transmission are shown as insets.

resolved chirp (TRC) software. The chirp parameter was measured as a function of the dc bias applied to the EAM with a 1.5-V_{PtoP} drive applied to the device. As shown in Fig. 15, the chirp parameter is reduced with increasing reverse bias and decreasing wavelength. The measurement bias range was limited such that the lowest TRC measured chirp value was 0.15. However, the chirp parameter is expected to reach zero in the reverse bias range of 4.5–5.0 V.

Bit-error-rate (BER) measurements were made for 40-Gb/s transmission through 2.3 and 5 km of standard Corning SMF-28 fiber. A PRBS of $2^7 - 1$ was used due to a noise floor resulting from a calibration issue in the BER tester (BERT) that manifested itself at longer word lengths. A schematic illustrating the BER test setup is shown in Fig. 16. In Fig. 17, the BER results and the respective eye diagrams are shown for a device employing a 125-μm-long EAM at a wavelength of 1553 nm, a 1.5-V_{PtoP} drive, and a dc bias of 4.9 V. As seen in the figure, the transmitter demonstrated only 0.2 dB of power penalty through 2.3 km and under 3 dB of penalty through 5.0 km. The BER was measured for a transmission through 2.3 km of fiber at wavelengths of 1542, 1553, and 1565 nm with the EAM biased in the 4.3–5.2-V range. Using the measured dispersion penalties of 0.4, 0.2, and 0.5 dB at the respective wavelengths and assuming a fiber dispersion of 16.45 ps/nm/km, the chirp parameters were calculated to be -0.15, -0.25, and -0.1, respectively. The lower chirp values than those shown in Fig. 15 are likely the result of the higher reverse biases used in the BER measurements.

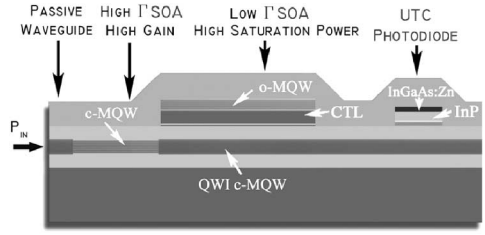

Fig. 18. Side-view schematic of receiver structure showing the high confinement c-MQW gain region (*left*), low-confinement o-MQW gain region (*middle*), and the UTC photodiode structure (*right*).

The transmitter reported here is the first widely tunable EAM-based transmitter operating at 40 Gb/s. Previous EAM-based 40-Gb/s transmitter devices used single-frequency DFB lasers and typically relied on BJR [24]. The device reported in [24], demonstrated under 0.5-dB power penalty through 2.6 km of fiber at 1552 nm, required 2.5V_{PtoP} drive voltage, and provided 1.3 dBm of output power. Our transmitter offers lower drive voltage over a wide wavelength range and is integrated with a 40-Gb/s receiver.

C. 40-Gb/s SOA/UTC Photodiode Receiver Performance

Waveguide receivers consisting of dual section SOAs and UTC photodiodes were placed on ridges parallel to the transmitters as depicted in the labeled SEM image of Fig. 4. Two different receiver designs were explored. The first made use of a 250-μm-long high-gain c-MQW SOA section followed by a 1650-μm high-saturation power o-MQW SOA section and a 30-μm-long UTC photodiode. The second design made use of a 400-μm long high-gain c-MQW SOA section followed by a 1500-μm high-saturation power o-MQW SOA section and a 40-μm-long UTC photodiode. A side-view schematic illustrating the receiver architecture is given in Fig. 18.

The continuous-wave (CW) gain properties of the dual section SOAs were characterized at an input wavelength of 1550 nm and are presented in Fig. 19 with the operation currents listed in the caption. The CW light was fed through a polarization controller and coupled into the input waveguide using a conical-shaped lensed fiber. The compressively strained QWs in the SOAs result in polarization sensitive performance. For maximum gain, the polarization controllers were used to couple only the transverse electric (TE) polarization mode into the device. Since the offset MQW used in the SOAs is independent of the laser gain region and is realized during regrowth, the SOA MQW could be redesigned for a polarization insensitive receiver.

As shown in Fig. 19, the design making use of a 250-μm-long c-MQW section provides a peak gain of $\sim$23 dB and a saturation power of 18.6 dBm while the design using a 400-μm-long c-MQW section provides a peak gain of $\sim$28 dB and a saturation output power of 18.2 dBm. These devices demonstrated only $\sim$0.5-dB gain rolloff for wavelengths ranging from 1535 to 1565 nm. For increased saturation power, the CTL thickness

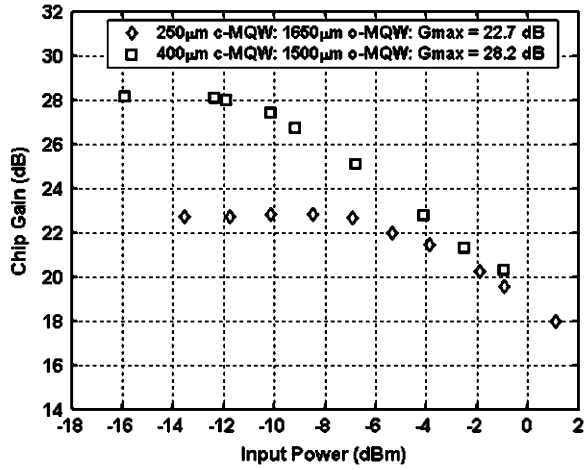

Fig. 19. Gain versus input power for dual section SOAs employing two different designs depicted in legend. In both cases the c-MQWs sections are operating at 15 kA/cm^2 and the o-MQWs sections are operating at 6 kA/cm^2 and the input wavelength is 1550 nm.

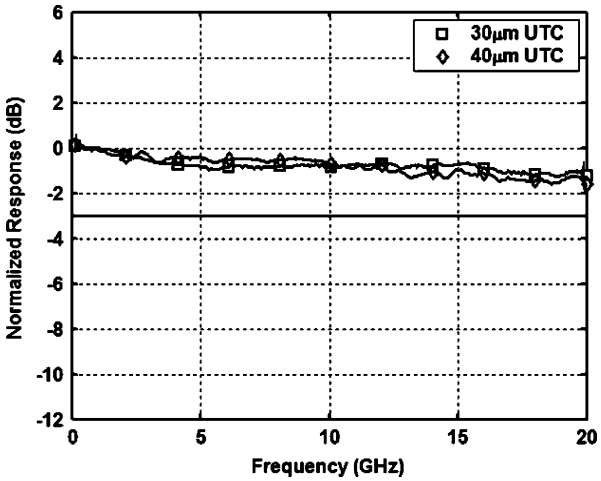

Fig. 20. Small signal response of 30- and 40-μm UTC photodiodes with 20 mA of average photocurrent, a 3-V reverse bias, and a 25-Ω termination.

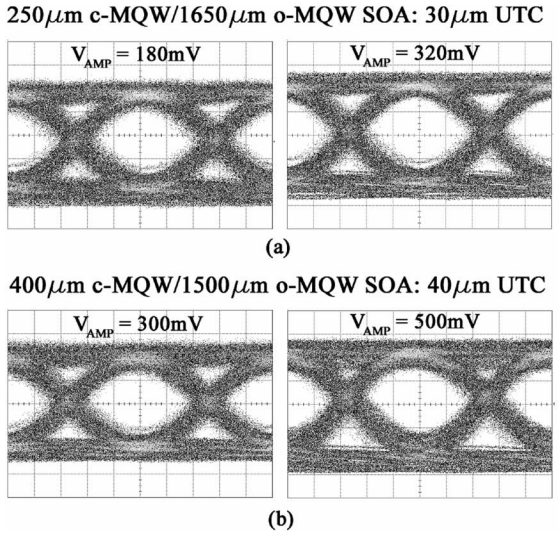

Fig. 21. 40 Gb/s eye diagrams. (a) Receiver design 1 at a c-MQW current density of 12 kA/cm^2. (b) Receiver design 2 at a c-MQW current density of 8 kA/cm^2. In both cases, the o-MQW sections were operated at 5 kA/cm^2 and the detectors were biased at 3 V.

could be increased as we have demonstrated 19.5–20.2-dBm saturation output power with slightly different SOA designs [30].

The frequency response of the 30- and 40-μm-long UTC photodiodes was measured using a 20-GHz Agilent lightwave component analyzer (LCA). A 50-Ω load was used on the RF probes for impedance matching the device to the test-set to avoid electrical reflections within the RF cables. The result of this matching load is an effective termination load of 25 Ω on the photodiode. Fig. 20 presents the response of the detectors with a 3-V reverse bias and an average photocurrent level of 20 mA. As can be seen in the figure, the photodetectors demonstrate only 1–1.5 dB of rolloff at 20 GHz.

The internal quantum efficiency of the UTC photodiodes was measured to be between 30%–35%. An error in the absorption coefficient used in the design simulations led to the choice of a nonoptimal absorber thickness. By increasing the thickness from 50 to 100 nm or above, the optical confinement in the absorber would be increased such that the quantum efficiencies would reach the 80%–90% range.

To demonstrate high-speed receiver functionality, eye diagrams and BER measurements were taken from the two different receiver designs at 40 Gb/s. A PRBS of $2^7 - 1$ was used due to the noise floor in the BERT at longer word lengths. A 40-Gb/s NRZ signal was fed through a band-pass filter, optical attenuator, and polarization controller before entering the input waveguide where it was then amplified in the SOA and detected in the UTC photodiode. Again the input signal was set to the TE polarization state for optimum performance. The output signal from the UTC passed through a bias tee that was connected directly to the oscilloscope or BERT. The optimal bias points of the receiver employing a 250-μm-long c-MQW gain section followed by a 1650-μm o-MQW gain section and a 30-μm-long UTC photodiode were found to be 12 kA/cm^2 in the c-MQW SOA section, 5 kA/cm^2 in the o-MQW SOA section, and a reverse bias of 3.3V on the detector. The receiver output eye diagrams presented in Fig. 21(a) are clear and open demonstrating up to a 320-mV amplitude. If the sensitivity is defined as the power to achieve a BER of 1E-9, the same receiver demonstrated a chip-coupled sensitivity of -16.8 dBm, as shown in the 40-Gb/s BER results of Fig. 22.

The optimal bias points for the receiver using a 400-μm-long c-MQW gain section followed by a 1500-μm o-MQW gain section and a 40-μm-long UTC photodiode were found to be 8 kA/cm^2 in the c-MQW SOA section, 5 kA/cm^2 in the o-MQW SOA section, and a reverse bias of 3.0 V on the detector. The lower optimal current density on the longer c-MQW section of this SOA design was a result of the increasing amplified spontaneous emission (ASE) with current density. The receiver output eye diagrams presented in Fig. 21(b) are clear and open demonstrating up to 500-mV amplitude over the 25-Ω termination. The chip-coupled sensitivity of this receiver design was -20.2 dBm, as shown in Fig. 22. The improved sensitivity of

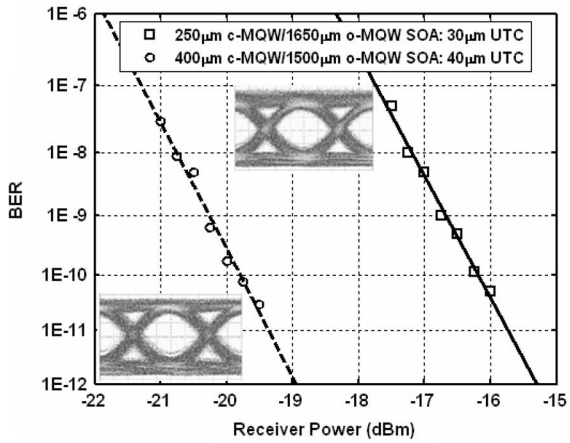

Fig. 22. 40 Gb/s BER versus received power for the two dual section SOA/UTC photodiode receiver designs with inset eye diagrams. The SOA operating conditions are identical to those stated in Fig. 21.

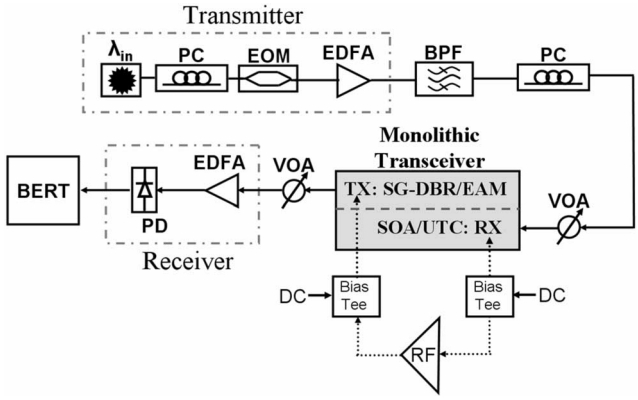

Fig. 23. Test setup used for 40-Gb/s wavelength converter testing. Schematic illustrates the monolithic transceiver from which the detected signal in the receiver is fed off-chip through an amplifier and then back into the EAM.

this receiver is due to the increased gain and quantum efficiency of the longer c-MQW SOA and photodetector, respectively.

State-of-the-art SOA preamplified receivers were reported in [25]. These impressive devices demonstrated a 40-Gb/s sensitivity of -17 dBm, a maximum output amplitude of 250 mV, and required BJR. If an estimated 4-dB coupling loss is subtracted from the chip-coupled sensitivity for the receivers reported here, we arrive at a sensitivity of -16.2 dBm, only slightly lower than that in [25]. However, the devices reported here can provide a $2\times$ greater output amplitude of 500 mV and are integrated with widely tunable 40-Gb/s transmitters. With an expected 4–5-dB increase in the UTC photodiode quantum efficiency by using a 100-nm absorber, the sensitivity will be significantly improved.

D. 40-Gb/s Wavelength Conversion

With the ability to transmit and receive data at 40 Gb/s, the single-chip transceivers were tested as wavelength converters. A 40-Gb/s NRZ input signal with a PRBS of $2^7 - 1$ was coupled into the SOA/UTC receiver for amplification and photodetection. The generated photocurrent was extracted from the UTC with a 50-Ω terminated probe, and then fed through a bias tee, a 26-dB gain RF amplifier, a 6- or 10-dB electrical attenuator, a second bias tee, and into the EAM using a 50-Ω probe. The EAM modulated the output wavelength from the widely tunable SG-DBR laser, resulting in wavelength conversion. The output optical signal was then fed through a variable optical attenuator and into a preamplified receiver before entering the BERT or oscilloscope. The complete test setup is shown in Fig. 23.

Back-to-back and wavelength converted 40-Gb/s eye diagrams are shown in Fig. 24 for a device making use of the dual section SOA design with a 400-μm-long c-MQW section followed by a 1500-μm-long o-MQW section and a 40-μm-long photodiode in the receiver, and a 175-μm-long EAM in the transmitter. The wavelength converted extinction ratios ranged from 10.6 to 11.8 dB for conversion from 1552 to 1542, 1553, and 1564 nm.

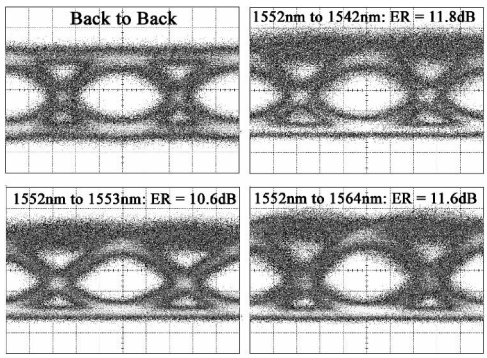

Fig. 24. 40-Gb/s back-to-back and wavelength converted eye diagrams from 1552 to 1542, 1553, and 1564 nm.

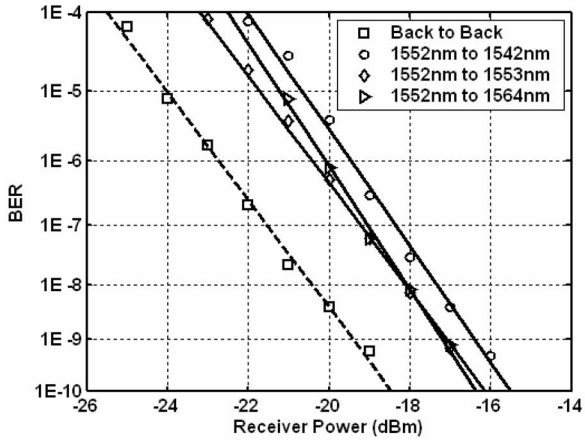

Fig. 25. 40-Gb/s wavelength conversion BER measurements from a transceiver device.

The back-to-back and wavelength converted BER measurements for the same device are shown in Fig. 25. As shown in the figure, error-free 40-Gb/s wavelength conversion is achieved. The device demonstrates between 2–3 dB of power penalty for conversion from 1552 nm to wavelengths of 1542–1564 nm. The optimal bias points for the wavelength conversion experiments were as follows: 1) chip-coupled input powers of -3 to 1 dBm; 2) the 400-μm-long high-gain

c-MQW section biased at 10 kA/cm^2; 3) the 1500-μm-long high-saturation power o-MQW section biased at 5 kA/cm^2; 4) the 500-μm-long laser gain section biased at 6–7 kA/cm^2; 5) the output SOA biased at 1–2 kA/cm^2; 6) the EAM reverse biased between 3–4.5 V; and 7) the photodiode reverse biased at 3–4 V. These operating conditions resulted in a fiber-coupled output power of between -0.5 and 0.5 dBm. Assuming a 4 dB per facet coupling loss, the device provided 3–7 dB of optical chip gain. The low optimal current density applied to the output SOA was a result of increased noise with increased bias level.

With an estimated electrical loss of 4–5 dB in the two bias tees and two RF cables, the total off-chip electrical gain is estimated to be 15–16 dB when a 6-dB attenuator was used and 11–12 dB when a 10-dB attenuator was used. This gain is in the vicinity of the loss associated with the low quantum efficiency of the UTC photodiodes since a 30%–35% internal quantum efficiency yields 9–10 dB of electrical loss over the case of 100% internal quantum efficiency. By modifying the UTC layer structure design the off-chip amplifier can be eliminated.

VII. Conclusion

We demonstrate the first single-chip 40-Gb/s transceivers. The devices integrate SG-DBR lasers, QW-EAMs, low-confinement SOAs, and UTC photodiodes. These unique component structures represent extremely advanced technologies for their respective functions. A high-flexibility integration platform combining QWI and MOCVD regrowth was used for device fabrication. The relatively simple method relies on blanket MOCVD regrowth to avoid regrowth interfaces in the core of the optical waveguide and the use of a dielectric mask pattern on the growth surface.

The SG-DBR lasers demonstrate a tuning range of over 30 nm and an output power of 35 mW. The EAMs provided up to 39-GHz optical bandwidth and required only a 1.5-V_{PtoP} drive to achieve nearly 9 dB of extinction. The low-drive-voltage widely tunable 40-Gb/s SG-DBR/EAM transmitters exhibit performance competitive with discrete single-frequency EAM based devices requiring BJR. The receiver SOAs achieved 23–28 dB of gain and saturation output powers up to 18.6 dBm, while the UTC photodiodes demonstrated 40-Gb/s operation. The -20.2-dBm chip-coupled SOA/UTC receiver sensitivity rivals state-of-the-art preamplified receivers requiring BJR. By using an off-chip electrical amplifier, we demonstrate low-power-penalty 40-Gb/s wavelength conversion.

References

[1] T. L. Koch and U. K. Koren, "Semiconductor photonic integrated circuits," *IEEE J. Quantum Electron.*, vol. 27, no. 3, pp. 641–653, Mar. 1991.

[2] M. Suzuki, Y. Noda, H. Tanaka, S. Akiba, Y. Kushiro, and H. Isshiki, "Monolithic integration of InGaAsP/InP distributed feedback laser and electroabsorption modulator by vapor phase epitaxy," *J. Lightw. Technol.*, vol. LT-5, no. 9, pp. 1277–1285, Sep. 1987.

[3] T. L. Koch, U. Koren, R. P. Gnall, F. S. Choa, F. Hernandez Gil, C. A. Burrus, M. G. Young, M. Oron, and B. I. Miller, "GaInAs/GaInAsP multiple quantum well integrated heterodyne receiver," *Electron. Lett.*, vol. 25, no. 24, pp. 1621–1623, 23, Nov. 1989.

[4] R. J. Deri, T. Sanada, N. Yasuoka, M. Makiuchi, A. Kurumata, H. Hamaguchi, O. Wada, and S. Yamakoshi, "Low-loss monolithic integration of balanced twin-photodetectors with a 3 dB waveguide coupler for coherent lightwave receivers," *IEEE Photon. Technol. Lett.*, vol. 2, no. 8, pp. 581–584, Aug. 1990.

[5] R. Nagarajan, C. H. Joyner, R. P. Schneider Jr., J. S. Bostak, T. Butrie, A. G. Dentai, V. G. Dominic, P. W. Evans, M. Kato, M. Kauffman, D. J. H. Lambert, S. K. Mathis, A. Mathur, R. H. Miles, M. L. Mitchell, M. J. Missey, S. Murthy, A. C. Nilsson, F. H. Peters, S. C. Pennypacker, J. L. Pleumeekers, R. A. Salvatore, R. K. Schlenker, R. B. Taylor, T. Huan Shang, M. F. Van Leeuwen, J. Webjorn, M. Ziari, D. Perkins, J. Singh, S. G. Grubb, M. S. Reffle, D. G. Mehuys, F. A. Kish, and D. F. Welch, "Large-scale photonic integrated circuits," *IEEE J. Sel. Topics Quantum Electron.*, vol. 11, no. 1, pp. 50–65, Jan./Feb. 2005.

[6] E. J. Skogen, J. S. Barton, S. P. DenBaars, and L. A. Coldren, "A quantum-well-intermixing process for wavelength-agile photonic integrated circuits," *IEEE J. Sel. Topics Quantum Electron.*, vol. 8, no. 4, pp. 863–869, Jul./Aug. 2002.

[7] M. K. Chin, "Comparative analysis of the performance limits of Franz–Keldysh effect and quantum confined Stark effect electroabsorption waveguide modulators," *Proc. Inst. Electr. Eng. Optoelectron.*, vol. 142, no. 2, pp. 109–114, Apr. 1995.

[8] K. Morito, S. Tanaka, S. Tomabechi, and A. Kuramata, "A broadband MQW semiconductor optical amplifier with high saturation output power and low noise figure," presented at the Semiconductor Optical Amplifiers and their Applications Meeting, San Francisco, CA, 30 Jun. 2004, (PD1-1).

[9] T. Ishibashi, T. Furuta, H. Fushimi, S. Kodama, H. Ito, T. Nagatsuma, N. Shimizu, and Y. Miyamoto, "InP/InGaAs uni-traveling-carrier photodiodes," *IEICE Trans. Electron.*, vol. E83-C, no. 6, Jun. 2000.

[10] J. Binsma, P. Thijs, T. VanDongen, E. Jansen, A. Staring, G. VanDenHoven, and L. Tiemeijer, "Characterization of butt-joint InGaAsP waveguides and their application to 1310 nm DBR-type MQW gain-clamped semiconductor optical amplifiers," *IEICE Trans. Electron.*, vol. E80-C, pp. 675–681, 1997.

[11] J. Wallin, G. Landgren, K. Streubel, S. Nilsson, and M. Öberg, "Selective area regrowth of butt-joint coupled waveguides in multi-section DBR lasers," *J. Cryst. Growth*, vol. 124, pp. 741–746, 1992.

[12] M. Aoki, M. Suzuki, H. Sano, T. Kawano, T. Ido, T. Taniwatari, K. Uomi, and A. Takai, "InGaAs/InGaAsP MQW electroabsorption modulator integrated with a DFB laser fabricated by band-gap energy control selective area MOCVD," *IEEE J. Quantum Electron.*, vol. 29, no. 6, pp. 2088–2096, Jun. 1993.

[13] M. N. Sysak, J. S. Barton, L. A. Johansson, J. W. Raring, E. J. Skogen, M. L. Maŝanović, D. J. Blumenthal, and L. A. Coldren, "Single chip wavelength conversion using a photocurrent driven (PD) EA modulator integrated with a widely tunable sampled grating DBR (SGDBR) laser," *IEEE Photon. Technol. Lett.*, vol. 16, no. 9, pp. 2093–2095, Sep. 2004.

[14] M. N. Sysak, J. W. Raring, J. S. Barton, M. Dummer, D. J. Blumenthal, and L. A. Coldren, "A single regrowth integration platform for photonic circuits incorporating tunable SGDBR lasers and quantum well EAMs," *IEEE Photon. Technol. Lett.*, vol. 18, no. 15, pp. 1630–1632, Aug. 2006.

[15] M. M. Dummer, M. N. Sysak, J. W. Raring, A. Tauke Pedretti, L. A. Coldren, M N. Sysak, J. W. Raring, D. J. Blumenthal, and L. A. Coldren, "Widely tunable single-chip transceiver for 10 Gb/s wavelength conversion," presented at the Device Research Conf., University Park, PA, Jun. 2006.

[16] V. M. Menon, F. Xia, and S. Forrest, "Photonic integration using asymmetric twin-waveguide (ATG) technology: Part I—Concepts and theory," *IEEE J. Sel. Topics Quantum Electron.*, vol. 11, no. 1, pp. 17–29, Jan./Feb. 2005.

[17] V. M. Menon, F. Xia, and S. Forrest, "Photonic integration using asymmetric twin-waveguide (ATG) technology: Part II—Devices," *IEEE J. Sel. Topics Quantum Electron.*, vol. 11, no. 1, pp. 30–42, Jan./Feb. 2005.

[18] D. Deppe and N. Holonyak Jr., "Atom diffusion and impurity-induced layer disordering in quantum well III–V semiconductor heterostructures," *J. Appl. Phys.*, vol. 64, pp. 93–113, 1988.

[19] S. K. Si, D, H. Yeo, K. H. Yoon, and S. J. Kim, "Area selectivity of InGaAsP-InP multiquantum-well intermixing by impurity-free vacancy diffusion," *IEEE J. Sel. Topics Quantum Electron.*, vol. 4, no. 8, pp. 619–623, Jul./Aug. 1998.

[20] B. C. Qui, A. C. Bryce, R. M. de la Rue, and J. H. Marsh, "Monolithic integration in InGaAs-InGaAsP multiquantum-well structure using laser processing," *IEEE Photon. Technol. Lett.*, vol. 10, no. 6, pp. 769–771, Jun. 1998.

[21] S. Charbonneau, P. Poole, Y. Feng, G. Aers, M. Dion, M. Davies, R. Goldberg, and I. Mitchell, "Band-gap tuning of InGaAs/InGaAsP/InP laser using high energy ion implantation," *Appl. Phys. Lett.*, vol. 67, pp. 2954–2956, 1995.

[22] E. J. Skogen, J. W. Raring, J. S. Barton, S. P. DenBaars, and L. A. Coldren, "Post-growth control of the quantum-well band-edge for the monolithic integration of widely tunable lasers and electroabsorption modulators," *IEEE J. Sel. Topics Quantum Electron.*, vol. 9, no. 5, pp. 1183–1190, Sep./Oct. 2003.

[23] E. Skogen, J. Raring, G. Morrison, C. Wang, V. Lal, M. Masonovic, and L. Coldren, "Monolithically integrated active components: A quantum well intermixing approach," *IEEE J. Sel. Topics Quantum Electron.*, vol. 11, no. 2, pp. 343–355, Mar./Apr. 2005.

[24] M. Okayasu, M. Akashi, and M. Aoki, "A 1550-nm 40-Gb/s electroabsorption DFB laser diode module for transponders with very short reach (< 2 km) applications," in *Proc. IEEE LEOS Annu. Meeting Conf.,* Puerto Rico, Nov. 7–11, 2004, vol. 2, pp. 513–515.

[25] B. Mason, J. M. Geary, J. M. Freund, A. Ougazzaden, C. Lentz, K. Glogovsky, G. Przybylek, L. Peticolas, F. Walters, L. Reynolds, J. Boardman, T. Kercher, M. Rader, D. Monroe, L. Ketelsen, S. Chandrasekhar, and L. L. Buhl, "40 Gb/s photonic integrated receiver with -17 dBm sensitivity," in *Proc. Opt. Fiber Commun. Conf. Exhib.,* Mar. 17–22, 2002, pp. FB10-1–FB10-3.

[26] V. Jayaraman, Z. Chuang, and L. Coldren, "Theory, design, and performance of extended tuning range semiconductor lasers with sampled gratings," *IEEE J. Quantum Electron.*, vol. 29, no. 6, pp. 1824–1834, Jun. 1993.

[27] J. Raring, E. Skogen, S. Denbaars, and L. Coldren, "A study of regrowth interface and material quality for a novel InP based architecture," *J. Cryst. Growth*, vol. 273, no. 1–2, pp. 26–37, Dec. 2004.

[28] J. W. Raring, E. J. Skogen, C. S. Wang, J. S. Barton, G. B. Morrison, S. Demiguel, S. P. DenBaars, and L. A. Coldren, "Design and demonstration of novel quantum well intermixing scheme for the integration of UTC-type photodiodes with QW-based components," *IEEE J. Quantum Electron.*, vol. 42, no. 2, pp. 171–181, Feb. 2006.

[29] T. Yamanaka, K. Tsuzuki, N. Kikuchi, E. Yamada, Y. Shibata, H. Fukano, H. Nakajima, Y. Akage, and H. Yasaka, "High-performance InP-based optical modulators," in *Proc. IEEE/OSA Opt. Fiber Commun. Conf. and Nat. Fibre Opt. Eng. Conf.* Mar. 5–10, 2006.

[30] J. Raring, E. Skogen, M. Mašanović, S. DenBaars, and L. Coldren, "Demonstration of high saturation power/high gain SOAs using quantum well intermixing and MOCVD regrowth," *Electron. Lett.*, vol. 41, no. 24, pp. 1345–1346, Nov. 2006.

James W. Raring was born in Ramsey, NJ, in 1978. He received the B.S. degree from California Polytechnic State University, San Luis Obispo, in 2001 and the Ph.D. degree in materials science from the University of California, Santa Barbara, in 2006.

His dissertation focuses on the design, growth, and fabrication of high-functionality wavelength-agile photonic integrated circuits operating at 10 and 40 Gb/s. The photonic circuits are based on sampled grating DBR lasers, electroabsorption modulators, semiconductor optical amplifiers, and photodiodes. His work explores novel integration methods coupling quantum-well intermixing with straightforward MOCVD regrowth steps. He has authored or coauthored over 70 technical papers.

Dr. Raring is a member of the Optical Society of America and The International Society for Optical Engineering.

Larry A. Coldren received the Ph.D. degree in electrical engineering from Stanford University, Stanford, CA in 1972.

After 13 years in the research area at Bell Laboratories, he joined the University of California, Santa Barbara (UCSB), in 1984, where he is now the Fred Kavli Professor of optoelectronics and sensors, and the Director of the Optoelectronics Technology Center. In 1990, he cofounded Optical Concepts, later acquired as Gore Photonics, to develop novel vertical-cavity surface-emitting laser (VCSEL) technology and in 1998 he cofounded Agility Communications to develop widely tunable integrated transmitters. At Bell Laboratories, he initially worked on waveguided surface-acoustic wave signal processing devices and coupled-resonator filters. He later developed tunable coupled-cavity lasers using novel reactive-ion etching (RIE) technology that he created for the then new InP-based materials. At UCSB he continued work on multiple-section tunable lasers, inventing, in 1988, the widely tunable multi-element mirror concept. During the late 1980s, he also developed efficient vertical-cavity multiple-quantum-well modulators, which led to novel VCSEL designs that provided unparalleled levels of performance. His current research interests include developing new photonic integrated circuit (PIC) and VCSEL technology, including the underlying materials growth and fabrication techniques, creation of vertical and in-plane GaN-based emitters, efficient all-epitaxial InP-based VCSELs, and a variety of PICs incorporating numerous optical elements for widely tunable integrated transmitters, receivers, and wavelength converters. He has authored or coauthored over 700 papers, five book chapters, one textbook, and is a holder of 36 patents.

Prof. Coldren has presented dozens of invited and plenary talks at major conferences. He is a Fellow of the Optical Society of America and Institute of Electrical Engineers, and a member of the National Academy of Engineering. He was the recipient of the 2004 John Tyndall Award.

High-Confinement Strained MQW for Highly Polarized High-Power Broadband Light Source

Steven C. Nicholes, James W. Raring, *Member, IEEE*, Mathew Dummer, *Student Member, IEEE*, Anna Tauke-Pedretti, *Student Member, IEEE*, and Larry A. Coldren, *Fellow, IEEE*

***Abstract*—This letter presents highly polarized edge light-emitting diodes with high-confinement, strained, multiple quantum-well active regions. We demonstrate +40 dB of polarization extinction along with 16 dBm of output power from an 800-μm-long centered quantum-well device. By characterizing the polarization extinction and gain of devices with different lengths and optical confinement, we show that the polarization extinction is dominated by the polarization sensitivity of the gain.**

***Index Terms*—Edge light-emitting diode (ELED), photonic integrated circuits, polarization.**

AS photonic devices evolve towards highly integrated architectures, polarization control of the optical signal becomes increasingly difficult. This results from a lack of chip-level polarization management components that can provide very high extinction between the transverse-electric (TE) and transverse-magnetic (TM) polarization modes. Most available on-chip polarization solutions utilize either interference effects or mode sorting effects to split polarization modes [1]. However, to the best of our knowledge, these devices have not demonstrated polarization extinctions in excess of about 20 dB in InP [1], [2].

In devices that require very high polarization extinction, such as a fiber-optic gyroscope (FOG), greater polarization extinction is needed. The FOG operates based on the Sagnac effect and thus requires high sensitivity to accurately sense small rotations [3]. Even with 30 dB of polarization extinction, the root-mean-square noise from polarization-induced signal drift approaches $10^{\circ}/\mathrm{h}$ [4]. Considering that a quality FOG should sense rotations on the order of $10^{-2\circ}/\mathrm{h}$, the need for a highly polarized optical signal is clear [3].

The use of a highly polarized on-chip light source such as a strained multiple-quantum-well (MQW) laser is another option for achieving high polarization extinction. The addition of strain modifies the band structure, offering reduced threshold currents, higher output powers, and higher polarization sensitivity over unstrained lasers. Polarization extinctions of $\sim$25 dB have been reported from a compressively strained MQW laser [5]. However, due to the fact that it has a spectrally narrow output, a strained MQW laser would not suffice in applications where a broadband source is required, as in the Sagnac-loop based FOG [6].

Manuscript received January 25, 2007. This work was supported in part by the Defense Advanced Research Projects Agency CS-WDM.

The authors are with the Department of Materials and Department of Electrical Engineering, University of California Santa Barbara, Santa Barbara, CA 93116 USA (e-mail: snicholes@engineering.ucsb.edu).

Digital Object Identifier 10.1109/LPT.2007.895896

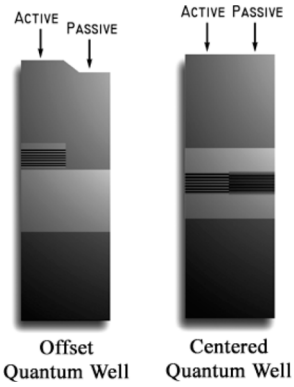

Fig. 1. Side-view schematic of MQWs used for ELED fabrication. The o-MQW (left) has a 6% confinement factor and the c-MQW (right) has a 13% confinement factor.

In this letter, we demonstrate high-optical-confinement, compressively strained MQW gain regions in edge light-emitting diodes (ELED) for the generation of high power, broadband light with over 40 dB of polarization extinction, and 16 dBm of amplified spontaneous emission (ASE) output power. We characterize InGaAsP MQW ELED devices with different lengths and optical confinement factors and show that the polarization extinction is dictated by the incremental gain of the ELED. The polarization extinction increases exponentially with device length and is roughly equal to the large signal gain of the device.

When strain is incorporated in the gain material, the light hole (LH)/heavy hole (HH) degeneracy in the valence band is lifted at the Γ point. The transition matrix element dictates that transitions involving the HH band provide gain/absorption to TE polarized light and those involving the LH band provide gain/absorption mostly to TM polarized light, and to a lesser extent to TE light [7]. Under compressive strain, the conduction band (CB)-HH bandgap shifts to a lower energy than the CB-LH bandgap and the spontaneous emission spectrum generated under forward bias will be heavily TE polarized [5]. As the spontaneously emitted light propagates through the ELED, the polarization extinction of the TE to the TM mode will increase since the incremental gain provided by the strained MQW is highly polarization-dependent.

Two different strained MQW epitaxial designs grown by metal–organic chemical vapor deposition were examined (Fig. 1). The first MQW consisted of ten 6.5-nm compressively strained (0.9%) InGaAsP QWs and 11 8.0-nm tensile strained (-0.3%) InGaAsP barriers centered within two 105-nm 1.3Q waveguide layers. This centered MQW (c-MQW) active region is designed to align the peak of the optical field with

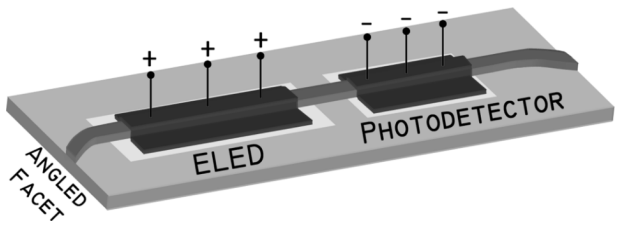

Fig. 2. Schematic of ELED device illustrating the integrated photodetector and angled output facet.

the MQW such that the modal confinement is maximized at ∼13%. The second MQW design made use of seven wells and eight barriers of similar composition and thickness to the first design. However, in this structure the MQW was placed above a single 350-nm-thick 1.3Q waveguide layer. This offset MQW (o-MQW) active region provides an optical confinement of only ∼6%.

For active–passive definition, a quantum-well intermixing method described in [8] was used to shift the as-grown c-MQW bandedge from a photoluminescence wavelength of 1520 nm to 1400 nm in the passive sections. The o-MQW device used selective removal of the offset wells as described in [8] to define passive regions. Using standard InP processing techniques, we fabricated 3-μm-wide surface ridge devices. The devices consisted of an ELED and an integrated photodetector separated by a short passive section (Fig. 2). The reverse biased photodetector was used to measure the ASE power generated in the forward biased ELED. The passive output waveguide employed a curved–flared design along with an antireflective coating to reduce reflections and improve fiber coupling efficiency.

We characterized the ELEDs in terms of polarization extinction, gain, detected output power in the photodetector, and the full-width at half-maximum (FWHM) of the output spectrum. Fig. 3 shows the TE and TM polarization-resolved ASE spectrums from two c-MQW ELEDs at 1.7 kA/cm^2/well. The output of the ELED was collimated through an objective lens into a Glan Thompson prism to split the polarization states, and then coupled into a multimode fiber. Because the CB-LH transition occurs at a higher energy than the CB-HH transition, the peak of the TM spectrum is shifted to a shorter wavelength (∼1450 nm) than that of the TE peak (∼1520 nm). The 200-μm-long device [Fig. 3(a)] demonstrates a TE peak power of −67.5 dBm while the TM mode demonstrates a peak of −79 dB, indicating 11.5 dB of polarization extinction. Fig. 3(b) shows the ASE spectrum from an 800-μm-long c-MQW ELED device exhibiting +40 dB of polarization extinction with the peak of the TE mode at −38 dBm and the TM at −80 dBm. The longer wavelength peak appearing in the TM resolved plot is an artifact of our polarizing prism, which itself was only capable of providing ∼27 dB of polarization extinction. Also shown in the figures are ASE spectrums measured without the polarizer. The TM mode appears as a well-aligned shoulder in the nonresolved spectrum demonstrating that the coupling efficiency was not affecting our extinction values.

The polarization extinction for c-MQW devices with lengths of 200, 400 , 600, and 800 μm are plotted in Fig. 4. As seen in the figure, the extinction is increased by ∼10 dB per 200 μm of ELED length. The TM power remained constant at ∼ −80 dBm

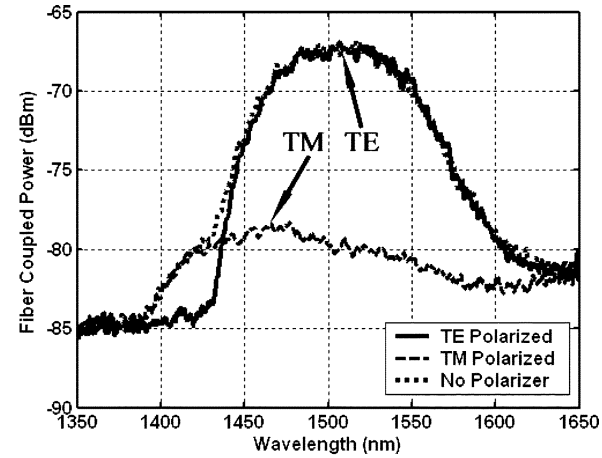

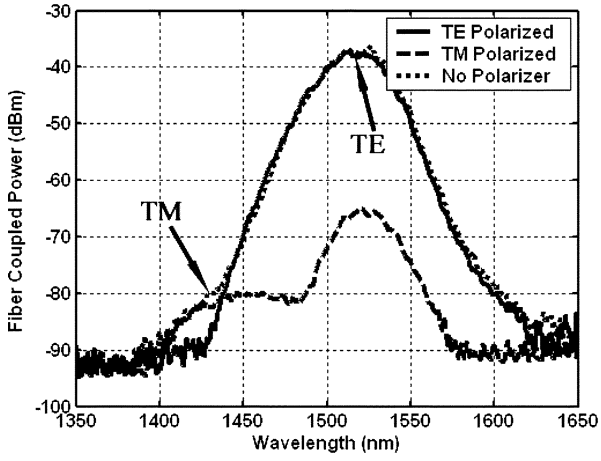

Fig. 3. Output ASE spectrum from (a) 200-μm-long device and (b) 800-μm -long c-MQW device biased at 1.7 Ka/cm^2/well. The figures show spectra for the TE resolved state (solid line), TM resolved state (dashed line), and nonresolved state (dotted line).

in all cases, indicating that the compressively strained MQW essentially provided no incremental gain to the TM mode. Fig. 4 also shows the polarization characteristics of o-MQW devices with lengths 400, 600, and 1000 μm at a current density of 1.4 kA/cm^2/well. These devices clearly do not provide the same degree of polarization extinction as the c-MQW devices, with a slope of only 10 dB per 500 μm of ELED length. In fact, the 1000-μm-long o-MQW device provides the same extinction as the 400-μm-long c-MQW device. Since the c-MQW device possesses an optical confinement factor (and hence an incremental gain) of over 2× that of the o-MQW device, the extinction improvement scales closely with the higher gain offered by the c-MQW ELED. The slightly higher current density per well on the c-MQW ELEDs likely adds to this effect.

A 1548-nm continuous-wave (CW) TE signal was coupled into the ELEDs from lensed fiber to characterize the TE gain of the devices. The chip-coupled input power was first determined by reverse biasing the ELED. Then, with the photodetector under reverse bias, a forward bias of the same current density used in the polarization experiment was applied to the ELED. The gain was calculated by comparing the input power to the photodetected power with the forward biased ELED (Fig. 4).

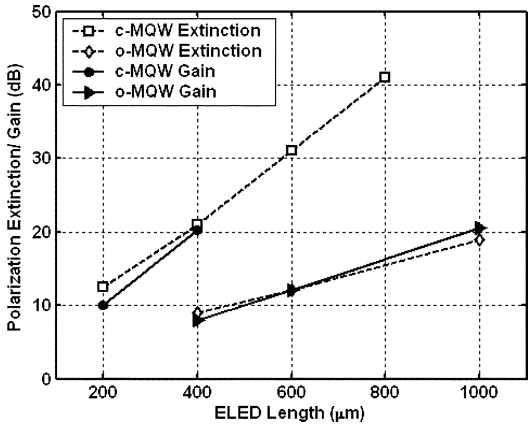

Fig. 4. Polarization extinction (dashed line) and large signal gain (solid line) for various length ELEDs using a c-MQW biased at 1.7 kA/cm^2/well and an o-MQW biased at 1.4 kA/cm^2/well.

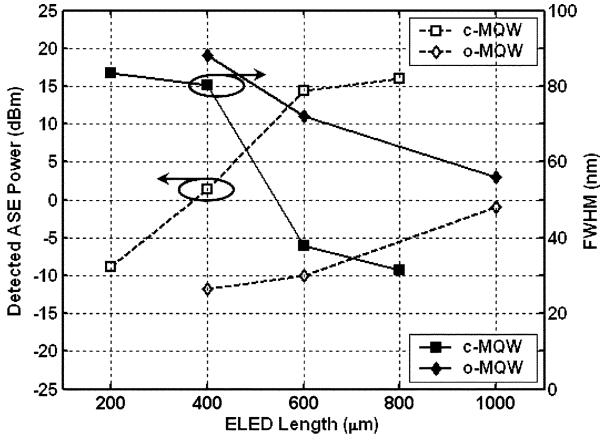

Fig. 5. ASE power (dashed line) and FWHM (solid line) for various length ELEDs using a c-MQW biased at 1.7 kA/cm^2/well and an o-MQW biased at 1.4 kA/cm^2/well.

Clearly, there exists a strong correlation between the gain and the polarization extinction, with the c-MQW device providing $\sim$10 dB of gain per 200 μm and the o-MQW device providing 10 dB of gain per 500 μm of length. This indicates that the polarization extinction in the ELED is dictated by the polarization-dependent gain and not by the polarization of the initial spontaneous emission.

The ASE power collected in the reverse biased (-3 V) photodetector is plotted in Fig. 5 for both ELED types. The c-MQW device generates orders of magnitude more ASE power than the o-MQW device at a fixed length due to the higher incremental gain. The output ASE power increases from -8 dBm in a 200-μm-long device to 14 dBm in a 600-μm-long c-MQW device with a slope of $\sim 11\ \text{dBm}/200\ \mu$m, but then only increases to 16 dBm for an 800-μm-long device. The rolloff in output ASE power is a result of gain saturation in the ELED. The 3-dB output saturation power was measured to be $\sim$15 and 14 dBm in the c-MQW and o-MQW ELEDs, respectively. Since the generated ASE power in the 600- and 800-μm-long c-MQW ELEDs surpasses the saturation power, the large signal gain to the input signal was compressed, explaining the use of only two points in the c-MQW device gain plot of Fig. 4. Beyond a c-MQW device length of 800 μm, we would expect to see a compression in the polarization extinction as the gain provided to the ASE is compressed due to the ASE itself. By employing a wider waveguide, the saturation power and the ASE output power could be improved [9].

The tapered superluminescent diode reported in [10] had a maximum ASE power of $\sim$23 dBm under quasi-pulse testing at an applied current of $\sim$6 A. Our ridge device demonstrates a CW output power of 16 dBm at a current of 410 mA, which is $6\times$ lower than the drive current required by the tapered device (2.5 A) for the same output power. Furthermore, our 3-μm-wide ridge ELED tapers to only 5.6 μm, enabling a higher fiber coupling efficiency than the 130-μm tapered output in [10].

In Fig. 5, we also show how the FWHM of the output spectrum decreases with ELED length. This is a result of the wavelength-dependent gain properties of the MQW. However, the c-MQW ELED offering $\sim$40 dB of polarization extinction still provides more than 30 nm of bandwidth. This could be increased with an alternate quantum-well design.

We have demonstrated strained MQW ELEDs for a high-power broadband light source offering $+40$ dB of polarization extinction. Since the polarization extinction and output power of the ELEDs scale with incremental gain, we confirm that using a maximum confinement c-MQW active region provides superior ELED performance over that of an o-MQW device.

REFERENCES

[1] J. J. G. M. Van der Tol, J. W. Pedersen, E. G. Metaal, Y. S. Oei, H. van Brug, and I. Moreman, "Mode evolution type polarization splitter on InGaAsP–InP," *IEEE Photon. Technol. Lett.*, vol. 5, no. 12, pp. 1412–1414, Dec. 1993.

[2] J. J. G. M. Van der Tol, J. W. Pedersen, E. G. Metaal, J. J.-W. Van Gaalen, Y. S. Oei, and F. H. Groen, "A short polarization splitter without metal overlays on InGaAsP–InP," *IEEE Photon. Technol. Lett.*, vol. 9, no. 2, pp. 209–211, Feb. 1997.

[3] R. Bergh, H. Lefevre, and H. Shaw, "An overview of fiber-optic gyroscopes," *J. Lightw. Technol.*, vol. 2, no. 2, pp. 91–107, Feb. 1984.

[4] S. Merlo, M. Norgia, and S. Donati, *Handbook of Fibre Optic Sensing Technology*, J. Lopez-Higuera, Ed. New York: Wiley, 2000.

[5] T. Tanbun-Ek, N. A. Olsson, R. A. Logan, K. W. Wecht, and A. M. Sergent, "Measurements of the polarization dependence of the gain of strained multiple quantum well InGaAs–InP lasers," *IEEE Photon. Technol. Lett.*, vol. 3, no. 2, pp. 103–105, Feb. 1991.

[6] W. Burns, C.-L. Chen, and R. Moeller, "Fiber-optic gyroscopes with broadband sources," *J. Lightw. Technol.*, vol. LT-1, no. 1, pp. 98–105, Jan. 1983.

[7] J. Burger, W. Steier, and S. Dubovitsky, "The energy-limiting characteristics of a polarization-maintaining Sagnac interferometer with an intraloop compressively strained quantum-well saturable absorber," *J. Lightw. Technol.*, vol. 20, no. 8, pp. 1382–1387, Aug. 2002.

[8] J. Raring *et al.*, "Advanced integration schemes for high-functionality/high-performance photonic integrated circuits," presented at the Proc. SPIE, San Jose, CA, Jan. 23–25, 2006, Paper 61260H.

[9] A. Tauke-Pedretti, M. Dummer, J. S. Barton, M. N. Sysak, J. W. Raring, and L. A. Coldren, "High saturation power and high gain integrated photoreceivers," *IEEE Photon. Technol. Lett.*, vol. 17, no. 10, pp. 2167–2169, Oct. 2005.

[10] F. Koyama, K.-Y. Liou, A. G. Dentai, T. Tanbun-ek, and C. A. Burrus, "Multiple-quantum-well GaInAs–GaInAsP tapered broad-area amplifiers with monolithically integrated waveguide lens for high-power applications," *IEEE Photon. Technol. Lett.*, vol. 5, no. 8, pp. 916–919, Aug. 1993.

Integration of a Traveling-Wave Electro-Absorption Modulator with a Widely Tunable SG-DBR Laser

Matthew M. Dummer[1], *Student Member, IEEE,* Matthew N. Sysak[1], *Student Member, IEEE,*
James W. Raring[2], *Member, IEEE,* Anna Tauke-Pedretti[1], *Student Member, IEEE,*
and Larry A. Coldren[1], *Fellow, IEEE*
[1]University of California Santa Barbara, ECE Department, Santa Barbara, CA 93106 USA
dummer@engineering.ucsb.edu
[2] Sandia National Laboratories, Abuquerque, NM 87185 USA

Abstract

A widely tunable transmitter integrating a sampled grating DBR laser and traveling wave EAM with on-chip termination is presented. The transmitter exhibits a 23 GHz bandwidth, greater than 1 mW output power, and wavelength tuning over 30 nm.

I. Introduction

TRAVELING wave electro-absorption modulators (TW-EAMs) are attractive solutions for high-bandwidth optical modulators in InP. These types of modulators are advantageous due to their small footprint, low drive voltage, and high speed operation. Although many discrete TW-EAMs have been reported [1]–[5] exhibiting 3-dB bandwidths as high as 90 GHz, very few devices have been integrated with semiconductor lasers [6]. In this work we demonstrate the first widely tunable transmitter based on a traveling wave electro-absorption modulator (TW-EAM) integrated with a sampled grating DBR (SG-DBR) laser. The EAM is designed with a transmission line electrode and integrated impedance matched termination, such that the response exceeds the RC time constant limitation of traditional lumped element devices. The 3-dB bandwidth is greater than 23 GHz and the frequency response roll-off is improved by 10 dB/decade due to traveling wave effects. The transmitter is capable of high output powers (>2 mW) with extinction ratios ranging from 8 to 12 dB for wavelengths between 1524 and 1555 nm at data rates of 10 Gbps.

II. Design and Fabrication

The transmitter consists of a five stage SG-DBR laser followed by an output semiconductor optical amplifier (SOA) and TW-EAM shown in Fig. 1. The device was fabricated using a dual quantum well (DQW) base structure similar to that in [7]. A diagram of the epitaxial layer structure is shown in Fig. 2. A quantum well (QW) stack grown above the waveguide with a photo luminescence peak (λ_{PL}) of 1540 nm provides the gain for laser and SOA. These upper QWs are selectively removed from all regions of the device except the 500 μm long laser gain section and 400 μm long SOA before the p-type cladding is grown. A second set of QWs centered in the waveguide provide modulation efficiency by utilizing the quantum confined stark effect (QCSE). However, the centered wells are detuned (λ_{PL} = 1455 nm) from the lasing wavelength to maintain low passive waveguide loss under no applied bias. The TW-EAM was designed with microstrip line geometry such that the electrical signal propagates in the same direction as the optical signal along the 400 μm long modulator ridge. The ridge of the TW-EAM is 2.5 μm wide supported on a 6 μm wide deeply etched mesa to reduce capacitance and allow for the incorporation of a AuGe ground plane close to the ridge for low RF loss. The ground plane and ridge are buried in a photo-defined benzocyclobutene (BCB) as a low-k dielectric. The microstrip electrode contacts the ridge through a via in the BCB as depicted in the schematic cross section in Fig. 3. High speed pads on the input side of the modulator allow for wirebonding or directly driving the TW-EAM with a signal-ground (SG) probe. The electrode is terminated by an impedance matched thin-film NiCr resistor deposited by electron-beam evaporation. In series with the resistor is a 30 pF on-chip capacitor formed by sandwiching 250 nm of silicon nitride between a top Au plate and the AuGe ground plane. The capacitor is designed to eliminate DC power dissipation in the resistor while still providing an effective RF ground path. Additionally, the on-chip capacitor is wire bonded to a larger capacitor (220 nF) mounted on the carrier in parallel to improve the low frequency response. This is especially important for achieving low pattern dependence

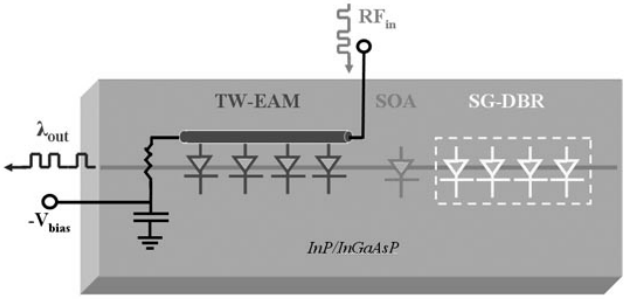

Fig. 1. Circuit diagram of fabricated TW-EAM transmitter with integrated load resistor and capacitor

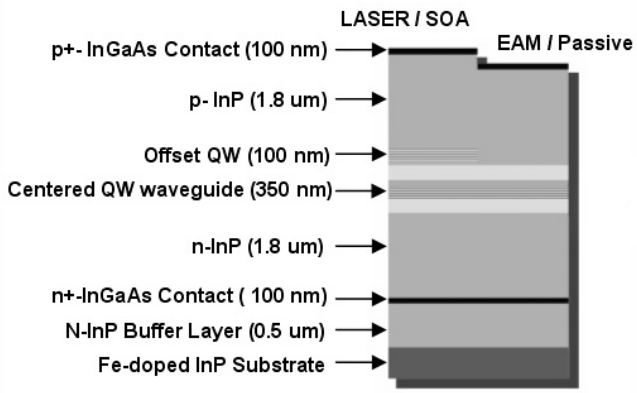

Fig. 2. Epitaxial layer structure for dual quantum well TW-EAM transmitter.

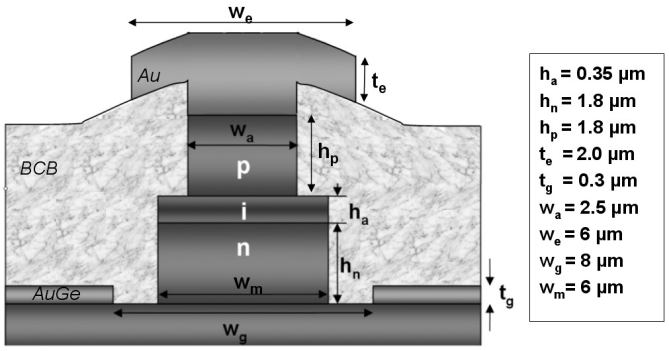

Fig. 3. Schematic cross section and dimensions of fabricated TW-EAM.

during transmission of digital data with long word lengths.

III. Traveling Wave Experiments

Two-port electrical S-parameter measurements have been performed on the TW-EAM to determine its transmission line behavior. The characteristic impedance, electrical effective index, and microwave loss versus frequency were determined using the ABCD method described in [8] and are shown in Fig. 4 & 5. The characteristic impedance (Z_0) is 22 Ω and the electrical index is about 6.5 demonstrating a 62% mismatch between the optical and electrical traveling waves. These values are typical of such capacitively loaded microstrip lines and we have observed good agreement with simulations using the method described in [9] based on the device geometry. The microwave loss is highly frequency dependant and increases as 0.55 cm^{-1}/GHz (or 0.24 $dB/(mm \cdot GHz)$). Measurements of both loaded and unloaded transmission lines show that over 80% of this loss is due to the series resistance of the reverse biased TW-EAM diode. The remainder can be attributed to the microwave losses of the metal electrode at high frequencies.

Due to the integration of the laser and electrical terminations on this device, it is not possible to directly measure the traveling wave benefit in the frequency response. Instead, discrete TW-EAMs were fabricated on the same wafer so that light could be coupled in from either facet to compare the co- and counter-propagating electrical-to-optical (EO) response.

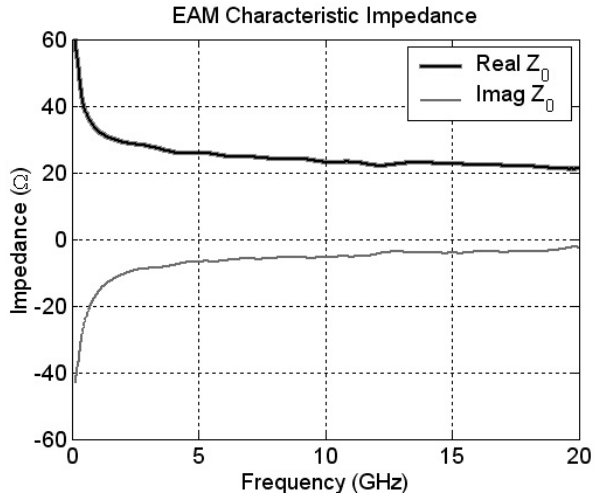

Fig. 4. Characteristic impedance (Z_0) vs. frequency of TW-EAM extracted from two-port S-parameters. The DC bias was -2 V.

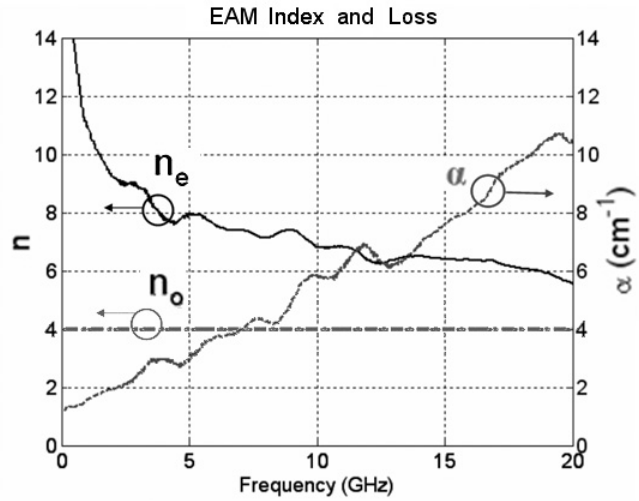

Fig. 5. Electrical effective index (n_e) compared with optical group index (n_o) and microwave loss coefficient (α).

The integrated resistor value used for this experiment was 20 Ω to be matched to Z_0 of the TW-EAM. The small signal frequency responses for the modulator are shown in Fig. 5. The response of the co-propagating measurement has a 3-dB bandwidth of 23 GHz and rolls off by 10 dB/decade compared to 20 GHz and 20 dB/decade when the optical and electrical signals travel in opposite directions.

IV. Transmitter Performance

The SG-DBR with post-amplifier is capable of producing up to 10 dBm of fiber coupled output power over the continuous tuning range of 1524 nm to 1565 nm (Fig. 8). The TW-EAM efficiency has been measured over the tuning range of SG-DBR laser. Figure 7 shows the measured DC extinction characteristics of the integrated modulator. The extinction curve is highly dependent on the lasing wavelength and shows significant improvement in efficiency as the detuning from the centered QW band edge is reduced. The maximum slope

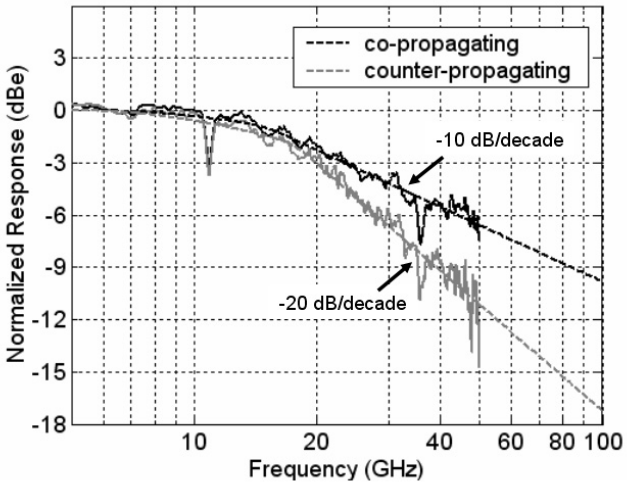

Fig. 6. Small signal EO measurement comparing co- and counter-propagating traveling wave response for -1.5 V bias.

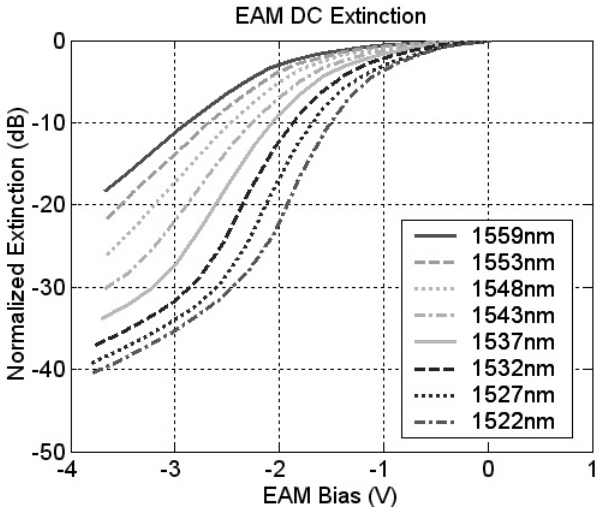

Fig. 7. Normalized DC extinction curves measured over the wavelength tuning range of the SG-DBR laser.

efficiency ranges from 10 dB/V for 1559 nm to as high as 25 dB/V for 1522 nm.

Transmission of digital data has been performed at 10 Gbps non-return to zero (NRZ). DC bias currents for the laser and SOA were 120 mA and 100 mA, respectively. The modulator was directly driven using a SG coplanar probe and biased across the on-chip capacitor as shown in Fig 1. An on-chip termination resistance of 35 Ω was used to reduce the mismatch between the EAM and the 50 Ω electrical driver circuit. Open eye diagrams were observed over a 30 nm range of wavelengths and are shown in Fig. 8. The TW-EAM DC bias for the 1524 nm, 1539 nm, and 1555 nm transmission were -2.1 V, -2.7 V, and -3.5 V to to take advantage of the steepest part of the modulator extinction curves for each respective wavelength. Extinction ratios (E.R.) as high as 12 dB and eye amplitudes (P_{out}) as high as 2 mW, fiber coupled, were achieved for an electrical drive voltage of 2 V peak-to-peak.

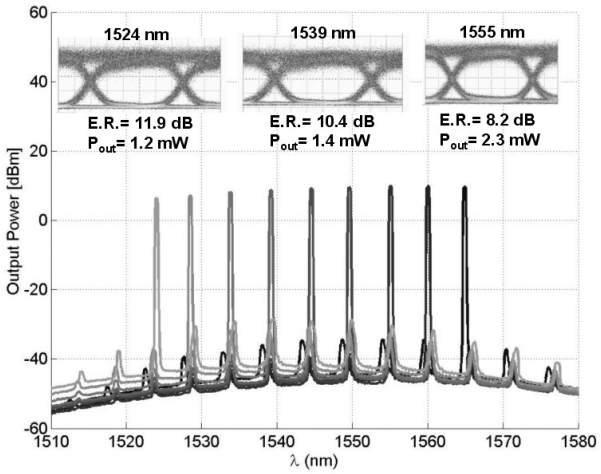

Fig. 8. Overlayed optical spectrums depicting the supermodes of the widely tunable SG-DBR. Inset: Transmitted eye diagrams at 10 Gbps NRZ. Wavelength, extinction ratio, and optical amplitude are shown.

V. Conclusion

We have demonstrated a traveling wave electro-absorption modulator based transmitter tunable over 30 nm. The device includes an integrated matched electrical termination to simplyfy biasing and reduce microwave loss. The TW-EAM design exhibits a 2x improvement in the response slope due to the traveling wave enhancement. Tranmission of digital data at 10 Gbps NRZ has been acheived with greater than 8 dB extinction and 1 mW output power over the laser tuning range. Future work will focus on improving device performance to accommodate much higher data rates. This will be accomplished by raising the characteristic impedance of the TW-EAM to reduce the mismatch and improve the series resistance for lower microwave loss.

References

[1] T. Yamanaka, K. Tsuzuki, N. Kikuchi, E. Yamada, Y. Shibata, H. Fukano, H. Nakajima, Y. Akage, and H. Yasaka, "High-performance inp-based optical modulators," in *Optical Fiber Communication Conference, 2006 and the 2006 National Fiber Optic Engineers Conference*, 2006, pp. 3 pp.–.

[2] Y.-J. Chiu, T.-H. Wu, W.-C. Cheng, F. Lin, and J. Bowers, "Enhanced performance in traveling-wave electroabsorption modulators based on undercut-etching the active-region," *Photonics Technology Letters, IEEE*, vol. 17, no. 10, pp. 2065–2067, 2005.

[3] R. Lewen, S. Irmscher, U. Westergren, L. Thylen, and U. Eriksson, "Segmented transmission-line electroabsorption modulators," *Lightwave Technology, Journal of*, vol. 22, no. 1, pp. 172–179, 2004.

[4] S. Zhang, V. Kaman, A. Keating, Y.-J. Chiu, P. Abraham, and J. Bowers, "30 gbit/s operation of a traveling-wave electroabsorption modulator," in *Optical Fiber Communication Conference, 1999, and the International Conference on Integrated Optics and Optical Fiber Communication. OFC/IOOC '99. Technical Digest*, vol. 3, 1999, pp. 290–292 vol.3.

[5] G. Li, S. Pappert, P. Mages, C. Sun, W. Chang, and P. Yu, "High-saturation high-speed traveling-wave ingaasp-inp electroabsorption modulator," *Photonics Technology Letters, IEEE*, vol. 13, no. 10, pp. 1076–1078, 2001.

[6] T. Knodl, C. Hanke, B. Saravanan, M. Peschke, R. Macaluso, and B. Stegmuller, "40 GHz monolithic integrated 1.3 μm InGaAlAs-InP laser-modulator with double-stack MQW layer structure," in *Lasers and Electro-Optics Society, 2004. LEOS 2004. The 17th Annual Meeting of the IEEE*, vol. 2, 2004, pp. 675–676 Vol.2.

[7] M. Sysak, J. Raring, J. Barton, M. Dummer, D. Blumenthal, and L. Coldren, "A single regrowth integration platform for photonic circuits incorporating tunable sgdbr lasers and quantum-well eams," *Photonics Technology Letters, IEEE*, vol. 18, no. 15, pp. 1630–1632, 2006.

[8] R. Spickermann and N. Dagli, "Experimental analysis of millimeter wave coplanar waveguide slow wave structures on gaas," *Microwave Theory and Techniques, IEEE Transactions on*, vol. 42, no. 10, pp. 1918–1924, 1994.

[9] R. Lewen, S. Irmscher, and U. Eriksson, "Microwave cad circuit modeling of a traveling-wave electroabsorption modulator," *Microwave Theory and Techniques, IEEE Transactions on*, vol. 51, no. 4, pp. 1117–1128, 2003.

Increased Modal Overlap for Improved Sensitivity in a Monolithic Intracavity Chemical Sensor

Jill A. Nolde, *Member, IEEE*, James W. Raring, *Member, IEEE*, and Larry A. Coldren, *Fellow, IEEE*

***Abstract*—We discuss the design and fabrication of an InP-based single-chip chemical sensor with increased modal overlap with a chemical analyte. The fabricated devices use a sensor design with frequency tunable lasers and heterodyne spectrometers. By reducing the waveguide ridge width in one section of the laser, the transverse modal overlap with the analyte increases by 17 times, increasing the sensitivity by the same ratio. A frequency shift of 72 GHz/refractive index unit was measured with temperature effects removed. The frequency stability of this sensor is as low as 436 kHz leading to a minimum detectable index difference of 6×10^{-6}.**

***Index Terms*—Distributed Bragg reflector (DBR) lasers, integrated optoelectronics, semiconductor lasers, transducers, waveguide couplers.**

I. Introduction

RAPID and reliable identification of a foreign substance has always been desirable, but events of recent years have heightened public interest. Many of the most established technologies and processes for identifying a substance require treatment of the sample with fluorescent markers before testing; therefore, these methods have a slow response time, are unable to test for several analytes in parallel through multiplexing, and are inconvenient outside of a laboratory. Even the available direct assay optical techniques require the use of external light sources, optics, and detectors, eliminating the portability of the device. With partial or hybrid integration of the optics, such as through the use of planar waveguides, the sensing system would still require careful packaging in order to move the light on- or off-chip—packaging which can represent more than half of the device cost [1]. By integrating all of the functionality onto a single chip, a portable, inexpensive system, which allows simple multiplexing to detect several analytes, is possible.

Refractometric techniques—based on surface plasmon resonance (SPR), interferometry, and intracavity resonances—have yielded some of the most promising results, in terms of integration and sensitivity. Portable sensors using SPR have demonstrated high enough sensitivities to allow commercialization [2]. An interferometric sensor has produced a high sensitivity approaching 5×10^{-8} with a long interaction length of 4 mm and an off-chip laser [3]. Another interferometry-based sensor using an on-chip diode laser reached a sensitivity of 1×10^{-5} [4]. Finally, approaches using intracavity resonance have been demonstrated using an external cavity laser [5] as well as a monolithically integrated laser [6], with promising results.

In this letter, we demonstrate a chemical sensor which measures changes in the lasing frequency resulting from the variation of the cladding material. The evanescent portion of the propagating mode overlaps the analyte, causing a variation in the effective index, and, in turn, the lasing wavelength. This frequency change is then measured through a heterodyne signal, which can be theoretically measured to within 1 Hz on a spectrum analyzer. In addition to this extreme resolution, the subtractive nature of heterodyning reduces the noise on the signal caused by temperature variation or caused, in biosensing, by nonspecific binding.

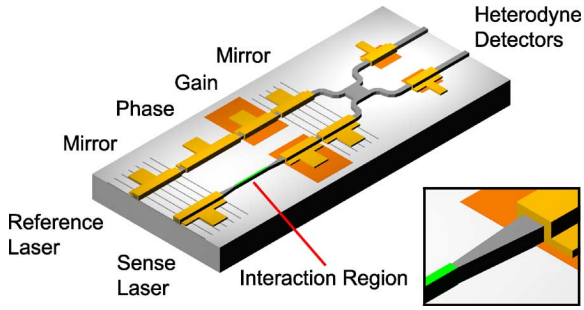

Fig. 1. Schematic of the intracavity sensor composed of two SG-DBR lasers and a heterodyne spectrometer utilizing a 2×2 combiner and quantum-well photodetectors. The interaction region of the sensing laser, shown in the inset, has no dielectric layer on the ridge and is narrowed to increase the modal overlap with the cladding index.

II. Device Overview

As shown in Fig. 1, this sensor is composed of two widely tunable, sampled-grating distributed Bragg reflector (SG-DBR) lasers, a multimode interference (MMI) combiner, and two quantum-well photodetectors. The reference laser is a common telecommunications design that can be continuously tuned from 1530 to 1570 nm via current injection. The sensing laser is similarly designed and tunes discontinuously over the same range. In order to be sensitive to the chemical analyte, the phase section of this laser is changed by reducing the ridge width. When the outputs of these two lasers are combined and

Manuscript received January 2, 2007; revised March 27, 2007. This work was supported in part by the Army Research Office through the Institute for Collaborative Biotechnology.

J. A. Nolde was with the Department of Electrical and Computer Engineering, University of California, Santa Barbara, CA 93106 USA. She is now with the Naval Research Laboratory, Washington, DC 20375 USA (e-mail: nolde@engineering.ucsb.edu).

J. W. Raring and L. A. Coldren are with the Department of Electrical and Computer Engineering, University of California, Santa Barbara, CA 93106 USA (e-mail: coldren@ece.ucsb.edu).

Color versions of one or more of the figures in this letter are available online at http://ieeexplore.ieee.org.

Digital Object Identifier 10.1109/LPT.2007.899452

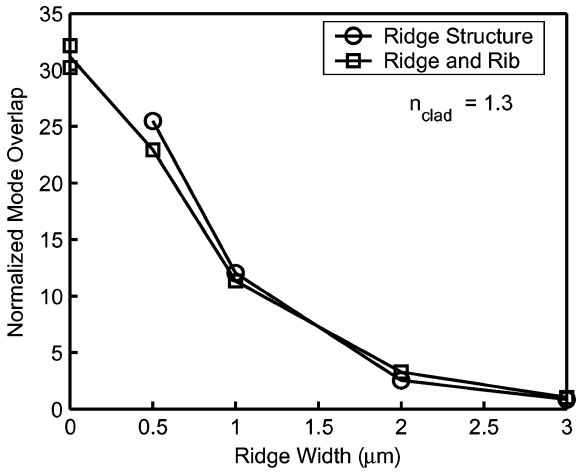

Fig. 2. Normalized modal overlap for narrowed ridge structures. The overlap values are normalized to the value for a 3-μm-wide ridge ($\Gamma_{xy} = 0.012\%$). The device with the highest overlap, the 0-μm ridge width structure, has the p-InP upper cladding completely removed in the sensing region.

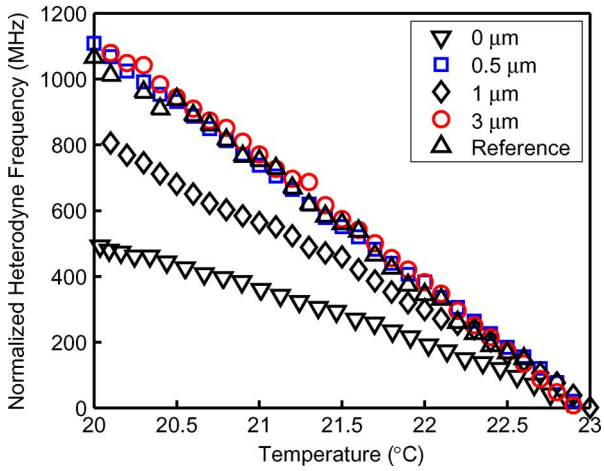

Fig. 3. Temperature sensitivity of heterodyne signal for devices with different ridge widths. This data was obtained by varying the heatsink temperature while continuously measuring the heterodyne frequency. The reference device has neither 3-μm ridge laser sensitized.

absorbed, the resulting photocurrent has a frequency component equal to the difference in the output frequencies of the individual lasers. As the analyte index changes, the heterodyne frequency shifts according to

$$\frac{\Delta n_{\text{analyte}}}{\overline{n}} = \frac{1}{\Gamma}\frac{\Delta\lambda}{\lambda} = \frac{1}{\Gamma}\left|\frac{\Delta f}{f}\right| \tag{1}$$

where f is the lasing frequency, $\overline{n}$ is the effective modal index of the entire cavity, $\Delta n_{\text{analyte}}$ is the change in the cladding or analyte index, Δf is the shift in heterodyne frequency, and Γ is the optical confinement factor between the optical mode and the analyte. The frequency shift can be directly measured as an analyte indicator. Alternatively, since both lasers are tunable, the photocurrent can be fed back into the reference laser in a closed-loop manner, in order to maintain a constant heterodyne frequency. This functionality reduces the dynamic range of the output.

Given a device structure with a specific effective index and wavelength, the modal overlap is the only adjustable parameter to increase the sensitivity ($\Delta f/\Delta n$). This is done by narrowing the laser ridge in the sensing region with the use of processing techniques and materials from established optoelectronics technologies. Except for the sensing region, the nominal ridge width is 3 μm throughout the device. From the simulation shown in Fig. 2, the ridge width must be reduced below 1 μm in order to achieve the desired order of magnitude improvement in sensitivity. Since the sensing region is within the laser cavity, the transition between ridge widths is accomplished through a gradual taper to avoid reflections. By using an angled abrupt transition with slightly modified processing, the tuning and control of the 0-μm device can be maintained without sacrificing extra chip length, at the cost of increased loss. Finally, the longitudinal fill factor Γ_z—the ratio of the sensing region length to the cavity length—is kept constant at 0.25 by adjusting the sensing region length.

The epitaxial structure and fabrication of these devices follows that of [7] and can be used to fabricate several photonic integrated circuits, producing ridges down to 0.5 μm wide. For the sensing region of the 0-μm structure, the ridge is removed and a rib is etched into the waveguide layer. The abrupt transition to the ribbed region is self-aligned to the ridge using the dry etch selectivity of SiN_x and SiO_2.

After fabrication and cleaving, each device was mounted on an AlN carrier; gold wirebonds connect all of the device contacts to the carrier. Then, each device was placed into a fluid reservoir made from a 12-pin butterfly package. Wirebonds were made between the carrier and the package pins. To eliminate evaporative cooling as well as liquid loss through evaporation, a lid for the package was used, with silicone adhesive sealing the edges. Solvents were added to the package using a pipette. Exchanges were performed by draining the solvent from a hole drilled in the bottom and flushing the package at least three times with the new solvent. Four solvents and the associated mixtures were tested: methanol, ethanol, 1-propanol, and 2-propanol. The temperature of the butterfly package device was controlled using a thermoelectric cooler and a thermistor on the outside of the package.

III. Sensing Results

A major concern of any sensor using semiconductor materials is the effect of temperature on the effective index and wavelength of the device. Like any single-frequency laser, the SG-DBR output wavelength will vary by approximately 1 Å/°C. This corresponds to a frequency shift of 13–15 GHz/°C. This level of sensitivity to temperature is unacceptable for chemical sensing. Through heterodyning, this effect will, at least partially, cancel. As can be seen in Fig. 3, all six device variations have a temperature sensitivity of less than 380 MHz/°C. Additionally, the reference pair, in which neither laser is sensitized, can be used as a temperature monitor. Since this latter device should show no chemical sensitivity, frequency changes will signal the current temperature of the system.

The data of Fig. 3 was measured with the mounted device in air; therefore, negligible heat dissipation occurred upward from the device. However, when the devices are tested in solvents

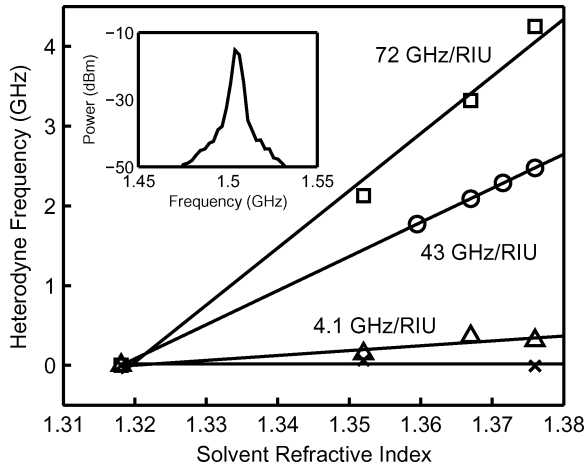

Fig. 4. Comparison of heterodyne shift for devices with different ridge widths: 0 μm (□), 1 μm (○), 3 μm (△), and reference (×). Temperature effects, corresponding to 7% of the raw values for the 0-μm device, have been removed from the data. Inset shows a typical heterodyne signal for 0-μm device with a 3-dB linewidth of 3.6 MHz.

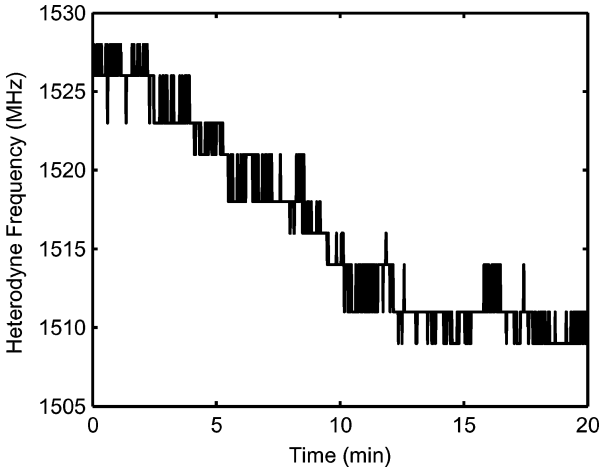

Fig. 5. Heterodyne frequency stability of 0-μm device. Device is held at a constant bias of 91 and 80 mA on the reference and sensing laser gain sections, respectively, and 3 mA on the reference laser phase section. Standard deviation of signal is 5.9, 1.5, and 0.4 MHz for 20-, 10-, and 1-min intervals, respectively.

of varying indices, heat will conduct into the liquids, varying the internal temperature of the active region, proportional to the thermal conductivity of the solvents. To verify the temperature shift as a function of index, a 2-D steady state analysis based on heat conduction was performed.

To remove the temperature effect from each data point, the response of the reference device—a measure of temperature change only—is scaled by the ratio of the temperature sensitivity (shown in Fig. 3) of the sensing device to the reference device. Then, this value is multiplied by the temperature shift for each solvent from the heat transfer simulation. Finally, this heterodyne shift value is subtracted from the raw data to yield the shift due solely to index. The results are shown in Fig. 4.

For each ridge width, a line is fit through the data points to provide an estimate of sensitivity. From (1), the modal overlap Γ for each device can be calculated. This value can then be multiplied by Γ_z to determine the modal overlap Γ_{xy}. The values for the cross-sectional overlap are 0.027%, 0.28%, and 0.47% for the 3-, 1-, and 0-μm devices, respectively. This increase over the simulated values can be explained either by the fill factor approximation for the longitudinal intensity distribution or by ridge width variation in processing.

From the measurements of sensitivity above, the minimum detectable index change can be derived by dividing the sensitivity values by the full-width at half-maximum (FWHM) of the signal being measured. For this device, the limiting value of the FWHM can be measured in terms of the fundamental linewidth and the thermal drift. From the inset of Fig. 4, the linewidth is 3.6 MHz, leading to a sensitivity limit of 5×10^{-5}. Fig. 5 shows the stability of the heterodyne signal when held with a constant bias. The standard deviation of the signal is 1.5 MHz for a 10-min period corresponding to an index sensitivity of 2.1×10^{-5}. The short-term standard deviation and sensitivity are 436 kHz and 6.1×10^{-6} for a 1-min measurement. Even without including a reference device inside the sensor package, the residual temperature sensitivity for the 0-μm device can be kept to 312 kHz using active temperature control (stability <2 mK possible), validating these estimates of sensitivity.

IV. Conclusion

In summary, we have demonstrated a method of increasing the index sensitivity of a refractometric transducer, in a way which is compatible with typical laser processing for telecommunications devices. By narrowing the ridge in the sensing region, we have increased the modal overlap with an analyte by 17 × over the standard 3-μm ridge device. The single-chip sensor demonstrated a sensitivity of 6×10^{-6}, which is comparable to other technologies that use interaction lengths 15 to 37 times larger.

Acknowledgment

The authors would like to thank D. A. Cohen for inspiration, discussion, and advice.

References

[1] B. W. Hueners and M. K. Formica, "Photonic component manufacturers move toward automation," *Photon. Spectra*, vol. 37, pp. 66–72, 2003.

[2] J. Melendez, R. Carr, D. Bartholomew, H. Taneja, S. Yee, C. Jung, and C. Furlong, "Development of a surface plasmon resonance sensor for commercial applications," *Sens. Act. B*, vol. B39, pp. 375–379, 1997.

[3] R. G. Heideman and P. V. Lambeck, "Remote opto-chemical sensing with extreme sensitivity: Design, fabrication and performance of a pigtailed integrated optical phase-modulated Mach–Zehnder interferometer system," *Sens. Act. B*, vol. 61, pp. 100–127, 1999.

[4] B. Maisenholder, H. P. Zappe, R. E. Kunz, P. Riel, M. Moser, and J. Edlinger, "A GaAs/AlGaAs-based refractometer platform for integrated optical sensing applications," *Sens. Act. B*, vol. 38–39, pp. 324–329, 1997.

[5] Y. Beregovski, O. Hennig, M. Fallahi, F. Guzman, R. Clemens, S. Mendes, and N. Peyghambarian, "Design and characteristics of DBR-laser-based environmental sensors," *Sens. Act. B*, vol. 53, pp. 116–124, 1998.

[6] D. A. Cohen, J. A. Nolde, A. Tauke Pedretti, C. S. Wang, E. J. Skogen, and L. A. Coldren, "Sensitivity and scattering in a monolithic heterodyned laser biochemical sensor," *IEEE J. Sel. Topics Quantum Electron.*, vol. 9, no. 5, pp. 1124–1131, Sep./Oct. 2003.

[7] J. S. Barton, E. J. Skogen, M. L. Masanovic, S. P. Denbaars, and L. A. Coldren, "A widely tunable high-speed transmitter using an integrated SGDBR laser-semiconductor optical amplifier and Mach–Zehnder modulator," *IEEE J. Sel. Topics Quantum Electron.*, vol. 9, no. 5, pp. 1113–1117, Sep./Oct. 2003.

Short-Cavity 980 nm DBR Lasers With Quantum Well Intermixed Integrated High-Speed EA Modulators

Chad S. Wang, *Member, IEEE*, Yu-Chia Chang, Uppili Krishnamachari, James W. Raring, *Member, IEEE*, and Larry A. Coldren, *Fellow, IEEE*

***Abstract*—Short-cavity, 980 nm distributed Bragg reflector (DBR) lasers with integrated electroabsorption modulators (EAMs) were designed and fabricated using a quantum-well intermixing (QWI) processing platform. Design curves are discussed and the QWI fabrication details are presented. The transmitters exhibited RF bandwidths of 20 GHz and demonstrated error-free operation at 10 Gb/s.**

***Index Terms*—Electroabsorption modulators, photonic integrated circuits, quantum well intermixing, semiconductor lasers.**

I. Introduction

FOR PHOTONICS to replace copper-based electronics in applications such as board-to-board and chip-to-chip level interconnects, there is a clear need for increased speed and efficiency. Traditionally, vertical-cavity surface-emitting lasers (VCSELs) have been the technology of choice for deployment in short-reach data link interconnect applications [1] because of their low power dissipation, ease of coupling, and ability to be integrated into arrays. However, in these traditional interconnect systems, most of the power consumption occurs over the receiver electronics, namely over transimpedance amplifiers. An alternative method to reduce the overall power consumption of the link is to use a "receiver"-less architecture to eliminate the receiver electronics. This requires high-output power transmitters to directly drive detectors controlling the decision circuits.

In order to achieve a high-power, high-speed, and low-power dissipation single-mode transmitter, we propose a short-cavity distributed Bragg reflector (DBR) laser structure with an integrated electroabsorption modular (EAM) to meet these requirements. This design crosses the advantages of VCSELs and edge-emitters. By reducing the active volume of the laser cavity, the efficiency of the device is improved, to a point where the mirror reflectivity must be increased. VCSELs have demonstrated high efficiencies, but operation to higher data rates is challenging. For VCSELs, the highest data rate reported is 25 Gb/s [2]. Edge-emitters with integrated EAMs have shown operation at 40 Gb/s. We have previously demonstrated high efficiency, short-cavity DBR lasers at 1.55 μm with integrated, high-bandwidth (25 GHz) EAMs [3]. By using a quantum-well intermixing (QWI) integration platform, the laser and modulator can be simultaneously optimized for high performance. Recently, 980 nm DBR lasers with quantum well intermixed passive sections have been demonstrated with output powers up to 400 mW [4]. Moreover, intermixed quantum well (QW) EAMs have also shown promise to extend data rates up to 40 Gb/s and beyond [5]. Here, we present a short-cavity, 980 nm, DBR laser using a QWI platform in the InGaAs/GaAs/AlGaAs material system, monolithically integrated with a high-speed EAM demonstrating 20 GHz of 3 dB bandwidth. Design curves are discussed and the QWI fabrication details are presented.

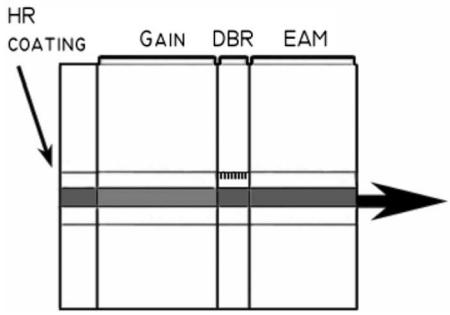

Fig. 1. Schematic cross section of DBR laser device with integrated EAM. Indicated are the sections of the DBR laser-EAM transmitter.

II. Experiment

A. Short-Cavity DBR Laser Design

We propose a short-cavity DBR laser with integrated EAM designed with three sections: gain, front DBR mirror, and EAM, with a high reflectivity (HR) coating applied to the rear facet of the DBR, as shown in the side-view schematic of Fig. 1. In designing a short-cavity laser, tradeoffs exist between the operating current as a function of mirror reflectivity and active region length. We can begin by simulating the operating current I as a function of front mirror reflectivity R_1 or equivalently, mirror length, as described by

$$I = \frac{qP_o(\alpha_i + \alpha_m)}{F_1 \eta_i h \nu \alpha_m} + I_{\text{th}} \tag{1}$$

Manuscript received November 1, 2006; revised July 22, 2007. This work was supported in part by the Defense Advanced Research Projects Agency under Chip-to-Chip Optical Interconnects.

C. S. Wang, Y.-C. Chang, U. Krishnamachari, and L. A. Coldren are with the Electrical and Computer Engineering Department, University of California, Santa Barbara, CA 93106 USA (e-mail: cswang@engineering.ucsb.edu).

J. W. Raring was with the Materials Department, University of California, Santa Barbara, CA 93106 USA. He is now with Sandia National Laboratories, Albuquerque, NM 87123 USA.

Digital Object Identifier 10.1109/JSTQE.2007.905095

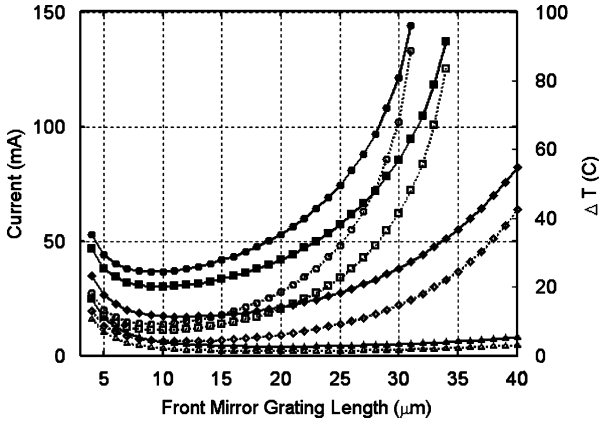

Fig. 2. Design curve of operating current (solid lines) and on-chip temperature rise (dotted lines) vs. front mirror grating length for a family of output powers at 1 mW (triangles), 10 mW (diamonds), 20 mW (squares), and 25 mW (circles). The active region length was set at 110 μm and κ of 650 cm^{-1}.

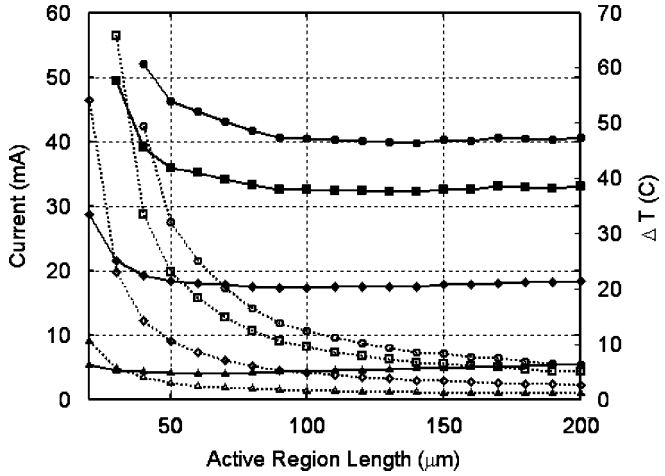

Fig. 3. Design curve of operating current (solid lines) and on-chip temperature rise (dotted lines) vs. active region length for a family of output powers at 1 mW (triangles), 10 mW (diamonds), 20 mW (squares), and 25 mW (circles). The front mirror length was optimized for each active region length at a κ of 650 cm^{-1}.

where P_o is the output power, α_i is the internal loss, α_m is the mirror loss, F_1 is the fractional power out the front mirror, η_i is the injection efficiency, and $I_{\rm th}$ is the threshold current [6]. $I_{\rm th}$ can be solved using the gain equation,

$$I_{\rm th} = wL_a NJ_{\rm tr} \exp \frac{(\alpha_i + \alpha_m)L}{\Gamma g_o L_a} \tag{2}$$

where w is the ridge width, L_a is the active region length, L is the total cavity length, N is the number of quantum wells, $J_{\rm tr}$ is the transparency current density, Γ is the confinement factor, and g_o is the material gain. Values of 15 cm^{-1}, 90%, 70 A/cm^2, 50 cm^{-1}, and 80% were used for $\alpha_i, \eta_i, J_{\rm tr}, \Gamma g_o$, and the rear HR mirror, R_2, respectively. As shown in Fig. 2, I can be plotted as a function of front mirror grating length for a fixed active region length. The on-chip temperature rise, ΔT, can also be simulated as given in (3) and iterated with (4) to find the equilibrium operating current [6].

$$\Delta T = (IV_d + I^2 R_s - P_o) Z_t \tag{3}$$

$$I = I_{\rm th} + I_{\rm po} \exp\left(\frac{T}{T_1}\right). \tag{4}$$

Assuming the light output power increases linearly with injection current above threshold, (4) is a modified form of the traditional temperature dependence equation for differential quantum efficiency, $\eta_d\ (T) = \eta_{do}\ \exp(s - T/T_1)$, obtained by substituting the equation for output power, $P_o = \eta_d\ (\text{h}\ \upsilon/\text{q})\ (\text{I}-\text{I}_{\rm th})$. $I_{\rm th}$ can be represented by the threshold temperature dependence, $I_{\rm th}(T) = I_0\ \exp(T/T_0)$. T_0 is the characteristic temperature, T_1 is the characteristic temperature for the above-threshold current increment, I_0 and $I_{\rm po}$ are constants, and Z_t is the thermal impedance, which we have assumed to be $3.46/L_a \cdot {}^\circ$C/W, using a thermal conductivity of 0.45 W/cm$\cdot\,{}^\circ$C [6]. We have assumed T_0 and T_1 to be 100 K and 200 K, respectively. As can be seen from Fig. 2, there lies an ideal front mirror length that gives the lowest operating current for a given active region length. Solving for the ideal front mirror length of each active region length, we can then solve (1) as a function of active region length, as shown in Fig. 3. This shows that the active region length for a short-cavity DBR laser can be reduced to as low as 50 μm before the operating current and on-chip temperature rise begins to increase sharply.

From these simulations we have designed the gain section of the device at 110 μm. A front DBR of 20 μm length was chosen, making use of deep gratings aimed at 40 nm etch depth, and targeting a coupling coefficient κ of 650 cm^{-1}. This DBR length is chosen to be slightly larger than the optimum minimum shown in Fig. 2 in order to compensate for fabrication and regrowth error [7]. Lastly, the transmitters were fabricated with 125 μm long EAMs. Passive waveguides were also included to facilitate postprocess cleaving and coating.

B. Quantum Well Intermixing Background

There are several main techniques used to accomplish QWI: ion-implantation enhanced interdiffusion (IIEI), impurity-induced disordering (IID), and impurity-free vacancy-enhanced disordering (IFVD). All are based on the generation of vacancies and its diffusion through the QW active region by a rapid thermal anneal (RTA). The IIEI method relies on the diffusion of point defects created during an ion implantation. This method can utilize implant energies ranging from tens of kiloelectronvolts up to megaelectronvolts, and has been shown to have good spatial resolution. The range of intermixing is also very controllable using anneal time, temperature, and implant dose [8], [9]. This process has been used with great success in developing high functionality wavelength-agile PICs on InP [3]. Moreover, impurity-free IIEI processes have also been translated to GaAs with some success [10], [11].

The IID method uses impurities, commonly dopants, to change the equilibrium defect concentration, which is dependent on the Fermi level, to enhance the group III or group V self-diffusion in the crystal, thereby promoting the intermixing [12]. Recently, IID has been applied to 980 nm VCSELs with modest

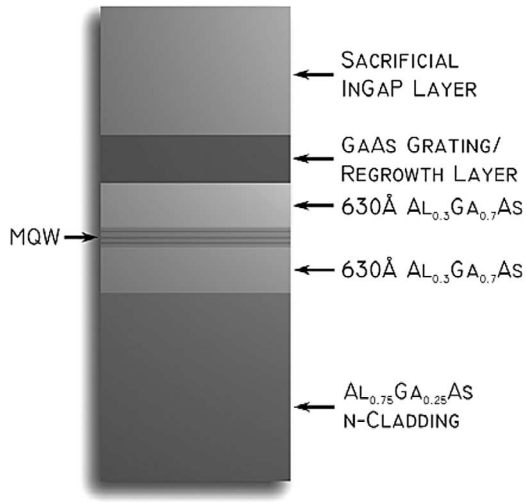

Fig. 4. Epitaxial base structure with three-QW active region.

success; however, the introduction of dopants used to promote intermixing could have adverse effects on the electrical nature of the devices structure [13], [14].

In this paper, we employ an impurity-free vacancy-enhanced disordering method, using a SiO_2 dielectric cap. Previous literature has shown intermixing to occur with a variety of deposition techniques, such as plasma-enhanced chemical vapor deposition (PECVD) or sputter deposition [12], [15]. All approaches use the concept of Ga outdiffusion into the SiO_2 capping layer, which creates vacancies in the group III sublattice which can then diffuse down to the QW region. Similar to the other intermixing techniques, IFVD can be performed on full laser structures, where the vacancies must diffuse long distances through the entire upper p-cladding before reaching the quantum wells. Although this is not detrimental to the intermixing itself, the device performance may be hindered by the redistribution of precisely placed doping interfaces. We have taken an approach which uses a partially grown laser structure and a sacrificial cap layer, which can be subsequently removed and the upper cladding regrown [9]. This approach is also advantageous for integrating gratings within the laser to precisely control the coupling and reflectivity. Recent work has demonstrated high power DBR lasers with intermixed passive sections [4].

We will show that by using a selective IFVD QWI processing platform, a DBR laser with EAM can be monolithically integrated into a single transmitter device.

III. Process

The epitaxial base structure, as shown in Fig. 4, was grown on a silicon doped GaAs substrate by molecular beam epitaxy (MBE). The active region consists of three 8 nm thick $In_{0.18}Ga_{0.82}As$ quantum wells with 8 nm GaAs barriers centered between $Al_{0.3}Ga_{0.7}As$ waveguide layers. The upper waveguide also includes a 65 nm GaAs layer used as a gratings and aluminum-free regrowth layer, followed by a 300 nm undoped sacrificial InGaP layer.

The intermixing process began by first subjecting the sample to a blanket surface fluorination treatment. This was done in a reactive ion etching plasma with SF_6 gas to create In-F and Ga-F bonds on the sample surface without etching the semiconductor [16], [17]. Next, SiO_2 was deposited by PECVD and used as a hard mask. In the passive regions, or areas of the sample to be intermixed, the SiO_2 was etched off using BHF and a developer (basic) solution was used to remove the fluorine bonds. Lastly, another layer of SiO_2 was deposited by PECVD. Intermixing then occurred during the RTA, whereby areas of the sample that were in direct contact with the SiO_2 yielded a blue-shift in the photoluminescence spectra. The areas of the sample that still possessed the fluorine bonds remained at the as-grown band-edge because it prevented group-III outdiffusion into the SiO_2. The reason for covering the entire sample with SiO_2 was to prevent arsenic decomposition from the sample during the high-temperature RTA. Additional details of the intermixing process can be found in [18].

Following QWI of the passive waveguide, DBR, and EAM sections, the sacrificial InGaP layer is removed by wet selective etching, and first order gratings are patterned using an immersion holography technique and dry etched into the GaAs regrowth layer [7]. A 2 μm regrowth of the upper p-cladding and p-contact was performed by MBE [7]. Ridge waveguides 3 μm wide were patterned, benzocyclobutene (BCB) was defined beneath the EAM contacts for low capacitance, and isolation was accomplished by proton implantation. The wafers were thinned, backside metalized, and cleaved into bars. Subsequently, the front and rear facets of cleaved bars were AR and HR-coated, respectively. Finally, the devices were mounted onto AlN carriers and wire-bonded to RF pads for high-speed testing. Including passive waveguides, the entire transmitter totaled around 425 μm in length.

IV. Experimental Results

A. QWI

The intermixing process was calibrated using several samples cleaved from the base structure, as described in the previous section. These samples were annealed at 800 and 850 °C for various times ranging from 10 to 180 s and the extent of the intermixing was measured by room-temperature photoluminescence. As can be seen in Fig. 5, the intermixing occurs rapidly within the first 30 s, then begins to saturate with increasing time. With greater anneal temperatures, intermixing occurs at a faster rate; greater overall amount of intermixing is obtainable due to an increased diffusion coefficient and Ga outdiffusion in the SiO_2. Assuming intermixing occurs only on the group III sublattice for InGaAs/GaAs QWs, we calculate the maximum obtainable amount of intermixing to be 40 nm [19].

The DBR lasers with integrated EAMs fabricated using this selective intermixing process had an active band-edge at $\lambda_{\rm pl} =$ 977 nm and a passive band-edge at $\lambda_{\rm pl} = 949$ nm. The EAMs used the same band-edge as the passive section. While this process can be used to selectively achieve two band-edges on chip, repeating the process to achieve multiple or intermediate band-edges have not been successful as in [11].

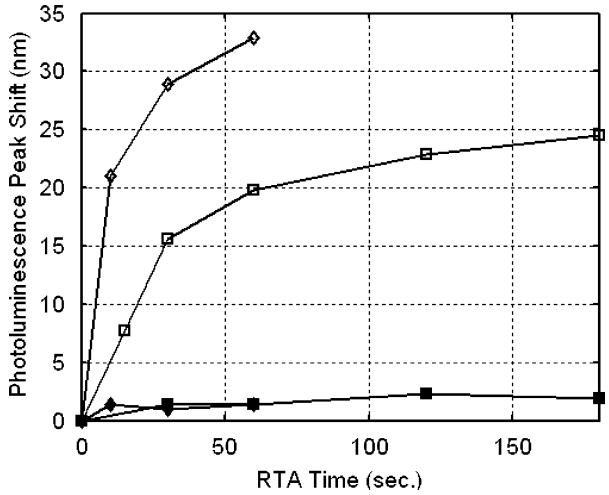

Fig. 5. Photoluminescence peak shift as a function of anneal temperature and time. Open and closed symbols indicate intermixed and nonintermixed at anneal temperatures of 800 °C (squares) and 850 °C (diamonds).

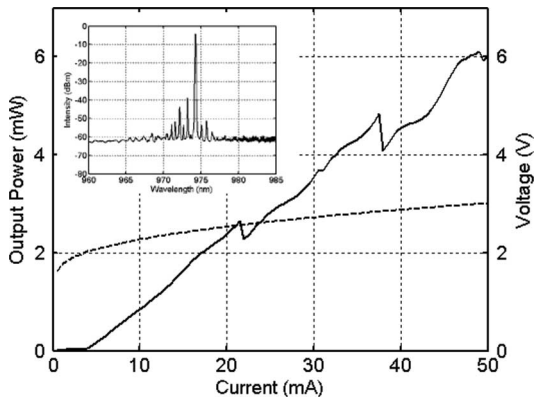

Fig. 6. Room temperature CW light (solid) and voltage (dashed) characteristics of the integrated DBR laser-modulator. The inset shows the single mode lasing spectrum at 35 mA bias.

B. DBR Laser

Operating in continuous wave (CW) mode, the DBR laser exhibited single mode lasing at 975 nm with greater than 30 dB side-mode suppression ratio, as targeted from the design. The mode spacing of ∼6 Å is slightly lower than the estimated mode spacing of ∼7 Å, indicating weaker reflection from the DBR section resulting in a longer cavity length. The additional spurious modes are due to reflections from the front fact.

The lasers also exhibited a threshold current of 5 mA and demonstrated output powers up to 6 mW at a gain section current of 50 mA, as shown in Fig. 6. We believe the low output powers of these devices are due to nonoptimal regrowth conditions, where both interface cleanliness and gratings overgrowth can be improved. Furthermore, we expect to see higher output powers upon improving the low injection efficiency of these devices, currently down at around 50%, which were measured from test ridge laser structures fabricated on the same chip. The higher voltage turn-on was due to high contact resistance resulting from damage to the contact layer during processing.

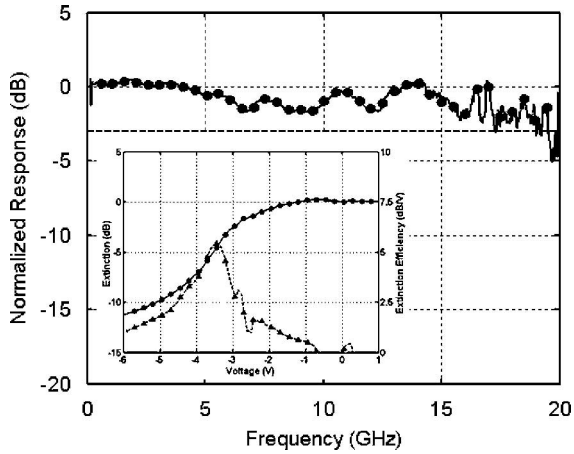

Fig. 7. Bandwidth curve showing 20 GHz of −3 dB bandwidth for a 125 μm long EAM. The inset shows the corresponding DC extinction curve.

The kinks in the output power were due to mode hopping. This was observed in the lasing spectrum, and can be explained from red shifting of the reflection spectrum with on-chip temperature rise. Using (3), the kinks occurring at 22 and 38 mA correspond to a 17 and 33 °C on-chip temperature rise, respectively. Assuming the refractive index changes with temperature by 1.2e-4/°C for AlGaAs, then the change in center wavelength of the grating with change in the index is 6.1 and 11.8 Å, respectively, equal to the mode spacing of the laser. With future improvement on the material quality, as well as reducing the excess voltage drop, less power would be dissipated in the device, leading to lower on-chip temperature rise and fewer kinks in the output power.

C. EA Modulator

As can be seen in the inset in Fig. 7, the 125 μm long integrated EAMs exhibited over 10 dB of optical extinction at −5 V with a peak extinction efficiency of 5 dB/V at −3.5 V. Fig. 7 also shows the small signal 3dB modulation bandwidth measured to be 20 GHz. Large signal digital modulation experiments were performed at 10 Gb/s using a nonreturn to zero pattern and a pseudorandom-bit-sequence of $2^{31}-1$. Open eye diagrams were achieved with 7.7 dB dynamic extinction at a DC bias of −2.5 V and a 3 V peak-to-peak swing. Corresponding bit error rate (BER) curve is plotted in Fig. 8, demonstrating error-free operation down to 10^{-10}. Higher data rates were not able to be tested due to equipment limitations; however, we expect data rates up to 30 Gb/s possible with the demonstrated bandwidths. Extinction ratios and extinction efficiency can also be improved with less intermixing of the EAM band-edge, resulting in bringing the exciton peak and absorption edge closer to the lasing wavelength [20], [21].

V. Conclusion

We have demonstrated short-cavity DBR lasers emitting at 980 nm with integrated QW-EA modulators fabricated using a QWI platform. Short-cavity DBR lasers present a solution for achieving higher power lasers for use in "receiver"-less data link

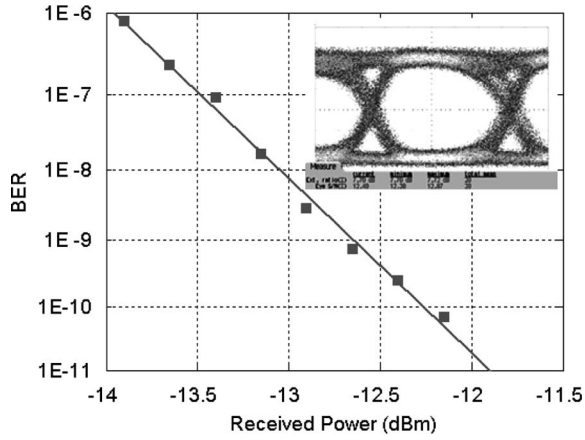

Fig. 8. BER curve showing 10 Gb/s error-free operation down to 1e-10. The inset shows corresponding eye at 10 Gb/s.

interconnect architectures. A QWI processing platform is used for integration and is capable of achieving greater than 30 nm of shift between the active and passive band-edges on a chip. The integrated QWI EAMs demonstrated 20 GHz bandwidth and error-free operation at 10 Gb/s, with further optimization possible for increased high-speed performance. With QWI, the band-edge of each section of the device can be individually optimized, resulting in monolithic integration of lasers with high-performance QW-EAMs.

REFERENCES

[1] J. Kash *et al.*, "Chip-to-chip optical interconnects," presented at the Opt. Fiber Commun. Conf., Tech. Dig., 2006, Paper OFA3.

[2] N. Suzuki, H. Hatakeyama, K. Fukatsu, T. Anan, K. Yashiki, and M. Tsuji, "25-Gbps operation of 1.1-μm-range InGaAs VCSELs for high-speed optical interconnections," presented at the Opt. Fiber Commun. Conf., Tech. Dig., 2006, Paper OFA4.

[3] E. J. Skogen, J. W. Raring, G. B. Morrison, C. S. Wang, V. Lal, M. Mašanović, and L. A. Coldren, "Monolithically integrated active components: A quantum well intermixing approach," *IEEE J. Sel. Topics Quantum Electron.*, vol. 11, no. 2, pp. 343–355, Mar./Apr. 2005.

[4] K. Song, Y. Li, N. Visovsky, M. Hu, H. K. Nguyen, X. Liu, S. Coleman, B. Paddock, M. Turner, C. Catherine, R. Bhat, and C. E. Zah, "High power 1060 nm DBR lasers with quantum well intermixed passive sections," in *Proc. 18th Annu. Meeting IEEE Lasers Electro-Opt. Soc.,* Oct. 23–27, 2005, pp. 949–950.

[5] J. W. Raring, L. A. Johansson, E. J. Skogen, M. N. Sysak, H. N. Poulsen, S. P. DenBaars, and L. A. Coldren, "Low drive voltage, negative chirp 40 Gb/s EA-modulator/widely tunable laser transmitter, using quantum-well intermixing," presented at the Opt. Fiber Commun. Conf. Tech. Dig., 2006, Postdeadline Paper PDP26.

[6] L. A. Coldren and S. W. Corzine, *Diode Lasers and Photonic Integrated Circuits*. New York: Wiley, 1995.

[7] C. S. Wang, G. B. Morrison, E. J. Skogen, and L. A. Coldren, "Fabrication and molecular beam epitaxy regrowth of first-order high contrast AlGaAs/GaAs gratings," *J. Vac. Sci. Technol.: B*, vol. 24, no. 3, pp. 1559–1563, 2006.

[8] S. Charbonneau, P. J. Poole, P. G. Piva, G. C. Aers, E. S. Koteles, M. Fallahi, J. He, J. P. McCaffrey, M. Buchanan, and M. Dion, "Quantum-well intermixing for optoelectronic integration using high energy ion implantation," *J. Appl. Phys.*, vol. 78, no. 6, p. 3697, 1995.

[9] E. J. Skogen, J. S. Barton, S. P. DenBaars, and L. A. Coldren, "A quantum-well-intermixing process for wavelength-agile photonic integrated circuits," *IEEE J. Sel. Topics Quantum Electron.*, vol. 8, no. 4, pp. 863–869, Jul./Aug. 2002.

[10] P. G. Piva, R. D. Goldberg, I. V. Mitchell, S. Fafard, M. Dion, M. Buchanan, S. Charbonneau, G. Hillier, and C. Miner, "Reduced 980 nm laser facet absorption by band gap shifted extended cavities," *J. Vac. Sci. Technol. B*, vol. 16, no. 4, pp. 1790–1793, Jul. 1998.

[11] E. J. Skogen, L. A. Coldren, J. W. Raring, and S. P. DenBaars, "Multiple-band-edge quantum-well intermixing in the InGaAs/InGaAsP/InGaP material system," *Appl. Phys. Lett.*, vol. 86, pp. 241117-1–241117-3, 2005.

[12] D. Deppe and N. Holonyak, Jr., "Atom diffusion and impurity-induced layer disordering in quantum well III–V semiconductor heterostructures," *J. Appl. Phys.*, vol. 64, pp. 93–113, 1988.

[13] R. L. Naone, P. D. Floyd, D. B. Young, E. R. Hegblom, T. A. Strand, and L. A. Coldren, "Interdiffused quantum wells for lateral carrier confinement in VCSEL's," *IEEE J. Sel. Topics Quantum Electron.*, vol. 4, no. 4, pp. 706–714, Jul./Aug. 1998.

[14] D. D. Lofgreen, Y.-C. Chang, and L. A. Coldren, "Vertical-cavity surface-emitting lasers with lateral carrier confinement," *Inst. Electr. Eng. Electron. Lett.*, vol. 43, no. 3, pp. 163–164, Feb. 2007.

[15] S. D. McDougall, O. P. Kowalski, C. J. Hamilton, F. Camacho, B. Qiu, M. Ke, R. M. De La Rue, A. C. Bryce, and J. H. Marsh, "Monolithic integration via a universal damage enhanced quantum-well intermixing technique," *IEEE J. Sel. Topics Quantum Electron.*, vol. 4, no. 4, pp. 636–646, Jul./Aug. 1998.

[16] D. D. Lofgreen, "Investigation of selective quantum well intermixing in vertical cavity lasers," Ph.D. dissertation, Univ. California, Santa Barbara, 2004.

[17] L. R. Williston, I. Bello, and W. M. Lau, "X-ray photoelectron spectroscopic study of the interactions of CF^+ ions with gallium arsenide," *J. Vac. Sci. Technol. A*, vol. 11, no. 4, pp. 1242–1247, 1993.

[18] C. S. Wang, Y.-C. Chang, J. W. Raring, and L. A. Coldren, "Short-cavity 980 nm DBR lasers with quantum well intermixed integrated high-speed EA modulators," in *Proc. Int. Semicond. Laser Conf.*, 2006, pp. 129–130.

[19] J. W. Raring, "Advanced InP based monolithic integration using quantum well intermixing and MOCVD regrowth," Ph.D. dissertation, Univ. California, Santa Barbara, 2006.

[20] G. B. Morrison, C. S. Wang, E. J. Skogen, D. D. Lofgreen, and L. A. Coldren, "980 nm DBR lasers monolithically integrated with EA modulators for optical interconnect applications," presented at the Integr. Photon. Res. Appl., 2005, Paper IWF2.

[21] G. B. Morrison, E. J. Skogen, C. S. Wang, J. W. Raring, Y.-C. Chang, M. Sysak, and L. A. Coldren, "Photocurrent spectroscopy for quantum-well intermixed photonic integrated circuit design," *IEEE Photon. Technol. Lett.*, vol. 17, no. 7, pp. 1414–1416, Jul. 2005.

Chad S. Wang (S'99–M'07) received the B.S. degree from the University of Texas at Austin, in 2001 and the M.S. degree from the University of California, Santa Barbara, in 2002, where he is currently working toward the Ph.D. degree in electrical and computer engineering.

His current research interests focus on the development of integrated laser modulators for optical interconnect applications. He is also involved in molecular beam epitaxial growth of III–V semiconductors, including vertical-cavity lasers and avalanche photodetectors.

Yu-Chia Chang received the B.S. in electrical engineering and M.S. degree in electro-optical engineering from National Taiwan University in 1997 and 1999, respectively. He worked for BenQ Inc., Taiwan during 1999–2001 and National Taiwan University during 2001–2002. He is currently working toward the Ph.D. degree in electrical and computer engineering at the University of California, Santa Barbara.

His current research interests are the design, growth, and characterization of high-efficiency, high-speed vertical-cavity surface-emitting lasers for optical interconnect applications.

Uppili Krishnamachari, photograph and biography not available at the time of publication.

James W. Raring (M'00) received his B.S. degree in materials engineering from California Polytechnic State University, San Luis Obispo, in 2001 and the Ph.D. in materials science from the University of California, Santa Barbara, in 2006. His dissertation focused on the design, growth, and fabrication of high-functionality wavelength-agile InGaAsP based photonic integrated circuits (PIC).

By coupling quantum well intermixing with MOCVD regrowth, he combined widely tunable sampled grating DBR lasers, 40 Gb/s electroabsorption modulators, low-confinement high-saturation power semiconductor optical amplifiers, and 40 Gb/s unitraveling carrier photodiodes to demonstrate the first single-chip 40 Gb/s optical transceiver. In 2006, James joined the RF/optoelectronic group at Santa National Laboratories where he continues to work on leading edge PICs. He has authored or co-authored over 75 technical papers and is a member of IEEE LEOS, OSA and SPIE.

Larry A. Coldren (M'00) received the Ph.D. degree in electrical engineering from Stanford University in 1972.

After 13 years of research at Bell Laboratories, he joined UCSB in 1984 where he now holds appointments in Materials and Electrical & Computer Engineering, and is Director of the Optoelectronics Technology Center. He is the Fred Kavli Professor of Optoelectronics and Sensors at UCSB. In 1990 he cofounded Optical Concepts, later acquired as Gore Photonics, to develop novel VCSEL technology; and in 1998 he cofounded Agility Communications, recently acquired by JDSU, to develop widely tunable integrated transmitters. At Bell Labs, he initially worked on waveguided surface-acoustic-wave signal processing devices and couple-resonator filters. He later developed tunable coupled-cavity lasers using novel reactive-ion etching (RIE) technology that he created for the then new InP-based materials. At UCSB he continued work on multiple-section tunable lasers, in 1988, inventing the widely tunable multielement mirror concept. During the late eighties he also developed efficient vertical-cavity multiple-quantum-well modulators which led to novel vertical-cavity surface-emitting laser (VCSEL) designs that provided unparalleled levels of performance. He continues to be active in developing new photonic integrated circuit (PIC) and VCSEL technology, including the underlying materials growth and fabrication techniques. In recent years, for example, he has been involved in the creation of efficient all-epitaxial InP-based and high-modulation speed GaAs-based VCSELs as well as a variety of InP-based PICs incorporating numerous optical elements for widely tunable integrated transmitters, receivers, and wavelength converters operating up to 40 Gb/s. He has authored or coauthored over 800 papers, five book chapters, one textbook, and has been issued 61 patents. He has presented dozens of invited and plenary talks at major conferences.

Prof. Coldren is a member of Optical Society of America and the recipient of the Institution of Electrical Engineers, 2004 John Tyndall Award, and a member of the National Academy of Engineering.

Towards 40 Gb/s Operation of Integrated DBR Laser-EA Modulators at 980 nm

Chad S. Wang, Yu-Chia Chang, and Larry A. Coldren
ECE Dept. University of California, Santa Barbara, CA 93106

Phone: 805.893.7065, Fax: 805.893.4500, E-mail: cswang@engineering.ucsb.edu

Abstract: Short-cavity, 980nm DBR lasers with integrated EAMs were designed and fabricated using a quantum well intermixing processing platform. Open eyes at 40Gb/s and preliminary error free operation at 25Gb/s were achieved, suitable for optical interconnect applications.

1. INTRODUCTION

As photonics continue to push towards faster bit-rates, they become more attractive in replacing electronics for use in interconnect applications [1]. Currently, the fastest vertical cavity lasers have shown 30 Gb/s operation and 3 dB bandwidths of 24 GHz at 1.1 µm [2]. Direct modulation of vertical cavity laser suffers from relaxation oscillation effects, resulting in distorted eyes that require preemphasis to reshape [3]. Using an integrated modulator outside of the laser cavity, such as an electroabsorption modulator (EAM), produces cleaner eyes without difficult driver circuitry. This approach has demonstrated efficient transmitters at 1.55 µm operating at 40 Gb/s [4]. Here we present high-speed performance of a distributed Bragg reflector (DBR) laser integrated with an EAM operating at 980 nm. Open eyes at 40 Gb/s and preliminary error free operation at 25 Gb/s were achieved.

2. DEVICE

We have previously demonstrated short-cavity DBR lasers integrated with EAMs [5,6]. The integrated DBR laser-EAM consists of 5 sections: rear absorber, rear DBR mirror, gain section, front DBR mirror, and EAM, followed by a curved output waveguide for low back reflection, as shown in the side-view schematic of Fig. 1a. The gain section of the device is 110 µm long designed for low thresholds and high slope efficiency, and the integrated EAM is 125 µm long. An impurity-free quantum well intermixing process was used to monolithically integrate high-speed QW-EAMs with the DBR laser. The passive and EAM band-edge was detuned from the active and lasing band-edge by ~25 nm. Details of the device structure and process can be found in [5,6].

3. RESULTS

The DBR laser had a threshold current of 11 mA and demonstrated output powers up to 2.5 mW at a gain section current of 50 mA. The 125 µm long integrated EAM exhibited slightly greater than 15 dB of optical extinction at -6 V with greater than 7 dB/V peak extinction efficiency at -2.8V. Small-signal modulation of the integrated EAM exceeded 20 GHz of 3 dB bandwidth, as shown in Fig. 1b. Fig. 2b shows the setup used for various large-signal modulation experiments. The NRZ signal from the pattern generator was amplified using a 38 GHz SHF 806E amplifier and fed into an Anritsu V255 65 GHz bias tee. This was used to drive the integrated EAM which was terminated with a 50 Ω load mounted directly on ground-signal probes. Approximately -1 dBm of power was coupled into a single mode lensed fiber at a 50 mA laser bias. The optical signal was first measured using an

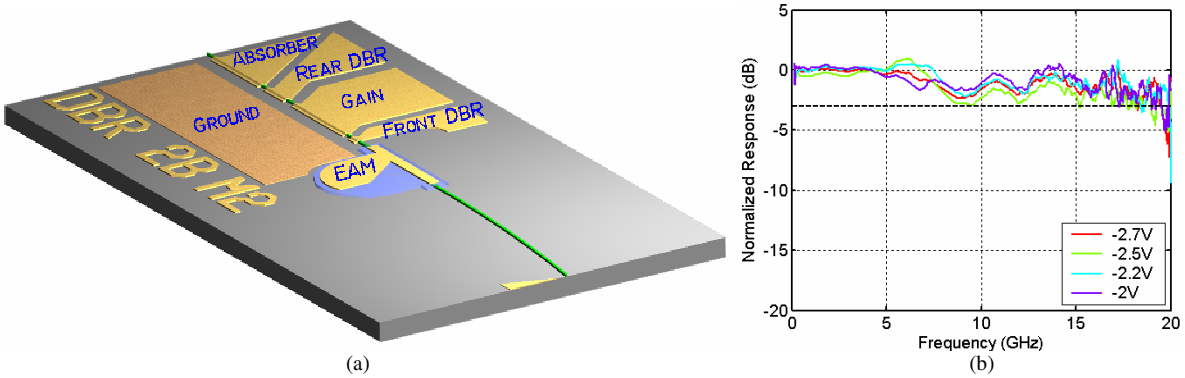

(a) (b)

FIGURE 1. (a) Side view schematic of the integrated short-cavity DBR laser-modulator, illustrating the Absorber, Rear DBR, Gain, Front DBR, and EAM sections. (b) 3 dB modulation bandwidth of 125 µm EAM at various biases. The noise at high frequency was due to equipment limitations; the bandwidth was measured using a calibrated 6 GHz New Focus photodiode and two 20 GHz New Focus amplifiers.

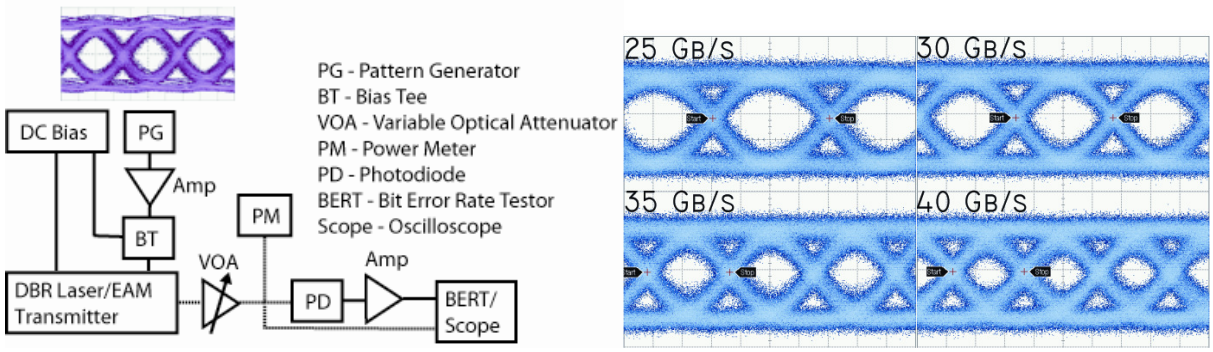

(a) (b)

FIGURE 2. (a) Test-set used to obtain BER and eye-diagrams. Dashed lines denote optical connections made with optical fibers. Also shown is the 40 Gb/s input eye from the bias tee to the EAM. (b) Optical eye diagrams at 25, 30, 35, and 40 Gb/s were measured using the oscilloscope optical port.

Agilent 86109A oscilloscope which contains a 30 GHz internal photodiode. Fig. 2b shows open optical eye diagrams measured using this oscilloscope optical port, taken at 25, 30, 35, and 40 Gb/s. They demonstrate RF extinction ratios ranging from 5 down to 3.8 dB using a DC drive voltage of -2.8 V with peak-to-peak drive swings ranging from 1.8 V_{pp} at 20 Gb/s down to 1.6 V_{pp} at 40 Gb/s. Electrical eye diagrams were measured using a 25 GHz New Focus 1434 IR external photodetector followed by a 25 GHz SHF 100CP amplifier, producing ~50 mV amplitude eyes. Corresponding electrical eyes measured using the New Focus detector and SHF amplifier are shown in Fig. 3a, taken at 20 and 25 Gb/s. Higher data rates at 30 Gb/s and beyond could not be taken due to the limited performance of the receiver photodetector and amplifier. Using an SHF 50 Gb/s BERT, Fig. 3b shows error-free bit error rate measurements (BER) at 2^7-1 word lengths achieved at 20 and 25 Gb/s using the current receiver electronics.

4. CONCLUSION

Short-cavity DBR lasers emitting at 980 were integrated with high-speed QW-EA modulators using a QWI platform. Open eyes diagrams were achieved at 40 Gb/s, and error-free BER were performed at 25 Gb/s. To the best of our knowledge, these results represent the fastest integrated EAMs at the datacom wavelengths. Higher-speed BER measurements plan to be performed with faster receiver electronics.

5. REFERENCES

[1] H. Cho, P. Kapur, and K.C. Saraswat, "Power comparison between high-speed electrical and optical interconnects for interchip communication," *IEEE J. of Lightwave Tech.*, vol. 22, no. 9, pp. 2021-2033, 2004.

[2] K. Yashiki, N. Suzuki, K. Fukatsu, T. Anan, H. Hatakeyama, and M. Tsuji, "1.1-µm-Range Tunnel Junction VCSELs with 27-GHz Relaxation Oscillation Frequency," *Proc. Optical Fiber Communications Conf.*, paper no. OMK1, 2007.

[3] L. Schares, et al., "Terabus: Terabit/Second-Class Card-Level Optical Interconnect Technologies," *IEEE J. of Sel. Topics in Quant. Electron.*, vol. 12, no. 5, pp. 1032-1034, 2006.

[4] J.W. Raring, L.A. Johansson, E.J. Skogen, M.N. Sysak, H.N. Poulsen, S.P. DenBaars, and L.A. Coldren, "40-Gb/s Widely Tunable Low-Drive-Voltage Electroabsorption-Modulated Transmitters," *IEEE J. of Lightwave Tech.*, vol. 21, no. 1, pp. 239-248, 2007.

[5] G.B. Morrison, C.S. Wang, E.J. Skogen, D.D. Lofgreen, and L.A. Coldren., "980 nm DBR Lasers Monolithically Integrated with EA Modulators for Optical Interconnect Applications," *Proceedings of the Integrated Photonics Research and Applications*, paper no. IWF2, 2005.

[6] C.S. Wang, Y.-C. Chang, J.W. Raring, and L.A. Coldren., "Short-Cavity 980 nm DBR Lasers with Quantum Well Intermixed Integrated High-Speed EA Modulators," *Proc. International Semiconductor Laser Conf.*, paper. no. WC8, 2006.

(a) (b)

FIGURE 3. (a) Electrical eye diagrams at 20 and 25 Gb/s measured by electrical receiver and amplifier, and (b) corresponding bit error rate at for 20 (squares) and 25 (triangles) Gb/s operation.

35 Gbit/s error-free operation of 980 nm DBR laser with integrated electroabsorption modulator

C.S. Wang, Y.-C. Chang and L.A. Coldren

High-speed, single-frequency transmitters at 980 nm are reported, with open eye diagrams up to 40 Gbit/s and error-free operation up to 35 Gbit/s. The transmitters consist of a short-cavity, distributed Bragg reflector (DBR) laser with an integrated electro absorption modulator fabricated using a quantum well intermixing processing platform. This represents the fastest bit-rate operation to date from a single transmitter in the 830–1100 nm datacom wavelength range.

Introduction: Parallel optical interconnects are becoming increasingly cost-beneficial over copper-based electronics for board and chip-level interconnect applications as their bandwidth–path-length product continues to increase [1]. Current efforts are aimed towards extending the bit-rate operation of vertical cavity lasers, and presently the fastest vertical cavity lasers have shown 30 Gbit/s operation and 3 dB bandwidths of 24 GHz at 1.1 μm [2]. However, direct modulation of vertical cavity lasers suffers from relaxation oscillation effects, resulting in distorted eyes that require pre-emphasis to reshape [3]. Using an integrated modulator outside of the laser cavity, such as an electroabsorption modulator (EAM), produces cleaner eyes without difficult driver circuitry. This approach has demonstrated efficient transmitters at 1.55 μm operating at 40 Gbit/s [4]. In this Letter, we report high-speed performance of a small-footprint distributed Bragg reflector (DBR) laser integrated with an EAM operating at 980 nm. Open eye diagrams at 40 Gbit/s and error-free operation at 35 Gbit/s were achieved. To the best of the our knowledge, this represents the fastest demonstrated bit-rate operation of a single transmitter at the 830–1100 nm datacom wavelengths.

Device structure: We have previously demonstrated short-cavity DBR lasers integrated with EAMs that can be formed in dense arrays [5, 6]. The integrated DBR-laser/EAM-transmitter consists of five sections: rear absorber, rear DBR mirror, gain section, front DBR mirror and EAM, followed by a curved output waveguide for low back reflection, as shown in the schematic diagram in Fig. 1. The gain section of the device is 110 μm long designed for low thresholds and high slope efficiency, and the integrated EAM is 125 μm long. The entire transmitter totalled 465 μm in length without the curved output waveguide. The active region contains three 8 nm-wide $In_{0.18}Ga_{0.82}As$ quantum wells (QWs) with 8 nm GaAs barriers. An impurity-free quantum well intermixing process was used to blue-shift the absorption edge to monolithically integrate high-speed QW-EAMs with the DBR laser. The passive and EAM band-edge was detuned from the active and lasing band-edge by ~25 nm. Details of the device structure and process can be found in [5, 6].

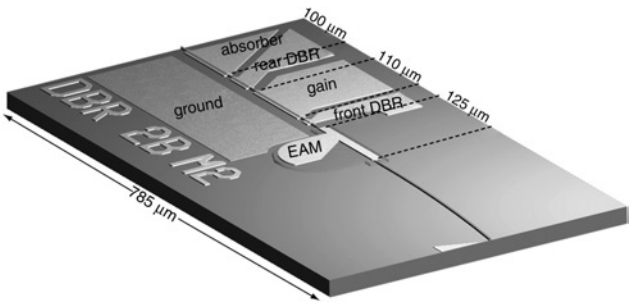

Fig. 1 *Schematic diagram of integrated short-cavity DBR laser-modulator, illustrating absorber, rear DBR, gain, front DBR and EAM sections*

Results: The DBR laser had a threshold current of 11 mA and demonstrated output powers up to 2.5 mW. The 125 μm-long integrated EAM exhibited slightly greater than 15 dB of optical extinction at −6 V with greater than 7 dB/V peak extinction efficiency at −2.8 V. More efficient EAMs have been demonstrated with less band-edge shift [5]. Small-signal modulation of the integrated EAM exceeded 20 GHz of 3 dB bandwidth [6].

Fig. 2 shows the test setup used for the large-signal modulation experiments. The NRZ signal from the pattern generator was amplified using a 38 GHz SHF 806E amplifier and fed into an Anritsu V255 65 GHz bias tee. This was used to drive the integrated EAM which was terminated with a 50 Ω load mounted directly on the ground-signal probe. Approximately −1 dBm of power was coupled into a 1 m-long single-mode lensed fibre. The optical signal was first measured using an Agilent 86109A oscilloscope, which contains a 30 GHz internal photodiode. Fig. 3*a* shows open optical eye diagrams measured using the oscilloscope optical port, taken at 25, 30, 35 and 40 Gbit/s. They demonstrate RF extinction ratios ranging from 5 down to 3.8 dB using a DC drive voltage of −2.8 V with peak-to-peak drive swings ranging from 1.75 V_{pp} at 25 Gbit/s down to 1.6 V_{pp} at 40 Gbit/s. Electrical eye diagrams were measured using a 25 GHz New Focus 1414 IR external photodetector followed by a 40 GHz SHF 810 amplifier, producing ~150 mV amplitude eyes. Corresponding electrical eyes measured using the New Focus photodetector and SHF amplifier are shown in Fig. 3*b*, taken at 25, 30, 35 and 40 Gbit/s. The noise in the electrical eyes is due to the receiver electronics, and the 40 Gbit/s eye diagram begins to suffer slight degradation owing to bandwidth limitations of the New Focus photodetector. Using an SHF 12100A/11100A 50 Gbit/s bit error rate (BER) tester and an Ando AQ-3105 calibrated variable optical attenuator, error-free BER measurements at $2^7 - 1$ word lengths were achieved at 30 and 35 Gbit/s, as shown in Fig. 4. 40 Gbit/s operation possessed an error floor of 5×10^{-8} BER at −1 dBm fibre coupled power.

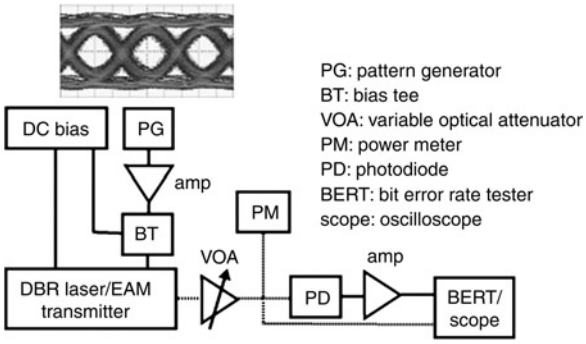

Fig. 2 *Test setup used to obtain BER and eye diagrams*

Dashed lines denote optical connections made with optical fibres. Also shown is 40 Gbit/s input eye diagram from bias tee to EAM

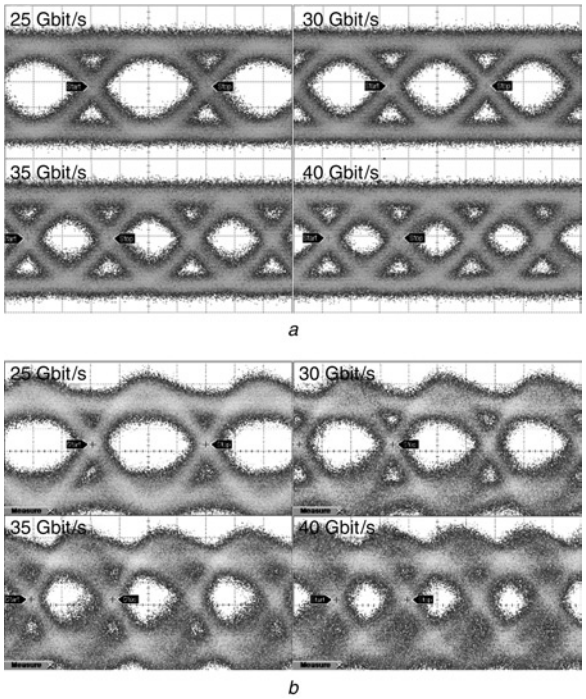

Fig. 3 *Optical eye diagrams at 25, 30, 35 and 40 Gbit/s measured using oscilloscope optical port: extinction ratios range from 5 dB at 25 Gbit/s down to 3.8 dB at 40 Gbit/s; and corresponding electrical eye diagrams at 25, 30, 35 and 40 Gbit/s measured using external photodetector and amplifier*

a Optical eye diagrams
b Corresponding electrical eye diagrams

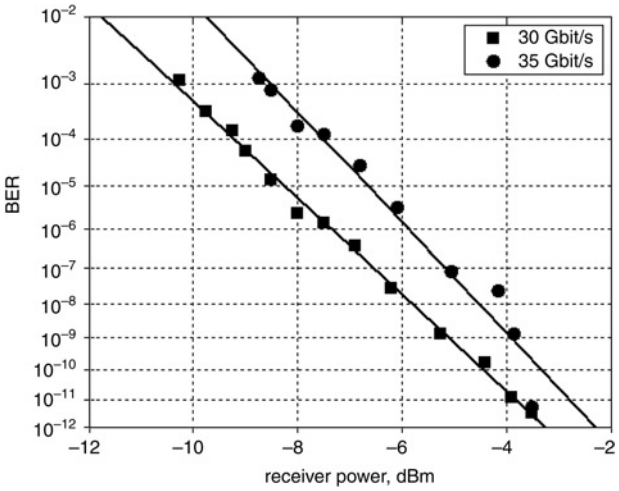

Fig. 4 *Bit error rate measurements at 30 (squares) and 35 (circles) Gbit/s*

Conclusion: Short-cavity DBR lasers emitting at 980 were integrated with high-speed QW-EA modulators using a quantum well intermixing platform. Open eye diagrams at 40 Gbit/s and error-free BER at 35 Gbit/s were achieved. To the best of our knowledge, these results represent the fastest bit-rate operation from a single transmitter at the datacom wavelength range.

Acknowledgments: The authors thank D.J. Blumenthal and H.N. Poulsen at the University of California, Santa Barbara, for helping with the RF test setup. This work is sponsored by DARPA through C2OI.

14 July 2007
Electronics Letters online no: 20072073
doi: 10.1049/el:20072073

C.S. Wang, Y.-C. Chang and L.A. Coldren (*Department of Electrical and Computer Engineering, University of California, Santa Barbara, CA 93106-9560, USA*)

E-mail: cswang@engineering.ucsb.edu

References

1 Cho, H., Kapur, P., and Saraswat, K.C.: 'Power comparison between high-speed electrical and optical interconnects for interchip communication', *IEEE J. Lightwave Technol.*, 2004, **22**, (9), pp. 2021–2033
2 Yashiki, K., Suzuki, N., Fukatsu, K., Anan, T., Hatakeyama, H., and Tsuji, M.: '1.1-μm-range tunnel junction VCSELs with 27-GHz relaxation oscillation frequency'. Proc. Optical Fiber Communications Conf., 2007, paper no. OMK1
3 Schares, L., *et al.*: 'Terabus: terabit/second-class card-level optical interconnect technologies', *IEEE J. Sel. Top. Quantum Electron.*, 2006, **12**, (5), pp. 1032–1034
4 Raring, J.W., Johansson, L.A., Skogen, E.J., Sysak, M.N., Poulsen, H.N., DenBaars, S.P., and Coldren, L.A.: '40-Gbit/s widely tunable low-drive-voltage electroabsorption-modulated transmitters', *IEEE J. Lightwave Technol.*, 2007, **21**, (1), pp. 239–248
5 Morrison, G.B., Wang, C.S., Skogen, E.J., Lofgreen, D.D., and Coldren, L.A.: '980 nm DBR lasers monolithically integrated with EA modulators for optical interconnect applications'. Proc. Integrated Photonics Research and Applications, 2005, paper no. IWF2
6 Wang, C.S., Chang, Y.-C., Raring, J.W., and Coldren, L.A.: 'Short-cavity 980 nm DBR lasers with quantum well intermixed integrated high-speed EA modulators'. Proc. Int. Semiconductor Laser Conf., 2006, paper. no. WC8

I. Photonic IC Technology and Devices

B. Analog PICs and RF-Photonics

High Output Saturation and High-Linearity Uni-Traveling-Carrier Waveguide Photodiodes

Jonathan Klamkin, *Student Member, IEEE*, Anand Ramaswamy, *Student Member, IEEE*, Leif A. Johansson, *Member, IEEE*, Hsu-Feng Chou, *Member, IEEE*, Matthew N. Sysak, *Member, IEEE*, James W. Raring, *Student Member, IEEE*, Navin Parthasarathy, Steven P. DenBaars, *Fellow, IEEE*, John E. Bowers, *Fellow, IEEE*, and Larry A. Coldren, *Fellow, IEEE*

***Abstract*—Waveguide uni-traveling-carrier photodiodes (UTC-PDs) have been fabricated and tested. Output saturation currents greater than 40 mA at 1 GHz are demonstrated for a 10 μm $\times$ 150 μm photodiode (PD). The third-order intermodulation distortion is also measured and exhibits a third-order output intercept point of 43 dBm at 20 mA and 34 dBm at 40 mA for this same PD. UTC-PDs with geometries of 5 μm $\times$ 100 μm and 10 μm $\times$ 100 μm are also compared and it is shown that a wider waveguide PD has improved saturation characteristics due to the lower optical power density which reduces the saturation at the front end of the device.**

***Index Terms*—Fiber-optic link, linearity, photodiode (PD), saturation current, third-order intermodulation distortion (IMD3), third-order output intercept point (OIP3), uni-traveling-carrier photodiode (UTC-PD).**

I. Introduction

HIGH-POWER photodetectors are required for high-performance analog fiber-optic links. To increase the spur-free dynamic range (SFDR), high transmitted optical power can be used in conjunction with high saturation power and high-linearity photodetectors [1]. Coherent fiber-optic links have the potential to further improve SFDR, however, the limiting factor to achieving high linearity is the optical receiver. In [2], a coherent receiver with feedback to a local tracking phase modulator has been proposed to significantly enhance the linearity of the phase demodulator and in turn the SFDR of the link. For successful operation at high frequency, the delay of this feedback must be kept short. With a monolithically integrated receiver, operation at 1 GHz is feasible. For such a coherent receiver, a balanced photodiode (PD) configuration can be utilized for shot noise limited operation, and this balanced PD should be integrated with a coupler for mixing the received radio-frequency (RF) signal with a local oscillator wave, and a local tracking phase modulator. Therefore, it is desirable to fabricate high-power and high-linearity photodetectors that can operate at 1 GHz and can be monolithically integrated with other optical components such as couplers and phase modulators. It is imperative that a waveguide PD is employed. Waveguide p-i-n photodetectors have been reported with an OIP3 of 27 dBm at 20 mA of photocurrent and a frequency of 20 GHz [3]. Uni-traveling-carrier photodiodes (UTC-PDs) have the potential for improved saturation current and linearity because of reduced space charge effects [4]. UTC-PDs have demonstrated an OIP3 of 37.5 dBm at 22 mA and around 5.8 GHz [5] and 30 dBm at 21.3 mA and 40 GHz [6]. Because the *RC* requirements are relaxed for operation at 1 GHz, the PD can be designed for higher saturation current and higher linearity.

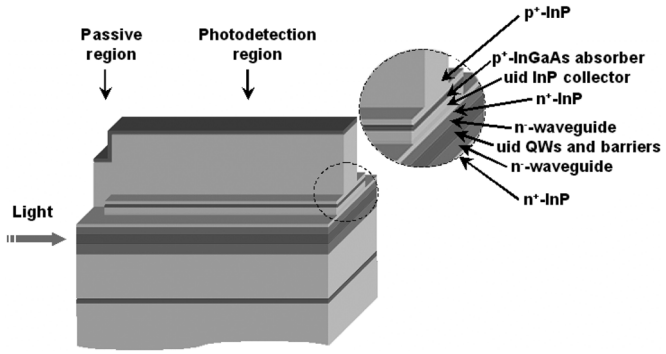

Fig. 1. Device schematic of UTC-PD.

An advanced device architecture has recently been developed allowing for the monolithic integration of UTC-PDs with low loss passive waveguides and quantum-well (QW)-based components [7]. In this letter, we report waveguide UTC-PDs that demonstrate both high saturation current and high linearity at a frequency of 1 GHz. To the best of our knowledge, the OIP3 values obtained for these PDs are the highest reported for a waveguide PD at comparable frequencies. These UTC-PDs are fabricated on a platform that readily allows for the integration of other optical components such as optical phase modulators and multimode interference couplers. The saturation current was characterized by measuring the optical-to-electrical frequency response of the PDs at varying photocurrent levels, and the third-order intermodulation distortion (IMD3) was measured using a two-tone setup [8].

II. Device Design

A schematic of the UTC-PD structure is shown in Fig. 1. The structure is grown on a semi-insulating InP substrate by MOCVD. The optical waveguide consists of unintentionally doped (uid) InGaAsP QWs and barriers sandwiched between

Manuscript received September 1, 2006; revised November 13, 2006. This work was supported by Defense Advanced Research Projects Agency (DARPA) through the PHORFRONT Program under U.S. Air Force Contract FA8750-05-C-0265.

The authors are with the Materials Department and the Electrical and Computer Engineering Department at the University of California, Santa Barbara, CA 93116 USA (e-mail: klamkin@engineering.ucsb.edu).

Digital Object Identifier 10.1109/LPT.2006.890101

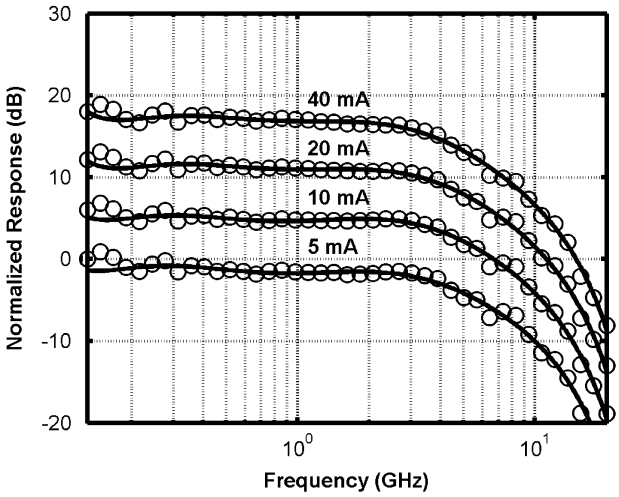

Fig. 2. Normalized response of a 10 μm × 150 μm UTC-PD at various photocurrent levels. The bias voltage is −5 V.

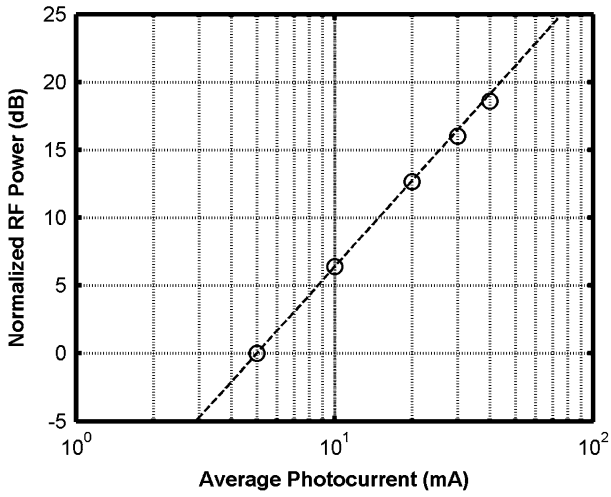

Fig. 3. Normalized RF power as a function of average photocurrent at 1 GHz for a 10 μm × 150 μm UTC-PD. The bias voltage is −5 V.

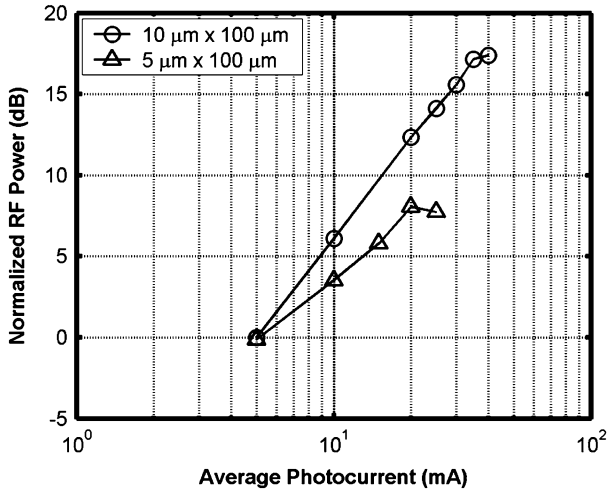

Fig. 4. Normalized RF power as a function of average photocurrent at 1 GHz for a 10 μm × 100 μm and a 5 μm × 100 μm UTC-PD. The bias voltage is −6 V for both devices.

two lightly n-doped InGaAsP waveguide layers. The UTC-PD structure grown above the optical waveguide consists of a highly n-doped InP layer, a uid InP collector, some band smoothing layers, and a highly p-doped InGaAs absorber. Photodetection regions are formed by selectively removing these UTC-PD layers. The highly n-doped InP layer serves to terminate the field on the n-side of the InP collector in the photodetection regions and prevents the applied field from depleting the optical waveguide below. After forming these regions, a p-cladding regrowth is performed. Fabricated PDs consist of a short passive region, where the UTC layers have been removed, followed by a photodetection region. Light is coupled from an optical fiber to the waveguide in the short passive region. Because the device area can be made larger, the overlap of the optical mode in the absorber is lower than that in [7] resulting in a longer absorption profile and in turn a more uniform distribution of carriers. The PDs are made longer to compensate for any potential loss in quantum efficiency. Although the regions with UTC layers removed serve as passive regions in these experiments, they can also be used as modulation regions. With this single regrowth process, several components can be monolithically integrated to form more highly functional photonic circuits such as the coherent receiver described in the introduction.

Following regrowth, ridges are formed. Topside n- and p-contacts are then deposited and annealed. Benzocyclobutene dielectric is used for reducing parasitic pad capacitance. UTC-PDs were fabricated with width by length geometries of 5 μm × 100 μm, 10 μm × 100 μm, and 10 μm × 150 μm.

III. Experiment and Results

Optical-to-electrical frequency response measurements were performed with a lightwave component analyzer. The optical output of the lightwave component analyzer was amplified with an erbium-doped fiber amplifier (EDFA) and then coupled to the PDs using single-mode lensed fiber. The frequency response was measured at various bias voltages and photocurrent levels. The normalized response for a 10 μm × 150 μm PD is shown in Fig. 2 for up to 40 mA of photocurrent. The bias voltage for these measurements was set to −5 V. The response does not appear to degrade for the measured levels of photocurrent. Fig. 3 shows the normalized RF power as a function of average photocurrent along with a line fit through the first few points. For this device, the saturation current is greater than 40 mA. Fig. 4 shows a plot of the normalized RF power as a function of average generated photocurrent at 1 GHz for both a 10 μm × 100 μm and a 5 μm × 100 μm UTC-PD. In both cases, the bias voltage was set to −6 V. These devices are compared because they have equal length and subsequently the same quantum efficiency of around 94%. From this measurement, it is clear that the output saturation current level is significantly higher for the wider device.

To measure the IMD3 of the UTC-PDs, a two-tone setup was used similar to that in [8]. Two distributed feedback lasers were externally modulated; one at a frequency of 0.8 GHz and the other at 1.0 GHz. The signals were combined, and an EDFA was used to vary the optical power input to the PD. The IMD3 measurements for the 10 μm × 150 μm PD are shown in Fig. 5. The input electrical modulation power was varied and the data points

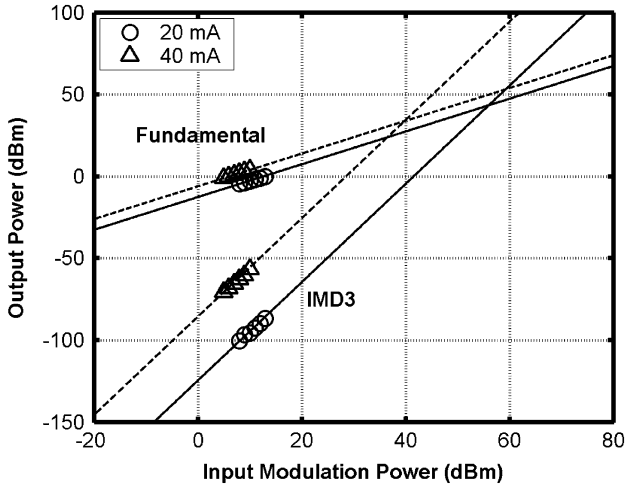

Fig. 5. IMD3 measurements for a 10 μm $\times$ 150 μm UTC-PD. At 20 mA, the bias voltage is -8 V and at 40 mA the bias voltage is -5.8 V.

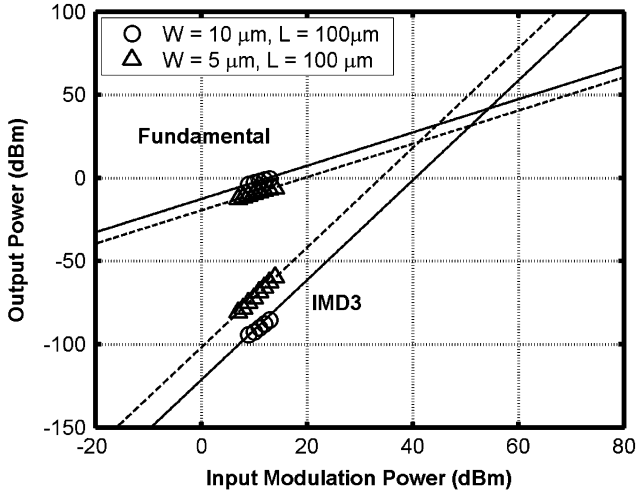

Fig. 6. IMD3 measurements for a 10 μm $\times$ 100 μm and a 5 μm $\times$ 100 μm UTC-PD. The bias voltage is -6 V and the photocurrent level is 20 mA.

shown correspond to a range of around 40%–75% modulation index. These measurements are for a bias of -8 V and a photocurrent level of 20 mA, and a bias of -5.8 V and a photocurrent level of 40 mA. The OIP3 for these settings was measured to be 43 and 34 dBm, respectively. To the best of our knowledge, these are the highest OIP3 values reported for a waveguide PD. Fig. 6 shows the IMD3 measurements for the 10 μm $\times$ 100 μm and the 5 μm $\times$ 100 μm PDs. For these measurements, the bias voltage was -6 V and the photocurrent level was 20 mA. The OIP3 for the 10 μm $\times$ 100 μm PD is 42 dBm and that for the 5 μm $\times$ 100 μm PD is 22 dBm. The OIP3 for the wider PD is much higher than that for the narrower PD, which is consistent with the saturation currents observed for these devices. This enhancement is due in part to the reduced power density in the wider PDs, which spreads the generation at the front end of the device. According to simulation, nearly 50% of the light is absorbed in the first 25 μm of length, therefore it is advantageous to reduce the power density at the front end in order to reduce space charge saturation in this region of the device.

IV. Conclusion

We have fabricated and tested waveguide UTC-PDs that demonstrate high-saturation currents and high linearity. A 10 μm $\times$ 150 μm UTC-PD has a saturation current greater than 40 mA and OIP3 values of 43 and 34 dBm at photocurrent levels of 20 and 40 mA, respectively. Comparing devices of different widths, a 10 μm $\times$ 100 μm UTC-PD has a saturation current near 40 mA and an OIP3 of 42 dBm at 20 mA and -6 V, whereas a 5 μm $\times$ 100 μm UTC-PD has a much lower saturation current and an OIP3 of 22 dBm at the same operating conditions. This difference is believed to be due in part to the reduced power density at the front end of the device for the wider PD.

References

[1] K. J. Williams, L. T. Nichols, and R. D. Esman, "Photodetector nonlinearity limitations on a high-dynamic range 3 GHz fiber optic link," *J. Lightw. Technol.*, vol. 16, no. 2, pp. 192–199, Feb. 1998.

[2] H.-F. Chou, A. Ramaswamy, D. Zibar, L. A. Johansson, J. E. Bowers, M. Rodwell, and L. Coldren, "SFDR improvement of a coherent receiver using feedback," in *Coherent Optical Technologies and Applications Conf. (COTA)*, Whistler, Canada, 2006.

[3] D. C. Scott, T. A. Vang, J. Elliott, D. Forbes, J. Lacey, K. Everett, F. Alvarex, R. Johnson, A. Krispin, J. Brock, L. Lembo, H. Jiang, D. S. Shin, J. T. Zhu, and P. K. L. Yu, "Measurement of IP3 in p-i-n photodetectors and proposed performance requirements for RF fiber-optic links," *IEEE Photon. Technol. Lett.*, vol. 12, no. 4, pp. 422–424, Apr. 2000.

[4] T. Ishibashi, T. Furuta, H. Fushimi, S. Kodama, H. Ito, T. Nagatsuma, N. Shimizu, and Y. Miyamoto, "InP/InGaAs uni-traveling-carrier photodiodes," *IEICE Trans. Electron.*, vol. E83-C, pp. 938–949, Jun. 2000.

[5] T. Ohno, H. Fukano, Y. Muramoto, T. Ishibashi, T. Yoshimatsu, and Y. Doi, "Measurement of intermodulation distortion in a unitraveling-carrier refracting-facet photodiode and a p-i-n refracting-facet photodiode," *IEEE Photon. Technol. Lett.*, vol. 14, no. 3, pp. 375–377, Mar. 2002.

[6] T. Ohno, H. Fukano, and Y. Muramoto, "Measurement of intermodulation distortion in high-output-power uni-traveling-carrier refracting-facet photodiode at 40 GHz," *Electron. Lett.*, vol. 36, pp. 1954–1955, Nov. 2000.

[7] J. W. Raring, E. J. Skogen, C. S. Wang, J. S. Barton, G. B. Morrison, S. Demiguel, S. P. DenBaars, and L. A. Coldren, "Design and demonstration of novel QW intermixing scheme for the integration of UTC-type photodiodes with QW-based components," *IEEE J. Quantum Electron.*, vol. 42, no. 2, pp. 171–181, Feb. 2006.

[8] H. Jiang, D. S. Shin, G. L. Li, T. A. Vang, D. C. Scott, and P. K. L. Yu, "The frequency behavior of the third-order-intercept point in a waveguide photodiode," *IEEE Photon. Technol. Lett.*, vol. 12, no. 5, pp. 540–542, May 2000.

A Dynamic Measurement Technique for Third-Order Distortion in Optical Phase Modulators

Matthew N. Sysak, *Member, IEEE*, Leif Johansson, *Member, IEEE*, Jonathan S. Klamkin, *Student Member, IEEE*, Larry A. Coldren, *Fellow, IEEE*, and John E. Bowers, *Fellow, IEEE*

***Abstract*—A novel two-tone measurement technique for characterizing distortion in optical phase modulators is proposed and demonstrated. The technique is used to characterize an InGaAsP–InP modulator in a monolithically integrated receiver. Results for forward and reverse bias conditions in the modulator show a phase IP3 of 7.2π and 0.97π rad, respectively.**

***Index Terms*—Carrier injection, phase distortion, phase modulators, quantum confined stark effect.**

I. Introduction

TRANSMISSION systems that utilize optical phase modulation are attractive for both analog and digital communication links. In analog transmission applications, phase modulation is attractive since it is not limited by the zero and full rail levels in standard intensity modulated systems. For digital transmission links, phase modulated systems provide tolerance to fiber dispersion effects and wide wavelength transparency.

To evaluate the performance of various phase modulators, several characterization techniques have been employed. For static characterization, phase efficiency experiments can be performed using shifts in a Fabry–Pérot cavity or by utilizing a Mach–Zehnder interferometer (MZI) [1], [2]. However, dynamic distortion characterization of phase modulators has been limited to single tone measurements because nonlinearities in the phase detection process are difficult to separate from the nonlinearities produced by the modulator [3].

In this work, we propose and demonstrate a two-tone measurement technique for characterizing the distortion generated by optical phase modulators that is not limited by the distortion in the phase recovery process. The technique relies on a linear external $LiNbO_3$ phase modulator to cancel the fundamental response of the test modulator, keeping the phase to amplitude phase recovery process within the linear regime of an optical MZI. Cancellation of the fundamental response does not effect the third-order distortion terms. Using this technique, we have compared the linearity of an InGaAsP phase modulator under forward and reverse bias conditions that is part of an integrated InGaAsP–InP photonic receiver chip. The comparisons are based on a modulator phase third-order intercept point (IP3), where the distortion and fundamental phase response of the test device are equivalent.

Manuscript received July 26, 2006; revised November 9, 2006. This work was supported by Defense Advanced Research Projects Agency (DARPA)/MTO Phorfront under Grant N66001-02-C-8026.

The authors are with the Department of Electrical Engineering and the Department of Materials, University of California Santa Barbara, Santa Barbara, CA 93116 USA (e-mail: mnsysak@engineering.ucsb.edu).

Digital Object Identifier 10.1109/LPT.2006.890026

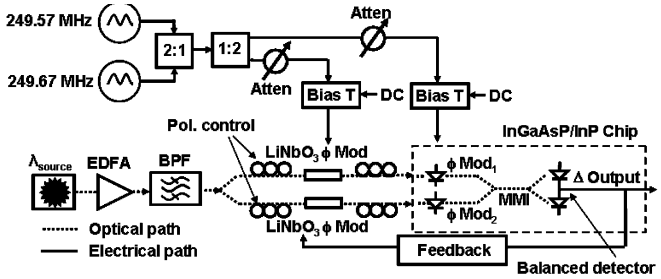

Fig. 1. Experimental setup for the dynamic characterization of third-order distortion products in InGaAsP phase modulators. Optical paths are denoted by dashed lines and electrical paths are show as solid lines.

II. Experimental Setup

The experimental setup used in these measurements is shown in Fig. 1. The setup is divided into electrical and optical sections. The optical portion consists of an optical transmitter, including a laser source at 1550 nm, an erbium-doped fiber amplifier, and an optical filter, that is split into two arms of an MZI and then recombined in a balanced photodetector (PD). Both arms of the MZI contain an external $LiNbO_3$ modulator and a 500-μm-long InGaAsP phase modulator that is part of the photonic receiver chip. Polarization controllers are utilized before and after each $LiNbO_3$ modulator. The photonic chip contains two parallel waveguides, each with an integrated InGaAsP phase modulator, a 2×2 multimode interference combiner, and a set of 100-μm-long uni-traveling-carrier (UTC)-PDs placed in a balanced configuration [4]. The InGaAsP phase modulator (ϕ mod $_2$) in the lower arm of the MZI is used to bias the interferometer. The InGaAsP modulators utilize 7×6.5 nm quantum wells and 6×5 nm barriers with a photoluminescence peak of 1465 nm centered in an optical waveguide layer for phase efficiency.

The electrical portion of the test setup consists of two signal generators and a series of electrical splitters and combiners. The individual tones from each function generator are combined in a 2 : 1 combiner, then split into two electrical paths using a 1 : 2 splitter. The outputs from the splitter contain signal tones from both function generators. One of the outputs from the splitter is routed to the $LiNbO_3$ modulator, while the second output is routed to the test modulator ($\phi \bmod 1$). A set of attenuators are used to control the electrical power delivered to the modulators. A portion of the signal from the balanced detector is routed to a low frequency feedback circuit. The output from the circuit is connected to a second $LiNbO_3$ modulator, which compensates low frequency drift in the test bed and forces the power difference at the output of the balanced detector to zero [5]. To

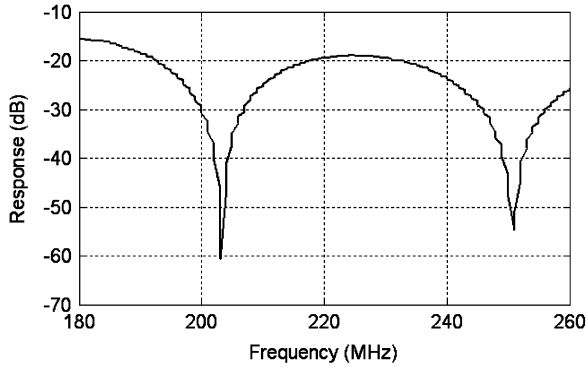

Fig. 2. Frequency response measurements between the 1 : 2 splitter and the balanced UTC-PD. Nulls correspond to frequencies where the path length mismatches between the $LiNbO_3$ and InGaAsP modulators are separated by an odd multiple of π radians.

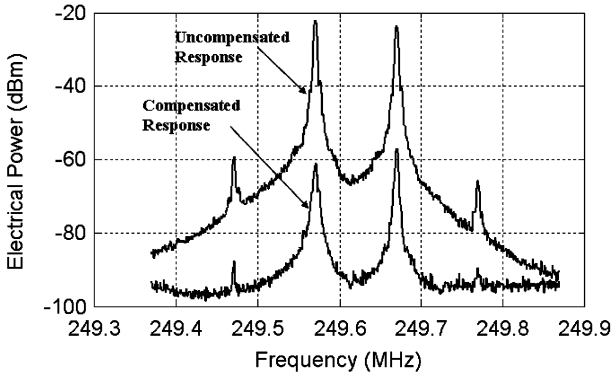

Fig. 3. Compensated and uncompensated spectra for forward biased InGaAsP phase modulator. Electrical drive power is -15 and 0 dBm to the InGaAsP and $LiNbO_3$ modulators, respectively. The compensated spectra has not been optimized for maximum distortion suppression.

ensure that the nonlinearities associated with the test equipment and the various splitters and combiners in the test bed are minimized, the two-tone electrical signal used to drive the $LiNbO_3$ and InGaAsP modulators was examined over a range of electrical powers. The drive signals contained no observable distortion for power levels up to and exceeding the levels utilized in our experiments. To eliminate the possibility that distortion might be generated in the UTC-PDs, two-tone measurements were performed on a set of test devices with the same dimensions as the photodiodes in the receiver chip. Results showed an output power IP3 of $> +30$ dBm for the $100\times10\ \mu m^2$ UTC-PD at a bias of -5 V [4].

The center frequency of the two-tone signal is chosen so that the path length difference between the 1 : 2 electrical splitter and the InGaAsP or $LiNbO_3$ modulator corresponds to a phase delay of an odd multiple of π radians. To investigate the electrical delay between the two paths, the function generators and the 2 : 1 combiner were removed and a frequency response measurement was performed between the 1 : 2 splitter and the balanced UTC-PD. Results from this measurement are shown in Fig. 2 when the InGaAsP modulator is forward biased. Dips in the response correspond to frequencies where the electrical path lengths are mismatched by an odd multiple of π radians. Under these conditions, the 180° phase lag between the signals to each modulator cause the phase response of the two devices to cancel. The roll off of the response in this measurement is a result of a low ($\sim$150 MHz) 3-dB bandwidth of the forward biased InGaAsP modulator [2].

III. Measurement Technique

Characterization of the reverse and forward bias InGaAsP phase modulator requires a set of two experiments. All measurements are performed at an MZI bias where the average photocurrent in both UTC-PDs is 1.7 mA.

The first set of experiments examines the fundamental response of the test modulator. This experiment uses only the test InGaAsP modulator and does not utilize the $LiNbO_3$ modulator. The bias-T in the electrical path sets either forward or reverse bias conditions in the device. In this experiment, the power from the two electrical signal generators that is routed to the test device is varied and the fundamental and third-order signal tones from the balanced UTC-PD are measured in a 50-Ω terminated electrical spectrum analyzer (ESA). Although the distortion measured at the output of the balanced detector has components associated with both the modulator and the optical MZI, the fundamental phase response of the InGaAsP modulator remains proportional to the fundamental tone produced in the balanced detector. An output spectrum from these experiments with the forward biased modulator is shown in Fig. 3. The spectrum is labeled "Uncompensated Response."

The second set of experiments utilizes both modulators and is used to extract the InGaAsP modulator distortion. In these measurements, the electrical power to the test and reference modulators is varied and the output from the balanced UTC-PD is examined in an ESA. The phase difference between the electrical signals to the two modulators causes the phase response of the $LiNbO_3$ modulator to compensate the phase response of the InGaAsP device. Since the $LiNbO_3$ modulator relies on the linear electrooptic effect and the forward or reverse biased InGaAsP modulator relies on the highly nonlinear quantum confined stark effect and plasma effect, the phase cancellation between these modulators affects primarily the fundamental response of the InGaAsP device while the preserving modulator distortion products. The reduced fundamental permits the phase-to-amplitude conversion to remain in the linear regime of the MZI, preserving the distortion produced in the test modulator without adding distortion from the phase recovery process. A sample spectrum from the UTC-PDs in these experiments is shown in Fig. 3 and labeled "Compensated Response."

IV. Results

Results for characterization of the forward biased InGaAsP modulator with a 10-mA DC bias are shown in Fig. 4.

In the uncompensated measurements, Fig. 4 shows an input power IP3 of $+7.6$ dBm. Using a modulator V_π of 0.5 V, this translates into a peak phase IP3 of 1.5π rad. The phase IP3 can also be calculated based on the output power IP3 in Fig. 4. Based on the phase efficiency of 3.4 mA/rad in the balanced detector, this translates into a peak phase IP3 of 0.45π rad. Both results are in relatively good agreement with the 0.9π peak phase limit that is associated with an optical MZI [6]. It should be noted that any RF losses at the detector or any deviation from the quadrature point in the test setup caused by imbalance coupler splitting

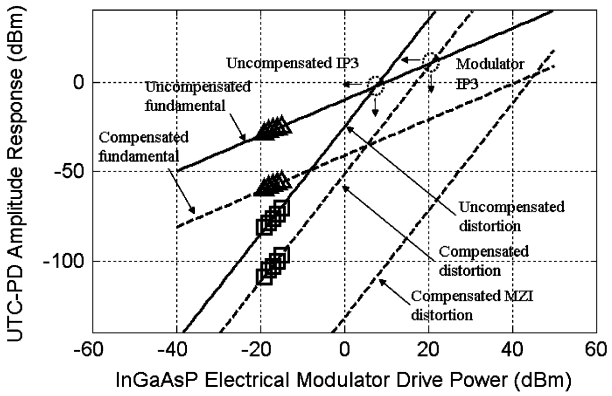

Fig. 4. Uncompensated and compensated experimental results generated by the forward biased InGaAsP phase modulator.

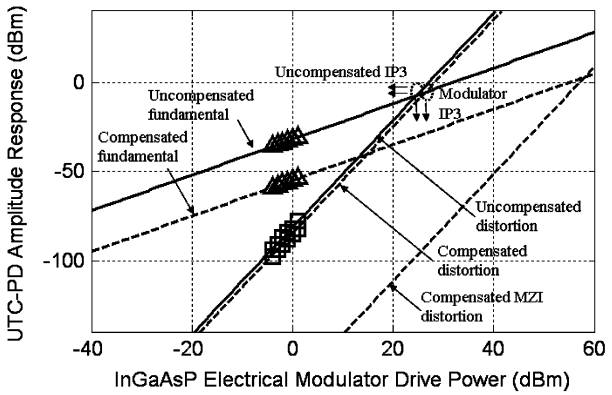

Fig. 5. Uncompensated and compensated experimental results generated by the reverse biased InGaAsP phase modulator.

reduces the output power IP3 in these measurements and would cause an artificially low phase IP3.

For the compensated measurements, the cancellation of the InGaAsP fundamental by $\sim$33 dB leads to a suppression of the MZI nonlinearities and isolation of the modulator distortion. The corresponding reduction of the measured distortion is $\sim$33 dB. It is important that although the fundamental phase response is reduced, it is not eliminated, and the compensated measurements are still limited by the theoretical phase IP3 of 0.9π associated with the MZI. The theoretical distortion generated by the test setup is included in Fig. 4 and labeled "compensated MZI distortion." The experimental data in these measurements is $>$20 dB above the theoretical MZI distortion, indicating that the test bed nonlinearities have been sufficiently removed to expose the modulator distortion.

Combining the fundamental response in the uncompensated measurements with the third-order response in the compensated measurements allows extraction of the forward biased modulator phase characteristics. From Fig. 4, the input power IP3 is $+$20.9 dBm, which corresponds to a phase IP3 of 7.2π. As mentioned previously, the output power IP3 can also be used to calculate phase IP3. The $+$10.85-dBm output power IP3 in Fig. 4 corresponds to a phase IP3 of 2.1π rad. However, the most accurate measure of the modulator performance is most likely the calculation of phase IP3 based on the input power. This is because the UTC-PD losses and MZI imbalance or bias offsets from quadrature reduce the RF power from the detector and make the phase IP3 appear artificially small.

Results for the reverse biased modulator characterization are shown in Fig. 5. The applied DC bias is -2 V. Examining the distortion and fundamental tones in the uncompensated measurements shows an output and input power IP3 of -7.2 and $+24.7$ dBm, respectively. Converting this to an output phase change gives 0.8π rad based input power IP3 ($V\pi$ is 6.8 V) and 0.25π rad based on the output power IP3. The phase IP3 based on the input power IP3 is in good agreement with the 0.9π that should limit the MZI, and indicates that the modulator distortion is roughly equal to the distortion generated by the test setup.

In the compensated measurements when the test bed nonlinearities are reduced, the very small ($\sim$3–4 dB) reduction in the distortion data supports the conclusion that the modulator and test bed distortion are roughly equivalent. As in Fig. 4, the distortion associated with the MZI in the compensated measurements is included in Fig. 5, and is labeled "compensated MZI distortion."

Extrapolating the fundamental response from the uncompensated measurements and the distortion in the compensated measurements gives input and output power IP3s $+$26.4 and -5.65 dBm, respectively. Converting the input power power IP3s to phase gives a phase IP3 for the reverse biased modulator of 0.97π rad.

V. Conclusion

We have proposed and demonstrated a dynamic measurement technique for characterizing distortion products in optical phase modulators. The technique has been used to characterize the nonlinearities in an InGaAsP phase modulator under forward and reverse bias conditions. Measurements of the test modulator under forward and reverse bias conditions showed a phase IP3 of $\sim 7.2\pi$ and 0.97π, respectively.

References

[1] H. Mohseni, H. An, Z. A. Shellenbarger, M. H. Kwakernaak, A. N. Lepore, J. H. Abeles, and P. J. Delfyett, "Highly linear and efficient GaInAsP-InP phase modulators," in *Conf. Lasers Electro-Optics (LEOS)*, 2004, vol. 1, p. 2.

[2] M. N. Sysak, L. A. Johansson, J. W. Raring, M. Rodwell, L. A. Coldren, and J. E. Bowers, "A high-efficiency, current injection based quantum well phase modulator monolithically integrated with a tunable laser for coherent systems," in *Coherent Optical Technol. and Appl. (COTA) CFC6*, Whistler, BC, Canada, Jun. 2006.

[3] R. E. Tench, J. M. P. Delavaux, L. D. Tzeng, R. W. Smith, L. L. Buhl, and R. C. Alferness, "Performance evaluation of waveguide phase modulators for coherent systems at 1.3 and 1.5 μm," *J. Lightw. Technol.*, vol. LT-5, no. 4, pp. 492–501, Apr. 1987.

[4] J. Klamkin, L. A. Johansson, A. Ramaswamy, H. F. Chou, M. N. Sysak, J. W. Raring, N. Parthasarathy, S. P. Denbaars, J. E. Bowers, and L. A. Coldren, "Monolithically integrated balanced uni-travelling-carrier photodiode with tunable MMI coupler for microwave photonic circuits," *COMMAD*, 2006, submitted for publication.

[5] H. F. Chou, D. Zibar, L. A. Johansson, and J. E. Bowers, "SFDR Improvement of a Coherent Receiver Using Feedback," in *Coherent Optical Technol. and Appl. (COTA) CFA3*, Whistler, BC, Canada, Jun. 2006.

[6] B. Kolner and D. W. Dolfi, "Intermodulation Distortion and compression in an Integrated Electrooptic Modulator," *Appl. Opt.*, vol. 26, no. 2, pp. 3676–3680, Sep. 1987.

Coherent Receiver Based on a Broadband Optical Phase-Lock Loop

A. Ramaswamy[*], L.A. Johansson[*], J. Klamkin[†], C. Sheldon[*], H.F. Chou[††], M.J. Rodwell[*], L.A. Coldren[*†] and J.E. Bowers[*]

[*] *ECE Dept. University of California, Santa Barbara, CA 93106*
[†] *Materials Dept. University of California, Santa Barbara, CA 93106*
[††] *LuminentOIC Inc., Chatsworth, CA 91311*
anand@ece.ucsb.edu

Abstract: We propose and demonstrate a 1.45GHz bandwidth optical phase-lock loop receiver for linear optical phase demodulation. Using the receiver in a link application, a spurious free dynamic range of 125 $dBHz^{2/3}$ is measured at 300MHz.

OCIS codes: (250.3140) Integrated optoelectronic circuits, (060.1660) , Coherent communications (060.5060), Phase modulation, (060.2360) Fiber optics links and subsystems.

1. Introduction

Optical phase-locked loops have found renewed interest with the reemergence of coherent optical link technologies. For data transmission, a homodyne optical phase-lock loop can generate the highest sensitivity when sufficient loop bandwidth can be maintained [1]. This technique becomes particularly attractive at high bit-rates when alternative DSP-based solutions are not yet mature, or when low receiver power consumption is desirable. Alternative phase-lock loop applications are coherent synchronization of laser arrays [2] or frequency synthesis by offset locking [3].

In this work, a broadband optical phase-lock loop is demonstrated for demodulation of analog phase-modulated optical links. Phase modulation has attracted interest for application in linear optical links with the existence of very linear optical $LiNOb_3$ phase modulation as an alternative to non-linear intensity modulators. The challenge is now transferred to the receiver side. In a standard optical interferometer based phase demodulation, there is a sinusoidal relation between the optical phase and the detected photocurrent. This nonlinearity limits the available link dynamic range. In contrast, a high-gain optical phase-lock loop will provide linear demodulation provided phase feedback is supplied to a linear optical phase modulator.

Figure 1 shows a schematic of the receiver architecture, previously demonstrated in a low-frequency proof-of-principle experiment [4]. Here, a common source is split in two paths, each containing an optical phase modulator. The input signal is applied to the first modulator. Upon recombination with the second part, the detected optical signal has a sinusoidal dependence on the optical phase. The photocurrent is then measured, amplified and provided as negative feedback to the second reference modulator. The detected net phase is now reduced by a factor *1/(1+T)* where T is the loop roundtrip phase gain, such that the interferometer is now operating within its linear range. It should be noted that the feedback cannot separate detector shot-noise from signal so that the shot-noise limited SNR remains unchanged despite the reduction in net received phase.

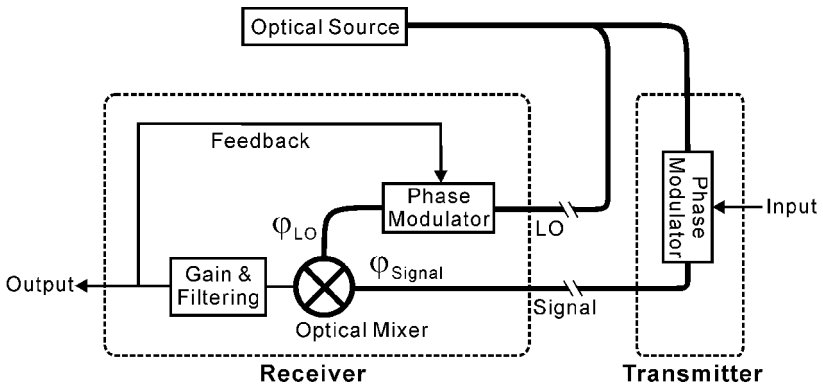

Fig. 1. Concept schematic of the demonstrated coherent receiver with feedback. Thick lines: optical link; thin lines: electrical link.

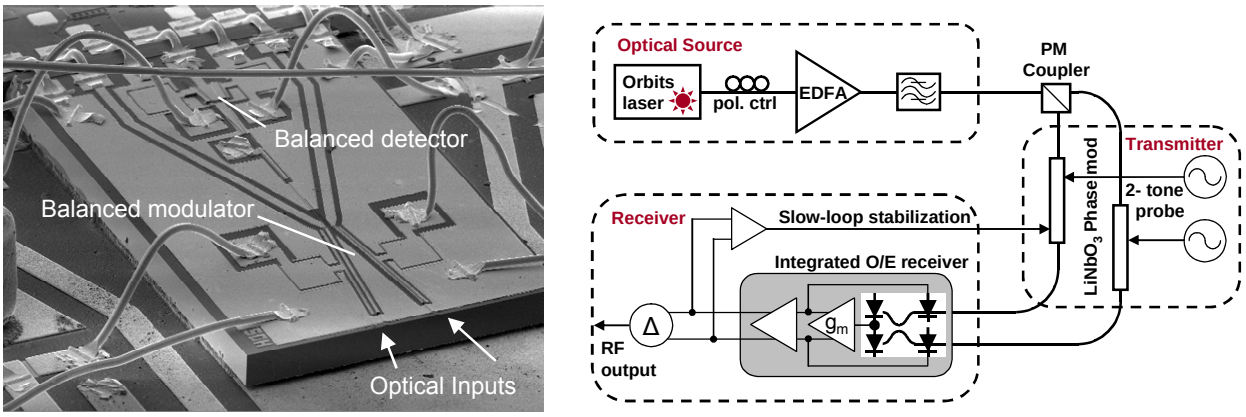

Fig.2. a) SEM of Integrated O/E Receiver b) Schematic of Experimental Setup

2. Integrated Receiver

The optical phase demodulator consists of two integrated chips – one photonic, one electronic – mounted on a common microwave carrier. Figure 2a) shows the photonic integrated circuit consisting of a balanced UTC photodetector [5], tracking phase modulators and a 2x2 waveguide MMI coupler. The wirebonds connecting to the hybrid integrated electronic IC (not shown) can be seen in the upper part of the figure. In quadrature, this type of balanced receiver discriminates against common-mode and second-order nonlinearities. The tracking optical phase modulators are driven differentially so as to add opposite-sign phase shifts to the incoming signal and LO resulting in a cancellation of even-order nonlinearities and common-mode noise. Additionally, driving the modulators in a differential fashion doubles the drive voltage presented to the modulator thereby reducing the maximum voltage required. The capacitances of the photodiodes and modulators are exploited as circuit elements rather than being parasitics that need to be eliminated. They perform the desired loop integrations and hence, can be much larger. The electronic chip that interfaces with the PIC is primarily a trans-conductance amplifier that converts the voltage generated by photodiode integration into a modulator drive current. The modulator integrates this current to produce the required phase shift. It also has a pair of buffer amplifier capable of driving 50 ohms. The electronic chip improves the phase margin and thereby provides stability to the system.

3. Analog Link Experiment

A schematic of the experimental setup is shown in Figure 2 a). The CW optical source consists of an Orbits low noise, high power, frequency stabilized laser at 1537.40nm. The output of the laser is amplified using a high power EDFA. The polarization controller prior to the EDFA is used to adjust the splitting ratio of the power in the two branches emerging from the PM Coupler. After the coupler, polarization maintaining fibers and components are used for managing polarization and maintaining stability.

To ensure no mixing products are generated in the two-tone drive signal, separate $LiNbO_3$ phase modulators were used to combine the two closely spaced RF tones (Δf=2MHz) in the optical domain. The phase modulators have V_π's of 4.4V and 5.5V respectively. At the output of the receiver the differential signal is tapped into a slow feedback loop which generates a low frequency drive signal to one of the phase modulators as seen in Figure 2 b). This stabilizes the system against environmental drifts and maintains the bias of the phase demodulator at quadrature. The RF outputs are 180° out of phase and are differentially combined.

Due to the feedback architecture of the system, the effective swing across the phase demodulator is suppressed by a factor of *1/(1+T)* where *T* is the loop transmission gain. The frequency response of the device for varying values of photocurrent is shown in Figure 3 a). At high photocurrent and lower frequencies, the loop gain is sufficiently high such that the reference phase modulator is able to closely track the received signal phase. The optical link gain *(G)* is here dependent on the ratio of drive voltage between source and reference modulator and is in this link -5dB. At high frequencies or at low photocurrent values, the loop transmission gain is low and hence, the link gain is proportional to the photocurrent and the loop filter transfer function as expected. The loop bandwidth, here defined by the 3-dB point, approximately where the loop transmission $|T|$ crosses unity, reaches 1.45 GHz at 12 mA. The delay-limited bandwidth, within where the loop remains stable, is on the order of 4 GHz.

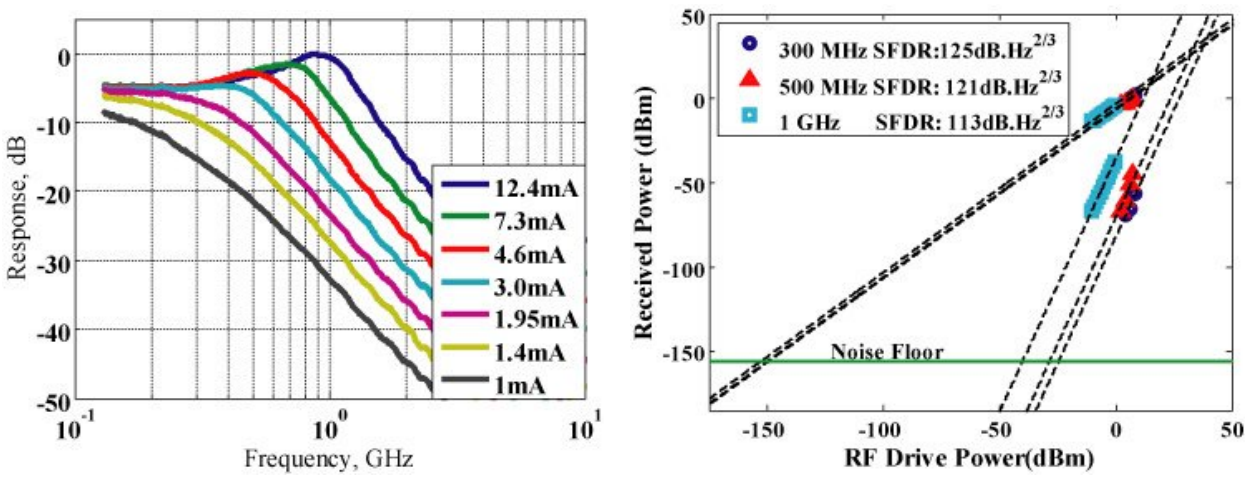

Fig. 3. a) Link gain at different detected photocurrent levels b) SFDR at 300 MHz, 500 MHz and 1 GHz

Figure 3 b) shows SFDR data taken at three different frequencies with 12mA of photocurrent in each detector. Due to the imperfect optical source used, the spontaneous emission noise from the EDFA has been removed from the noise level to reflect shot-noise limited receiver performance. With detector balance and a low-RIN source, this should be readily available. It was verified that the receiver noise was well below the calculated shot noise level. An SFDR of 125dB.Hz$^{2/3}$ was measured at 300 MHz. At higher frequencies with reduced feedback, the SFDR degrades as can be seen in Figure 3b) to the point where there is no reduction in the net received phase (1 GHz). At 12 mA, the shot noise limited SFDR can be calculated at 116 dBHz$^{2/3}$.

4. Summary

In this paper we have described and experimentally demonstrated a novel coherent integrated receiver based on a broadband optical phase locked loop. At 12mA of average photocurrent per photodiode the loop bandwidth is 1.45 GHz and the shot noise limited SFDR is 125dB.Hz$^{2/3}$ at 300 MHz. Going to higher photocurrent values will increase the feedback effect, resulting in an enhanced dynamic range and high linearity over a wide band. The integration of the photonics and electronics in this receiver allows for the feedback delay to be short enough to sustain large amounts of loop gain at high frequencies. Thus it is successful in reducing the distortion due to a normal phase demodulator without any penalty in SNR.

Acknowledgements

The authors would like to thank helpful discussions with Larry Lembo, Steve Pappert and Jim Hunter. Further acknowledgement should be provided to Northrop Grumman Space Technologies for providing the electronic IC. This work was supported by the DARPA PHOR-FRONT program under United States Air Force contract number FA8750-05-C-0265.

References

[1] E. Ip, J.M. Kahn, "Carrier synchronization for 3- and 4-bit-per-symbol optical transmission," Journal of Lightwave Technology, vol. 23, Issue 12, pp. 4110 - 4124 Dec. 2005.

[2] A. Yariv, "Dynamic analysis of the semiconductor laser as a current-controlled oscillator in the optical phased-lock loop: applications," Optics letters, 30(17), 2191-2193, 2005.

[3] U. Gliese, N.T. Nielsen, M. Bruun, E.L. Christensen, K.E. Stubkjaer, S. Lindgren and B. Broberg, "A wideband heterodyne optical phase-locked loop for generation of 3-18 GHz microwave carriers", IEEE Photon. Technol. Lett., vol. 4, pp. 936–938, 1992.

[4] Hsu-Feng Chou, A. Ramaswamy, D. Zibar, L.A. Johansson, J.E. Bowers, M. Rodwell, and L.A. Coldren, "SFDR Improvement of a Coherent Receiver Using Feedback," OSA topical meeting of Coherent Optical Techniques and Applications (COTA), Whistler, BC, 2006.

[5] J. Klamkin, L.A. Johansson, A. Ramaswamy, Hsu-Feng Chou, M.N. Sysak, J.W. Raring, N.Parthasarathy, S.P. DenBaars, J.E. Bowers, L.A. Coldren, "Monolithically Integrated Balanced Uni-Traveling-Carrier Photodiode with Tunable MMI Coupler for Microwave Photonic Circuits," Conference on Optoelectronic and Microelectronic Materials and Devices (COMMAD), Perth, Australia. Dec. 2006.

Highly Linear Coherent Receiver With Feedback

Hsu-Feng Chou, *Member, IEEE*, Anand Ramaswamy, Darko Zibar, Leif A. Johansson, *Member, IEEE*, John E. Bowers, *Fellow, IEEE*, Mark Rodwell, *Fellow, IEEE*, and Larry A. Coldren, *Fellow, IEEE*

***Abstract*—We propose and demonstrate a novel coherent receiver with feedback for high-linearity analog photonic links. In the proposed feedback receiver, a local phase modulator tracks the phase change of the signal and reduces the effective swing across the phase demodulator without reducing the transmitted signal. The signal-to-noise-ratio is thus maintained while linearity is improved. Up to 20-dB improvement in spur-free dynamic range (SFDR) is achieved experimentally. At 3.13 mA of average photocurrent per photodiode, the measured SFDR is 124.3 dB $\cdot$ Hz$^{2/3}$, which corresponds to an SFDR of 131.5 dB $\cdot$ Hz$^{2/3}$ when the link is shot-noise-limited.**

***Index Terms*—Analog links, coherent communication, feedback, microwave photonics, phase-modulation.**

I. Introduction

FROM residential CATV broadcasting to demanding military communications, analog photonic links have found a broad range of applications. In terms of linearity, the performance of an intensity-modulated analog link is mainly determined by the intensity modulator in the transmitter [1]. Interferometer-based intensity modulators have a sinusoidal response while absorption-based ones are typically exponential. In general, the modulation depth must be restrained and the bias point properly tuned to obtain a high degree of linearity [2]. On the other hand, electrooptic phase modulators can be quite linear compared to intensity modulators. The modulation depth is no longer hard-limited by the optical power to 100% as in an intensity-modulated link but by the range in which the phase modulator is linear. However, the challenge in constructing a high-linearity link is now moved to the receiver side. A traditional phase demodulator based on optical interference has a sinusoidal response and thus limits the linearity of a coherent link [3]. In other words, the same (sinusoidal) distortion remains in the link. Reducing the strength of the transmitted signal may reduce the distortion but the spur-free dynamic range (SFDR) remains unchanged.

To overcome this problem, we recently proposed a novel coherent receiver with a feedback design that is capable of reducing the distortion and improving the SFDR [4]. SFDR of 103.5 dB $\cdot$ Hz$^{2/3}$ was demonstrated, showing a 15-dB improvement from a traditional receiver. In this letter, we further improve the work in [4] using an all-optical construction and achieve SFDRs as high as 131.5 dB $\cdot$ Hz$^{2/3}$ in the shot-noise-limited scenario and a 20-dB improvement from a traditional receiver.

Manuscript received October 2, 2006; revised March 11, 2007. This material is based upon work supported by the Defense Advanced Research Projects Agency (DARPA) PHOR-FRONT Program under United States Air Force Contract FA8750-05-C-0265.

H.-F. Chou was with the Department of Electrical and Computer Engineering, University of California, Santa Barbara, CA 93106 USA. He is now with LuminentOIC, Inc., Chatsworth, CA 91311 USA (e-mail: Hsu-Feng.Chou@ieee.org).

A. Ramaswamy, D. Zibar, L. A. Johansson, J. E. Bowers, M. Rodwell, and L. A. Coldren are with the Department of Electrical and Computer Engineering, University of California, Santa Barbara, CA 93106 USA.

Digital Object Identifier 10.1109/LPT.2007.898811

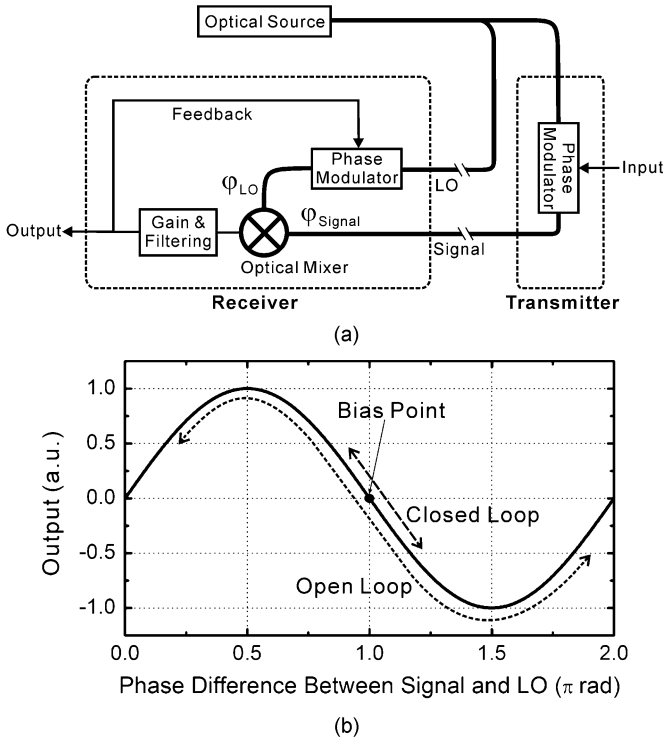

Fig. 1. (a) Concept of the proposed coherent receiver with feedback. Thick lines: optical link; thin lines: electrical link. (b) Transfer function of an interferometer-based phase demodulator (optical mixer). After closing the loop, the swing of the phase difference is reduced, resulting in a more linear output.

II. Principle of Operation

The proposed receiver in a coherent link is illustrated in Fig. 1(a). The optical source is first split into two branches: one goes directly to the "LO" input of the receiver while the other is phase modulated by the transmitter and then fed into the "signal" input of the receiver. The phase demodulator (an optical mixer) compares the phase of the two inputs and generates a differential signal. Fig. 1(b) shows the transfer function of an interferometer-based optical mixer, which possesses a sinusoidal response. The bias point is set to the quadrature point to eliminate the even-order distortions and obtain the highest slope efficiency. The modulation depth can be larger than π rad (equivalent to 100% in an intensity-modulated link) but the distortion in the demodulated signal increases with modulation depth. However, in the proposed feedback receiver, as shown in Fig. 1(a), the output from the optical mixer is fed back to a local phase modulator in the LO branch after amplification and filtering. The effect of such feedback is to reduce the difference

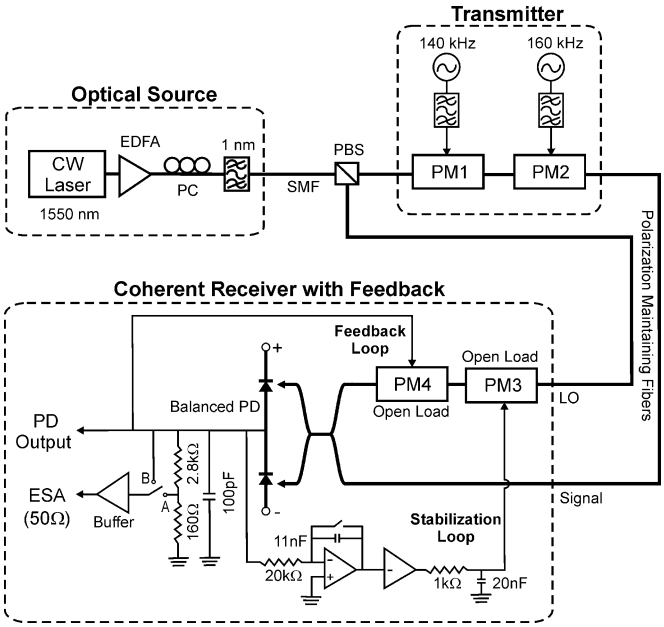

Fig. 2. Experimental setup. In order to handle the high dynamic range of the receiver, the buffer amplifier is connected to A for measuring signal and to B for measuring noise. PC: polarization controller. SMF: single-mode fiber. PBS: polarization-beam splitter. PM#: phase modulator. ESA: electrical spectrum analyzer.

in phase between the LO and the signal branches. The effective swing across the phase demodulator is thus reduced, leading to a more linear output [Fig. 1(b)]. Note that this reduction in swing is not achieved by decreasing the strength of the transmitted signal and the signal-to-noise ratio (SNR) of the transmitter remains the same. On the receiver end, the SNR of the output signal is also preserved after closing the loop since both the signal and the noise are reduced by the same factor. The benefit of such reduction in swing is the improvement in receiver linearity without decreasing the transmitted power and degrading the SNR, which leads to an effective improvement in SFDR.

III. Experiment

The experimental setup is schematically shown in Fig. 2. The bandwidth of this particular setup is limited to a few megahertz due to the loop delay caused by fiber patch cords of the discrete components used in the receiver. Therefore, 140 and 160 kHz are chosen for the two-tone SFDR measurements. The delay of an integrated receiver should be three orders of magnitude smaller. An external cavity tunable semiconductor laser is used as the CW optical source at 1550 nm whose output is amplified by a high-power erbium-doped fiber amplifier (EDFA). This interferometer-like coherent link is constructed with polarization-maintaining fibers and components for polarization management and stability. The lengths of the two interferometer branches are matched with an optical delay line to minimize the impact of laser noise. The polarization controller after the EDFA is used to adjust the power ratio between the two branches through the polarization beam splitter. The transmitter is composed of two sets of electrical synthesizer, bandpass filter, and $LiNbO_3$ phase modulator. This arrangement decouples the driving electronics at respective tones to ensure spectral purity. The harmonic distortions are suppressed to better than -80 dBc. The nominal $V\pi$ of the phase modulators is 4.4 V.

On the receiver side, two phase modulators, PM3 and PM4, are placed on the LO branch. Both have open termination (very high impedance). The optical mixer is composed of a single-polarization optical coupler and a balanced photodetector with 0.9-A/W responsivity and biased at ± 12 V. The saturation power of the photodetector is over 12 dBm. Not shown in Fig. 2 are two 10-μF polypropylene capacitors that bypass the RF signal from the power supplies to the ground. In contrast to our previous work in [4], the feedback loop does not contain active amplifiers to provide loop gain. Instead, the passive load of the balanced photodetector is designed to provide gain and filtering. The balanced photodetector is thus directly driving the local phase modulator without using electrical amplifiers. This "all-optical" construction reduces the extra delay, noise, as well as distortion associated with the electrical amplifiers. More significantly, this direct-drive architecture makes it easier to integrate the feedback receiver monolithically on a single chip [5] in order to minimize the loop delay for higher operation speed, without resorting to hybrid packaging.

PM4 is the local phase modulator that provides feedback. The load of the balanced photodetector is 100 pF // 2.96 kΩ // 20 kΩ. Since the electrical spectrum analyzer has 50-Ω input impedance, an electrical buffer (LMH6703, nominal third-harmonic distortion < -103 dBc) is used to match the impedance. To prevent the feedback loop from oscillation, it is critical that unity gain of the loop is reached before the phase shifts by -180°. The capacitance of the load governs the roll-off of the loop gain and inevitably consumes -90° of phase margin. As a result, the loop delay is the main bottleneck that limits the bandwidth. The shorter the delay, the higher frequency the receiver can operate at without oscillation. The loop delay in the current setup is approximately 3 m. PM3 is driven by a slow feedback loop to stabilize the interferometer against environmental drifts and maintains the bias of the phase demodulator to the quadrature point. A first-order *RC* filter is added to the output stage to suppress the noise that is generated by the stabilization electronics from entering the signal loop. The DC drift from the quadrature point is less than $\pm 0.04\%$.

The open loop transmission of the LO phase T is defined as the open-loop round-trip gain in the feedback path. It can be expressed as

$$T = 2 \cdot < I_{\rm PD} > \cdot Z \cdot \pi / V_\pi \tag{1}$$

where $< I_{\rm PD} >$ is the average photocurrent per photodiode and Z is the load impedance. Fig. 3 shows the SFDR measurements at $< I_{\rm PD} >= 3.13$ mA ($T = 11.24$), where the LO optical power is 3.5 mW. By equating the optical phase of the feedback loop, it can be derived that the effective swing across the phase demodulator can be suppressed by a factor of $1/(1+T)$ from its original strength after closing the loop. In the case of $T = 11.24$, the effective swing is suppressed to 8%. As a result, SFDR is improved from 104.5 dB $\cdot$ Hz$^{2/3}$ to 124.3 dB $\cdot$ Hz$^{2/3}$, showing a 19.8-dB improvement by using the feedback receiver. The noise levels are measured by switching the buffer input to point B in Fig. 2.

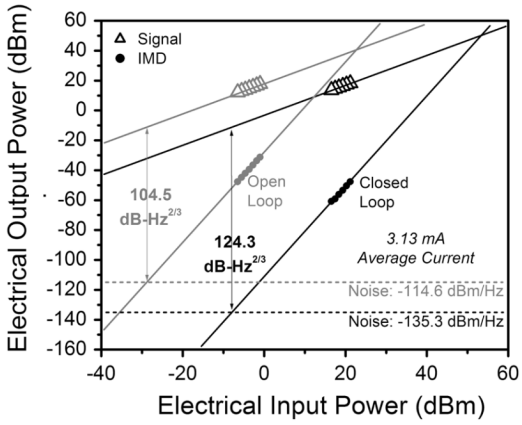

Fig. 3. SFDR measurements at 3.13 mA of average photocurrent. The powers are referring to a 50-Ω load. The noise level is normalized and measured with 300 Hz of resolution bandwidth. Gray lines: open loop. Black lines: closed loop. IMD: third-order intermodulation distortion.

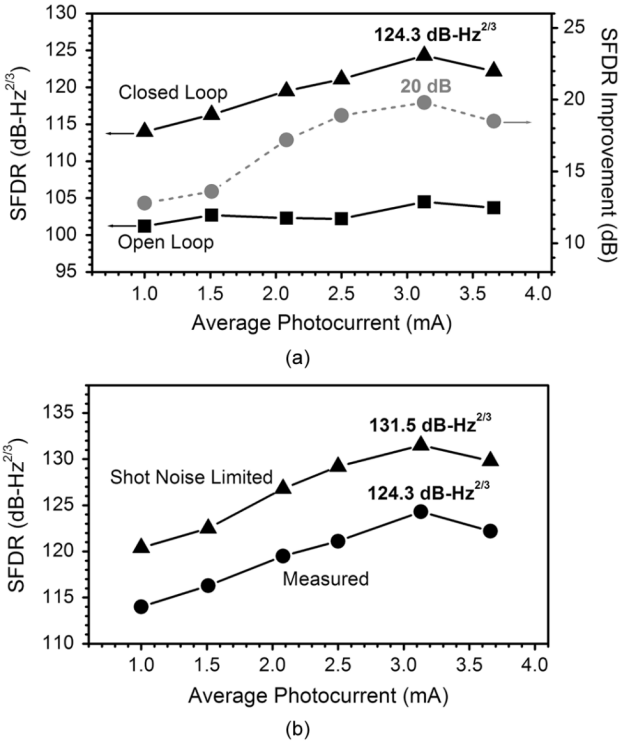

Fig. 4. (a) SFDR of the open and the closed loops. (b) SFDR with measured and shot-noise-limited noise levels for the closed loop case.

Theoretically, the RF gain of the link is given by $[T/(1+T)]^2$, which approaches unity when T is high. The SNR is dominated by the shot-noise in the receiver and the phase noise of the laser. It is preserved after closing the loop as can be observed in Fig. 3. On the other hand, the intermodulation distortion is suppressed at the same output level after closing the loop, resulting in the increase of linearity. The SFDR can be improved by $(1+T)^2$ compared to a traditional receiver but is subject to the linearity of all the components used in the receiver.

Fig. 4(a) shows the dependence of SFDR on the average photocurrent per photodiode for the open loop and the closed loop cases. For the open loop (a traditional receiver), increased photocurrent does change the maximum swing of the phase demodulator but it cannot improve linearity. Therefore, the measured SFDR shows little dependence on average photocurrent. On the other hand, for the closed loop, the loop transmission increases with average photocurrent [as expressed in (1)], which leads to a smaller effective swing across the phase demodulator and thus better linearity and SFDR. Nevertheless, the SFDR starts to roll off beyond 3.13 mA of average photocurrent and becomes unstable (even before the loop oscillates). This is believed to be caused by the degradation of photodetector linearity at high photocurrent levels.

The currently measured noise levels are approximately 10 dB above the theoretical shot noise level, leading to about 6.7-dB penalty in SFDR, as indicated in Fig. 4(b). At several milliamperes of photocurrent, shot-noise dominates over thermal noise, representing the theoretical limit of noise level. If the shot noise limit can be achieved, up to 131.5 dB $\cdot$ Hz$^{2/3}$ of SFDR can be obtained. The excess noise is believed to be caused by the finite linewidth of the laser source (50 kHz) [3] and the noise from the high-power EDFA.

Ideally, the achievable SFDR of the proposed feedback receiver does not have fundamental limitations as long as the loop delay is short enough to sustain a desirable amount of loop gain at the bandwidth of interest. The practical challenge for extreme linearity lies on the linearity of the components in the link (phase modulators, photodetectors, and loop amplifiers if utilized). To scale the bandwidth to the gigahertz range, hybrid or monolithic integration of the receiver is necessary to keep the loop delay down to $\sim$10-ps level.

IV. Conclusion

A novel all-optical receiver with feedback is proposed and experimentally demonstrated to improve the SFDR of a coherent analog photonic link. The feedback design is successful in reducing the distortion due to the sinusoidal response of a traditional phase demodulator without degrading the SNR. SFDR improvement of 20 dB is demonstrated at the highest measured SFDR of 124.3 dB $\cdot$ Hz$^{2/3}$, which corresponds to a shot-noise-limited SFDR of 131.5 dB $\cdot$ Hz$^{2/3}$.

Acknowledgment

The authors would like to thank L. Lembo, P. Ly, S. Pappert, and J. Hunter for helpful discussions.

References

[1] C. H. Cox III, E. I. Ackerman, G. E. Betts, and J. L. Prince, "Limits on the performance of RF-over-fiber links and their impact on device design," *IEEE Trans. Microw. Theory Tech.*, vol. 54, no. 2, pp. 906–920, Feb. 2007.

[2] B. Liu, J. Shim, Y.-J. Chiu, A. Keating, J. Piprek, and J. E. Bowers, "Analog characterization of low-voltage MQW traveling-wave electroabsorption modulators," *J. Lightw. Technol.*, vol. 21, no. 12, pp. 3011–3019, Dec. 2003.

[3] R. F. Kalman, J. C. Fan, and L. G. Kazovsky, "Dynamic range of coherent analog fiber-optic links," *J. Lightw. Technol.*, vol. 12, no. 7, pp. 1263–1277, Jul. 1994.

[4] H.-F. Chou, A. Ramaswamy, D. Zibar, L. A. Johansson, J. E. Bowers, M. Rodwell, and L. Coldren, "SFDR improvement of a coherent receiver using feedback," in *Proc. IEEE Conf. Coherent Optical Technologies and Applications (COTA)*, Whistler, BC, Canada, Jun. 25–30, 2006, Paper CFA3.

[5] M. N. Sysak, J. W. Raring, J. S. Barton, M. Dummer, A. Tauke-Pedretti, H. N. Poulsen, D. J. Blumenthal, and L. A. Coldren, "Single-chip, widely-tunable 10 Gbit/s photocurrent-driven wavelength converter incorporating a monolithically integrated laser transmitter and optical receiver," *Electron. Lett.*, vol. 42, no. 11, pp. 657–658, May 2007.

Coherent Optical Receiver for Linear Optical Phase Demodulation

Leif A. Johansson, Hsu-Feng Chou, Anand Ramaswamy, Jonathan Klamkin,
Larry A. Coldren, Mark Rodwell and John E. Bowers.

Electrical and Computer Engineering Department, University of California,
Santa Barbara, California 93106, USA.

Abstract — **A novel optical coherent receiver architecture for linear optical phase modulation is presented. A proof-of-concept demonstration has been performed using discrete components and at low frequency. High dynamic range has been confirmed at 3.13mA average photocurrent; 124.3 dBHz$^{2/3}$, corresponding to a 131.5 dBHz$^{2/3}$ if a shot-noise limited noise floor were achieved (here limited by low-frequency 1/f-type noise). Further, efforts to increase the operating frequency to the GHz region and beyond has been outlined in the efforts to develop compact, low latency integrated chip technology and the development of novel sampling downconversion receiver architectures.**

Index Terms — Optical phase locked loops, Optical communication, Integrated optoelectronics, Optical receivers.

I. INTRODUCTION

Optical modulator-based analog optical links has the potential for high performance. The combination of a high power, low noise optical source and a low Vπ modulator results in a link with gain and low noise figure [1,2]. The linearity of an intensity modulated, direct detection (IMDD) link has been limited by full and zero transmission, between which a linear transfer function is difficult to fit. At best the transfer function can be linearized. This can result in a large SFDR in 1 Hz bandwidth [3], however the high order dependence of intermodulation terms still limits the available linear modulation depth.

Up to date, most analog links have used IMDD. This despite the fact that other modulation formats may be more suited for high performance analog transmission. Phase modulation is not limited in modulation depth in the same way as intensity modulation, it is in practice limited by the drive signal that can be applied to the modulator. This leads to the availability of highly linear modulators such as LiNbO3 phase modulators, which predominantly relies on the linear electro-optic effect. Further, a higher signal-to-noise ratio (SNR) can be supported in a phase modulated link than is possible using intensity modulation. This can be understood in terms of a tradeoff between SNR and spectral width of modulated optical signal.

The main challenge in constructing a linear phase modulated optical link is the problem of how to linearly convert the optical phase into an electrical current. The conventional phase receiver mixes the phase modulated optical signal with an optical reference, producing a sinusoidal relation between photocurrent and optical phase, resulting in a link performance similar to that of a Mach-Zehnder modulated link [4]. In this work, we will show how a linear optical phase receiver can be built.

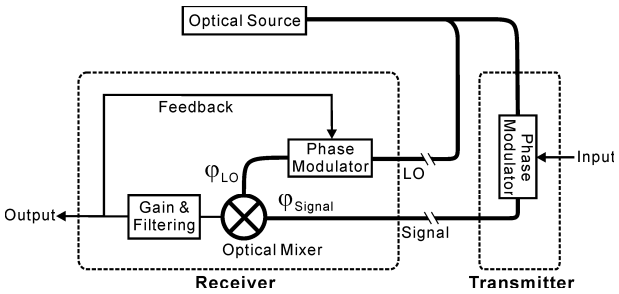

Fig. 1. Concept schematic of the proposed coherent receiver with feedback. Thick lines: optical link; thing lines: electrical link.

II. APPROACH

We are proposing a feedback receiver concept. The base function of the receiver is illustrated in Fig.1, above. Like in a conventional PM receiver, the received optical phase is mixed with an optical reference, producing a sinusoidal response to optical phase. The detected photocurrent is now amplified and fed back to a reference phase modulator. The received phase is now given by standard control theory:

$$\varphi_S - \varphi_{LO} = \frac{\varphi_S}{1+T} \tag{1}$$

Where φ_S and φ_{LO} are signal and reference optical phase, and T is the loop transmission gain. It can be observed that for high loop gain, the reference phase will closely track the received signal phase. Linear operation can be understood in two ways, the net detected phase gain will fall within the linear range of the sine transfer function of the optical mixing process, or using a linear reference phase modulator, or the driving signal must be linearly related to the received optical phase. It should be noted that the feedback reduces receiver noise sources just as much as net detected signal, such that the SNR remains unchanged when the loop is closed.

A common limitation in any feedback system is bandwidth limitations due to latency in the loop. The delay

will subtract a frequency dependent phase, and the loop bandwidth is limited by the requirement to keep the feedback phase away from -180° at unity loop gain to retain stability. To reach linear operation at 1 GHz, the loop bandwidth must approach 10 GHz, which require the loop delay to be in the 10-20ps range. This corresponds to only 3-6mm roundtrip path length in vacuum. For this reason fiber coupled components, or even $LiNbO_3$ based optics cannot be used. Only a very compact optical components material base, such as InP, can deliver this short latency.

Even using compact InP based technology, the high gain operating frequency of the receiver is limited to frequencies below 2GHz. To access higher RF frequencies, photonic RF downconversion is required. Simple photonic mixing, applying a sinusoidal modulation on the optical carrier converting the received RF signal to a detected IF signal, falling within the bandwidth of the loop, is a nonlinear process when closing the feedback loop. Instead, a pulsed optical source can be used where the pulse duration is short compared to the RF period, approximating an ideal sampling process. The baseband signal is then recovered by the integration in the loop.

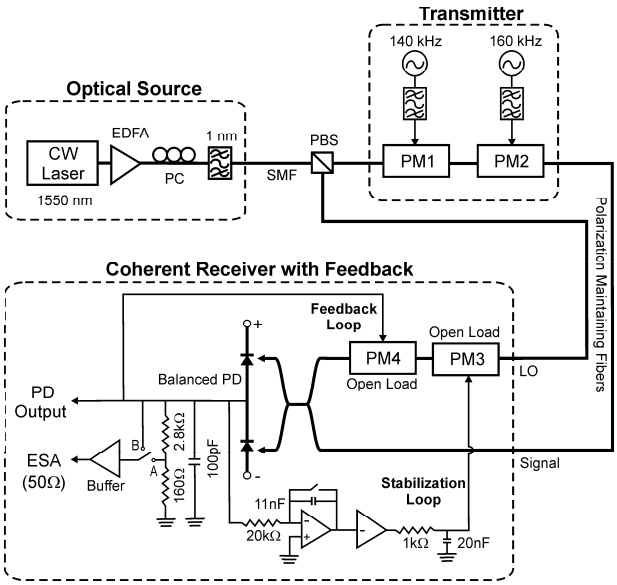

Fig. 2. Experimental setup. PC: polarization controller; SMF: single-mode fiber; PBS: polarization beam splitter; PM#: phase modulator; PD: photodetector; ESA: electrical spectrum analyzer

III. PROOF-OF-CONCEPT DEMONSTRATION

To demonstrate the feasibility and validity of the concept, a proof-of-principle demonstrator experiment has been built. This is built using fiber-coupled optical components with up to four order of magnitude longer path-length than the equivalent integrated parts. For this reason, the operating frequency is limited to the 100 kHz range. The experimental arrangement used is outlined in Fig. 2. A more detailed description of the experiment can be found in [5]. The output from the optical source is split into a signal and reference path using a polarization beam splitter and polarization maintaining fiber. A two-tone RF probe signal (140 and 160 kHz) is applied to the signal path using separate phase modulators. In the receiver signal and reference is mixed and photodetected. The output from the balanced detector pair is then directly connected to the reference modulator to provide the feedback path. The feedback gain and filter function is regulated by the detector load, converting photocurrent to modulator drive voltage.

The power of detected fundamental and intermodulation terms from the buffer output is plotted in Fig. 3 against the link input power. With the feedback path disabled, a SFDR of 104.5 $dBHz^{2/3}$ is obtained, limited by the sine response of the optical mixing. Closing the loop, a number of effects can be observed. First, we see that the detected power at the signal frequency is reduced as a result of the reduced net phase difference between signal and LO. However, as predicted the SNR remains unchanged as the noise floor is suppressed as much. The second effect is a dramatic reduction in intermodulation terms, appearing at 120 and 180 kHz. In fact, more than 20 dB increase in input drive power is required to generate detectable intermodulation terms. All in all, this translates in an improvement in SFDR of about 20 dB to 124.3 $dBHz^{2/3}$.

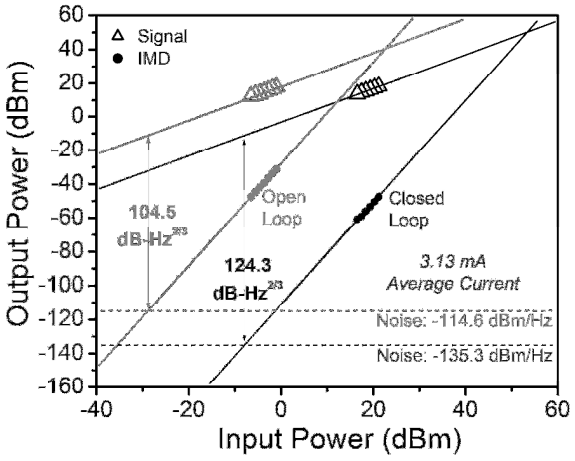

Fig.3. SFDR measurements at 3.13 mA of average photocurrent. Gray: open loop; Black: closed loop. IMD: 3rd-order intermodulation distortion.

The improvement is SFDR is dependent of the available loop transmission gain, T, and is proportional to $1/(T+1)^3$. Therefore, increasing the loop gain by increasing the optical power should show a strong effect on the dynamic range. This is also observed in Fig. 4, where the dynamic range increases to a peak value at 3.13mA of received photocurrent, after which the dynamic range degrades. This degradation can in part be attributed to nonlinearities of the photodetectors. These are terminated by a high impedance to provide the full voltage swing to the reference modulator (4.4V V_π).

At several mA of photocurrent, shot-noise dominates over thermal noise, representing the theoretical limit of noise level. As a consequence of operating at these low frequencies, shot noise limited operation has not been reached due to *1/f*-type noise contributions from the optical source, etc. The currently measured noise levels are approximately 10 dB above the theoretical shot noise level, leading to about 6.7 dB penalty in SFDR, as indicated in Fig. 4. In a system operating at higher frequencies, shot noise limited operation should be available, particularly in this configuration where both laser intensity and phase noise is being cancelled when the signal and reference paths are matched. The projected shot noise limited performance corresponds to 131.5 dB·Hz$^{2/3}$ at 3.13 mA.

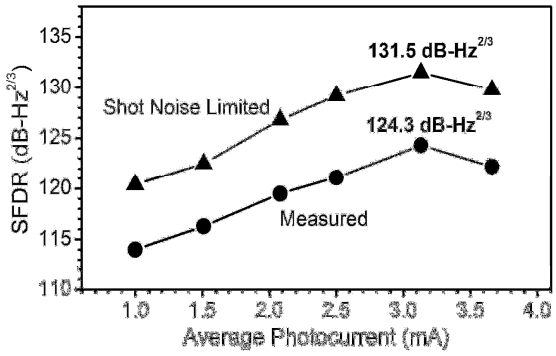

Fig. 4. SFDR with measured and shot-noise-limited noise levels for the closed loop case.

The sampling downconversion receiver approach has been demonstrated using the proof-of-principle demonstration outlined above in section III. For this demonstration, the received IF signal remained 140 and 160 kHz, while the received RF frequency was 110 MHz. Similar effects can be observed as for the baseband loop; closing the loop simultaneously reduces the noise floor, the signal and the intermodulation terms in a manner that increases the SDFR by 14 dB, from 85.9 dBHz$^{2/3}$ to 100 dBHz$^{2/3}$. The reduced dynamic range can mainly be attributed to increased noise of the amplified Mach-Zehnder based pulsed source used.

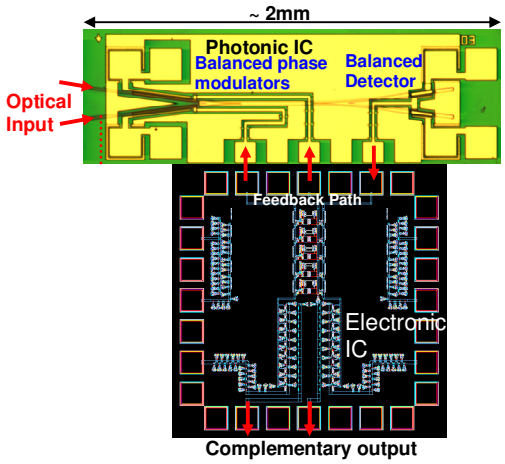

Fig. 5. Low-latency feedback receiver arrangement for linear demodulation of microwave phase-modulated optical links, showing electronic and photonic ICs.

IV. INTEGRATED RECEIVER DEVELOPMENT

The proof-of concept demonstration was performed at frequencies in the 100 kHz region, limited by the delay of the discrete components used in the feedback receiver. To reach an operating frequency of 1-2GHz, a low latency (10-25ps) receiver must be built. Figure 5 shows a current effort to realize this, based on close integration of an electronic integrated circuit, shown in schematic form and a photonic integrated circuit shown as a photograph. The photonic IC consists of a balanced detector pair, a coupler and optical phase modulators in a balanced configuration. The electronic chip is fundamentally a transimpedance amplifier, converting the differential output current from the detectors to modulator drive voltage. Additionally, it provides stability adding loop filtering and a buffer function for the output signal.

As the received photocurrent increases, lower amplifier transimpedance is required to provide feedback in the phase-lock loop. In fact, for sufficiently high photocurrent the modulator impedance can be tailored to provide adequate filtering and stable phase feedback, forming a feedback path on a single chip. The electronic IC is still needed to provide a buffered output.

To fully take advantage of the potential performance of a phase-modulated optical link, stringent performance requirements for modulator and detector performance must be met. In the proof-of-concept demonstration above, the obtained dynamic range was limited by the amount of photocurrent that could be detected without degradation, 3.13mA per detector at peak dynamic range. It is predicted that if this number can be increased to 100mA, potentially 90dB SFDR in 500MHz noise bandwidth should be available. Although, to support this performance, the output IP3 of a single detector must be higher than 50 dBm at this photocurrent.

A second critical performance requirement is the linearity of the phase modulators. While the closed-loop operation suppresses nonlinearities from the optical interferometer as well as of the amplifier, any nonlinear response of the phase modulator will remain. Since the feedback loop will force the reference phase to closely track the signal phase, a nonlinear phase modulator will consequently be modulated by a nonlinear drive signal. Using LiNbO3 modulators, this is not a limiting problem. However, Stark effect InP phase modulators predominantly rely on the more efficient quadratic electro-optic effect. The high efficiency leads to very short modulator structures and low latency, but the linearity of a single modulator will limit the available receiver performance.

An improved modulator configuration is obtained by placing two phase modulators, one in the signal arm and one in the LO arm, in a push-pull configuration. These are now driven in antiphase. The compound response is now given by:

$$\varphi_m = \varphi_1(v_m) - \varphi_2(-v_m) = \sum_n a_n v_m^n - \sum_n a_n (-v_m)^n = \\ = \sum_{n'} 2a_{2n'+1} v_m^{2n'+1} \quad (2)$$

Where φ_m and v_m is the modulation phase and drive voltage and a_n are the Taylor expansion terms around the modulator bias point. It is seen that the quadratic term along with any higher even order terms are cancelled using this configuration. A second beneficial effect is that the amplitude modulation from the phase modulators is to a first order approximation cancelled using the balanced modulator approach.

VII. SUMMARY

The continuing work to realize a linear optical phase demodulating receiver has been summarized. It is shown that the feedback receiver concept not only allows the analog link designer to take advantage of the existence of linear optical phase modulators to generate highly linear optical links, it also supports optical links where the available signal to noise ratio exceeds what is possible using standard intensity modulation links.

A proof-of-concept demonstration has been performed using discrete components and at low frequency. High dynamic range has been confirmed at 3.13mA average photocurrent; 124.3 $dBHz^{2/3}$, corresponding to a 131.5 $dBHz^{2/3}$ if a shot-noise limited noise floor were achieved (here limited by low-frequency 1/f-type noise).

Further, efforts to increase the operating frequency to the GHz region and beyond has been outlined in the efforts to develop compact, low latency integrated chip technology and the development of novel sampling downconversion receiver architectures.

ACKNOWLEDGEMENT

The authors wish to acknowledge support of the DARPA/MTO PHORFRONT program.

REFERENCES

[1] E. Ackerman, C. Cox, G. Betts, H. Roussell, K. Ray, and F. O'Donnell, "Input impedance conditions for minimizing the noise figure of an analog optical link," in IEEE MTT-S Int. Microw. Symp. Dig., Denver, CO, 1997, pp. 237–240.

[2] E. Ackerman, G. Betts, W. Burns, J. Prince, M. Regan, H. Roussell, and C. Cox, "Low noise figure, wide bandwidth analog optical link," in Proc. IEEE Int. Microw. Photon. Top. Meeting, Seoul, Korea, 2005, pp. 325–328.

[3] Y. Zhuang, W. Chang, and P. Yu, "Peripheral-coupled-waveguide MQW electroabsorption modulator for near transparency and high spurious free dynamic range RF fiber-optic link," IEEE Photon. Technol. Lett., vol. 16, no. 9, pp. 2033–2035, Sep. 2004.

[4] Frank Bucholtz, Vincent J. Urick, Matthew S. Rogge, Keith J. Williams, "Performance of Analog Photonic Links Employing Phase Modulation, Proc. OSA topical meeting in Coherent Optical Technologies and Applications (COTA), paper CFA6, Whistler, BC, 2006.

[5] Hsu-Feng Chou, Anand Ramaswamy, Darko Zibar, Leif A. Johansson, John E. Bowers, Mark Rodwell, and Larry A. Coldren,," High-Linearity Coherent Receiver with Feedback," Submitted to IEEE Photonics Technol. Lett.

Analysis of Sampled Optical Phase-Lock Loops

Leif A. Johansson, Darko Zibar*, Anand Ramaswamy, Larry Coldren, Mark Rodwell and John E. Bowers.
Electrical and Computer Engineering Department
University of California, Santa Barbara
Santa Barbara, USA.
Email: leif@ece.ucsb.edu
*Now at Research Center COM, Technical University of Denmark

***Abstract*—Sampled optical phase-lock loops are analyzed using the Z-transform. It is found that the finite sampling rate will result in an effective delay limiting the available stable gain of the loop. The analysis is applied to three example applications, optical wavelength synthesis from a pulsed reference, linear phase-tracking receivers and coherent optical receivers.**

I. INTRODUCTION

Optical Phase-Lock Loops (OPLLs) are used in a range of applications including carrier recovery in coherent optical receivers [1], wavelength synthesis from an optical frequency comb reference [2], offset locking for RF or THz frequency synthesis [3], synchronization of laser arrays [4] or linear phase demodulation in analog optical links [5]. For many of these applications, standard PLL control theories using the Laplace-transform to evaluate closed-loop behavior provide an accurate description of loop stability and performance [6].

In a sampled OPLL the phase information is obtained in discrete measurements. It is difficult to generate a rigorous analysis including the effect of sampling rate using standard Laplace-transform PLL theory. Instead the Z-transform, commonly used for analysis of sampled data systems [7] generates a much fuller model of these systems. In this paper the Z-transform is applied to sampled OPLLs and the relation between laser linewidth, loop delay and sampling rate are derived. Applications where this analysis apply include comb line selection by locking to a pulsed reference, phase locking in sampling downconversion optical systems and coherent phase-locked receivers where phase marker bits are used for LO laser synchronization.

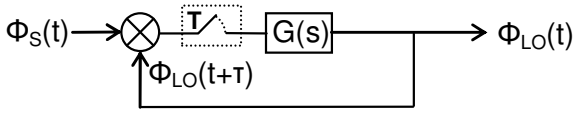

Figure 1. Basic operational schematic of the optical phase-lock loop.

This research is supported by the DARPA PHOR-FRONT program under United States Air Force contract number FA8750-05-C-0265.

II. THEORY

The basic operation of an optical phase-lock loop is illustrated by the schematic in Fig. 1. This illustrates a loop in which the LO laser phase forms the output signal. The open-loop transmission, *G(s)*, is given by the phase detection gain, the loop filter function and the LO laser tuning efficiency. A first order loop gain function contains one integration, typically within the frequency tuning of the LO laser. The loop transmission can be reduced to:

$$G(s) = is_0 \cdot e^{-s\tau} / s \tag{1}$$

where s_0 represents to the unity-gain frequency. The $e^{-s\tau}$ term accounts for the feedback group delay, τ. A second order loop contains a second integration and the loop transfer function can be expressed by:

$$G(s) = \frac{-s_n^2\left(1-2i\xi\, s/s_n\right)\cdot e^{-s\tau}}{s^2} \tag{2}$$

s_n corresponds here to the natural frequency and ξ is the loop damping factor. In standard OPLL theory, no sampling occurs, as represented by a closed gate in Fig. 1. The output phase, φ_{LO} is then related to the input phase, φ_S as:

$$\varphi_{LO} = \frac{G(s)}{1+G(s)}\varphi_S \tag{3}$$

Loop stability is ensured by keeping open loop gain below unity at the frequency where the phase crosses -180° due to the delay term.

We can use the modified Z-transform of eq. 1 and eq. 2 to evaluate a sampled loop with delay [7]. The first order loop transmission is then expressed as:

$$G(Z) = \frac{-iS_0T}{Z^n(Z-1)} \tag{4}$$

and the second order loop:

$$G(Z) = \frac{-S_n^2T^2}{Z^n(Z-1)^2}\left[1+(Z-1)\left(\frac{\tau_d}{T}+\frac{2i\xi}{S_nT}\right)\right] \tag{5}$$

Z is the Z-transform variable given by $Z(f) = exp(2\pi ifT)$ where T is the sampling period. It can be observed that the effect of delay in the loop is expressed differently than for a standard OPLL. The delay is here expressed in the form $\tau=nT+\tau_d$ where the integer number of periods in the loop have the largest impact on loop behavior. Again, the output phase, φ_{LO} is then related to the input phase, φ_S as:

$$\varphi_{LO} = \frac{G(Z)}{1+G(Z)}\varphi_S \tag{6}$$

The validity of the sampled model is confirmed by increasing the sampling rate and a convergence between the sampled and baseband OPLL performance is observed (Fig. 2). At higher sampling rates, a close correlation to the continuous loop response is seen at lower frequencies. As the frequency increases, the sampled loop gain finds a minimum at $f=1/2T$ before it starts to increase to reach a maximum at $f=1/T$. This can be understood in terms of Nyquist sampling where the relation $G(f) = G(f+1/T)$ should be valid.

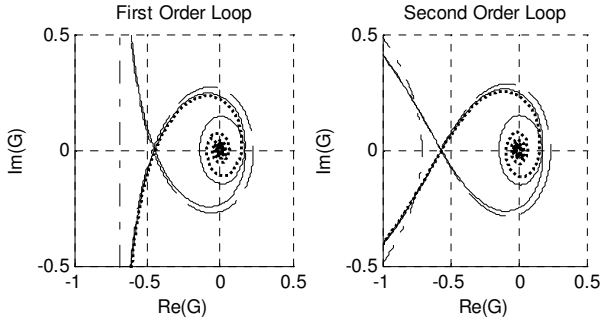

Figure 2. Nyquist diagram for first and second order loop gain function for non-sampled operation (dotted line), pulse period; T = 2τ (dash-dot line), T = 2τ/3 (dashed line) and T = 2τ/5 (solid line).

III. Application Examples

The above analysis can be applied to a number of applications for a sampled OPLL for analysis not readily available using standard Laplace theory. Examples include phase-locking to a pulsed reference, sampling downconversion systems and coherent receivers utilizing phase marker bits. In the following, a second order loop with critical loop damping ($\xi = 1/\sqrt{2}$) and 10 dB loop gain margin for stability will be assumed.

A. *Phase Locking to a Pulsed Reference*

Carrier-envelope locked femtosecond frequency combs provide a highly stable optical frequency reference [2]. By phase-locking a laser to any of the comb lines, a stable optical frequency synthesis system is formed. The accuracy to which this can be achieved is dependent on the pulse repetition rate. The phase information obtained from comparing the local oscillator (LO) laser phase to that of a first pulse is used to tune the LO phase to match the phase of a second pulse. This generates an effective delay in the loop corresponding to the pulse period, with the attributed feedback gain restrictions to maintain stability.

The total phase error variance is calculated by:

$$\sigma^2 = \int \frac{d\nu}{2\pi f^2}\left|\frac{1}{1+G(Z(f))}\right|^2 df \tag{7}$$

where $d\nu$ is the linewidth of the beat term between reference and LO laser, here equal to that of the LO laser assuming that the phase jitter of the pulsed laser is negligible. For clarity, a Lorentzian linewidth has been assumed here. More elaborate linewidth models can also be used in the above formula.

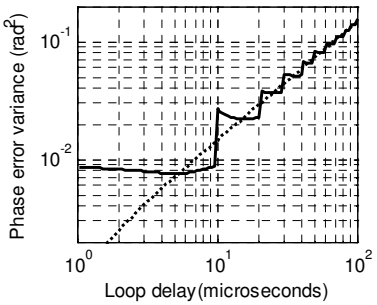

Figure 3. Integrated phase error variance versus loop delay for standard (dotted line) and sampled (solid line) OPLL. 1kHz laser linewidth and 1 MHz sampling rate is assumed.

Figure 3 shows the integrated phase error variance for a 1-kHz linewidth laser versus delay in the feedback loop, both for a standard OPLL and with 1 MHz sampling rate. At long delays the sampled loop performance approaches that of the standard loop. At very low delays, the sampled loop performance is determined by the effective delay introduced by the sampling rate, where further decrease in physical loop delay does not translate into improved performance. Figure 4 illustrates this point by showing the integrated phase noise as a function of the ratio of pulse frequency and LO laser linewidth. If a 1-MHz repetition rate is assumed, it is seen that a 1-kHz linewidth laser will result in a 0.01 rad^2 integrated phase error variance, even a high-quality 1-Hz linewidth will generate a modest 10^{-5} rad^2 variance. This illustrates a difficulty in transferring a highly stable pulsed optical reference to a highly stable CW optical frequency.

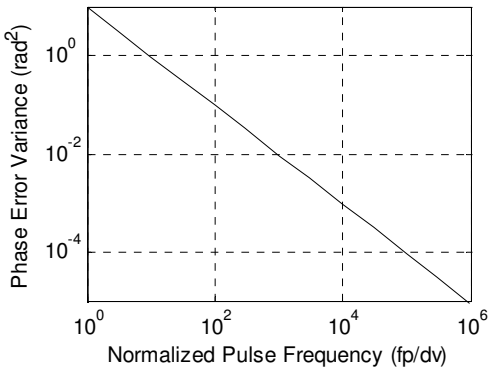

Figure 4. Integrated phase error variance versus laser linewidth normalized by pulse repetition rate for phase locking to a pulsed reference.

B. Downsampling OPLL receiver

Optical phase-tracking loops can be used to generate linear optical phase demodulation, as outlined in Fig. 5 [5]. The tracking phase is related to input phase by the loop gain in eq. 3. If a linear reference modulator is used to track the phase of an incoming optical signal, the reference drive voltage is also linearly related to the input phase if the gain is high. The delay in the tracking loop will limit the stable loop gain as the signal frequency increases, as shown by the baseband trace in Fig. 4. A compact tracking loop with 20 ps latency is assumed, similar to [8].

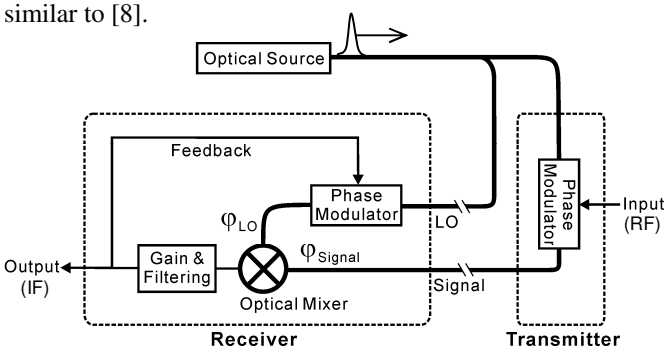

Figure 5. Concept schematic of linear coherent receiver with feedback [5]. Thick lines: optical link; thin lines: electrical link.

One method to extend the frequency range of this receiver is to use optical downconversion of a received RF signal to IF within the bandwidth of the tracking loop. It has been shown that to preserve linearity in the tracking loop, a pulsed optical signal must be used [9]. The reference modulator now tracks the downsampled received signal with a phase given by eq. 6. The available loop gain as a function of input signal frequency is shown in Fig. 6 assuming downsampling to 500 MHz. It is found that this type of receiver has the highest performance in baseband operation below 1 GHz or sampled above 10 GHz. The flattening in the frequency dependence of the sampled gain at higher frequencies represents the transition between latency limited by pulse rate and limited by physical delay in the loop.

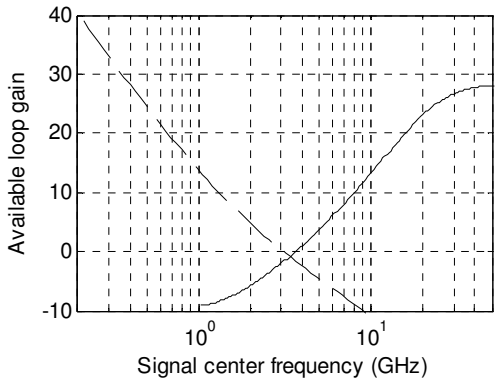

Figure 6. Available feedback gain in a linear tracking optical phase lock loop demodulator. The dashed line represents available stable feedback gain versus frequency of baseband tracking using a CW optical carrier. The solid line represents available stable feedback gain using a pulsed optical carrier and downconverting to 500 MHz.

C. Coherent Receiver

This analysis is well suited for the analysis of certain types of optical phase-lock loop receivers. The phase error variance of the LO laser can be expressed by:

$$\sigma^2 = \int \frac{d\nu}{2\pi f^2}\left|\frac{1}{1+G(f)}\right|^2 + \frac{q(P_S+P_{LO})}{2RP_{LO}P_S}\left|\frac{G(f)}{1+G(f)}\right|^2 df \quad (8)$$

The second term in the integration is the phase noise resulting from conversion of receiver shot-noise which can be significant at low power. It has been shown that the loop bandwidth is in fact a tradeoff between the need for phase tracking and the requirement to filter shot-noise [10]. Figure 7, thin solid line shows an example where this is observed. Even though here the loop delay is assumed to be negligible, the optimum natural frequency, f_n of the loop is limited to ~100 MHz assuming a 100 kHz beat linewidth and 100 photons per bit at 10 Gbps. In a sampled loop, where the phase sample from one bit is integrated and used to track the phase of the following bit, as shown by the thick solid trace in Fig. 7, the loop becomes unstable at f_n > 2.2 GHz due to the added effective delay.

For more complex modulation formats such as n-QAM, the carrier phase is not easily recovered. One option is to use designated phase marker bits for LO laser synchronization, in effect representing a sampled feedback loop with reduced sampling rate. The dot-dash, dashed and dotted thick traces in Fig. 7 shows a sampling rate of every 3rd, 10th and 30th bit, respectively. Two effects are observed from the reduced sampling rate: the loop oscillation is pushed to lower frequencies and the signal-to-noise ratio is reduced, as less received power is used to synchronize the phase. The penalty is higher than predicted from the equivalent reduction in SNR using standard non-sampled theory (thin lines) as a result of instabilities introduced in the loop.

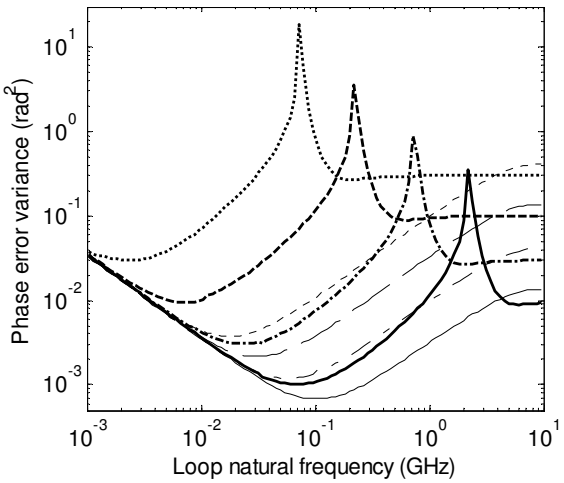

Figure 7. Integrated phase error variance versus laser linewidth normalized by pulse repetition rate for phase locking to a pulsed reference (thick lines). The solid line represents sampling every bit, dot-dash every 3rd, dashed every 10th and dotted every 30th. Comparative curves using standard Laplace theory are also included (thin lines).

Taking these plots as an illustrative example, we see that we require every 3rd bit to carry the phase information to reach a phase-noise limited BER of 10^{-9} for 16-QAM modulation ($\sigma^2 \approx$ 2.7e-3 rad^2). To require every 10th bit to carry the phase information while retaining the same phase error, we will need to reduce the linewidth from 100 kHz to 10 kHz.

IV. Conclusion

With the application of the Z-transform to optical phase-lock loop a range of applications with a sampled discrete feedback signal can be analyzed. It is found that the sampled feedback signal is attributed with an effective delay term that limits the available stable gain in such system. Examples include phase locking to a pulsed reference where the finite pulse rate fundamentally limits the ability to correlate the locked phase to that of the pulsed reference. A second example is in linear optical phase demodulation where a feedback receiver structure is used. Using a pulsed optical carrier, the received RF is downconverted to fall in the loop bandwidth. It is found that the best performance is obtained at a high RF to IF ratio. The last example involves a phase-locked coherent receiver where the phase of received signal and LO laser are synchronized using phase marker bits at regular intervals. It is found that instabilities introduced in the loop from reduced sampling rate degrade performance more than a simple SNR analysis would suggest.

Acknowledgment

The authors would like to thank Larry Lembo, Roy Smith, Peter Ly, Steve Pappert and Jim Hunter for helpful discussions.

References

[1] J.M. Kahn, "BPSK homodyne detection experiment using balanced optical phase-locked loop with quantized feedback," IEEE Photonics Technology Letters, Volume 2, Issue 11, Pages 840 - 843, Nov. 1990.

[2] David J. Jones, Scott A. Diddams, Jinendra K. Ranka, Andrew Stentz, Robert S. Windeler, John L. Hall and Steven T. Cundiff, "Carrier-Envelope Phase Control of Femtosecond Mode-Locked Lasers and Direct Optical Frequency Synthesis," Science, Vol. 288. no. 5466, Pages 635 - 639, 28 April 2000.

[3] A.J. Seeds, C.C. Renaud, M. Pantouvaki, M. Robertson, I. Lealman, D. Rogers, R. Firth, P.J. Cannard, R. Moore, R. Gwilliam, "Photonic synthesis of THz signals," Proc. 36th European Microwave Conference, 2006. Pages 1107 - 1110, Sept. 2006.

[4] Wei Liang, Amnon Yariv, Anthony Kewitsch and George Rakuljic, "Coherent combining of the output of two semiconductor lasers using optical phase-lock loops," Optics Letters, Vol. 32, No. 4, Pages 370 - 372, February 15, 2007.

[5] Hsu-Feng Chou, A. Ramaswamy, D. Zibar, L.A. Johansson, J.E. Bowers, M. Rodwell, and L.A. Coldren, "SFDR Improvement of a Coherent Receiver Using Feedback," OSA topical meeting of Coherent Optical Techniques and Applications (COTA), Whistler, BC, 2006. CFA3.

[6] M. Ohtsu, "Highly coherent semiconductor lasers," Artech House Ltd, Norwood, MA, 1992.

[7] E. I. Jury, "Sampled-Data Control Systems," Whiley and Sons, Inc. New York, 1958.

[8] Anand Ramaswamy, Leif A. Johansson, Jonathan Klamkin, Colin Sheldon, Hsu-Feng Chou, Mark J. Rodwell, Larry A. Coldren, John E. Bowers, "Coherent Receiver Based on a Broadband Optical Phase-Lock Loop," Optical Fiber Communications Conference. (OFC). Postdeadline Technical Digest. Opt Soc. America. PDP3, 2007.

[9] Darko Zibar, Leif A. Johansson, Hsu-Feng Chou, Anand Ramaswamy, Mark Rodwell, and John E. Bowers, "Novel Optical Phase Demodulator Based on a Sampling Phase-Locked Loop," IEEE Photonic Technology Letters, Vol. 19, no. 9. Pages 686 - 688, 2007.

[10] L. Kazovsky, "Decision-driven phase-locked loop for optical homodyne receivers: Performance analysis and laser linewidth requirements," Journal of Lightwave Technology, Volume 3, Issue 6, Pages 1238 - 1247, Dec 1985.

Linear Coherent Receiver based on a Broadband and Sampling Optical Phase-Locked Loop

John E. Bowers, Anand Ramaswamy, Leif A. Johansson, Jonathan Klamkin, Larry A. Coldren and Mark J. Rodwell
Electrical and Computer Engineering Department
University of California, Santa Barbara
Santa Barbara, U.S.A
bowers@ece.ucsb.edu

***Abstract*—A novel coherent receiver for linear optical phase demodulation is proposed. The receiver, based on a broadband optical phase-lock loop is demonstrated to have a bandwidth of 1.45 GHz. Using the receiver in an analog link experiment, a spurious free dynamic range of 125dBHz$^{2/3}$ is measured at 300 MHz. Further, theoretical investigations are presented demonstrating receiver operation at high frequencies (>2GHz) using a sampling phase –locked loop.**

I. INTRODUCTION

Optical Phase-Lock Loops (OPLL) have diverse applications in future communication systems. They can be used in high sensitivity homodyne PSK receivers for phase noise reduction, provided sufficient loop bandwidth is maintained. Alternate phase lock loop applications include coherent synchronization of laser arrays [1] and frequency synthesis by offset locking [2].

In this work, a broadband optical phase lock loop is utilized in a coherent receiver for the linear demodulation of analog-phase modulated optical links. Demanding military communications require linear links with high dynamic range. Traditionally, linearity improvements in analog optical links have been focused on intensity modulated / direct detection (IMDD) links, with the addition of coherent and incoherent optical FM techniques. However, the performance of such links is constrained by the modulation depth (between 0 and 100%) and non-linear response of intensity modulators. Phase modulators, on the other hand, have no inherent limitation to their modulation depth and can be swung over many π. Hence, they result in improved SNR and have the potential to be utilized in high performance analog links. However, the challenge of constructing such a high linearity link resides in the receiver architecture. In standard interferometer based phase demodulation, a sinusoidal relation exists between the phase and detected current. This inherent non-linearity in the phase recovery process limits the available link dynamic range and consequently, the benefits of phase modulation are lost.

To overcome this problem, we proposed and demonstrated at low frequency, a novel coherent receiver with feedback that is capable of distortion suppression [3]. Subsequently, an integrated version of the receiver has been developed for operation at close to GHz frequencies [4].

In order to operate the receiver at frequencies greater than 2 GHz the baseband loop bandwidth has to be very large. For example, a loop operating at 20GHz requires a loop bandwidth >100 GHz [5]. This is impractical from the standpoint of overcoming physical delays in the feedback path as well as the challenge of designing electronics that operates beyond 100 GHz. Instead we have chosen to explore optical sampling as an alternate to baseband operation [6, 7]. The basic idea is to use a pulsed laser source at the receiver to down convert the received high frequency input RF signal to within the operating bandwidth of the receiver by sampling at a rate close to the pulse repetition rate of the laser source. Detailed numerical models that explore the feasibility of such systems have been developed [8].

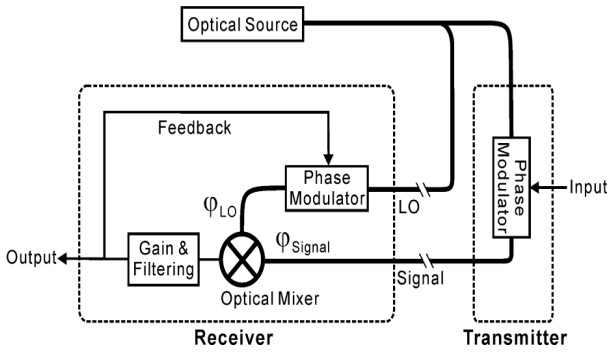

Figure 1. Concept of demonstrated coherent receiver with feedback. Thick lines: optical link; thin lines: electrical link

II. SYSTEM ARCHITECTURE

Figure 1 shows a schematic of the base receiver architecture. The received optical phase is mixed with an optical reference, producing a sinusoidal response to optical phase. The detected photocurrent is amplified and fed back to

This material is based upon work supported by the DARPA-PHOR-FRONT program under United States Air Force contract number FA8750-05-C-0265

a reference phase modulator. The received phase is now given by standard control theory:

$$\varphi_S - \varphi_{LO} = \frac{\varphi_S}{1+G} \quad (1)$$

Where φ_S and φ_{LO} are signal and reference optical phase, and G is the loop transmission gain. The reduction in the net detected phase results in the demodulator operating within its linear regime. Further, it should be noted that the feedback cannot discriminate between the detector shot noise and signal. As a consequence, the shot noise limited SNR remains unchanged despite the reduction in net phase.

The architecture of the receiver for sampled operation remains relatively unchanged. The only difference is that the c.w. optical source is replaced with a singled pulsed optical source in order to obtain an intermediate frequency (IF) component that falls within the bandwidth of the baseband phase demodulator.

III. INTEGRATED RECEIVER

To scale the operation of the receiver to microwave frequencies compact monolithic or hybrid integration of receiver elements is necessary for low loop latency. Our receiver consists of two integrated chips-one photonic and other electronic – mounted on a common microwave carrier. Figure 2 shows the photonic integrated circuit consisting of a balanced UTC photodetector [9], tracking phase modulators and a 2x2 MMI coupler. The receiver has the following features:

- Balanced (i.e. push-pull) modulator design that results in the cancellation of even order non-linearities and common-mode noise
- Exploitation of capacitances of photodiodes and modulators as circuit elements to perform the desired loop integrations in the feedback path.
- Electronic chip that enhances the phase margin of the system and also provides transconductance amplification to drive the modulators.

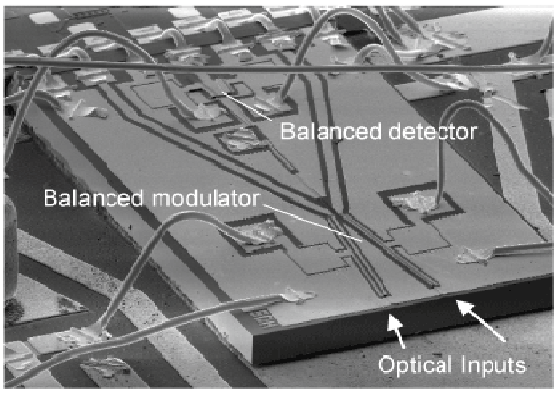

Figure 2. SEM of integrated Optoelectronic Receiver

IV. LINK DEMONSTRATION

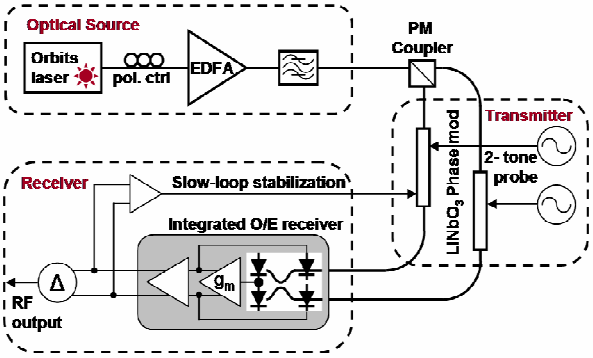

Figure 3. Schematic of Experimental Setup

The experimental setup is shown in Figure 3. The output of the optical source block is a high-power, amplified laser signal at 1537.40nm. The power emerging from the polarization maintaining (PM) coupler into the individual branches of the interferometer can be adjusted using the polarization controller. After the coupler, PM fiber and components are used for polarization management and stability.

Separate $LiNBO_3$ modulators are used in the transmitter block, in order to ensure that no mixing products are generated from the two-tone RF drive signal. A portion of the output signal from the receiver is tapped into a 'slow' feedback loop that generates a low frequency drive signal to one of the phase modulators for system stability against environmental drifts.

A. *Link Response*

The frequency response of the device for varying values of photocurrent is shown in Figure 4. The combination of high photocurrent and lower frequencies results in a sufficiently high loop transmission gain (G) such that the reference modulator is able to closely track the received signal phase. The optical link gain is now dependent on the ratio of drive voltage between source and reference modulator and in this link is -5dB.

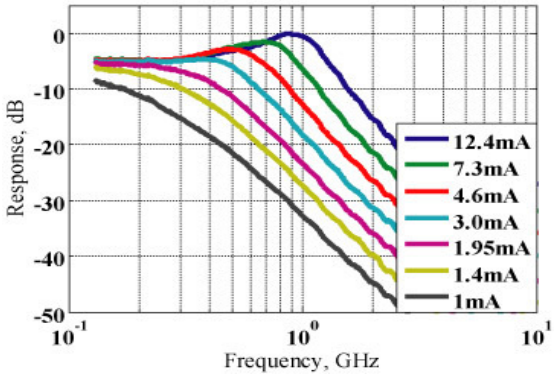

Figure 4. Link gain at different detected photocurrent values

At high frequencies or at low photocurrent values, loop transmission gain is low and hence, link gain is proportional to the photocurrent and loop filter transfer function as expected. The loop bandwidth, here defined by the 3dB point and approximately where the unity gain crosses over, is 1.45GHz at 12mA. The delay-limited bandwidth, within which the loop remains stable, is on the order of 4GHz.

B. *Spurious Free Dynamic Range (SFDR)*

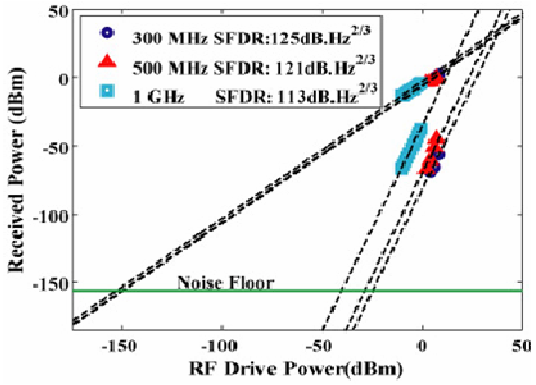

Figure 5. SFDR at different frequencies

Figure 5 shows SFDR data taken at 300 MHz, 500 MHz and 1 GHz. At 300 MHz, the high gain in the feedback loop results in enhanced linearity and consequently, an SFDR of 125dB.Hz$^{2/3}$ was measured. At higher frequencies, with reduced feedback (as seen in Figure 4), the SFDR degrades to the point where is there no reduction in net received phase. Consequently, the SFDR measured at 1GHz (113dB. Hz$^{2/3}$) with 12mA of photocurrent is close to the calculated shot noise limited SFDR at that frequency (116dB. Hz$^{2/3}$)

This is a fundamentally linear technique. However, further improvements in SFDR performance would require short feedback delay in order to sustain high, yet, stable loop gain at high frequency. Additionally, higher photocurrent in the detectors coupled with efficient, linear phase modulators will improve linearity performance of the receiver.

V. SAMPLING

In order to extend the frequency range of the receiver, the input RF signal has to be optically downconverted in order to fall within the bandwidth of the PLL. Standard optical downconversion for a balanced receiver involves using a frequency shifted optical reference tone, such that the frequency difference between one of the modulation sidebands and the RF signal is detected. However, in a phase modulated link, the signal, as obtained from the Bessel expansion, consists of several frequency components. Frequency shifting can access the information of only one of the tones and thus a severe limitation is placed on the linearity of the downconverted signal.

Optical sampling does not have this limitation. Using a pulsed laser source for signal and reference path, the input RF signal is sampled at a rate close to the RF period, and after detection, the resulting downconverted signal is obtained.

A. *Time Domain Analysis*

Previously, we reported a detailed time domain analysis of the baseband receiver operation [8]. The model has now been expanded to include sampled receiver operation as well [5]. The model suggests that to preserve linearity, a pulsed optical signal needs to be used. Moreover, by showing that the signal-to-intermodulation ratio (SIR) degrades with increased pulse width of the assumed Gaussian shape pulsed optical source, as shown in Fig. 6, it confirms that sampling induces extra non-linearities in the loop response. Further, by modeling the effect of loop gain on pulse width and taking into account the effective feedback delay of the sampled loop, it is found that for most efficient operation, very short pulses (<2ps) and high input signal frequencies are required [5].

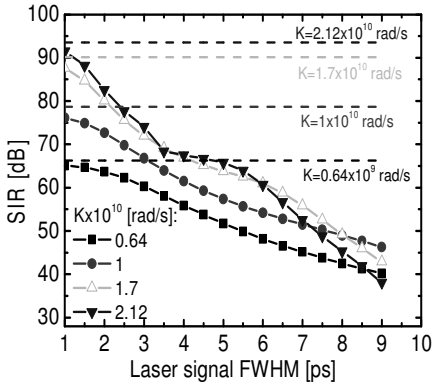

Figure 6. Signal to IR as a function of FWHM of the pulsed laser signal for selected values of the loop gain (K)

B. *Analysis Using Z-Transform Theory*

An elegant alternative to the computationally intense time domain model is to use Z transform theory for the analysis of sampled optical phase-lock loops [10]. In standard OPLL theory, the output phase and input phase are related thru equation 1. The Z-transform of the open loop transmission, G(Z), for a second order loop, taking into account delay is given as follows:

$$G(Z) = \frac{-S_n^2 T^2}{Z^n (Z-1)^2}\left[1 + (Z-1)\left(\frac{\tau_d}{T} + \frac{2i\xi}{S_n T}\right)\right] \qquad (2)$$

Here, Z is the Z transform variable and is given by $Z(f) = exp(2\pi ifT)$ where T is the sampling period. The delay, is expressed in the form $\tau = nT + \tau_d$ where the integer number of periods in the loop have the largest impact on loop behavior. The second term in the square bracket determines loop stability. It can be seen that increasing pulse period will decrease stability. Assuming a second order loop, a critical loop damping factor ($\xi = 1/\sqrt{2}$) and a loop natural frequency, f_n $(=s_n/2\pi i)$ adjusted to 10 dB loop gain margin for stability, we apply the Z-transform technique to the sampled receiver. Figure 7 shows the available stable loop gain as a function of input signal frequency assuming downsampling to 500 MHz. It is interesting to note that model predicts superior baseband performance below 1 GHz or sampled performance above 10GHz. The sampled gain does not vary with frequency at

high frequencies and is a consequence of a transition from latency limited by pulse repetition rate to latency limited by physical delay in the feedback path.

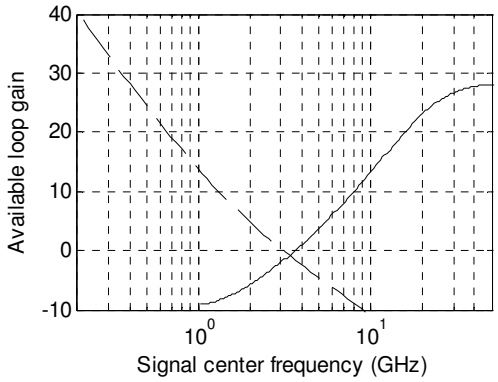

Figure 7. Available feedback gain in a linear tracking optical phase lock loop demodulator. The dashed line represents available stable feedback gain versus frequency of baseband tracking using a CW optical carrier. The solid line represents available stable feedback gain using a pulsed optical carrier and downconverting to 500 MHz.

VI. CONCLUSION

In this paper we have described and experimentally demonstrated the baseband operation of a novel coherent integrated receiver that is based on a broadband optical phase lock loop. We have shown that the receiver concept is a true linear technique, not realized by linearization or distortion cancellation and as such has the potential for high dynamic range. A loop bandwidth of 1.45 GHz and SFDR of 125dB.$Hz^{2/3}$ corresponding to 66dB in 500 MHz is reported. Additionally, we report an extremely low link loss: -5dB at low frequencies, when the loop is closed and the reference phase modulator is closely tracking the input signal phase.

We also explore the idea of porting the link to a much higher carrier frequency by using optical sampling. Two techniques 1) Time domain large signal model based on nonlinear differential equations and 2) Z transform theory; have been utilized to develop a comprehensive theoretical model of optical sampling in the context of the balanced receiver architecture. The results suggest that best performance is obtained at high RF to IF ratio. Put in another way, if the pulse widths of the pulsed optical source are shorter than 2ps and high input signal frequencies are used, the concept of optical sampling could become a practical reality for high-frequency analog optical links.

ACKNOWLEDGMENT

The authors would like to thank useful discussions with Larry Lembo, Steve Pappert and Jim Hunter. Further acknowledgment should be provided to Northrop Grumman Space Technologies for providing the electronic integrated circuit.

REFERENCES

[1] Wei Liang, Amnon Yariv, Anthony Kewitsch and George Rakuljic, "Coherent combining of the output of two semiconductor lasers using optical phase-lock loops," Optics Letters, Vol. 32, No. 4, Pages 370 - 372, February 15, 2007.

[2] U. Gliese, N.T. Nielsen, M. Bruun, E.L. Christensen, K.E. Stubkjaer, S. Lindgren and B. Broberg, "A wideband heterodyne optical phase-locked loop for generation of 3-18 GHz microwave carriers", IEEE Photon. Technol. Lett., vol. 4, pp. 936–938, 1992.

[3] Hsu-Feng Chou, A. Ramaswamy, D. Zibar, L.A. Johansson, J.E. Bowers, M. Rodwell, and L.A. Coldren, "SFDR Improvement of a Coherent Receiver Using Feedback," OSA topical meeting of Coherent Optical Techniques and Applications (COTA), Whistler, BC, 2006. CFA3.

[4] Anand Ramaswamy, Leif A. Johansson, Jonathan Klamkin, Colin Sheldon, Hsu-Feng Chou, Mark J. Rodwell, Larry A. Coldren, John E. Bowers, "Coherent Receiver Based on a Broadband Optical Phase-Lock Loop," Optical Fiber Communications Conference. (OFC). Postdeadline Technical Digest. Opt Soc. America. PDP3, 2007.

[5] Darko Zibar, Leif A. Johansson, Hsu-Feng Chou, Anand Ramaswamy, Mark Rodwell, and John E. Bowers, "Novel Optical Phase Demodulator Based on a Sampling Phase-Locked Loop," IEEE Photonic Technology Letters, Vol. 19, no. 9. Pages 686 - 688, 2007.

[6] Darko Zibar, Leif A. Johansson, Hsu-Feng Chou, Anand Ramaswamy, Mark Rodwell, and John E. Bowers, " Investigation of a Novel Optical Phase Demodulator Based on a Sampling Phase-Locked Loop," International Topical Meeting on Microwave Photonics (MWP '06), Grenoble, France, 2006.

[7] Hsu-Feng Chou, Leif A. Johansson, Darko Zibar, Anand Ramaswamy, Mark Rodwell, and John E. Bowers, " All-Optical Coherent Receiver with Feedback and Sampling," International Topical Meeting on Microwave Photonics (MWP '06), Grenoble, France, 2006.

[8] D. Zibar, L.A. Johansson, H.F. Chou, A. Ramaswamy, and J.E. Bowers, " Time domain analysis of a novel phase-locked coherent optical demodulator," OSA topical meeting of Coherent Optical Techniques and Applications (COTA), Whistler, BC, 2006. JWB1.

[9] J. Klamkin et al., "Monolithically Integrated Balanced Uni-Traveling-Carrier Photodiode with Tunable MMI Coupler for Microwave Photonic Circuits," Conference on Optoelectronic and Microelectronic Materials and Devices (COMMAD), Perth, Australia. Dec. 2006.

[10] Leif A. Johansson, Darko Zibar, Anand Ramaswamy, Larry Coldren, Mark Rodwell and John E. Bowers, " Analysis of Sampled Optical Phase-Lock Loops," submitted to MWP'07.

Uni-Traveling-Carrier Photodiodes with Increased Output Response and Low Intermodulation Distortion

Jonathan Klamkin[1], Anand Ramaswamy[2], Yu-Chia Chang[2], Leif A. Johansson[2], Matthew M. Dummer[2], John E. Bowers[2], Steven P. DenBaars[1,2], Larry A. Coldren[1,2]
1. Materials Department, University of California, Santa Barbara, CA 93106 USA
2. Electrical and Computer Engineering Department, University of California, Santa Barbara, CA 93106 USA
Email: klamkin@engineering.ucsb.edu

***Abstract*— Waveguide uni-traveling-carrier photodiodes have been fabricated and tested to investigate the influence of the doping profile in several of the device layers on saturation characteristics and linearity. Two particular photodiode (PD) structures are discussed. Compared to PD A, PD B has a lower and more graded p-doping profile in the absorber layer and also a higher n-doping level in the collector layer. For PD B a higher field is induced in the absorber layer and the higher doping in the collector layer provides charge compensation. An enhancement in the response for PD B is observed with increasing photocurrent. At a frequency of 1 GHz the saturation current for PD A is 65 mA and that for PD B is 63 mA. The third-order intermodulation distortion was also measured at various photocurrent levels. For PD A, the third-order output intercept point (OIP3) for photocurrent levels of 10 mA, 20 mA, and 30 mA is 34.7 dBm, 38.6 dBm, and 35.8 dBm respectively. Those for PD B are 28.1 dBm, 41.0 dBm, and 37.2 dBm. These are all for a bias of -5 V. While PD A has a higher OIP3 at lower photocurrent levels, PD B is favorable for high current operation.**

I. Introduction

To improve signal-to-noise ratio and spur-free dynamic range in analog fiber-optic links, a novel coherent receiver architecture has been proposed requiring photodetectors that have high saturation current and high linearity at GHz frequencies [1]. The uni-traveling-carrier photodiode (UTC-PD) demonstrates both high speed and high current operation [2]. In a UTC-PD light is absorbed in an undepleted p-type narrow bandgap layer (absorber) and photogenerated electrons subsequently diffuse to a wide bandgap drift layer (collector). Because electrons are the only active carriers and electrons have a higher drift velocity than holes, space charge saturation effects should be reduced when compared to a traditional PIN photodiode (PD). Several techniques for improving the performance of UTC-PDs have been demonstrated. Charge compensation was used to improve the saturation current by intentionally n-doping the collector layer [3]. By doing so, the electric field is preconditioned to be higher in the presence of a large mobile space charge density. Others have reported an enhancement in the response of UTC-PDs that have a graded doping profile in the p-type absorber [4]. This grade results in a potential profile that can aid electron transport. This same effect was also observed for UTC-PDs with uniform but relatively lower absorber doping [5]. We previously reported waveguide UTC-PDs that demonstrated output saturation currents greater than 40 mA at 1 GHz and a third-order output intercept point (OIP3) of 43 dBm at 20 mA and 34 dBm at 40 mA [6]. Here we have closely investigated the effects of the doping profile in several layers of UTC-PDs on the output response, saturation current, and third-order intermodulation distortion (IMD3). In particular, two different waveguide UTC-PDs were fabricated and characterized. The most significant differences in these devices are the doping profiles within the absorber and collector layers. The devices are referred to as PD A and PD B. For PD A, the p-doping in the absorber layer is not only higher, but also more uniform. The n-doping in the collector layer is lower in PD A at around 7E15 cm^{-3} whereas for PD B it is around 6E16 cm^{-3}. For PD B an enhancement in the output response is observed at high current. This is believed to be due to the combination of the lower and more graded absorber doping profile as well as the higher collector doping level. The lower and more graded doping level in the absorber results in a small field induced at high current levels, and the higher collector doping level provides charge compensation. Both PDs exhibit very high saturation current levels that, to the best of our knowledge, are some of the highest reported for waveguide photodiodes at comparable frequencies. Due to the response enhancement with increasing photocurrent for PD B, the OIP3 increases with photocurrent more so than for PD A. Therefore PD B exhibits higher linearity at high photocurrent levels.

II. Device Design and Fabrication

The PD structures are grown directly above an InGaAsP optical waveguide. Passive regions are formed by selectively removing the PD layers. This is followed by a blanket InP cladding and InGaAs contact layer regrowth. The layer structure following regrowth is shown in Table 1. The p-doping level in the absorber and the n-doping level in the collector are denoted P and N respectively. The doping levels for those layers which are unintentionally doped are denoted UID. The n-InP field termination layer terminates the applied field across

TABLE I
UTC-PD LAYER STRUCTURE

Layer	Thickness (nm)	Doping (cm^{-3})
p-InGaAs contact	150	2E19
p-InP cladding	2,000	1E18
p-InGaAs absorber	**75**	**P**
InGaAs	8	UID
InGaAsP	16	UID
InP	6	UID
n-InP	7	1E18
n-InP collector	**200**	**N**
n-InP field termination	25	2E18

the collector layer of the PD in the photodetection regions and prevents depletion of the optical waveguide below. Light is coupled into the optical waveguide in a passive region and then absorbed as it passes through a photodetection region. Because of the spatial separation of the absorber layer in the UTC-PD structure and the peak of the incoming optical mode, carrier generation is distributed more uniformly along the length of the device. This as well as a wide input waveguide help to reduce front-end saturation. Of particular interest are the doping profiles in the absorber layer and collector layer. The absorber p-doping level was intended to be greater than 2E18 cm^{-3}. Zn, which is used as the p-dopant, diffuses readily during growth therefore the grading in the doping profile can vary. For PD B, the absorber peak doping level is around 25% lower than that for PD A, and the profile is more graded (high to low) toward the absorber/collector interface. The n-doping in the collector layer is also nearly an order of magnitude higher for PD B at around 6E16 cm^{-3}. This doping level is adequate for providing charge compensation. Devices were fabricated with various geometries. The results that follow are for devices that are 10 μm wide and 150 μm long.

III. RESULTS AND DISCUSSION

The electrical frequency response of the UTC-PDs was measured at various biases for photocurrent levels up to around 70 mA. Fig. 1 shows the normalized RF power as a function of DC photocurrent at 1 GHz for both devices. For PD A, the response is fairly constant with photocurrent until the onset of saturation. For PD B, there is a significant enhancement in the response with increasing photocurrent. This enhancement is due in part to a small field induced in the absorber at high photocurrent levels. The p-doping in the absorber of PD B is lower and more graded so this field should be greater in this device. The enhancement could also be due to the higher n-doping in the collector of PD B. This doping provides some charge compensation and preconditions the electric field for operation at high photocurrent levels. The saturation current, defined here as the photocurrent level where the RF response decreases by 1 dB, is around 65 mA for PD A and around 63 mA for PD B for biases of around -3.5 V. Because the device areas are large, the 3-dB bandwidth is RC-limited. Therefore any enhancement in the response should be attributed more so to improvements in the field distribution in the depletion region or the capacitance of the device rather than improvements

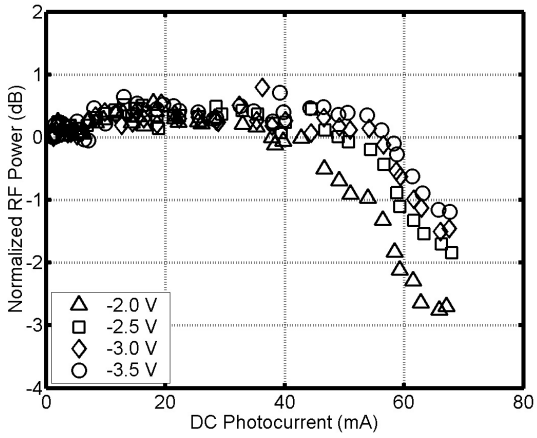

(a)

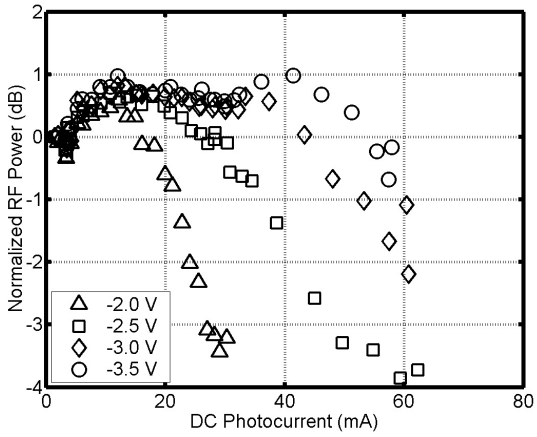

(b)

Fig. 1. Normalized RF power as a function of DC photocurrent at 1 GHz for (a) PD A and for (b) PD B.

in carrier transit time. The change in 3-dB bandwidth as a function of DC photocurrent level is shown in Fig. 2 for both PDs. At 1 mA the 3-dB bandwidth of PD A is 2.2 GHz and that for PD B is 1.6 GHz. As expected, there is a larger enhancement with increasing photocurrent for PD B. For this PD the 3-dB bandwidth is enhanced by as much as 40-50% whereas for PD A it is enhanced by at most around 30%. The saturation current was also extracted at 0.5 GHz and 2 GHz. For PD A, the saturation current at these frequencies is 67 mA and 62 mA respectively. For PD B it is 60 mA and 62 mA. To characterize the linearity of the PDs, a two-tone setup was used. Tones were generated at 1 GHz and 0.8 GHz. The output fundamental and IMD3 power were measured as a function of input modulation power at various photocurrent levels and biases. Fig. 3 shows the results of the IMD3 measurements at 10 mA and 20 mA for both UTC-PDs. For these measurements the bias for both devices was -5 V. For PD A, the measured OIP3 was 34.7 dBm and 38.6 dBm for photocurrent levels of 10 mA and 20 mA respectively. For PD B the OIP3 was 28.1 dBm and 41.0 dBm at the

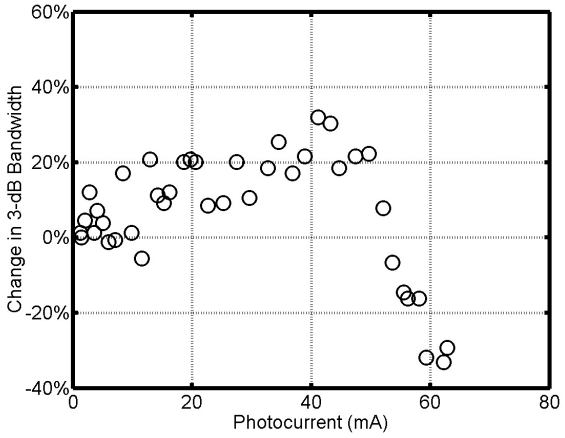

(a)

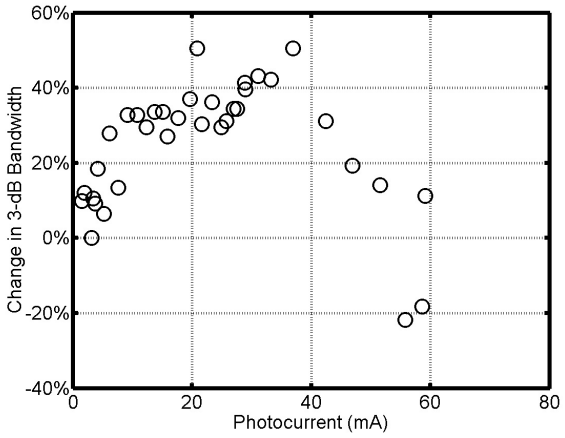

(b)

Fig. 2. Change in 3-dB bandwidth as a function of DC photocurrent for (a) PD A and for (b) PD B. The bias is -3.5 V for both devices.

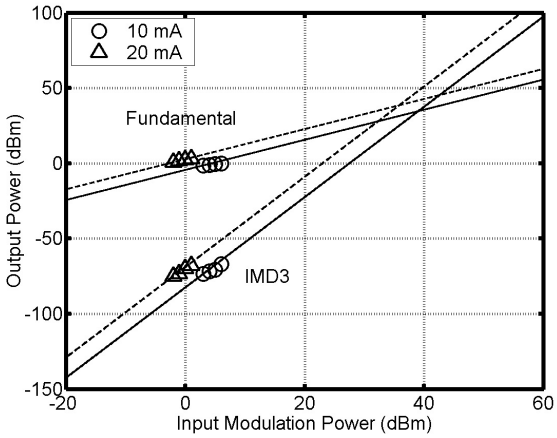

(a)

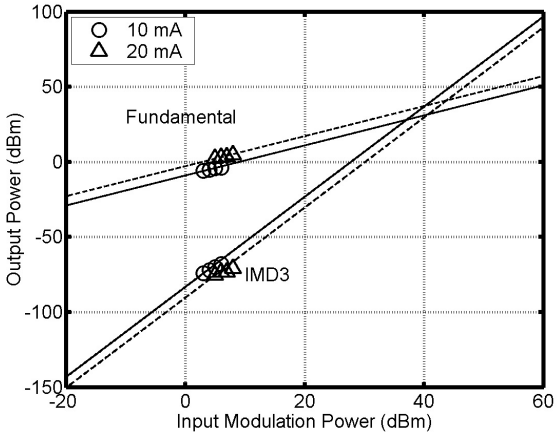

(b)

Fig. 3. IMD3 measurements at 10 mA and 20 mA for (a) PD A and for (b) PD B. The bias is -5 V for both devices.

same photocurrent levels. Although the OIP3 improves with increasing photocurrent for both devices, this improvement is far greater for PD B. Fig. 4 shows the IMD3 measurements for both devices at a photocurrent level of 30 mA and a bias of -5 V. The OIP3 at these conditions for PD A is 35.8 dBm and that for PD B is 37.2 dBm. The bias was kept constant at -5 V for these measurements to make a fair comparison. Increasing the bias improves the OIP3 for both PDs, however the maximum achievable OIP3 for photocurrent levels higher than 10 mA is greater for PD B. It appears that because of its enhanced response, this PD exhibits lower IMD3 at high photocurrent levels.

IV. Conclusions

We have fabricated and tested UTC-PDs with different absorber and collector layer doping profiles. An enhancement in the response is observed for PD B which has a lower and more graded absorber doping as well as a higher collector doping. These result in a higher induced field in the absorber layer and charge compensation respectively. Saturation currents of

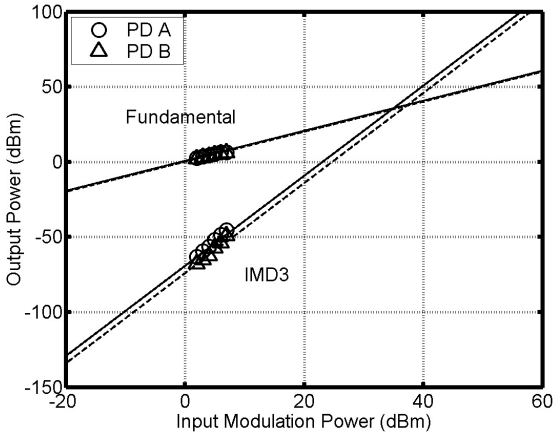

Fig. 4. IMD3 measurements at 30 mA for PD A and for PD B. The bias is -5 V for both devices.

65 mA for PD A and 63 mA for PD B are demonstrated. To the best of our knowledge these represent some of the highest saturation currents reported for waveguide PDs. IMD3 measurements were also performed to investigate the effects of the response enhancement observed for PD B on linearity. The OIP3 at photocurrent levels of 10 mA, 20 mA, and 30 mA was measured to be 34.7 dBm, 38.6 dBm, and 35.8 dBm for PD A and 28.1 dBm, 41.0 dBm, and 37.2 dBm for PD B. The linearity is better at high photocurrent levels for PD B therefore this PD is preferable for high current operation.

ACKNOWLEDGMENT

This research was supported by the DARPA PHOR-FRONT program under United States Air Force contract number FA8750-05-C-0265.

REFERENCES

[1] A. Ramaswamy, L. A. Johansson, J. Klamkin, C. Sheldon, H.-F. Chou, M. J. Rodwell, L. A. Coldren, and J. E. Bowers, "Coherent receiver based on a broadband optical phase-lock loop," in *OFC Postdeadline Papers*, 2007.

[2] T. Ishibashi, T. Furuta, H. Fushimi, S. Kodama, H. Ito, T. Nagatsuma, N. Shimizu, and Y. Miyamoto, "InP/InGaAs uni-traveling-carrier photodiodes," *IEICE Transactions on Electronics*, vol. E83-C, no. 6, pp. 938–949, June 2000.

[3] N. Li, X. Li, S. Demiguel, X. Zheng, J. C. Campbell, D. A. Tulchinsky, K. J. Williams, T. D. Isshiki, G. S. Kinsey, and R. Sudharsansan, "High-saturation-current charge-compensated InGaAs-InP uni-traveling-carrier photodiode," *IEEE Photonics Technology Letters*, vol. 16, no. 3, pp. 864–866, March 2004.

[4] N. Shimizu, N. Watanabe, T. Furuta, and T. Ishibashi, "InP-InGaAs uni-traveling-carrier photodiode with improved 3-db bandwidth of over 150 ghz," *IEEE Photonics Technology Letters*, vol. 10, no. 3, pp. 412–414, March 1998.

[5] N. Shimizu, N. Wantanabe, T. Furuta, and T. Ishibashi, "Improved response of uni-traveling-carrier photodiodes by carrier injection," *Japanese Journal of Applied Physics*, vol. 37, pp. 1424–1426, 1998.

[6] J. Klamkin, A. Ramaswamy, L. A. Johansson, H.-F. Chou, M. N. Sysak, J. W. Raring, N. Parthasarathy, S. P. DenBaars, J. E. Bowers, and L. A. Coldren, "High output saturation and high-linearity uni-traveling-carrier waveguide photodiodes," *IEEE Photonics Technology Letters*, vol. 19, no. 3, pp. 149–151, February 2007.

Monolithically Integrated Coherent Receiver for Highly Linear Microwave Photonic Links

Jonathan Klamkin[1], Leif A. Johansson[2], Anand Ramaswamy[2], John E. Bowers[2],
Steven P. DenBaars[1,2], Larry A. Coldren[1,2]
1. Materials Department, University of California, Santa Barbara, CA 93106 USA
2. Electrical and Computer Engineering Department, University of California, Santa Barbara, CA 93106 USA
Email: klamkin@engineering.ucsb.edu

***Abstract*— A compact monolithically integrated coherent receiver with feedback has been fabricated for linear optical phase demodulation. The photodiodes demonstrate a saturation current greater than 60 mA and an OIP3 of 35 dBm at 40 mA.**

I. Introduction

Phase modulation can be used to improve the signal-to-noise ratio (SNR) and spur-free dynamic range in microwave photonic links as long as the signal phase can be linearly demodulated. Traditional interferometer based demodulators have a sinusoidal response therefore a novel approach is required to build a linear phase demodulator. We have demonstrated a coherent receiver with feedback to a reference phase modulator [1], [2]. For high loop gain the received signal phase is closely tracked and the phase detection falls within the linear regime of the sinusoidal response. In order to operate at high frequency, the delay of the feedback loop must be kept short to prevent instability. A monolithically integrated receiver is therefore required to realize high frequency operation. Here we present a compact monolithic coherent receiver that consists of MQW phase modulators, a 2x2 multimode interference (MMI) coupler, and a high power balanced uni-traveling-carrier photodiode (UTC-PD) as shown in Fig. 1. This photonic integrated circuit is designed for hybrid integration with an electronic integrated circuit that can provide transconductance amplification of the feedback signal.

II. Device Design and Results

The device structure is designed to incorporate the following optical functions: phase modulation, low loss propagation, and photodetection. The structure is grown on a semi-insulating InP substrate by MOCVD. The optical waveguide consists of a MQW stack for efficient phase modulation. The UTC-PD structure is grown directly above the waveguide. The layers of the photodiode (PD) structure are selectively removed prior to the p^+-InP cladding and p^{++}-InGaAs contact layer regrowth in order to form the photodetection regions. The 2x2 MMI coupler is fabricated in a surface ridge and is 350 μm in length. A metal pad is integrated in a section in the center of the MMI for current injection tuning. In order to build a balanced UTC-PD, adjacent PDs are electrically isolated with high energy Helium implantation and then connected in series with a monolithic metal interconnect.

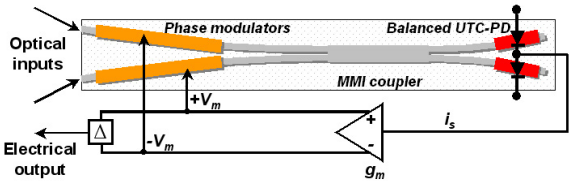

Fig. 1. Integrated coherent receiver device schematic.

Although the feedback loop suppresses nonlinearities in the interferometer, the linearity of the reference phase modulator needs to be addressed. Phase modulation in InP QCSE modulators is dominated by the quadratic electro-optic effect. By incorporating phase modulators into both input arms and driving them differentially, the linear term is doubled while the second order term as well as higher even order terms are canceled. With this push-pull configuration, the efficiency is therefore doubled and the third-order nonlinearities can be suppressed by adjusting the bias. The absorption spectra of the phase modulator structure were measured and from these measurements the efficiency of a single modulator was extracted using a Kramers-Kronig transformation. For a modulator length of 560 μm, V_{pi} is 5.0 V at 1540 nm. The efficiency can be improved simply by increasing the modulator length. With a more efficient modulator, the feedback loop gain requirements are less stringent, however with a longer modulator the loop delay increases. Therefore it is desirable to use very efficient modulator structures so that the modulator length can be kept short.

The design of the MMI is important in that the excess loss should be kept low so that maximum transmission of optical power to the PDs is allowed. The tuning of the splitting in a MMI relies on a refractive index change in one interval where the field is imaged in order to produce new phase relations in the next interval. Fig. 2 shows the splitting properties of the MMI coupler. With low levels of injected current the splitting ratio can be fine tuned. The effect of the tuning section length on the tuning efficiency is shown in Fig. 3. As shown, a 100 μm long tuning section is more efficient than a 300 μm long tuning section.

It is important that the PDs can operate under high current, for high SNR, and that they are linear. UTC-PDs are used

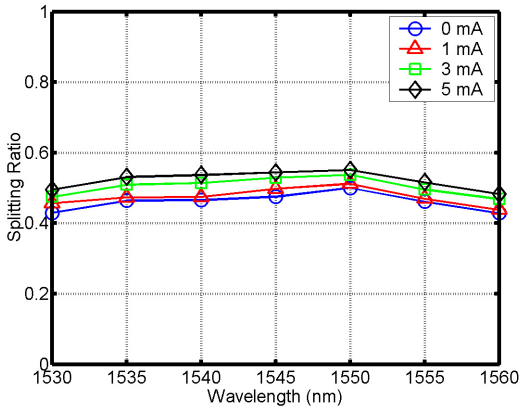

Fig. 2. MMI splitting ratio as a function of wavelength for different levels of tuning current.

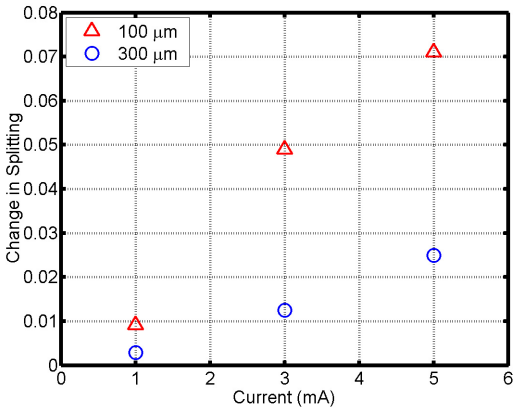

Fig. 3. Change in splitting as a function of injected tuning current for a 100 μm long tuning pad and a 300 μm long tuning pad.

because they are designed for high current operation. We previosly reported UTC-PDs with 40 mA saturation current and an OIP3 of 34 dBm at 40 mA [3]. We have since improved the design of the UTC-PD structure to increase the output saturation current. Fig. 4 shows the normalized RF power as a function of DC photocurrent at several frequencies. The saturation current is greater than 60 mA in all cases. This is among the highest reported saturation current for a waveguide PD at comparable frequencies. Fig. 5 shows the results of third-order intermodulation distortion measurements at a DC photocurrent level of 40 mA. The measured OIP3 is 31 dBm for a bias of -5 V and 35 dBm for a bias of -5.8 V.

III. Conclusions

We have demonstrated a monolithic coherent integrated receiver for a novel feedback loop architecture. The performance of the optical phase modulators, the 2x2 MMI coupler, and the balanced UTC-PD as well as their impact on the operation of the feedback system have been discussed.

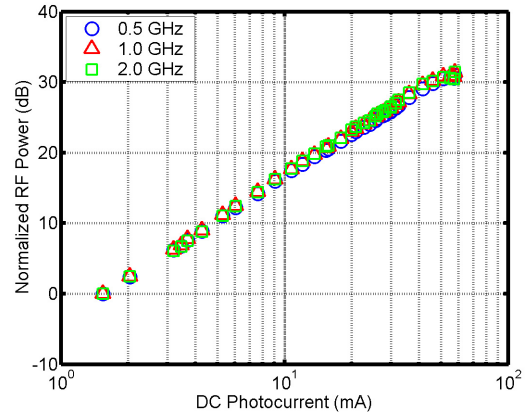

Fig. 4. Normalized RF power as a function of DC photocurrent at 0.5 GHz, 1.0 GHz, and 2.0 GHz. The bias is -3.5 V for all measurements.

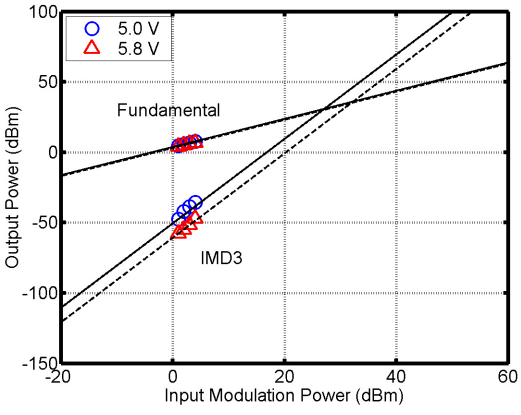

Fig. 5. Two-tone IMD3 measurements at a DC photocurrent level of 40 mA for biases of -5.0 V and -5.8 V.

Acknowledgment

This research was supported by the DARPA PHOR-FRONT program under United States Air Force contract number FA8750-05-C-0265.

References

[1] H.-F. Chou, A. Ramaswamy, D. Zibar, L. A. Johansson, J. E. Bowers, M. Rodwell, and L. Coldren, "Sfdr improvement of a coherent receiver using feedback," in *Coherent Optical Technologies and Applications Conference*, 2006.

[2] A. Ramaswamy, L. A. Johansson, J. Klamkin, C. Sheldon, H.-F. Chou, M. J. Rodwell, L. A. Coldren, and J. E. Bowers, "Coherent receiver based on a broadband optical phase-lock loop," in *OFC Postdeadline Papers*, 2007.

[3] J. Klamkin, A. Ramaswamy, L. A. Johansson, H.-F. Chou, M. N. Sysak, J. W. Raring, N. Parthasarathy, S. P. DenBaars, J. E. Bowers, and L. A. Coldren, "High output saturation and high-linearity uni-traveling-carrier waveguide photodiodes," *IEEE Photonics Technology Letters*, vol. 19, no. 3, pp. 149–151, February 2007.

Ultra-compact Grating-based 2x2 Beam Splitter for Miniature Photonic Integrated Circuits

Chin-Hui Chen, Matt N. Sysak, Jonathan Klamkin, and Larry A. Coldren
ECE Dept. University of California, Santa Barbara, CA 93106

Phone: 805.893.5955, Fax: 805.893.4500, Email: janet@ece.ucsb.edu

Abstract: A novel, InGaAsP/InP ultra-compact grating-based beam splitter that has less than 1.8dB of loss has been fabricated. The beam splitter exhibits 50/50 splitting with a length of less than 25μm for 1555nm wavelength

1. INTRODUCTION

Compact beam splitters have attracted considerable interests during the last few decades. There has been an ever-increasing demand for photonic integrated circuits, analogous to their electronic counterparts, to be small in size and also achieve high data rates and low losses. Moreover, in some applications with optical feedback circuits, such as the optical phase-locked loops in [1], the system stability greatly relies on ultra-short loop delays. Conventional directional couplers and MMI-based beam splitters, usually a few hundred microns or even millimeters in length, cannot meet the compactness requirements. Other advanced technologies such as photonic crystals [2] and air trenches [3] can be used to construct beam splitters with ultra compactness within submicron order; however, their performance is sensitive to the processing, and they are usually hard to fabricate with large throughput.

A grating-based beam splitter proposed in this paper has the advantage of (1) meeting the short delay requirement with a length less than 25 μm, (2) having well-established processes for robust fabrication and large throughput, and (3) being compatible with existing integrated platforms. Another point worth mentioning is that the total footprint of a splitter includes not only the central splitting region but also connecting waveguides between the splitter and other components e.g. phase modulators and photo detectors in our case. As is typically the case with these devices, the final footprint of our compact beam splitter is limited by the pad layout and beam separation issues, hence is usually dominated by the connecting lengths. Therefore, the grating-based beam splitter is a very desirable solution for circuits that require compactness without a trade-off in the fabrication complexity.

2. DESIGN

The splitter is designed by using the 2-D, quasi-free space, and two-wave interference method. The schematic diagram and FDTD simulations [4] are shown in Figure 1. The incoming guided light from each side first diverges out in the quasi-free space region without reaching its waveguide boundary, and is divided by a Bragg grating section into transmitted and reflected waves. Here, a grating period of 245 nm for the Bragg condition has been used. The goal for our grating-based beam splitter is to have an equal splitting ratio, low loss, and high degree of interference between the two waves.

In the case of large incident angles and wide grating regions, signal distortions and resulting degradation of interference are typically observed due to the oblique incidence and the finite widths of both gratings and input

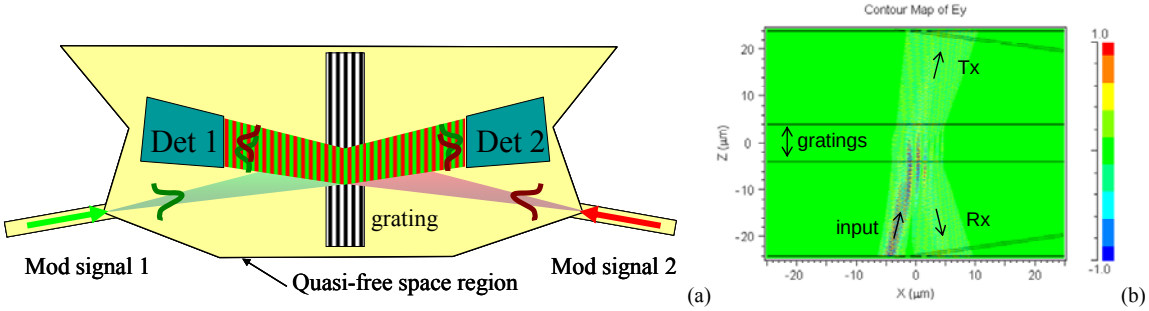

FIGURE 1. (a) Schematic diagram of grating-based beam splitter. Waveguide boundary is far away from the diverged beams in quasi-free space region. Green and red colors represent two input signals from modulators. (b) FDTD simulation shows 50% splitting ratio.

beams. Therefore, a small angle of 10° and a large coupling coefficient achieved by deep etching, which allows a short grating length, are desirable. However, perturbation theories cannot be applied to splitters using deeply etched gratings. The possibility of low scattering loss with high reflectivity has been theoretically proven in [5]. In order to minimize the scattering loss and to provide more uniform interference, a grating depth which extends completely through the slab waveguide layer is required.

3. DEEP GRATING FABRICATION

The gratings are first patterned with holographic exposure, and then transferred to an 800Å SiO_2 hard mask layer using ICP CHF_3 etching. Methane/hydrogen/argon (MHA)-based reactive ion etching (RIE) is generally used in InP-based materials. However, deeply etched profiles with high aspect ratios usually suffer from polymer deposition and methyl radical undercut. It is known that the presence of oxygen within the MHA RIE process is beneficial for preserving the etch profile and enabling sufficient etch depth. In this work, we adopt a hybrid fabrication method [6] in which the continuous addition of oxygen is present during the etching steps (0.5/4/20/10sccm O_2:MHA, 60mTorr, -450V), and also in which oxygen ashing steps (40sccm, 125mTorr, -200V) are cyclically applied until the desired etch depth is reached. The small amounts of continuous oxygen prevent lateral overgrowth, and cyclic oxygen plasma helps clean up any polymer accumulated during etching. Subsequently a cladding layer of 2 μm InP is regrown on top of the etched grating grooves. As shown in Figure 2 (a), the gratings are almost completely etched through the slab waveguide layer to achieve high index contrast and the absence of apparent air vacancies implies a low void-stimulated scattering loss.

4. RESULTS AND CONCLUSIONS

The grating-based beam splitter performance is characterized by measuring the photocurrents of the two photo detectors for transmitted and reflected. Two examples are shown in Figure 2 (b) and (c). These splitters have grating lengths of 10 μm and 25 μm and the peak reflections at Bragg wavelength of 47% and 66% respectively. As expected, the peak reflections are larger for longer gratings. The total measured insertion loss for the devices is between 1 and 1.8 dB for the wavelength range shown in Fig 2 (b) and (c). It includes the propagation loss in the quasi-free space region and the grating scattering loss.

In this paper, we have fabricated a novel, ultra-compact grating-based beam splitter with low scattering loss and splitting ratio close to and greater than 50%. The physical dimensions of our ultra-compact beam splitter, including two 350 μm phase modulators, two 100 μm photo detectors, 90 μm splitter regions (grating and connection waveguides) and all the electrical pads for wire-bonding, are less than 850 μm x 350 μm.

5. REFERENCES

[1] A. Ramaswamy, et al., "Coherent Receiver Based on a Broadband Optical Phase-Lock Loop," *OFC Conference* post deadline paper, 2007.
[2] S. Shi, et al., "Dispersion-based beam splitter in photonic crystals," *Optics Letters*, Vol. 29, No. 6, March 2004.
[3] Y. Lin, et al., "Compact and high efficiency polymer air-trench waveguide bends and splitters," *Proceedings of SPIE,* Vol. 6462, March 2007.
[4] Rsoft Inc. FullWAVE.
[5] J. Ctyroky, et al., "Analysis of a deep waveguide Bragg grating," *Optical and Quantum Electronics*, Vol. 30, pp. 343-358, May 1998.
[6] J. E. Schramm, et al., "Fabrication of high-aspect-ratoi InP-based vertical-cavity laser mirrors using $CH_4/H_2/O_2/Ar$ reactive ion etching," *Journal of Vacuum Science & Technology B: Microelectronics and Nanometer Structures*, Vol. 15, No. 6, pp. 2031-2036, Nov. 1997.

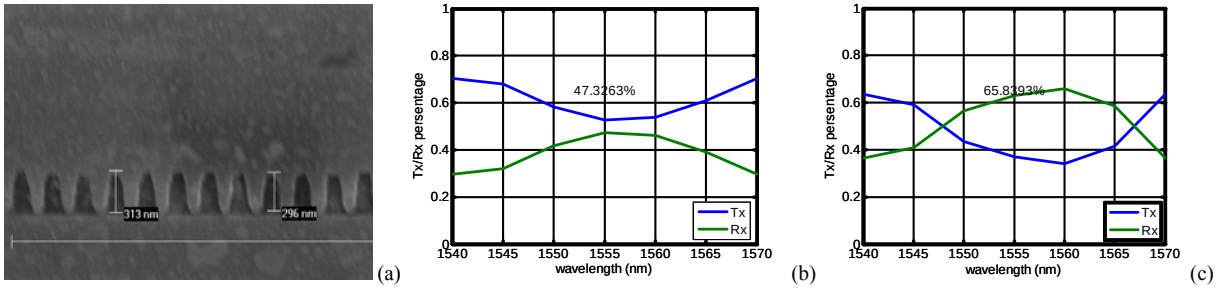

FIGURE 2. (a) SEM picture of the fabricated gratings after regrowth. The vertical waveguide layer is revealed by a selective wet etch. (b) Beam splitter with grating length = 10μm and peak reflection of 47%. (c) Beam splitter with grating length = 25μm and peak reflection of 66%.

Integrated All-Photonic Coherent Receiver

Anand Ramaswamy[1], Leif A. Johansson[1], Jonathan Klamkin[2], Mark J. Rodwell[1],
John E. Bowers[1], and Larry A. Coldren[1,2]
[1]University of California Santa Barbara, ECE Department, Santa Barbara, CA 93106, USA
[2]University of California Santa Barbara, Materials Department, Santa Barbara, CA 93106, USA
Email: anand@ece.ucsb.edu

An integrated all-photonic coherent receiver is presented for linear optical demodulation of phase modulated analog signals. The output of a balanced detector pair is directly connected to a tracking phase modulator to provide feedback phase tracking. The resulting measured link SFDR is 110dBHz$^{2/3}$.

High-performance analog optical links require high linearity in the optical transmitter and receiver. Phase modulation has emerged as a viable alternative to standard intensity modulation with the prevalence of lineal optical phase modulators (e.g. $LiNbO_3$). The main source of nonlinearity then resides in the receiver architecture due to the inherent non-linearity associated with any interferometer based phase detection process. By using a feedback loop in an optical interferometer receiver we have demonstrated that the net phase swing across the demodulator can be reduced without any penalty in SNR with a resulting improvement in receiver SFDR [1]. An integrated, optoelectronic version of the receiver, with a 3dB bandwidth of 1.45GHz, was demonstrated to have an SFDR of 125dB.Hz$^{2/3}$ at 300 MHz [2]. In this work we present link experiment results from an all-photonic version of the receiver. Figure 1 shows a schematic of the receiver architecture in which the output of a balanced receiver pair is directly interconnected to a balanced optical phase modulator with a 2x2 MMI coupler located between modulator and detector. Figure 2 shows a scanning electron micrograph (SEM) of the integrated device.

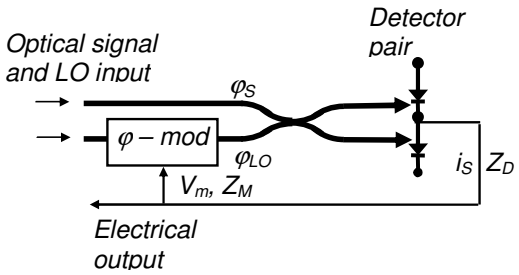

Fig. 1. Schematic of the receiver architecture.

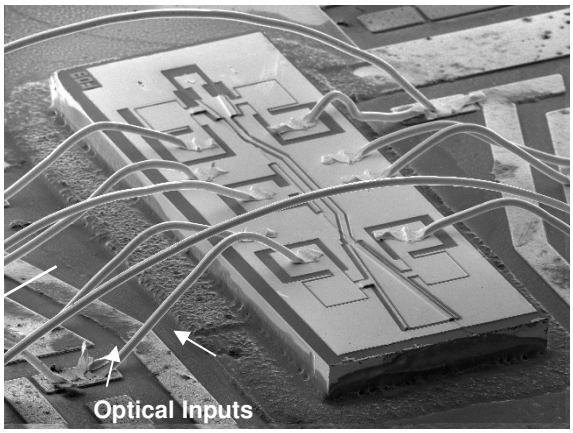

Fig. 2. SEM of Integrated All-photonic receiver

Unlike the optoelectronic receiver, the all photonic receiver has no electronic amplifiers in the feedback path. Instead, there is a direct interconnect between the detector and modulator. When the detected photocurrent is sufficiently high, it drives the sum of the photodiode and modulator capacitance, generating a voltage across the reference modulator that's proportional to the photocurrent. The modulator response is tailored to provide adequate filtering and stable phase feedback [3].

Figure 3a) shows the frequency response of the device with the modulators in this experiment is forward biased for greater efficiency. At lower frequencies and higher photocurrents, the link gain is determined by the ratio of the drive signals to the source and reference modulator. We can consequently observe that the response does not vary with received photocurrent. This suggests that the loop gain is sufficiently high for the reference modulator to closely track the incoming phase so. Figure 3b) shows the open-loop gain that is extracted from the response. It confirms that at higher photocurrent and low frequencies the link gain is proportionally higher. The increased loop gain at low frequency is attributed to higher phase modulation efficiency of the forward biased reference modulator. This is also mirrored in the reduction in loop gain at lower frequencies, as a lower drive voltage is required for phase tracking in the integrated receiver.

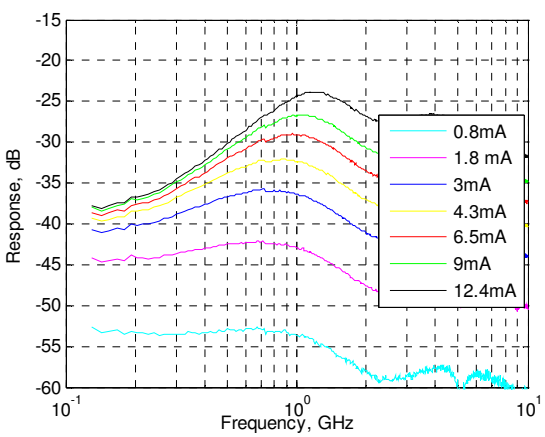

Fig. 3a). Frequency Response

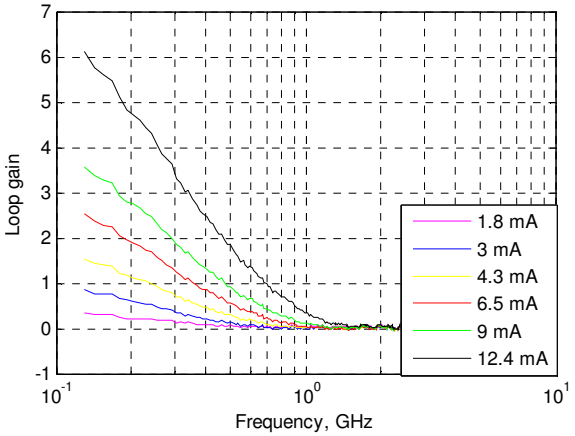

b) Extracted loop gain

Figure 4 shows SFDR data taken at 500 MHz with 15mA of photocurrent in the detectors. The experimental setup used for this measurement is discussed in [2]. The noise floor is calculated from receiver and shot noise contributions where the ASE noise contribution of the amplified optical source has been compensated for. Ideally, with detector balance, a low RIN source and higher photocurrent, shot noise limited receiver performance should be achievable. It was verified that receiver noise was well below the calculated shot noise level. An SFDR of 110dB.Hz$^{2/3}$ was measured. The detectors themselves have saturation current greater than 40 mA and OIP3 values of 43 dBm and 34 dBm at photocurrent levels of 20 mA and 40 mA respectively [4] and hence, can handle high optical powers. Efforts are being made to realize lower loss through the device so that the link gain can be increased. This is a fundamentally linear technique and with improved modulator efficiency, lower loss and shorter feedback delay the linearity performance of the receiver can be enhanced over a wide frequency range.

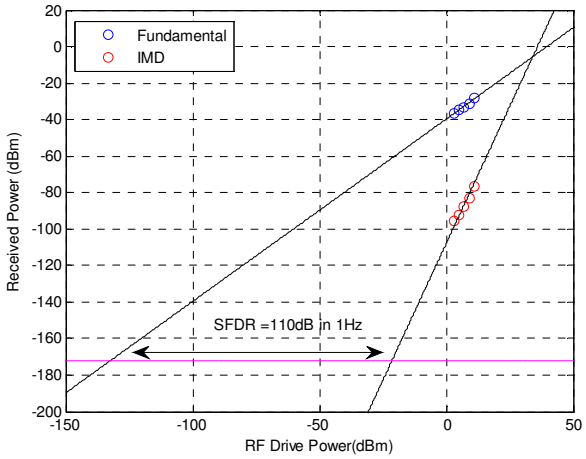

Fig. 4. SFDR at 500MHz with 15mA of detected photocurrent

[1] H.F. Chou, *et al*., "High-Linearity Coherent Receiver with Feedback", *IEEE Photonics Technol. Lett*., vol. 19, no. 12, pp. 940-942, June 2007.

[2] A. Ramaswamy, *et al*., "Coherent Receiver Based on a Broadband Optical Phase-Lock Loop," Optical Fiber Communications Conference. (OFC). Postdeadline Technical Digest. Opt Soc. America. PDP3, 2007.

[3] L.A. Johansson, *et al* , "Coherent Optical Receiver for Linear Optical Phase Demodulation", *IEEE MTT-S International Microwave Symposium,* Honolulu, Hawaii, June 2007.

[4] J. Klamkin *et al*., "High Output Saturation and High-Linearity Uni-Traveling-Carrier Waveguide Photodiodes," *IEEE Photonics Technol. Lett*., vol. 19, no. 3, pp. 149-151, Feb. 2007.

I. Photonic IC Technology and Devices

C. Photocurrent-Driven Wavelength Converter PICs

Analysis of Digital System Performance in EAM-Based Photocurrent Driven Wavelength Converter

Matthew N. Sysak, *Member, IEEE*, James W. Raring, *Member, IEEE*, Matthew Dummer, *Student Member, IEEE*, Henrik N. Poulsen, *Member, IEEE*, Daniel J. Blumenthal, *Fellow, IEEE*, and Larry A. Coldren, *Fellow, IEEE*

***Abstract*—This work describes the factors that influence the digital system performance of a monolithically integrated photocurrent driven wavelength converter. For an optimized input power to the receiver section of the device, experiments show <1-dB power penalty for conversion between 1548 and 1563 nm at 10 Gb/s. Under optimized conditions, performance is limited by the output extinction ratio of the converted signals.**

***Index Terms*—Monolithic integration, photonic integrated circuits, wavelength converters.**

I. Introduction

PHOTONIC integrated circuits that are capable of wavelength switching and signal regeneration are critical components for extending the reach of present day optical networks. Several devices are currently available that can perform these functions. These include semiconductor optical amplifiers (SOAs) that utilize cross-gain modulation or cross-phase modulation, electroabsorption modulators (EAMs) based on photocurrent effects, and fiber-based wavelength converters that employ wave mixing [1]. Of these approaches, small form factor wavelength switching elements that are compatible with monolithic integration offer additional benefits, such as low optical coupling losses between components and reduced packaging costs.

Recently, we have demonstrated a monolithically integrated photocurrent driven wavelength converter (PD-WC) that can perform signal regeneration. The device is compatible with a range of input and output wavelengths, and does not require optical filtering to separate input and converted signals [2]. The wavelength converter is based on the dual-quantum-well (QW) integration platform where fabrication requires a single blanket InP regrowth in combination with simple selective wet etching steps to form optical gain and passive routing/EAM regions [3]. The device utilizes photocurrent driven technology where an optically preamplified receiver drives an EAM that is part of a tunable optical transmitter. Similar devices based on this principle have been demonstrated at bit rates of 500 Gb/s [4].

Manuscript received August 29, 2006; revised November 2, 2006. This work was supported by Defense Advanced Research Projects Agency (DARPA)/MTO CS-WDM under Grant N66001-02-C-8026 and by Intel Corporation under Grant TXA001630000.

The authors are with the Department of Electrical Engineering and the Department of Materials, University of California Santa Barbara, Santa Barbara, CA 93116 USA (e-mail: mnsysak@engineering.ucsb.edu).

Digital Object Identifier 10.1109/LPT.2006.888954

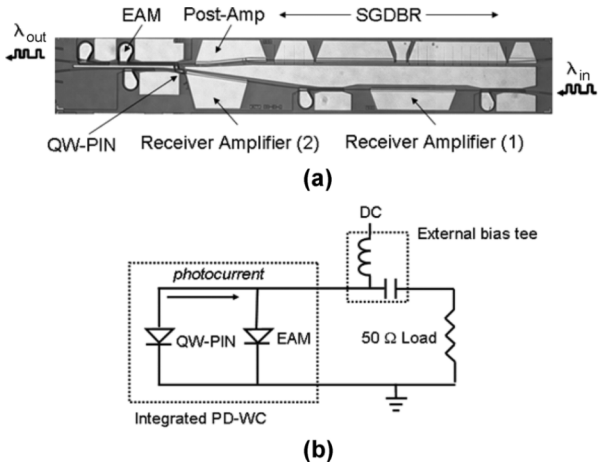

Fig. 1. (a) Scanning electron micrograph (SEM) of the PD-WC. (b) Circuit schematic for PD-WC operation.

In this work, we use bit-error-rate (BER) measurements to optimize the digital system power penalty through the wavelength converter. Under optimum conditions, the PD-WC does not introduce significant noise or jitter onto the wavelength-converted signals. Furthermore, when optimized, the power penalty through the wavelength converter is limited by the converted signal extinction ratio (ER).

II. Device Overview

A schematic of the PD-WC along with an equivalent circuit for device operation is shown in Fig. 1. The device consists of a monolithically integrated optical receiver section and widely tunable transmitter section. The receiver is comprised of a 600-μm-long straight waveguide SOA that is 3-μm-wide (receiver amplifier 1) and a 400-μm-long flared waveguide SOA (receiver amplifier 2). The second SOA waveguide width is exponentially flared from 3 to 12 μm along the length of the device. A linearly tapered $(12-3\ \mu\text{m})$ waveguide QW-PIN photodetector follows the flared SOA [5].

The transmitter section of the PD-WC consists of a four-section sampled-grating distributed Bragg reflector (SGDBR) laser, a 550-μm-long postamplifier SOA, and a 400-μm-long EAM. A voltage source and a bias tee are used to simultaneously reverse bias both the QW-PIN and the EAM, and a 50-Ω load resistor is used to enhance the bandwidth. An equivalent circuit for the device is shown in Fig. 1(b). A 35-μm-long metal interconnect routes the photocurrent generated in the QW-PIN to the EAM and the load resistor, where the resulting voltage drop changes

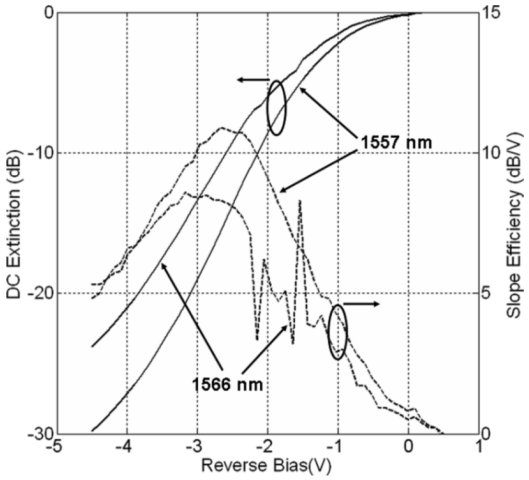

Fig. 2. DC extinction (solid line) and slope efficiency (dashed line) results for a 400-μm EAM at output wavelengths of 1557 and 1566 nm.

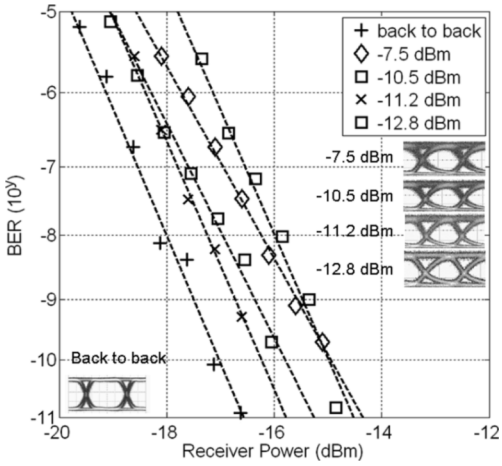

Fig. 3. BER curves for various input powers to the integrated receiver in the PD-WC. The input wavelength is 1548 nm, the input extinction is 15 dB, and the output wavelength is 1563 nm.

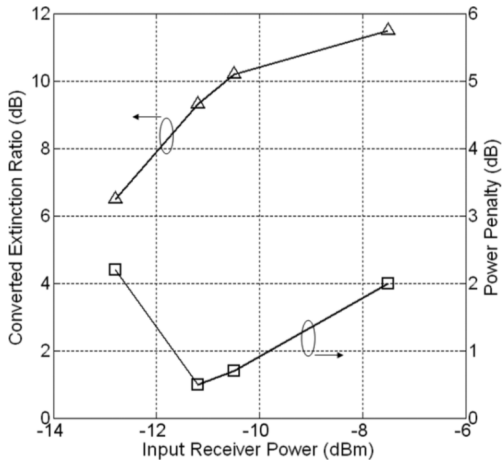

Fig. 4. Summary of BER measurements for various input powers to the PD-WC receiver. Input and output wavelengths are 1548 and 1563 nm, respectively, and applied reverse bias is -3 V.

the transmission properties of the EAM. This writes the signal from the receiver to the output wavelength of the transmitter. For transverse electric (TE) polarized signals, the receiver gain is 20 dB with a current density of 6 kA/cm^2 applied to both SOAs. The receiver exhibits a 1-dB gain compression at -7-dBm input power, and has a sensitivity $(\text{BER} = 10^{-9})$ of -18.5 dBm at 10 Gb/s for an input wavelength of 1548 nm.

III. Experiment

To optimize the performance of the PD-WC, a set of two BER measurements were performed using nonreturn-to-zero (NRZ) data at 10 Gb/s. The NRZ data contained a $2^{31}-1$ pseudo-random bit sequence. The experimental setup was the same as in [2], where an optical signal at 1548 nm with a 15-dB ER was fed to the PD-WC receiver. The polarization of the input signal was optimized using a polarization controller, and was selected for maximum gain in the integrated receiver. The compressively strained QWs used for optical gain in the PD-WC render the receiver SOAs highly polarization-sensitive, with preferential gain for TE guided modes. This issue could be circumvented by including an additional regrowth in the fabrication process, where an optimized bulk active region could be grown and subsequently removed for the receiver amplifiers similar to that employed for high-speed photodetectors in [6].

The first set of BER measurements was used to determine an optimum input power level for the PD-WC. BER curves were generated for back-to-back (without the device) and wavelength-converted signals for a range of input powers to the integrated PD-WC receiver. The optimum input power was defined as where the power penalty, measured as the difference in receiver power (the receiver in the test setup) between back-to-back and converted signals at a BER of 10^{-9}, was minimized. In these experiments, the output wavelength from the PD-WC was fixed at 1563 nm and the reverse bias conditions were set to -3 V to achieve maximum EAM slope efficiency. The DC extinction and slope efficiency of the EAM for wavelengths of 1566 and 1557 nm are shown in Fig. 2. The receiver SOAs are biased at 6 kA/cm^2 and the SGDBR gain and postamplifier SOA are biased at 100 mA.

To further optimize the PD-WC performance, a second set of BER measurements was performed for various QW-PIN/EAM reverse bias conditions. The input power to the device was fixed based on the results from the first set of BER measurements and the output wavelength from the PD-WC was again 1563 nm. The bias conditions for the receiver SOAs, transmitter SOA, and the SGDBR are identical to that in the first set of measurements.

IV. Results

Results from the first set of BER measurements are shown in Fig. 3 along with wavelength-converted eye diagrams for fiber coupled receiver input powers of -12.8, -11.2, -10.5, and -7.5 dBm. All eye diagrams are clear and open indicating that jitter through the PD-WC is not significant. The input and output optical signal-to-noise ratios (OSNRs) in these experiments was >30 dB, which is well above the region where OSNR limits BER. For increasing optical power to the PD-WC, Fig. 3 shows that the power penalty initially decreases, then increases. The power penalty through the device as a function of input power and output ER from the wavelength converter are shown in Fig. 4. At low input powers (-12.8 dBm), increasing optical power to the integrated receiver increases the photocurrent from the QW-PIN, which generates a larger voltage across the

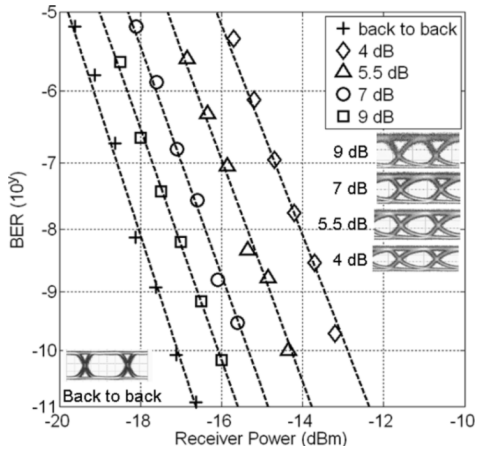

Fig. 5. BER measurements for QW-PIN/EAM reverse biases of −2, −2.3, −2.7, and −3 V. Wavelength converted ERs at these biases are 4, 5.5, 7, and 9 dB, respectively.

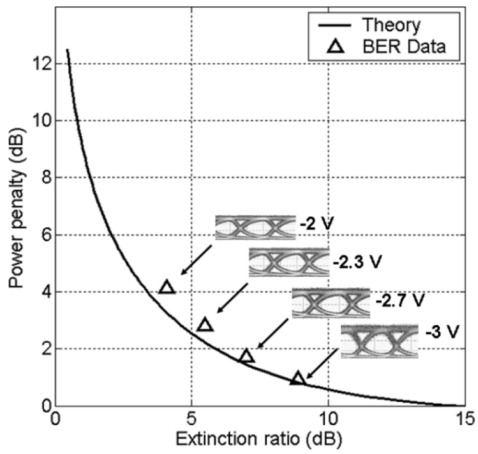

Fig. 6. Theoretical power penalty versus ER and experimental data for wavelength conversion from 1548 to 1566 nm. Applied reverse bias conditions are −2, −2.3, −2.7, and −3 V.

load resistor. The larger voltage swing drives the EAM through greater changes in transmission, improving the output extinction of the device. However, as the input power to the receiver increases beyond −11.2 dBm, the power penalty begins to increase despite improvements in output ER. This increase originates from a change in slope in the BER curves shown in Fig. 3, and is indicative of modified noise statistics in the wavelength-converted signals. The changing noise distribution most likely results from pattern-dependent gain overshoot and recovery in the receiver SOAs [8], which can be seen as "one" noise in the eye diagrams in Fig. 3 for power levels > -10.2 dBm. Based on minimizing the power penalty through the device, the optimal input power to the PD-WC is −11.2 dBm. Under these conditions, the clear eye diagrams and the parallel BER slopes between back-to-back and converted data indicates that device performance is not limited by jitter or pattern dependence generated in the PD-WC receiver.

Results from the second set of BER measurements, which investigates how changing the wavelength converter bias effects digital system performance, are shown in Fig. 5. For reverse biases of −2.0, −2.3, −2.7, and −3 V, wavelength-converted signals show ERs of 4, 5.5, 7, and 9 dB, respectively. Eye diagrams are included for the wavelength-converted signals at each of the examined bias conditions. The increase in ER as a function of bias comes from the increasing EAM slope efficiency shown in Fig. 2. From Fig. 5, as the ER improves, there is a clear reduction of the power penalty between back-to-back and converted signals. To determine if the output ER from the PD-WC limits BER performance, the extracted power penalty through the wavelength converter is compared with theory from [7] in Fig. 6. The theoretical predictions are based on the increase in receiver power (the receiver used to measure BER) that would be required to achieve a BER of 10^{-9} given a range of signal ERs. To convert the increased receiver power to a power penalty through the device, a constant is subtracted from the theoretical predictions to account for the 15-dB ER in the input signal to the PD-WC. The excellent agreement between the predictions and data indicates that under these optimized input power conditions, converted signal ER limits device performance.

V. Conclusion

We have demonstrated that the digital system performance of the PD-WC can be limited by the ER of the converted signals at 10 Gb/s. Under optimized input conditions, the bias across the EAM and QW-PIN can be changed to achieve less than 1-dB power penalty through the device. By improving receiver saturation or EAM efficiency in the PD-WC, the converted ER could be improved, leading to lower power penalties and a larger dynamic range.

References

[1] S. B. Yoo, "Wavelength conversion technologies for WDM network applications," *J. Lightw. Technol.*, vol. 14, no. 6, pp. 955–966, Jun. 1996.

[2] M. N. Sysak, J. W. Raring, L. A. Johansson, H. N. Poulsen, J. S. Barton, D. J. Blumenthal, and L. A. Coldren, "Optical 2R and 3R regeneration with dynamic wavelength switching using a monolithically integrated, widely tunable photocurrent driven wavelength converter," in *Eur. Conf. Optical Commun. (ECOC)*, Cannes, France, Sep. 2006.

[3] M. N. Sysak, J. W. Raring, J. S. Barton, M. Dummer, D. J. Blumenthal, and L. A. Coldren, "A single regrowth integration platform for photonic circuits incorporating tunable SGDBR lasers and quantum well EAMs," *IEEE Photon. Technol. Lett.*, vol. 18, no. 15, pp. 1630–1632, Aug. 1, 2006.

[4] S. Kodama, T. Yoshimatsu, and H. Ito, "500 Gbit/s optical gate monolithically integrating photodiode and electroabsorption modulator," *Electron. Lett.*, vol. 40, no. 9, pp. 555–556, Apr. 2004.

[5] A. Tauke-Pedretti, M. Dummer, J. S. Barton, M. N. Sysak, J. W. Raring, and L. A. Coldren, "High saturation power and high gain integrated receivers," *IEEE Photon. Technol. Lett.*, vol. 17, no. 10, pt. 10, pp. 2167–2169, Oct. 2005.

[6] J. W. Raring, E. J. Skogen, C. S. Wang, J. S. Barton, G. B. Morrison, S. Demiguel, S. P. Denbaars, and L. A. Coldren, "Design and demonstration of novel QW intermixing scheme for the integration of UTC-type photodiodes with QW-based components," *IEEE J. Quantum Electron.*, vol. 42, no. 2, pp. 171–181, Feb. 2006.

[7] G. P. Agarwal, *Fiber Optic Communication Systems*. New York: Wiley, 1997, p. 169.

[8] K. Morito, M. Ekawa, T. Watanabe, and Y. Kotaki, "High-output-power polarization-insensitive semiconductor optical amplifier," *J. Lightw. Technol.*, vol. 21, no. 1, pp. 176–181, Jan. 2001.

Monolithic 40 Gbps Separate Absorption and Modulation Mach-Zehnder Wavelength Converter

Anna Tauke-Pedretti[1], **Matthew Dummer**[1], **Matthew N. Sysak**[1], **Jonathon S. Barton**[1], **James W. Raring**[2], **Jonathan Klamkin**[1] **and Larry A. Coldren**[1]

[1] *University of California Santa Barbara, Santa Barbara, CA 93106*
TEL:(805)893-5955, FAX:(805)893-4500, email:atauke@engineering.ucsb.edu
[2] *Sandia National Laboratories, Albuquerque, NM 87123*

Abstract: The first 40 Gbps monolithic SAM Mach-Zehnder wavelength converter is demonstrated. The device exhibits a bandwidth is in excess of 20 GHz and power penalties less than 2.5 dB at 40 Gbps using NRZ data.

OCIS codes: (250.5300) Photonic integrated circuits; (250.7360) Waveguide modulators

1. Introduction

Wavelength converters are an important part of the next generation of optical networks to provide dynamic wavelength management within WDM systems. Monolithic approaches are able to reduce packaging costs and increase scalability. A popular approach to this problem is to utilize cross-gain or cross-phase modulation in semiconductor optical amplifiers (SOAs) [1, 2], however these devices are inherently limited by carrier lifetime. Recently, there has been success with the separate absorption and modulation region (SAM) approach to wavelength conversion in which input signal photocurrent generated by an on-chip photodiode is used to drive an optical modulator [3, 4]. This approach offers a number of advantages over SOA based approaches including conversion between identical input and output wavelengths, bit-rate transparency, and no optical filtering requirements.

In this paper we report the first monolithic Mach-Zehnder modulator (MZM) based SAM wavelength converter operating at 40 Gbps. The device implements a linear SOA, a quantum-well absorber, a widely tunable sampled-grating DBR (SGDBR) laser and a series-push-pull Mach-Zehnder modulator. Additionally, a capacitor and resistor are integrated on chip eliminating the need for bias tees, thus reducing microwave losses and simplifying biasing.

2. Device

A diagram of the Mach-Zehnder wavelength converter is shown in Fig. 1.

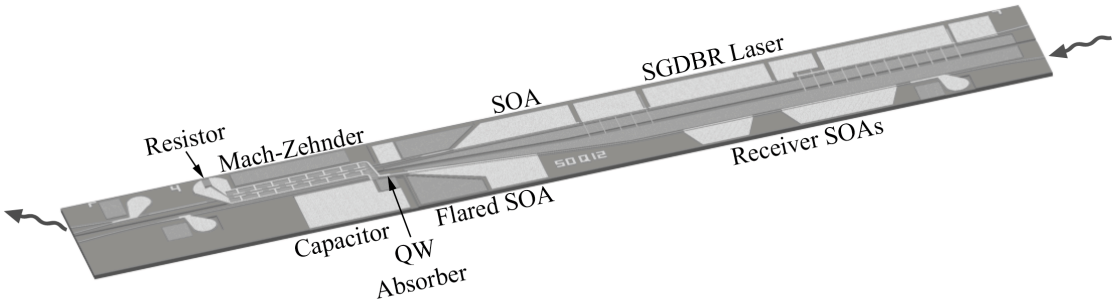

Fig. 1. Diagram of the wavelength converter

The SGDBR laser consists of five sections – an active absorber, a rear mirror, a phase section, a 500 μm long gain section, and a front mirror. A 500 μm SOA follows the SGDBR to increase the output power of the device and compensate for propagation losses. A phase section within the interferometer is implemented to allow for biasing

to π-phase-shift. A flared and curved output waveguide combined with an AR coating was used to reduce optical reflections and to aid in fiber coupling.

The modulator utilizes a traveling wave electrode segmented into 6-50 μm long T-sections to capacitively load the transmission line allowing for better impedance matching. To reduce the capacitance BCB is deposited under the modulator electrodes and the ridge width is reduced from 3 μm in the laser and SOA regions to 2 μm within the modulators. On chip termination is formed from an integrated 25 Ω semiconductor resistor fabricated out of the n-contact layer. The 300 μm long MZM is operated in a series-push-pull fashion with the photocurrent signal applied across the tops of the Mach-Zehnder arms. This configuration allows for improved bandwidth, reduced power consumption and small chirp values [5, 6].

The receiver section consists of a 500 μm long straight SOA, a 550 μm long linearly flared SOA and a 35 μm long tapered quantum well detector [7]. The flared pre-amplifier employs lateral flaring from 3 μm to 12 μm in order to increase the output saturation power. The absorber makes use of the offset quantum wells to obtain a high absorption coefficient. The detector is tapered from 9 μm to 2 μm to prevent saturation at the front end and uses BCB to reduce pad capacitance. A parallel-plate capacitor is formed by sandwiching SiN_x between the n-contact layer and p-metal is fabricated on-chip for biasing purposes.

The wavelength converter's dual-quantum-well epitaxial structure is comprised of two sets of quantum-wells as described in [8]. A set of offset quantum-wells (λ_{PL} = 1542 nm) are used in the gain section of the SGDBR and the SOAs. A separate set of seven quantum-wells (λ_{PL} = 1455 nm) centered in the InGaAsP waveguide are used for efficient modulation. Both sets of wells are used in the absorbing region. The fabrication of this device requires a single InP/InGaAs blanket regrowth following the selective removal of the offset quantum-wells from the passive sections and the etching of holographically defined gratings. Following fabrication, the devices were thinned, cleaved and mounted onto an aluminum nitride carrier for testing.

3. Experiments

All contacts were wirebonded to the carrier and contacted via a probe card. An on-carrier capacitor and 2 Ω damping resistor were wirebonded in parallel to the on-chip capacitor to provide a path for low frequency signal components. No bias tees were used, and all biases were applied with a DC probe card. The wavelength converter biasing configuration is shown in Fig. 2.

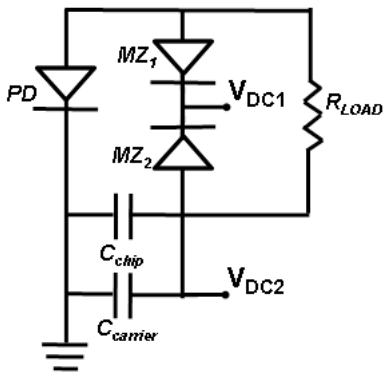

(a) Biasing Schematic

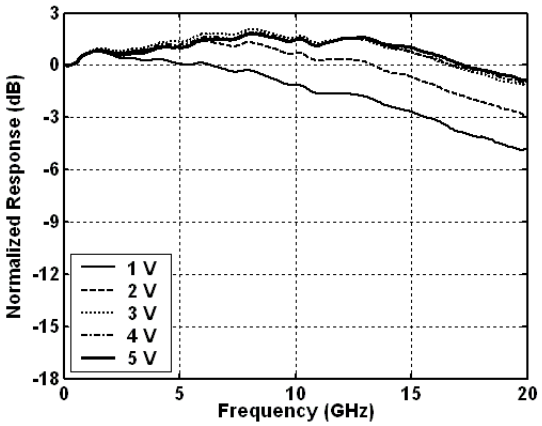

(b) Small signal response for R_{load} = 25 Ω, V_{DC2}-V_{DC1}=-2 V and varying bias for V_{DC2}.

Fig. 2.

The small signal response of the device was measured using a HP8703A network analyzer. The wavelength converter demonstrated greater then 20 GHz bandwidth as shown in Fig. 2. A slight bandwidth enhancement is seen due to the mismatched impedances of the termination (25 Ω) and the MZM coplanar stripline (53 Ω).

An SHF 40 Gbps Bit Error Rate Tester (BERT) was used to take bit error rate measurements at 40 Gb/s with a 2^7-1 pseudo-random bit sequence (the word length was limited by the BERT). The NRZ output signal from the SHF

BERT was amplified with a high power Erbium Doped Fiber Amplifier (EDFA). The signal traveled through a polarizer and optical filter before being coupled into the wavelength converter. The output of the wavelength converter was fed directly to the BERT's preamplified receiver. A high-speed probe with a 50 Ω load was placed in parallel to the on-chip termination to reduce the effective termination to 17 Ω to enhance the bandwidth. In future devices a smaller resistor can be fabricated on chip removing the need for the high-speed probe. Fiber coupled input power of 0.4 mW produced 28 mA of photocurrent used to drive the modulator. Data was converted from 1550 nm to output wavelengths of 1529 nm, 1545 nm and 1561 nm. The conversion range is limited by the tuning range of the SGDBR. Error free operation was observed for all wavelengths with power penalties of 1.5 dB – 2.5 dB.

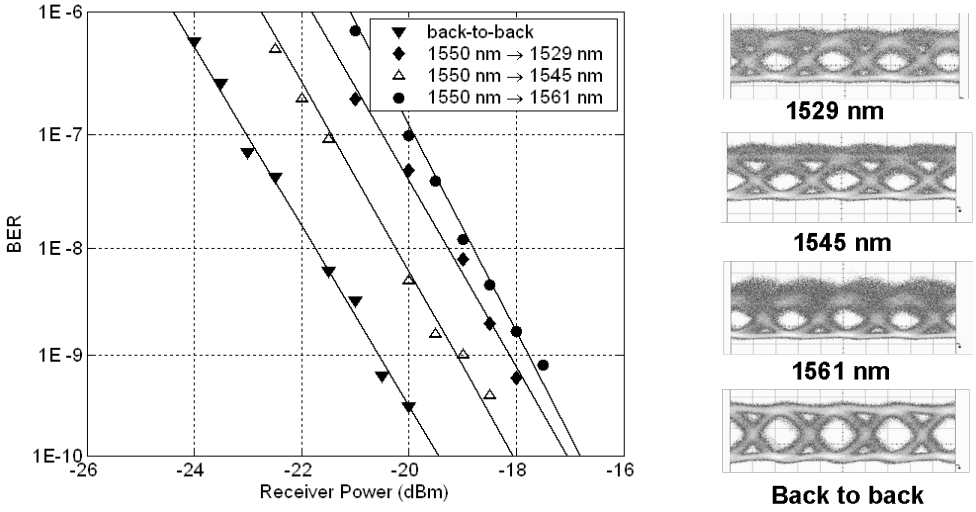

(a) BER at 40 Gbps with a 2^7-1 pseudo-random bit sequence.

(b) Eye Diagrams

Fig. 3. 40 Gbps measurement results. (I_{gain} = 130 mA; I_{TxSOA} = 110 mA; I_{RxSOA1} = 185 mA; I_{RxSOA2} = 250 mA; V_{DC2}-V_{DC1}=-2 V and V_{DC2} = -5.6 V)

4. Conclusion

For the first time a widely tunable SAM Mach-Zehnder based wavelength converter operating at 40 Gbps has been fabricated. The device exhibits greater then 20 GHz bandwidth and error free operation at 40 Gbps with power penalties less than 2.5 dB.

References

1. T. Hatta, T. Miyahara, Y. Miyazaki, K. Takagi, K. Matsumoto, T. Aoyagi, K. Motoshima, K. Mishina, A. Maruta, and K. Kitayama, "Polarization-Insensitive Monolithic 40-Gbps SOA MZI Wavelength Converter With Narrow Active Waveguides," *IEEE Journal of Selected Topics in Quantum Electronics*, vol. 13, no. 1, pp. 32–39, 2007.
2. V. Lal, M. L. Masanovic, J. A. Summers, G. Fish, and D. J. Blumenthal, "Monolithic Wavelength Converters for High-Speed Packet-Switched Optical Networks," *Selected Topics in Quantum Electronics, IEEE Journal of*, vol. 13, no. 1, pp. 49–57, 2007.
3. M. Sysak, J. Raring, J. Barton, M. Dummer, A. Tauke-Pedretti, H. Poulsen, D. Blumenthal, and L. Coldren, "Single-chip, widely-tunable 10 Gbit/s photocurrent-driven wavelength converter incorporating a monolithically integrated laser transmitter and optical receiver," *Electronic Letters*, vol. 42, pp. 657–658, May 25 2006.
4. J. W. Raring and L. A. Coldren, "40Gb/s Widely-Tunable Transceivers," *Journal of Selected Topics in Quantum Electronics*, vol. 13, no. 2, 2007.
5. A. Tauke-Pedretti, M. Sysak, J. Barton, J. Raring, L. Johansson, and L. Coldren, "40-Gb/s Series-Push-Pull Mach–Zehnder Transmitter on a Dual-Quantum-Well Integration Platform," *IEEE Photonics Technology Letters*, vol. 18, pp. 1922–1924, September 15 2006.
6. R. G. Walker, "High-speed III-V semiconductor intensity modulators," *IEEE J. Quantum Electron.*, vol. 27, pp. 654–667, Mar. 1991.
7. A. Tauke-Pedretti, M. Dummer, J. S. Barton, M. N. Sysak, J. W. Raring, and L. A. Coldren, "High Saturation Power and High Gain Integrated Photoreceivers," *IEEE Photon. Technol. Lett.*, vol. 17, pp. 2167–2169, Oct. 2005.
8. M. Sysak, J. Raring, J. Barton, M. Dummer, D. Blumenthal, and L. Coldren, "A single regrowth integration platform for photonic circuits incorporating tunable SGDBR lasers and quantum-well EAMs," *IEEE Photonics Technology Letters*, vol. 18, pp. 1630–1632, August 2006.

Widely Tunable 10 Gbps Separate Absorption and Modulation Mach-Zehnder Wavelength Converter

A. Tauke-Pedretti, M. Dummer, J. S. Barton, M. N. Sysak, J. W. Raring, J. Klamkin and L. A. Coldren

A fully monolithic separate absorption and modulation region wavelength converter requiring no bias tees has been fabricated. The device consists of a transmitter comprised of a sampled-grating DBR laser and series-push-pull Mach-Zehnder modulator, and a receiver composed of a linear semiconductor optical amplifier and a quantum well pin *photodetector. The wavelength converter has a 13 GHz bandwidth and demonstrates error-free operation at 10 Gbps with unity gain.*

Introduction: Wavelength converters will be an important part of the next generation of optical networks, allowing for dynamic wavelength management and enabling all-optical routers. Devices with bit-rate transparency, small form factors and low power consumption will best meet the demands of these networks. Monolithic devices lend themselves particularly well to these challenges. Semiconductor optical amplifier (SOA) based devices have been extensively studied, however these devices are inherently limited by carrier lifetime. Efforts in overcoming the carrier lifetime limitation with delayed interference have been successful, however these devices still have optical filtering requirements and are limited to return-to-zero (RZ) data formats [1], [2]. Recently there has been success with the separate absorption and modulation (SAM) approaches to wavelength conversion [3], [4] with electroabsorption modulators (EAM). Due to the spatial separation of the input and output waveguide, these devices have the advantage of no optical filtering requirement and are capable of converting to the input wavelength. Replacing the EAM with a Mach-Zehnder modulator (MZM) will allow for high extinction ratios and zero or negative chirp.

This paper presents a fully monolithic SAM wavelength converter utilizing a series-push-pull MZM. The wavelength converter is composed of a linearly flared SOA pre-amplifier, a tapered quantum well photodiode, a five section widely tunable laser and a series-push-pull MZM. External bias tees were not used; instead a capacitor and resistor were monolithically integrated on the wavelength converter chip to reduce signal attenuation and simplify biasing.

Device: The device was fabricated on an offset quantum well integration platform using ridge waveguides [5]. The epitaxial structure consists of an InGaAs n-contact layer, n-InP cladding, InGaAsP waveguide and a set of seven quantum wells all grown on a semi-insulating InP substrate. The use of a semi-insulating substrate is essential in order to isolate the semiconductor resistor as well as the receiver and transmitter grounds as required for biasing; an added benefit is a capacitance reduction for high-speed pads. The offset quantum wells (λ_{PL} = 1540 nm) provide gain for the SGDBR and SOAs when forward biased and absorption for the photodetector when reverse biased. The selective removal of the offset quantum wells from the passive sections and the etching of holographically defined sampled gratings is followed by a blanket regrowth of the p-InP cladding and p-InGaAs contact layer.

The SGDBR laser consists of five sections – an active absorber, a rear mirror, a phase section, a gain section, and a front mirror. A 500 μm-long SOA following the laser increases the output power of the device and compensates for propagation losses. A flared and curved output waveguide combined with an AR coating is used to reduce optical reflections and to enhance coupling efficiency.

The 300 μm-long MZM is operated in a series-push-pull fashion with the photocurrent signal applied across tops of the Mach-Zehnder arms. The capacitance associated with the two MZM arms are in series effectively halving the device capacitance and increasing the bandwidth. This configuration also provides small chirp values since the push-pull modulation cancels the modulation induced chirp [6]. An integrated 32 Ω semiconductor resistor fabricated from the n-contact layer provides on chip termination. The MZM was designed to operate as a traveling-wave device in order to achieve the bandwidth necessary for high speed operation. Due to the capacitance and resistance associated with the modulator ridge, the MZM coplanar striplines were periodically capacitively loaded using six 50 μm long T-electrodes in order to achieve a characteristic impedance close to 40 Ω [6], [7]. To further reduce the capacitance photo-bis-benzocylcocutene (BCB) is used as a low-k dielectric under the high-speed electrodes and the ridge width is reduced from 3 μm in the laser and SOA regions to 2 μm within the modulators. A forward biased phase section tunes the Mach-Zehnder interferometer to maximize the extinction ratio.

The receiver section consists of a 500 μm long straight SOA, a 550 μm long high-saturation power SOA and a 35 μm long tapered quantum well detector [8]. The high-saturation power amplifier employs lateral flaring from 3 μm to 12 μm in order to increase the output saturation power. Both SOAs are operated below their 1 dB saturation point to prevent signal distortion. The photodetector makes use of the offset quantum wells to obtain a high absorption coefficient. The 9 μm wide front end prevents saturation due to high photocurrent levels and lateral tapering down to 2 μm reduces capacitance. An on-chip parallel plate capacitor has been fabricated to provide an on-chip path to ground for the microwave signal components. This 20 pF capacitor is formed by sandwiching 300 nm of SiN_x between the n-contact layer and p-metal.

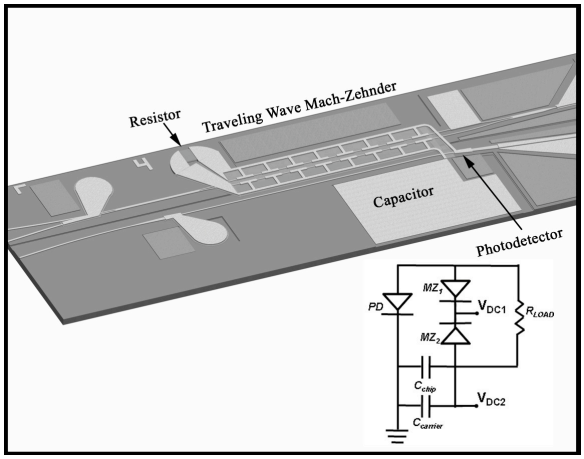

Fig. 1. Close-up of the modulator and photodiode section of the SAM wavelength converter. The schematic of the biasing scheme is shown in the lower right.

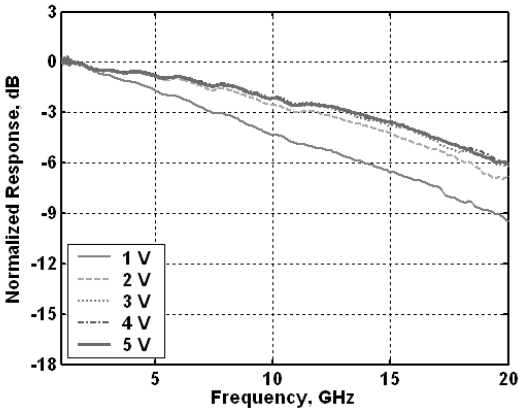

Fig. 2. Small signal response of the wavelength converter for sweeping V_{DC2} with the voltage across the MZM arm held at V_{MZ1} = 1 V.

Experiments: Following fabrication, the device was mounted on an AlN carrier, all contacts were wirebonded to the carrier and a DC probe card was used to apply all biases. An on-carrier chip capacitor was wirebonded in series with the on chip capacitor to act as a low frequency bypass capacitor. Additionally, a small (2 Ω) resistor was placed in series with the carrier capacitor to dampen LC resonances from the wirebonds. This simple biasing configuration keeps the microwave signal components on chip and increases scalability. The wavelength converter biasing configuration is shown in Fig. 1. All measurements were taken at a stage temperature of 15^o C.

Small signal measurements of the wavelength converter showed a 3-dB bandwidth of 13 GHz (Fig. 2). The voltage across the photodiode was swept for this measurement. There is a bandwidth improvement with voltage due to the depletion of the waveguide which decreases the capacitance. Characterization of discrete 300 μm MZMs demonstrated a 3-dB bandwidth greater than 20 GHz when terminated in 25 Ω and a V-pi of 2.25 V from single-sided DC extinction measurements. The detectors require reverse bias voltages of -5 V to prevent trapping the photo-generated carriers in the quantum wells which would create space charge effects that degrade the device bandwidth. When operated at this bias point discrete 50 μm long

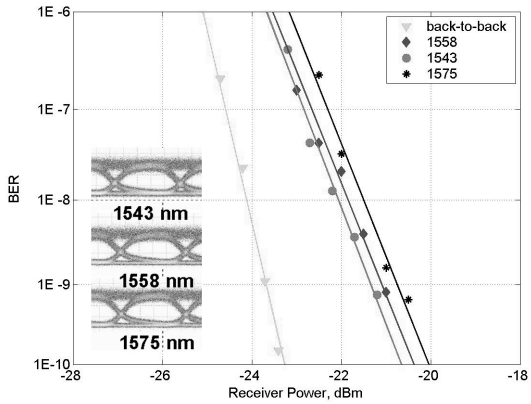

Fig. 3. BER measurements at 10 Gbps for wavelength conversion from 1548 nm to 1543 nm,1558 nm and 1575 nm.

photodetectors displayed no saturation characteristics for photocurrent levels as high as 40 mA and 3-dB bandwidths of 20 GHz when terminated in 25 Ω.

Bit-error-rate (BER) measurements at 10 Gbps were taken with a non-return-to-zero (NRZ) 2^{31}-1 pseudo-random bit stream (PRBS). The measurement setup consisted of a commercial transmitter which was amplified by an erbium-doped fiber amplifier (EDFA). The signal then passed through an optical filter and polarization controller before being fiber coupled into the device. The output of the wavelength converter was attenuated and then detected by a commercial lightwave receiver.

Error-free operation (BER of 1×10^{-9}) was demonstrated across the SGDBR tuning range with power penalties less than 3.5 dB (Fig. 3). Eye diagrams exhibited extinction ratios of 11.6 dB, 11.3 dB and 11.5 dB for conversion from 1548 nm to 1543 nm, 1558 nm and 1575 nm respectively. The device achieved facet-to-facet unity gain with input and output powers of 0.5 mW. The bias conditions for these measurements were as follows: SGDBR gain: 95 mA, transmitter SOA: 120 mA, straight receiver SOA: 180 mA, flared SOA: 250 mA, Mach-Zehnder: -1 V, photodiode: -5 V with 22 mA of photocurrent.

Conclusion: We have demonstrated a 10 Gbps monolithic SAM Mach-Zehnder wavelength converter. The device consists of a widely tunable laser, a series-push-pull MZM and a high saturation power receiver. The simple biasing configuration requires no external bias tees due to the on-chip resistor and capacitor. Error-free operation at 10 Gbps using NRZ data was achieved across the 32 nm tuning range of the integrated tunable laser with power penalties less then 3.5 dB and unity gain.

A. Tauke-Pedretti, M. Dummer, J.S. Barton, M.N. Sysak, J. Klamkin and L.A. Coldren *(Electrical and Computer Engineering and Materials Departments, University of California, Santa Barbara, CA 93106, USA)*

E-mail:atauke@engineering.ucsb.edu

J.W. Raring *(Sandia National Laboratories, Albuquerque, NM 87185, USA)*

REFERENCES

[1] V. Lal, M. L. Masanovic, J. A. Summers, G. Fish, and D. J. Blumenthal, "Monolithic Wavelength Converters for High-Speed Packet-Switched Optical Networks," *Selected Topics in Quantum Electronics, IEEE Journal of*, vol. 13, no. 1, pp. 49–57, 2007.

[2] P. Bernasconi, W. Yang, L. Zhang, N. Sauer, L. Buhl, I. Kang, S. Chandrasekhar, and D. T. Neilson, "40 Gbit/s RZ wavelength converter in a monolithically integrated chip with a tunable laser," *Electronics Letters*, vol. 41, no. 12, pp. 701–702, 2005.

[3] M. Sysak, J. Raring, J. Barton, M. Dummer, A. Tauke-Pedretti, H. Poulsen, D. Blumenthal, and L. Coldren, "Single-chip, widely-tunable 10 Gbit/s photocurrent-driven wavelength converter incorporating a monolithically integrated laser transmitter and optical receiver," *Electronic Letters*, vol. 42, no. 11, pp. 657–658, May 25 2006.

[4] M. Dummer, M. Sysak, J. Raring, A. Tauke-Pedretti, and L. Coldren, "Widely Tunable Single-Chip Transceiver for 10 Gb/s Wavelength Conversion," in *Device Research Conference (DRC)*, no. II.A-3, University Park, PA, June 2006.

[5] J. S. Barton, E. J. Skogen, M. L. Masanovic, S. P. Denbaars, and L. A. Coldren, "A widely tunable high-speed transmitter using an integrated SGDBR laser-semiconductor optical amplifier and Mach-Zehnder modulator," *Selected Topics in Quantum Electronics, IEEE Journal of*, vol. 9, no. 5, pp. 1113–1117, 2003.

[6] R. G. Walker, "High-speed III-V semiconductor intensity modulators," *IEEE J. Quantum Electron.*, vol. 27, pp. 654–667, Mar. 1991.

[7] R. Spickermann and N. Dagli, "Experimental analysis of millimeter wave coplanar waveguide slow wave structures on GaAs," *IEEE Transactions on Microwave Theory and Techniques*, vol. 42, no. 10, pp. 1918–1924, October 1994.

[8] A. Tauke-Pedretti, M. Dummer, J. S. Barton, M. N. Sysak, J. W. Raring, and L. A. Coldren, "High Saturation Power and High Gain Integrated Photoreceivers," *IEEE Photon. Technol. Lett.*, vol. 17, no. 10, pp. 2167–2169, Oct. 2005.

A 10 Gb/s Monolithically Integrated, Filterless, InGaAsP/InP Widely Tunable Wavelength Converter with Conversion Gain

Matthew N. Sysak, *Member IEEE*, James W. Raring, *Member, IEEE*, Jonathon S. Barton, *Member IEEE*, Henrik N. Poulsen, *Member, IEEE*, Daniel J. Blumenthal, *Fellow, IEEE*, and Larry A. Coldren, *Fellow, IEEE*

***Abstract*—In this letter we present the details of a monolithically integrated, filterless, wavelength converter based on photocurrent driven technology. The device consists of an integrated tunable laser transmitter and optical receiver. The transmitter includes a sampled grating DBR laser, electroabsorption modulator, and semiconductor optical amplifier. The optical receiver employs two semiconductor optical amplifiers and a PIN quantum well photodetector. The wavelength converter is characterized at 10 Gb/s over a variety of bias conditions at various input power levels in various digital system experiments. Bit-Error Rate measurements at 10 Gb/s over an output tuning range of 32 nm between 1531 and 1563 nm show power penalties less than 1 dB. Similar experiments over an input wavelength range of 25 nm from 1535 nm to 1560 nm show a power penalty less than 2.5 dB. For wavelength conversion from 1548 nm to a range of output wavelengths between 1531 and 1563 nm, the facet to facet gain ranges from 9-13 dB neglecting fiber coupling losses.**

***Index Terms*—Monolithic integrated circuits, optoelectronic devices, wavelength conversion, wavelength division multiplexing.**

I. Introduction

As bit rates and data traffic levels scale in optical communications systems, dynamic wavelength management is viewed as critical to reduce blocking probabilities and provide added flexibility to network architectures. Currently, dynamic wavelength switching is performed with the use of optical-electrical-optical (OEO) repeaters that are placed at high traffic network nodes. While these repeaters have been shown to be a viable solution at bit rates up to 10 Gb/s and are currently moving towards 40 Gb/s, they suffer from a variety of drawbacks. Repeaters usually consist of several discrete components that have been co-packaged together to perform wavelength management. Though this approach does allow for individual optimization of each discrete device, it suffers from inherent insertion loss issues that occur when multiple components with different optimal optical mode profiles are connected together. The narrow alignment tolerances that are created by these mismatched optical interfaces lead to complex packaging requirements that add cost and production time before the device can be brought to market. The other key drawback to OEO repeaters is their inherent dependence on electronic circuit components. Particularly at high data rates, electronic circuit elements can be quite complex and require significant amounts of power [1].

As an alternative to using these OEO repeaters for wavelength switching functionality, several monolithically integrated, small form factor all-optical wavelength switching elements have been proposed and demonstrated. Integrated devices that can combine several functionalities together on a single photonic chip offer significantly lower packaging costs with reduced power dissipation along with the potential for eliminating complex electronics. Examples of these integrated devices and the technologies that are utilized for wavelength switching include cross gain and cross phase modulation using optical amplifiers in interferometric structures [2], cross absorption and photocurrent effects in electroabsorotion modulators (EAMs) [3], photocurrent based optical gates [4], and wave mixing approaches in fiber and optical amplifiers [5]. In the case of photocurrent based optical gates, excellent switching performance has been demonstrated with extinction ratios in excess of 10 dB and bit-rates up to 500 Gb/s.

Recently, several of these wavelength switching elements have moved towards incorporating even more functionality onto a single small form factor device. Of particular interest in terms of adding new capabilities is an on-chip laser source [6]. Adding a laser to the integrated wavelength converter is attractive since it can enable further reduction in optical loss, and hence packaging costs and complexity. However, the integration of an on-chip laser source presents a new set of challenges. Previously, filterless wavelength conversion using cross absorption, cross phase and cross gain effects simply mandated counter-propagating optical pump and data signals. With an integrated laser, this is more challenging since the

Manuscript received July 31, 2006. This work was supported by DARPA/MTO CS-WDM under grant No. N66001-02-C-8026 and by Intel Corporation under grant No. TXA001630000.

The authors are with the Department of Electrical Engineering and the Department of Materials at the University of California Santa Barbara. Santa Barbara, CA 93116 USA (e-mail: mnsysak@engineering.ucsb.edu)

stability of the optical source requires tight control of any optical feedback. Several potential solutions to this issue have been proposed and demonstrated that use filtered co-propagating signals. These include cascaded wavelength converters, Dual-Order-Mode-Operation (DOMO) approaches and MMI based filtering [7,8]. However, it has been difficult to demonstrate a fully transparent, single stage solution due to optical beating effects between the on-chip pump and data signals when wavelength switching is not desired [7].

As a solution to these filtering issues, a set of devices has been demonstrated using a photocurrent driven approach where an on-chip optical receiver is used to drive a monolithically integrated electroabsorption modulator and tunable laser [9]. Similar to the other wavelength conversion techniques, this device does not require electronics aside from a simple bias-tee and load resistor. However, the key benefit to this approach is that the optical input and output signals are physically separated from one another. This eliminates the possibility of optical interference between common wavelength input and converted signals and problems with integrated laser stability. Furthermore, the integration of a tunable source allows for broadband wavelength conversion where switching between identical wavelengths is desired.

In this work we describe in detail the characterization and digital switching performance of a monolithically integrated EAM-based photocurrent driven wavelength converter (PD-WC). The device incorporates a widely tunable laser and a high gain broadband optical receiver, which makes it ideal for wavelength switching with complete wavelength transparency with no optical filtering requirements regardless of input or output wavelength. Although this device has been successfully used for 2R extinction ratio (ER) regeneration and signal re-amplification [10], and 3R regeneration including 2R regeneration with signal retiming [11], this article focuses on the wavelength switching aspects of the PD-WC without regeneration.

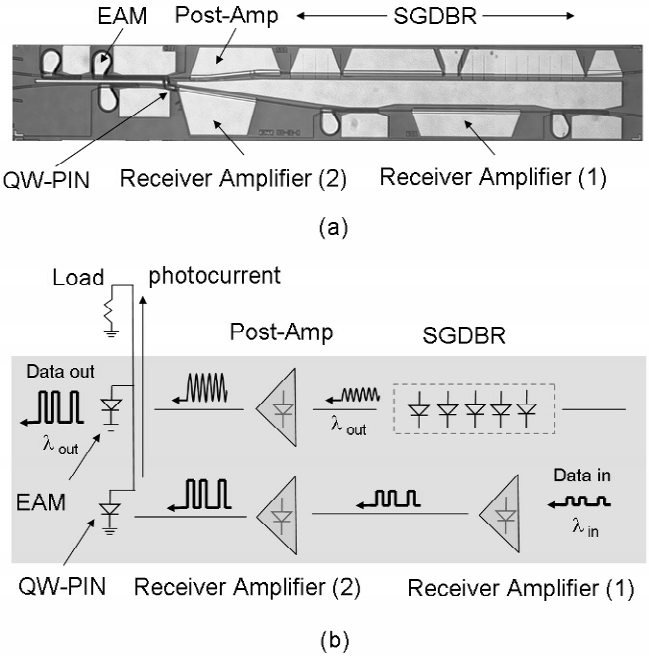

Fig. 1. (a) Scanning Electron Micrograph (SEM) of integrated photocurrent driven wavelength converter. The receiver section contains two SOAs and a QW-PIN photodetector. The transmitter contains a widely tunable four section SGDBR laser, transmitter SOA and an EAM. (b) Operating diagram of integrated PD-WC including details of the receiver amplification process and the wavelength conversion process.

II. Device Overview

The PD-WC used in this work consists of a monolithically integrated optical receiver and tunable transmitter in a parallel ridge architecture. A scanning electron micrograph image (SEM) along with a functional schematic of the device is shown in Fig. 1. The transmitter ridge includes a widely tunable sampled grating DBR (SGDBR) laser [12], a 550 μm semiconductor optical amplifier (SOA) and a 400 μm EAM. The receiver ridge contains a set of two SOAs and a 50 μm long quantum well (QW)-PIN photodetector. The photodetector ridge width is linearly tapered from 12 μm to 3 μm for increased saturation current while maintaining relatively low capacitance. The first SOA is 600 μm long and 3 μm wide. The second SOA is 400 μm long and has an exponentially flared waveguide width (3 μm to 12 μm). This geometry enhances the 1-dB output power compression of the amplifier as described in Section IV, subsection A of this paper. A Ti/Pt/Au metal line connects the photodetector and EAM contacts. A common DC bias is applied to both EAM and QW-PIN through an external bias tee. The EAM and QW-PIN share an electrical ground. A 50 Ω load resistor on the RF port of the bias tee sets the device bandwidth.

The wavelength conversion process begins when light is coupled into the receiver waveguide and is amplified by the two on-chip receiver SOAs. After the receiver SOAs, the amplified input is detected by the reverse biased QW-PIN photodetector. The 35-μm long Ti/Pt/Au interconnect routes the amplified photocurrent signal form the photodetector to the EAM on the transmitter ridge and through the bias tee to the load resistor. The photocurrent drops across the load resistor, inducing a voltage change on the EAM. This voltage modulation changes the EAM transmission characteristics thus transferring the input signal from the receiver to the output wavelength of the tunable laser.

To demonstrate the filtering characteristics of this device, a set of optical spectra from the output of the PD-WC were collected using an optical spectrum analyzer (OSA). The collected spectra are shown in Fig. 2. The "converted signal" data trace shows an output spectrum from the fully operational PD-WC tuned to an output wavelength of 1553 nm. In this case, the receiver SOAs are biased at 6 kA/cm^2, both the QW-PIN and EAM are biased to -2V, and the SGDBR and post-amplifier SOA are biased at 100 mA and 130 mA respectively. For an input signal to the integrated receiver at 1548 nm with -11 dBm of fiber coupled optical power, the output spectra from the PD-WC shows no indication of the input signal. The small peaks in the converted signal are a result of the mirror reflectivity spectrum in the sampled grating DBR laser.

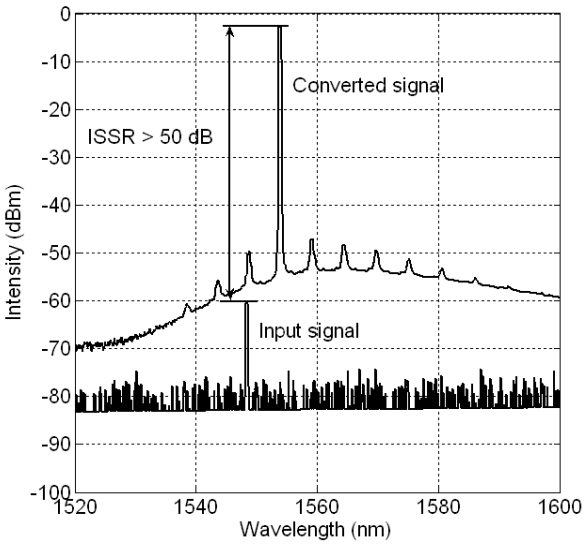

Fig 2. Input signal suppression ratio (ISSR) for the PD-WC operating with an input fiber coupled power of -11 dBm and an input wavelength of 1548 nm. The output wavelength is 1553 nm.

For the "input signal" curve, the output from the wavelength converter is shown with the transmitter turned off, but with the receiver amplifiers and QW-PIN biased as in the "converted signal" case with the same input power (-11 dBm). The "input signal" case represents the amount of light that manages to propagate from the input to the receiver, to the output lensed fiber that collects the wavelength converted signal from the transmitter. Taking the ratio of the peak power from the PD-WC in the "converted signal" case to the peak power in "input signal" case gives the input signal suppression ratio (ISSR). For the PD-WC, results from Fig. 2 show an ISSR > 50 dB.

III. Integration Platform

The wavelength converter is fabricated in the InP/InGaAsP material system using a dual quantum well (DQW) integration platform [13]. A schematic of the epitaxial layers used in device fabrication is shown in Fig. 3. This platform is similar to the commonly used offset quantum well (OQW) integration approach where a set of quantum wells above an optical waveguide region is used for optical gain and subsequently selectively removed to form EAM and passive waveguide routing regions. The removal step is followed by a single MOCVD InP regrowth over the entire wafer after which shallow ridges are patterned and etched.

In the DQW approach, the optical waveguide layer includes a second quantum well stack that has been shown to enhance modulation efficiency, increase device bandwidth, and reduce chirp of the integrated EAMs compared with the Franz-Keldysh modulators available on the OQW platform [14].

The offset quantum wells above the waveguide layer consist of 7x6.5 nm compressively strained wells and 8x8 nm tensile strained barriers. The photoluminescence (PL) peak is at 1550 nm. The waveguide quantum well stack consists of 7x9 nm compressively strained wells and 6x5 nm tensile strained barriers with a PL peak of 1480 nm. The PL of the waveguide

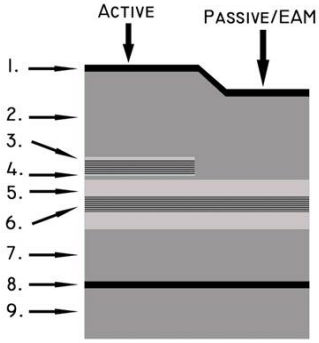

Region	Description
1	p-contact
2	p-cladding
3	Offset QWs
4	Stop Etch
5	Waveguide
6	Centered QWs
7	n-Buffer
8	n-contact
9	InP:Fe-substrate

Fig. 3. Dual quantum well integration platform with individual layer structure details.

wells has been selected to minimize the added optical loss that result from Urbach tails of the waveguide and offset quantum well stacks. The band offsets of the waveguide quantum wells are shallow to limit carrier screening effects in reverse biased EAM regions, and to facilitate efficient transport of injected carriers through the waveguide region into the offset wells under forward bias conditions. The upper and lower most 50 nm of the waveguide layer are Si doped at $5x10^{16}$ cm^{-3}.

To measure the effect that adding the quantum wells into the waveguide has on laser performance, pulsed measurements of the differential efficiency and threshold current were performed on a set of DQW and OQW broad area lasers (BAL) and narrow active ridge lasers (RL) using a cut-back technique. These measurements were used to extract a material gain curve along with the laser injection efficiency. The OQW test lasers have a waveguide layer with a 1.4 μm bandgap and are uniformly doped $2x10^{17}$ cm^{-3} n-type with Si. Results from the DQW and OQW BAL test structures are shown in Fig. 4. Transparency current density and extracted material gain were 269 A/cm^2 and 764 cm^{-1} for the DQW platform. For the OQW devices, the transparency current density was 246 A/cm^2 and the material gain was 826 cm^{-1}. Using RL differential efficiency and threshold current data, the injection efficiency was 73% and 75% for the OQW and the

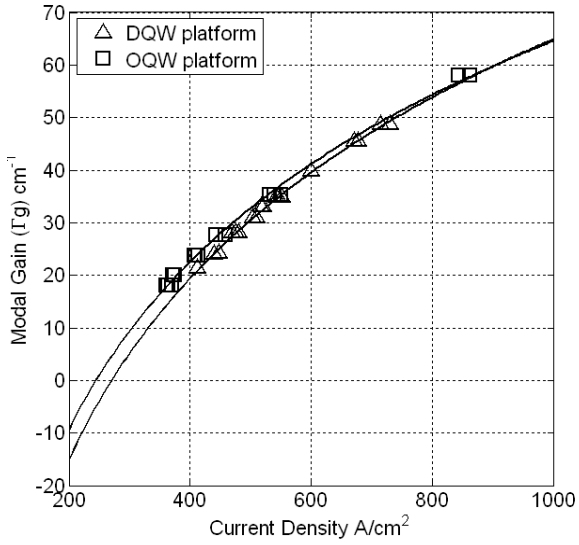

Fig. 4. Modal gain for OQW and DQW platforms. Results are from pulsed measurements of 50 μm wide broad area lasers.

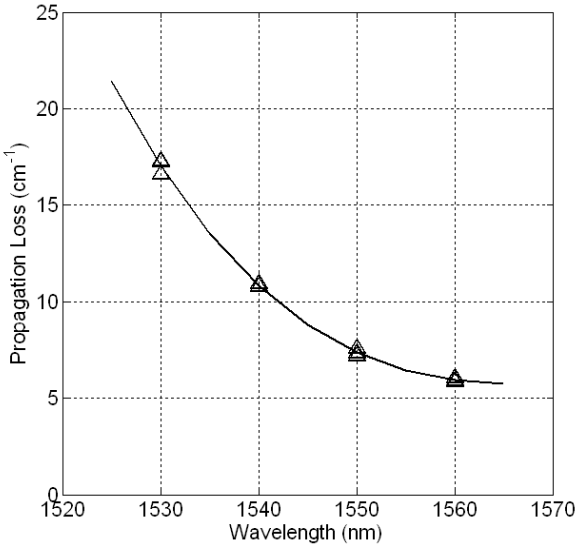

Fig. 5. Passive/EAM region propagation loss (units of cm^{-1}) at various operating wavelengths. Measurements were performed with integrated periodic tap structures.

DQW structures respectively. The excellent agreement in the data between the two platforms indicates minimal parasitic effects on carrier transport properties for active laser regions and optical amplifiers when adding the quantum wells into the waveguide.

The propagation loss has been measured for the DQW platform over a broad wavelength range using a long waveguide with identical periodic photocurrent monitoring structures. The loss is extracted as the ratio of the photocurrents at a fixed distance at each specific wavelength. Results for the wavelength dependent loss are shown in Fig. 5. The exponential increase in the loss is consistent with what is expected from the Urbach tail of the waveguide quantum wells [15].

IV. Integrated Receivers

The integrated wavelength converter receiver consists of two SOA pre-amplifiers followed by a 50 μm QW-PIN photodetector. The amplifiers and photodetector utilize the same offset quantum wells as in the SGDBR laser gain and are either forward or reverse biased depending on whether gain or absorption is desired. Since the offset wells are compressively strained for optimal laser performance, the integrated receiver is polarization sensitive with preferential gain for transverse electric (TE) guided modes. This issue could be circumvented by using a blanket growth and subsequent selective removal of a polarization insensitive offset gain region, similar to that employed for uni-traveling carrier photodetectors and low confinement SOAs [16].

A. Integrated Optical Amplifiers

The two on-chip receiver SOAs are designed to amplify the input signal to the device before the QW-PIN photodetector. For a highly linear and efficient design, this amplification process must be completed while simultaneously minimizing dissipated electrical power and avoiding optical saturation effects. To avoid optical saturation effects, the dimensions of the amplifiers are selected to keep the optical power at any point along each SOA at or below the 1-dB compression point. These required SOA dimensions are kept as small as possible to minimize electrical power dissipation. This receiver is designed for a current density of 6 kA/cm^2. A plot of amplifier gain as a function of SOA length for 3 μm wide amplifier is shown in Fig. 6. A plot of measured and predicted amplifier output power as a function of waveguide width and current density is shown in Fig. 7. The amplifier gain predictions use a many body gain model described in [17].

The first SOA in the integrated receiver is 3 μm wide and 600 μm long. This amplifier width is selected to balance waveguide propagation loss with dissipated power. If the waveguide is too narrow, the propagation loss that results from large modal overlap with the sidewalls becomes significant.

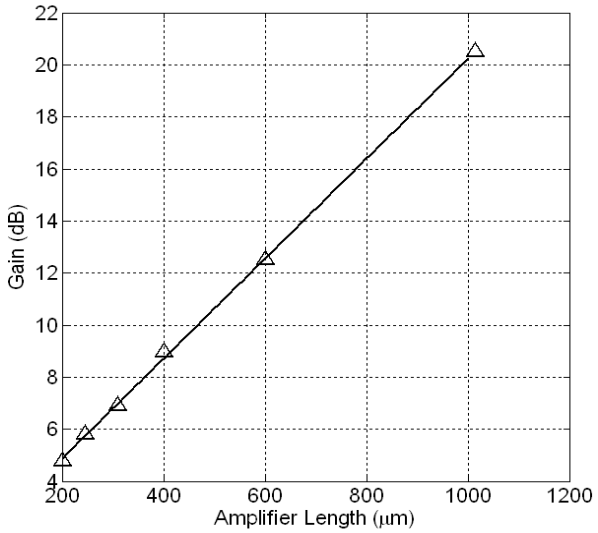

Fig. 6. SOA gain for 3 μm wide ridge waveguide SOAs as a function of device length for 1548 nm, TE polarized input light. The applied current density is 6 kA/cm^2. A trendline is added to guide the eye.

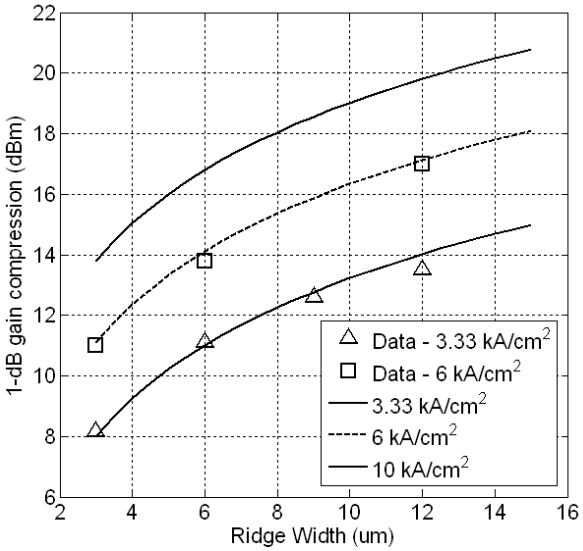

Fig. 7. Measured and simulated 1dB gain compression output powers for integrated receiver SOAs at an operating wavelength of 1548 nm with TE polarized light for various ridge widths and current densities.

The additional loss competes with the amplifier gain and an increase in total current (and hence electrical power) is required to compensate the waveguide sidewall effects as shown in Fig. 7. However, if the waveguide is too wide, the physical dimensions of the device require larger total current to achieve the same current density as in a smaller device. The case of wide amplifiers is particularly problematic since the power dissipation varies as the product of the square of the applied current and the series resistance of the diode. It should be noted that wider amplifiers do have lower series resistance, but the decrease in resistance counteracts only one of the applied current terms, and the overall power dissipation still scales linearly with amplifier width.

Measurements of the propagation loss show a sharp increase from 6 cm^{-1} to 10 cm^{-1} at 1548 nm wavelength when the waveguide width is reduced from 3 μm to 2.5 μm. For wider waveguides (5 μm), the propagation loss is only decreased from 6 cm^{-1} to 5 cm^{-1} at the same wavelength. To keep the waveguide as small as possible without the introduction of excess scattering loss, the waveguide width of the first amplifier is fixed at 3 μm.

The second receiver amplifier is 400 μm long and uses an exponentially flared waveguide width (from 3 μm to 12 μm) along the length of the SOA to allow the optical mode to laterally expand. As the modal cross sectional area increases, the photon density in the offset quantum well stack remains fixed, delaying the amplifier saturation effects and allowing the total waveguide power in the amplifier to increase beyond the 1-dB gain compression of a 3 μm wide SOA. For a 12 μm wide SOA, the output 1-dB gain compression is +17 dBm.

Given that the total length of the entire pre-amplifier is 1000 μm, the estimated gain for the both integrated SOAs is 20.5 dB. It should be noted that although results from the many body gain model shown in Fig. 7 predict further enhancements in the output power gain compression, significant heating issues prevented the bias conditions from exceeding 6 kA/cm^2. Improvements such as flip chip bonding the PD-WC and using a conducting substrate for low device resistance would provide significant improvements in terms of increasing the bias current to the receiver amplifiers.

B. Integrated QW-PIN Photodetectors

The QW-PIN photodetector consists of a reverse biased region that contains the offset quantum wells. The device is 50 μm long with a waveguide width that is linearly tapered from 12-3 μm.

Optically illuminated current-voltage (IV) characteristics for the integrated photodetector in the PD-WC receiver are shown in Fig. 8. For a CW signal fed into the receiver at 1548 nm and SOAs biased at 6 kA/cm^2, the QW-PIN generates a uniform amount of photocurrent for applied reverse bias conditions increasing beyond ~-1V. This is an important characteristic since this allows the reverse bias applied to both the QW-PIN and EAM to be selected independent of concerns for improving the QW-PIN absorption efficiency. Eliminating these concerns makes it possible to select the bias of the wavelength converter based on EAM efficiency optimization.

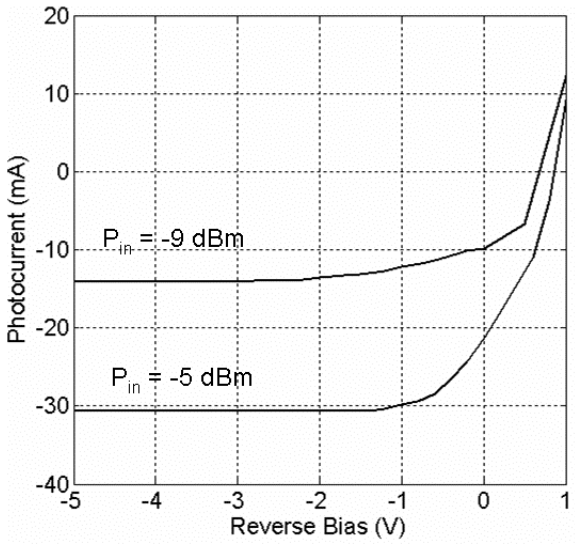

Fig. 8. Optically illuminated QW-PIN IV characteristics. The input signal wavelength is 1548 nm and the polarization is TE. Receiver input power levels are -9 and -5 dBm.

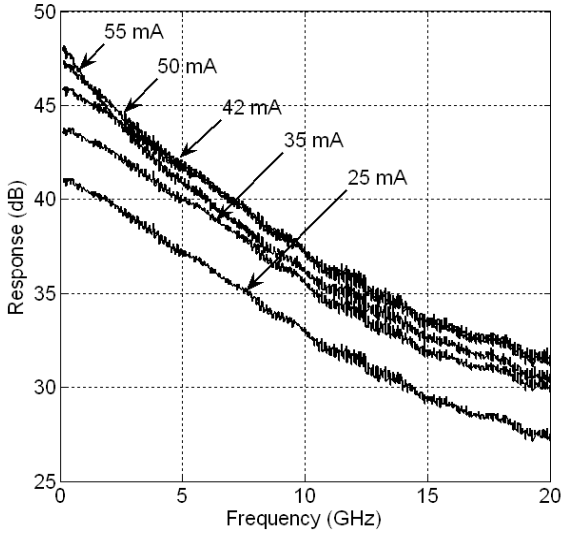

Fig. 9. Measured network analyzer bandwidth and response of QW-PIN photodetector test devices. Results show > 42 mA average photocurrent without bandwidth degradation.

Though these devices can be highly absorbing at low bias, QW-PIN structures typically suffer from front end saturation and carrier screening effects under high optical powers [18]. To counteract these effects, wide area detectors have been shown to be able to reduce the optical photon density at the absorbing medium by spatially spreading the optical mode in a similar manner to what is employed for the on-chip receiver amplifiers. Using this technique in the standard OQW integration platform, QW-PIN photodetectors have previously demonstrated 10 Gb/s operation with output voltage swings of 0.8V peak to peak across a 50 Ω load [19].

To investigate the properties of the wide area dual quantum well platform QW-PIN photodetectors, several test devices have been fabricated that are 100 μm long and 12 μm wide. Results of 50 Ω terminated S_{21} optical to electrical bandwidth as a function of applied bias and detected photocurrent are shown in Fig. 9. Up to 42 mA of average photocurrent can be

accommodated in the QW-PIN structures before the bandwidth of the device is degraded at an applied bias of -3V.

C. Integrated Receiver

The fully integrated receiver DC gain, including both SOA gain and QW-PIN quantum efficiency, is shown in Fig. 10 for various CW input powers at a wavelength of 1548 nm. Results show 20.1 dB of unsaturated optical gain at an applied current density of 6 kA/cm^2. The input and output power levels where the amplifier gain rolls off by 1 dB are -4 dBm and +16.1 dBm respectively.

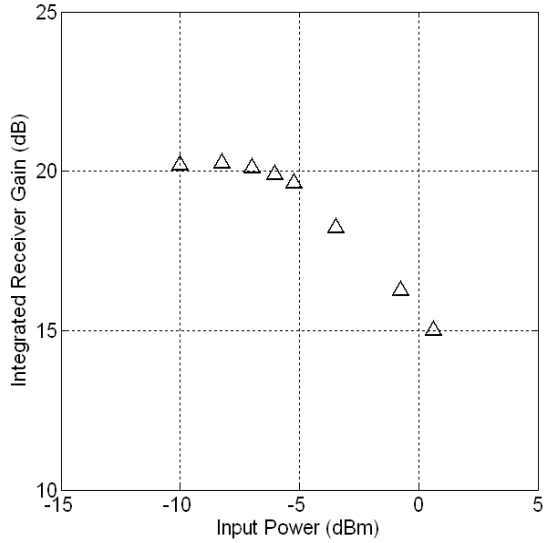

Fig. 10. Integrated wavelength converter receiver DC gain including QW-PIN and both receiver SOAs for 1548 nm TE polarized light. The receiver DC bias is -3 V and the receiver amplifiers were biased at 6 kA/cm^2.

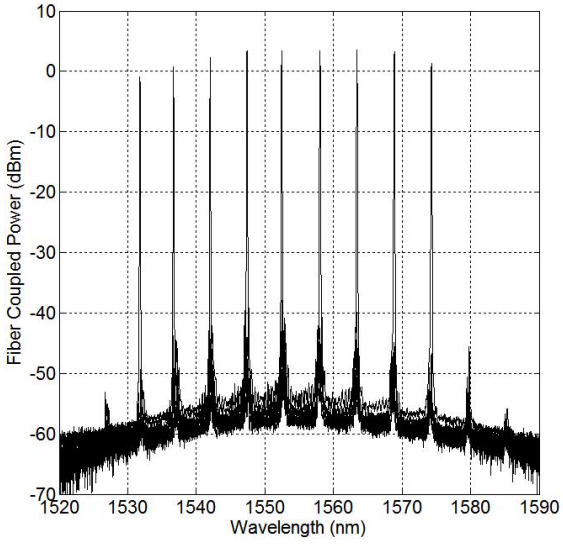

Fig. 11. Overlayed SGDBR fiber coupled output spectra showing tuning from 1532 to 1575 nm and output powers from +5 dBm to – 3 dBm. Laser gain and SOA post amplifier are biased at 100 mA respectively. Fiber coupling loss is 4.2 dB.

V. Integrated Transmitters

The transmitter section of the wavelength converter consists of a four section, widely tunable SGDBR laser along with a back-side absorber, a 550 μm long post-amplifier SOA to boost the laser output power, and a 400 μm long EAM. Overlaid transmitter output spectra with laser gain and SOA post amplifier biased at 100 mA each are shown in Fig. 11. Fiber coupled output power levels ranging between +5 dBm at 1560 nm to -3 dBm at 1532 nm. The fiber coupling loss was 4.2 dB. On-chip light vs. current and IV characteristics from the SGDBR laser were measured by reverse biasing the post-amplifier that follows the laser and are shown in Fig. 12. SGDBR output power at 1550 nm is > 20 mW with a gain bias on chip of 160 mA.

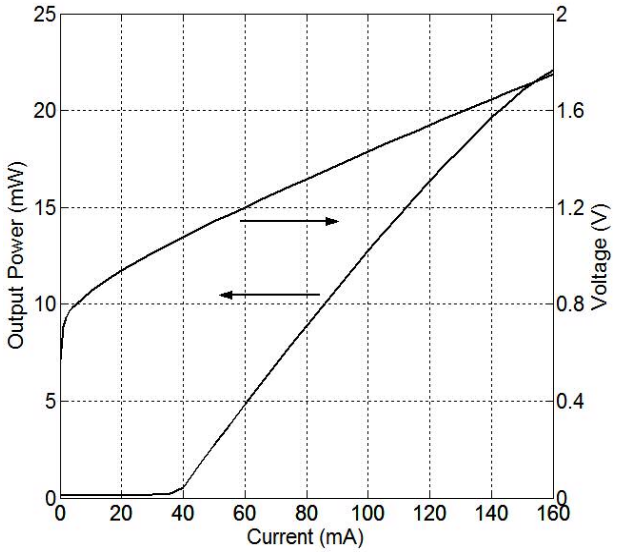

ig. 12. SGDBR IV and light vs. current characteristics measured into ıe reverse biased post-amplifier that follows the laser. Laser output ʻavelength is 1550 nm.

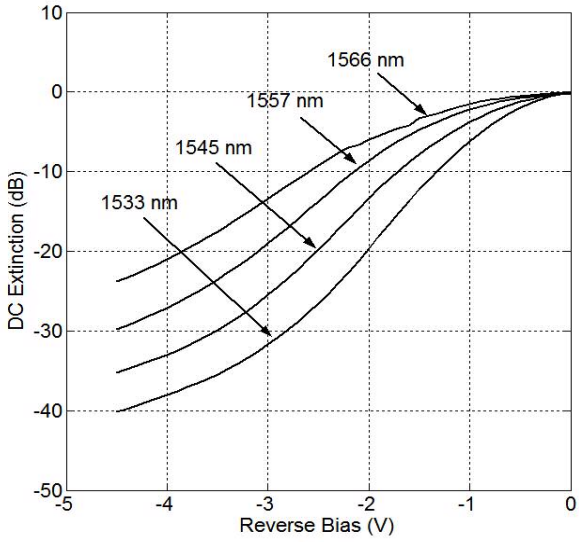

Fig. 13. Broadband DC extinction characteristics of 400 μm long DQW EAM. Measurements are performed by tuning the SGDBR to the indicated wavelength and fiber coupling the output to an optical power meter.

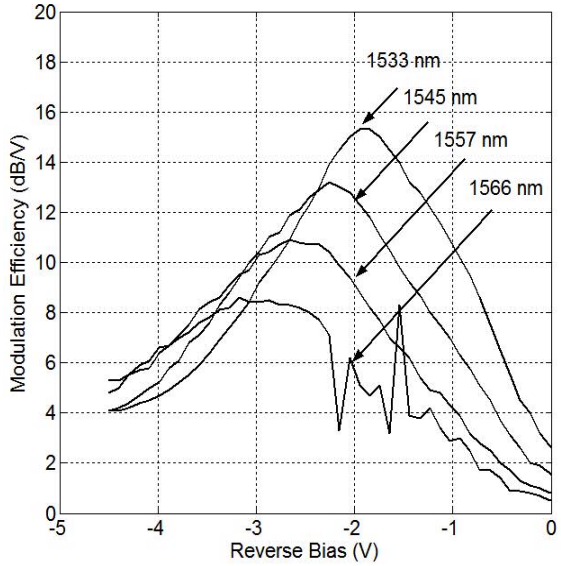

ig. 14. Local slope efficiency dT/dV (dB/V) for the integrated DQW 400 m long EAM. Greater than 8 dB/V can be achieved at all output avelengths at the appropriate DC bias position.

EAM DC extinction and slope efficiency over a range of wavelengths is shown in Fig. 13 and Fig. 14 respectively. For the 400 μm long EAM, greater than 8 dB/V slope efficiency is observed over a 30 nm wavelength range with absolute extinction ranging from 25 to 45 dB at a reverse bias of -4.5V.

The 50 Ω terminated S_{21} electrical to optical bandwidth of the 400 μm long EAM was 11 GHz and showed little variation with up to 17 mA of average photocurrent as discussed in [13].

VI. Dynamic Wavelength Converter Measurements

The Integrated wavelength converters described in section II were thinned, cleaved into bars, anti-reflection (AR) coated, wirebonded, and mounted on copper studs for testing. For characterization of the PD-WCs, the receiver SOAs are biased to 6 kA/cm^2 and the laser gain and transmitter post amplifier are biased to 130 mA and 100 mA, respectively.

The optical to optical 3 dB bandwidth of the 50 Ω terminated PD-WC was measured using a 20 GHz network analyzer for conversion from 1548 to 1555 nm. Results can be seen in Fig. 15 and show a 3-dB bandwidth of approximately 7 GHz with a reverse bias of -2.5 V. Although not included in the plot, the bandwidth of the PD-WC is relatively insensitive to reverse bias levels in excess of -1V. The low bias dependence is due to the low doping levels in both the EAM waveguide and the offsets QWs and the high doping in the InP n-buffer layer (Fig. 3). Once the applied voltage is sufficient to deplete the EAM and QW-PIN waveguides, the doping in the buffer (Si 1x10^{18} cm^{-3}) prevents the depletion width in these components from increasing as the bias voltage is increased. The fixed depletion width clamps the depletion capacitance and preserves the RC time constant that controls the PD-WC bandwidth.

To characterize the switching performance of the PD-WC, the receiver input power, output wavelength, and the applied DC bias conditions have been varied and the wavelength converted output signal extinction ratio and output power have been measured. The converted extinction ratio is measured in the eye diagram where the separation between the "one" and "zero" levels is at a maximum. Characterization is performed with a 1548 nm input signal at 10 Gb/s using a 2^{31}-1 psuedo random bit stream (PRBS). Light from an optical transmitter is fed through an EDFA, an optical filter (0.35 nm), and a polarization controller before being launched into the device using a lensed fiber. The output PD-WC extinction and output power characteristics are measured by examining the fiber coupled optical output into a component analyzer.

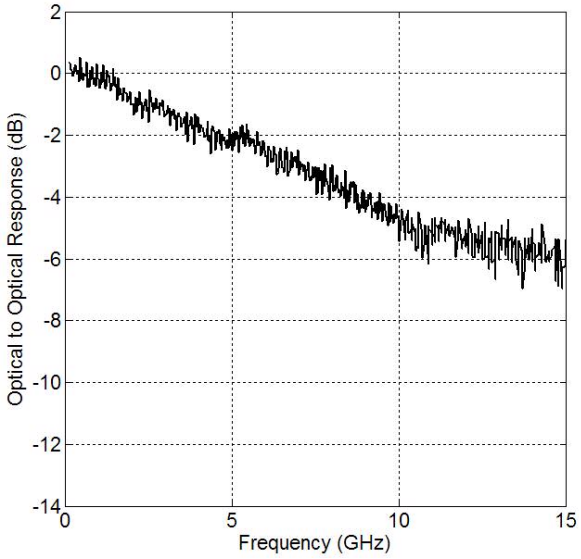

Fig. 15. Optical to optical S_{21} bandwidth measurements for the integrated PD-WC with an external 50 Ω termination. Input and output wavelengths are 1548 nm and 1555 nm respectively.

The effect that increasing the input power to the receiver has on the wavelength converted extinction and average converted fiber coupled output power is shown in Fig. 16. In this experiment, the reverse bias is -2.2V. The input wavelength is 1548 nm and the output of the PD-WC was 1555 nm. Eye diagrams are included in the figure for back to

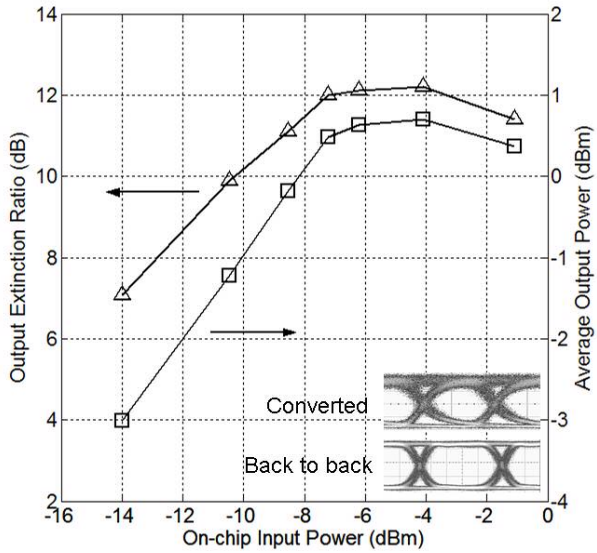

Fig. 16. Average fiber coupled output power and ER for the integrated PD-WC as a function of receiver input power. Applied reverse bias is -2.2V and output wavelength is 1555 nm. Eye diagrams are for back to back and wavelength converted signal with -7 dBm receiver input power.

back and wavelength converted signals with an input power of –7 dBm.

As the input power to the receiver increases, both extinction ratio and output power improve gradually, and then level off at 12 dB and +0.5 dBm respectively.

The shape of the extinction ratio response is due to a combination of EAM efficiency effects and receiver saturation effects. For low input powers where the receiver SOAs can operate in their linear regime, increases in input power create corresponding increases in photocurrent from the QW-PIN and hence an increasing voltage over the load resistor. This increase in voltage generates larger swings in EAM transmission and results in larger PD-WC extinction ratios.

However, as the input power to the receiver continues to increase, several factors begin to limit device performance. As voltage swings from the receiver get larger, the integrated EAM is driven well beyond the optimal slope efficiency point in Fig. 14. Under these conditions, even though the pre-amplified receiver is continuing to generate larger photocurrent levels, the reduced EAM efficiency leads to smaller incremental increases in PD-WC extinction.

The other factor that plays an important role in the wavelength converter extinction is the receiver pre-amplifier response (Fig. 10). As input powers approach the amplifier saturation power, the optical gain from the receiver is degraded. Under these conditions, the shape of the amplified signal to the photodetector becomes distorted by gain overshoot, and the photocurrent that is used to drive the integrated EAM adds significant noise to the converted signals, distorting the extinction ratio from the PD-WC.

The average output power characteristics from the wavelength converter shown in Fig. 16 are controlled by the combination of the "off" state set by the EAM reverse bias and by the extinction ratio at the output of the device. Since the reverse bias in this experiment is fixed, the output power follows the extinction ratio characteristics. For low input powers, the output power from the PD-WC initially increases before finally rolling over due to EAM slope efficiency degradation and amplifier saturation. Since the extinction and output power for the fixed bias conditions used in Fig. 16 do not significantly improve beyond input powers of -7 dBm, further device characterization is performed at this input power.

In the next set of experiments, the wavelength converter output power and extinction ratio performance is characterized over a range of electrical bias voltages and over a range of output wavelengths using the -7 dBm input power. Results are shown in Fig. 17 and Fig. 18 respectively for the wavelength converted extinction ratios and average output powers. Over output wavelengths ranging from 1533 nm to 1564 nm, greater than 10 dB extinction is achievable by setting the appropriate reverse bias conditions. For a particular output wavelength, as the reverse bias is moved toward the bias conditions that correspond with maximum EAM slope efficiency (Fig. 14) the output extinction is improved. However, as the bias is increased and the output extinction improves, the output power from the wavelength converter is reduced. For 10 dB extinction at output wavelengths of 1533nm, 1545 nm, 1555 nm, and 1564 nm, the corresponding reverse biases required are -1.35V, -1.6V, -1. 9V, and -2.4V, and the output powers at these biases are -5.2 dBm, -2.6 dBm, -1 dBm, and -0.5 dBm.

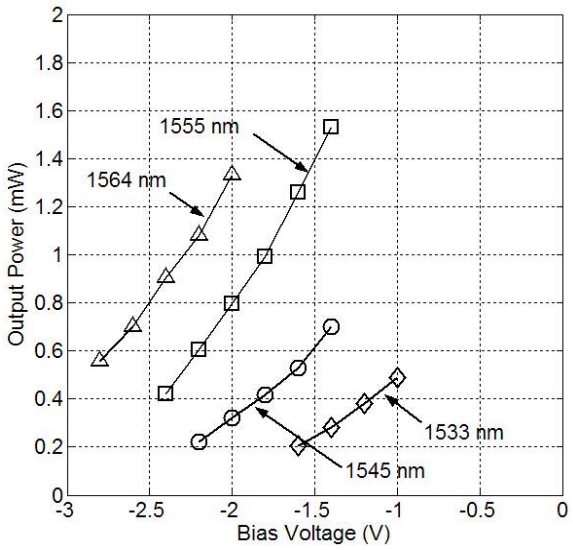

Fig. 17. Average fiber coupled output power vs. wavelength and reverse bias. 10 dB ER bias points are -1.3V, -1.7 V, -2.2V and -2.3V for 1533 nm, 1545 nm, 1557 nm, and 1565 nm respectively. Input wavelength is 1548 nm and input power is -7 dBm.

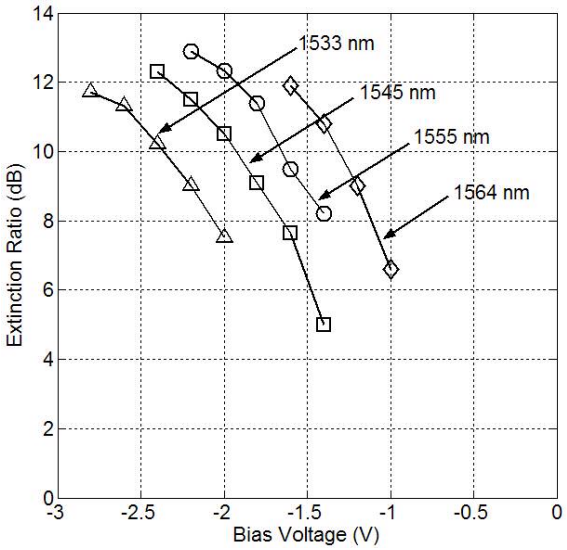

Fig. 18. Wavelength converted ER from the PD-WC. Bias points for 10 dB ER are -1.2V, -1.6V, -1.9V, and -2.4V at output wavelengths of 1533 nm, 1545 nm, 1557 nm, and 1566 nm respectively. Input wavelength is 1548 nm and input power is -7 dBm.

VII. Digital System Experiments

To examine the performance of the integrated wavelength converter in a digital transmission system, a set of bit error rate (BER) measurements were performed using the test setup outlined in Fig. 19. In the first set of measurements, the input power to the PD-WC receiver is identified that minimizes the system power penalty for conversion between 1548 nm and 1563 nm. This input power is then used to perform wavelength switching between a single input wavelength and a range of output wavelengths, followed by switching from a

range of input wavelengths to a single output wavelength. BER measurements were performed using a 2^{31}-1 PRBS at 10 Gb/s with non-return to zero (NRZ) data. SGDBR bias conditions and receiver amplifier bias conditions are the same as outlined in Section VI.

The first set of BER measurements is used to identify the input power to the PD-WC that will give the minimum power penalty for wavelength switching between 1548 nm and 1563 nm. In these experiments, a fixed reverse bias is applied to the EAM and QW-PIN for maximum EAM efficiency (-2.8V). Results for these BER experiments are shown in Fig 20 for input power levels of -7.5 dBm, -10.5 dBm, -11.2 dBm and -12.8 dBm. The power penalty for each PD-WC input power is calculated as the difference in optical power into the external receiver that is required for a BER of 10^{-9} between the wavelength converted signals and the signals from the transmitter in the test setup (back to back). As the power to the receiver increases from –12.8 dBm to -11.2 dBm, BER-results show the power penalty decreases. However, as the receiver power is increased from -11.2 dBm to -10.5 dBm then to -7.5 dBm, the power penalty actually increases, despite an increase in the wavelength converted signal extinction ratio. The increase in power penalty with higher input powers is accompanied by a change in BER slope. The change in slope of the BER curves at higher input powers indicates redistribution of the noise statistics through the device, and most likely comes as a result of saturation effects in the receiver pre-amplifier. This behavior is not necessarily unexpected as other authors have seen similar noise redistribution for pre-amplified receivers operating below their 1 dB gain compression points [20]. The power penalty as a function of input power and the wavelength converted signal extinction ratio for output signals from the PD-WC are summarized in Fig. 21. The figure also contains wavelength converted eye diagrams corresponding to each input power level. In the eye diagrams the additive noise on the "one" level at the higher input powers is a result of the receiver SOA gain overshoot, and most likely contributes to the noise redistribution seen in the BER results in Fig 20.

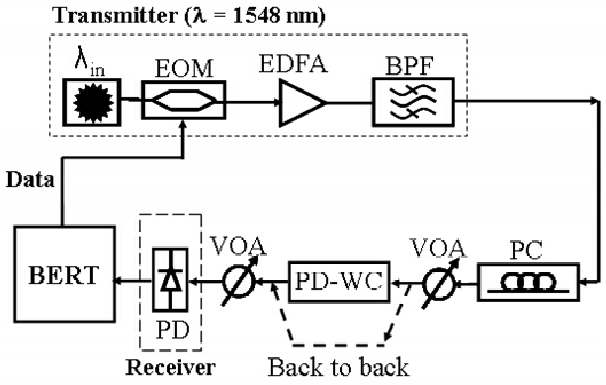

Fig. 19. Test setup used for digital system experiments. For experiments where a non-fixed wavelength input source is used, the transmitter light source (λ_{in}) is replaced with a tunable laser.

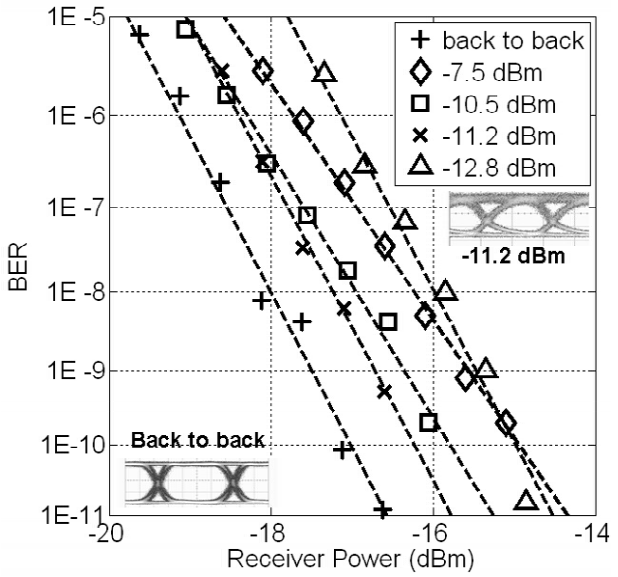

Fig. 20. Wavelength converted and back to back BER measurements for various input powers at a reverse bias of -3.1V. Input and output wavelengths are 1548 and 1563 nm respectively.

Using the optimized input power level (-11.2 dBm), wavelength conversion BER experiments were performed using an input signal at 1548 nm and output wavelength ranging from 1531 nm to 1564 nm. Results are shown in Fig. 22. The reverse bias points at output wavelengths of 1563, 1553, 1542 and 1531 nm were -2.9V, -2.7V, -2.0V, and -1.5 V and were selected to achieve wavelength converted extinction ratios between 8 and 9 dB. A summary of the output extinction and output power of the device at each of these bias conditions (with the 4.2 dB fiber coupling loss removed) is shown in Fig. 23. Taking into account the input facet power of -11 dBm, this gives gain of the wavelength converter of 9dB, 11dB, 12dB, and 13 dBm at output wavelengths of 1531, 1542 nm, 1553 nm, and 1563 nm respectively

The remaining critical factor for broadband operation of the integrated PD-WC is the performance of the device under

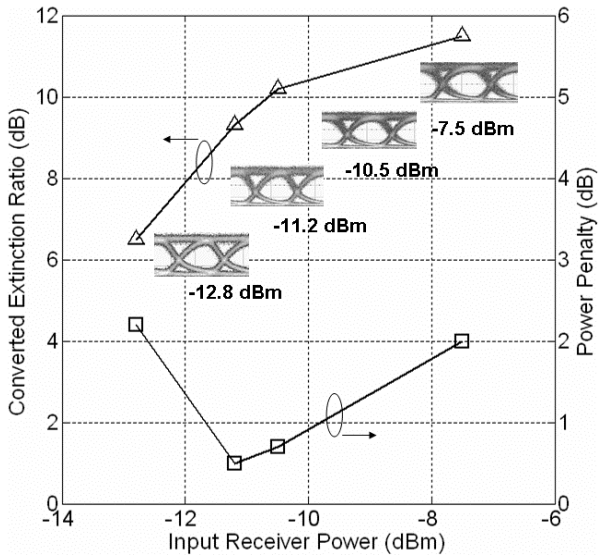

Fig. 21. Summary of wavelength converted extinction ratio and BER power penalty along with eye diagrams from BER experiments using various receiver input powers. Input and converted wavelengths are 1548 and 1563 nm respectively with an applied bias of -2.8V.

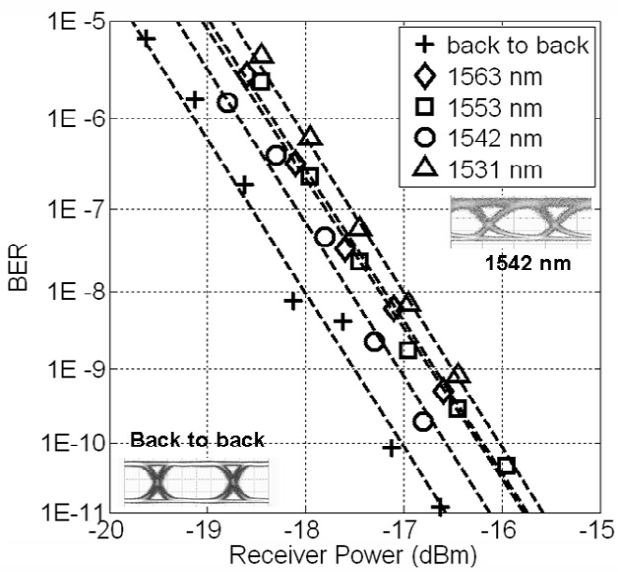

Fig 22. BER measurement results for the PD-WC with an input power of -11 dBm and various output wavelengths. Bias conditions are adjusted to achieve 8-9 dB ER. Input wavelength is 1548 nm.

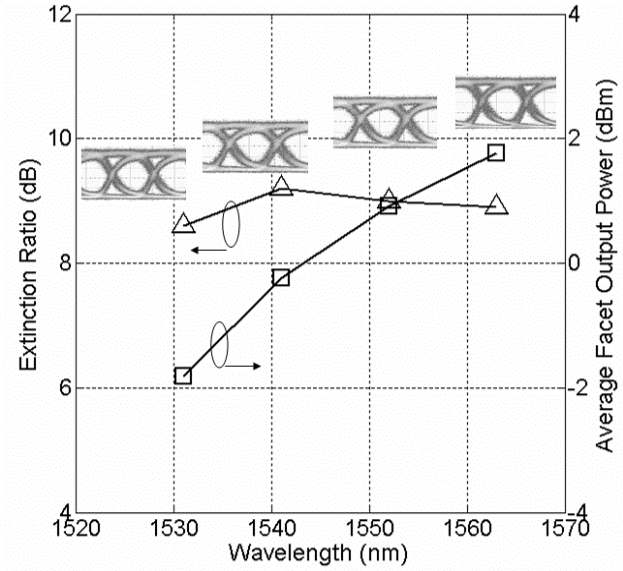

Fig 23. Output extinction and average output facet power (fiber coupling loss removed) in BER measurements to achieve less than 1-dB power penalty for wavelength converted signals.

various input wavelength conditions. A set of BER experiments were performed where the input wavelength was varied between 1535 nm and 1560 nm, and the output wavelength held fixed at 1553 nm. Results are shown in Fig. 24 along with back to back measurements at 1530 nm and 1550 nm. Less than 2.5 dB power penalty is observed when the bias conditions on the PD-WC were set for optimal extinction characteristics. The input power in each of these experiments was held fixed at –11 dBm. Extinction ratios for output wavelength of 1535 nm, 1550 nm, and 1560 nm, were 7.4 dB, 9 dB, and 6.5 dB, respectively. The lower extinction ratios at input wavelengths of 1530 and 1560 nm are a result of the increase in optical loss at the low end of the wavelength spectrum shown in Fig. 5, and a decrease in optical gain as the operating wavelength moves away from the photoluminescence peak of the offset quantum well stack.

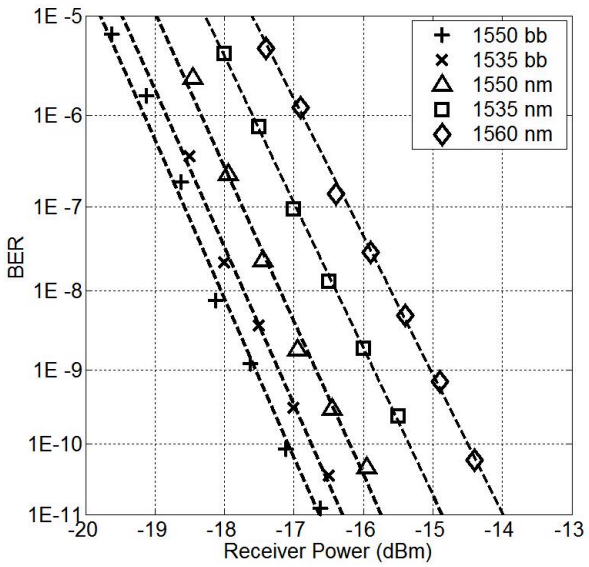

Fig 24. BER measurement results for fixed out wavelength (1553 nm) and variable input wavelengths. Receiver power is -11 dBm for all input wavelengths and PD-WC reverse bias is set to achieve maximum EAM slope efficiency.

VIII. Conclusion

We have presented a detailed study of a monolithic 10 Gb/s photocurrent driven wavelength converter that consists of a widely tunable laser source and optical receiver. The device is fabricated on a dual quantum well integration platform and utilizes quantum wells for modulation efficiency in integrated EAMs without incorporating multiple regrowth steps. Dynamic measurements of the wavelength converted extinction ratios show in excess of 10 dB over the full wavelength tuning range. Digital system performance measurements with a fixed wavelength input signal show less than 1 dB power penalty for converted signals over output wavelengths between 1533 and 1564 nm with a facet to facet conversion gain between 9-13 dB. BER measurements with variable input wavelengths and a fixed output wavelength show less than 2.5 dB power penalty for input wavelengths between 1535 and 1560 nm.

Acknowledgment

The authors would like to thank JDS Uniphase Corporation for AR coatings along with Professor John Bowers of the University of California Santa Barbara and Mario J. Paniccia of the Intel Corp. for their support during this work.

References

[1] S.B. Yoo, “Wavelength conversion technologies for WDM network applications,” *J. Lightwave Technol*, vol. 14, pp. 955-966, June 1996.

[2] W. Idler, K. daube, G. Laube, M. Schilling, P. Wiedemann, K. Dutting, M. Klenk, E. Lach, K. Wunstel, “10Gb/s wavelength conversion with integrated multiquantum-well-based 3-port Mach-Zehnder interferometer,” *IEEE Photon. Technol. Lett.*,. vol. 16, pp. 1163-1165, Sept. 1998.

[3] S. Hojfeldt, S, Bischoff, J. Mork, "All-Optical wavelength conversion and signal regeneration using an electroabsorption modulator," *J. Lightwave Technol.*, vol. 18, no. 8, pp. 1121-1127, Aug. 2000.

[4] S. Kodama, T. Yoshimatsu, H. Ito, "500 Gbit/s optical gate monolithically integrated photodiode and electroabsorption modulator," *Electron. Lett.*, vol. 40, no. 9, pp. 555-556, April 2004.

[5] A. Kelley, D. Marcenac, D. Nesset, "40 Gb/s wavelength conversion ocver 24.6 nm using FWM in a semiconductor optical amplifier with an optimized MQW active region," *Electron. Lett.,*, vol. 33, pp. 2123-2124, Dec. 1997..

[6] V. Lal, M.L. Masanovic, J.A. Summers, L.A. Coldren, D.J. Blumenthal, "Performance optimization of an InP-based widely tunable all-optical wavelength converter operating at 40 Gb/s," *IEEE Photon. Technol. Lett.,* vol. 18, no. 4, pp. 577-579, Feb. 2006.

[7] J. Leuthold, P. Besse, E. Gamper, M. Dulk, S. Fisher, G, Geukos, H. Melchior, "All-optical mach-Zehnder interferometer wavelength converters and switches with integrated data and control signal separation scheme," *J. Lightwave Technol*., vol. 17, no. 6, pp. 1056-1066, June, 1999.

[8] R. Doshi, M.L. Masanovic, D.J. Blumenthal, "Demonstration of an lin to any lout wavelength conversion using a 2-stage all-optical wavelength converter consisting of a XGM SOA-WC and InP monolithically-integrated widely-tunable MZI SOA-WC," *Meeting of the Lasers and Electro-Optics Society (LEOS)*, vol. 2, pp. 477-478, 2003.

[9] J.S. Barton, E.J. Skogen, M. L. Masanovic, J. Raring, M. N. Sysak, L. Johansson, S. P. DenBaars, L. A. Coldren. "Photonic integrated circuits based on sampled-grating distributed-Bragg-reflector lasers." *SPIE-Int. Soc. Opt. Eng. Proceedings of SPIE - the International Society for Optical Engineering*, vol.4998, 2003, pp.43-54.

[10] M. N. Sysak, J. W. Raring, J.S. Barton, H.N. Poulsen, D.J. Blumenthal, L.A. Coldren, "Extinction ratio regeneration, signal re-amplification (2R), and broadband wavelength switching using a monolithically integrated photocurrent driven wavelength converter," *Optics Express,* Vol. 14, no. 23, pp. 11343-11348, Nov. 2006.

[11] M. N. Sysak, L.A. Johannson, J. W. Raring, H.N. Poulsen, D.J. Blumenthal, L.A. Coldren, "Broadband Return to Zero (RZ) Signal Regeneration and Broadband Wavelength Conversion Using a Monolithically Integrated, Photocurrent Driven Wavelength Converter," *IEE Elec. Lett.,* Vol. 42, no. 25, Dec. 2006.

[12] Y.A. Akulova , G.A. Fish, H. Xu, E. Hall, M.C. Larson, P. Abraham, H. Marchand, C. Turner, C. Coldren, E. Hegblom, T.A. Strand, and L.A. Coldren, "Monolithically Integrated Tunable Transmitters", *Proc. IPRA 2005*, paper no. IWF4, San Diego, CA, April 11-15, 2005.

[13] M.N. Sysak, J.W. Raring, J.S. Barton, M. Dummer, D.J. Blumenthal, L.A. Coldren, "A single regrowth integration platform for photonic circuits incorporating tunable SGDBR laser and quantum well EAMs," *IEEE Photon. Technol. Lett*, vol. 18, no. 15, pp. 1630-1632, Aug. 2006.

[14] M.N. Sysak, J.W. Raring, D.J. Blumenthal, L.A. Coldren, "A Quantum Well EAM-SGDBR widely tunable transmitter fabricated in a novel dual quantum well integration platform," *Device Research Conf. (DRC)*, IIA-2, University Park, PA, June 2006.

[15] J. Dow, D. Redfield, "Toward a unified theory of Urbach's rule and exponential absorption edge," *Phys. Rev. B*, vol. 5, pp. 594-609, Jan. 1972.

[16] J.W. Raring, E.J. Skogen, C.S. Wang, J.S. Barton, G.B. Morrison, S. Demiguel, S.P. Denbaars, L.A. Coldren, "Design and demonstration of novel QW intermixing scheme for the integration of UTC-type photodiodes with QW-based components," *IEEE J. Quantum Electron.,* vol. 42, no. 2, pp. 171-181, Feb. 2006.

[17] V. Lal, W. Donat, A. Tauke-Pedretti, L.A. Coldren, D.J. Blumenthal, "Broadband rate-equation model including many-body gain for WDM traveling-wave SOAs," *Numerical Simulation of Optoelectronic Devices (NUSOD)*, Berlin, Germany, 2005.

[18] A. Tauke-Pedretti, M. Dummer, J.S. Barton, M.N. Sysak, J.W. Raring, L.A. Coldren, "High saturation power and high gain integrated receivers," *IEEE Photon. Technol. Lett*.,. vol. 17, no. 10, pp. 2167-2169, Oct. 2005.

[19] S. Hojfeldt, J. Mork, "Modeling of carrier dynamics in quantum-well electroabsorption modulators," *IEEE J. Select Topics Quantum Elec*., vol. 8, no. 6, pp. 1265-1276, Dec. 2002.

[20] K. Morito, M. Ekawa, T. Watanabe, Y. Kotaki, "High-output-power polarization-insensitive semiconductor optical amplifier," *J. Lightwave Technol.*, vol. 21, no. 1, pp. 176-181, Jan. 2001.

Matthew N. Sysak was born in Smithtown, NY in 1976. He received a B.S. degree from Pennsylvania State University in 1998 in chemical engineering, and M.S and Ph.D. degrees from the University of California Santa Barbara in 2002 and 2005 respectively in Electrical and Computer Engineering. His PhD thesis focused on design and fabrication of monolithically integrated widely-tunable Sampled Grating DBR semiconductor lasers, semiconductor optical amplifiers, electroabsorption modulators, and photodetectors for wavelength conversion and signal regeneration using a novel dual quantum well integration platform. He is currently working as a post-doctoral researcher with Professor John Bowers in the Ultrafast Optoelectronics Group in Santa Barbara, CA focusing on design, fabrication of ultra-linear monolithically integrated photonic links. He is a member of IEEE, OSA and SPIE.

James W. Raring was born in Ramsey, New Jersey in 1978. He received his B.S. degree from the materials engineering department at California Polytechnic State University, San Luis Obispo in 2001. He is pursuing a Ph.D. in materials science from the University of California, Santa Barbara. His current research focuses on the design, growth, and fabrication of high-functionality wavelength-agile photonic integrated circuits operating at 10 and 40 Gb/s. The photonic circuits are based on sampled grating DBR lasers, electroabsorption modulators, semiconductor optical amplifiers, and photodiodes. His work explores novel integration methods coupling quantum well intermixing with straightforward MOCVD regrowth steps. He has authored or co-authored over 60 technical papers and is a member of IEEE LEOS, OSA and SPIE.

Jonathon S. Barton obtained his bachelor's degree in electrical engineering and material science at the University of California, Davis in 1997. He was an Intel fellow during the time he received his doctorate at UC Santa Barbara in Electronic Materials. Currently he is an assistant project scientist for the LASOR DARPA grant working on the growth, fabrication and high speed testing of many monolithic optoelectronic components such as tunable lasers, modulators, and photocurrent-driven wavelength converters. Dr. Barton is a member of IEEE LEOS, OSA and SPIE.

Henrik N. Poulsen received the M.Sc.E.E. from the Technical University of Denmark in 1995. From 1995 to 2001 he worked first as a Research Associate and later as an Associate Research Professor in the field of high speed wavelength division multiplexed and optical time division multiplexing. His main interests were ultra high speed optical signal processing using non-linear fiber and semiconductor material, mainly semiconductor optical amplifiers, interferometric structures and electro-absoprtion modulators. In 2001 he moved from Copenhagen in Denmark to Santa Barbara in California to join Calient Networks, where he worked on optical amplification and performance monitoring for all-optical MEMS based switches.

He is currently working as a Associate Project Scientist in the Optical Communications and Photonics Network group with Professor D. J. Blumenthal at the Department of Electrical and Computer Engineering at the University of California, Santa Barbara. His main research area is all-optical packet switching using all-optical interferometric structures.

Larry A. Coldren is the Fred Kavli Professor of Optoelectronics and Sensors at the University of California, Santa Barbara, CA. He is also Chairman and Chief Technology Officer of Agility Communications, Inc. He received the Ph.D. degree in Electrical Engineering from Stanford University in 1972. After 13 years in the research area at Bell Laboratories, he joined UC-Santa Barbara in 1984 where he now holds appointments in Materials and Electrical & Computer Engineering, and is Director of the Optoelectronics Technology Center. In 1990 he co-founded Optical Concepts, later acquired as Gore Photonics, to develop novel VCSEL technology; and in 1998 he co-founded Agility Communications to develop widely-tunable integrated transmitters.

At Bell Labs Coldren initially worked on waveguided surface-acoustic-wave signal processing devices and coupled-resonator filters. He later developed tunable coupled-cavity lasers using novel reactive-ion etching (RIE) technology that he created for the then new InP-based materials. At UCSB he

continued work on multiple-section tunable lasers, in 1988 inventing the widely-tunable multi-element mirror concept, which is now fundamental to many of Agility's products. During the late eighties he also developed efficient vertical-cavity multiple-quantum-well modulators, which led to novel vertical-cavity surface-emitting laser (VCSEL) designs that provided unparalleled levels of performance. Prof. Coldren continues to be active in developing new photonic integrated circuit (PIC) and VCSEL technology, including the underlying materials growth and fabrication techniques. In recent years, for example, he has been involved in the creation of vertical and in-plane GaN-based emitters, efficient all-epitaxial InP-based VCSELs, and a variety of PICs incorporating numerous optical elements for widely-tunable integrated transmitters, receivers, and wavelength converters.

Professor Coldren has authored or co-authored over 700 papers, 5 book chapters, 1 textbook, and has been issued 36 patents. He has presented dozens of invited and plenary talks at major conferences, he is a Fellow of the IEEE, OSA, and IEE, the recipient of the 2004 John Tyndall Award, and a member of the National Academy of Engineering.

Daniel J. Blumenthal (M'97–F'03) received the B.S.E.E. degree from the University of Rochester, Rochester, NY, in 1981, the M.S.E.E. degree from Columbia University, New York, NY, in 1988, and the Ph.D. degree from the University of Colorado, Boulder, in 1993.

In 1981, he worked at StorageTek, Louisville, CO, in the area of optical data storage. In 1986, he worked at Columbia University in the areas of photonic switching systems, ultra-fast all-optical networks, and signal processing. From 1993 to 1997, he was an Assistant Professor in the School of Electrical and Computer Engineering, the Georgia Institute of Technology, Atlanta. He is currently a Professor in the Department of Electrical and Computer Engineering at the University of California, Santa Barbara, and the Associate Director for the Center on Multidisciplinary Optical Switching Technology (MOST). He heads the Optical Communications and Photonic Networks (OCPN) Research. He is Co-Founder of Calient Networks, a manufacturer of photonic switching systems based in San Jose, CA. His current research areas are in optical communications, wavelength division multiplexing, photonic packet switched and all-optical networks, all-optical wavelength conversion, and optical subcarrier multiplexing. He has authored or coauthored over 100 papers in these and related areas. Dr. Blumenthal is recipient of a 1999 Presidential Early Carreer Award for Scientists and Engineers (PECASE), a 1994 National Science Foundation Young Investigator (NYI) Award, and a 1997 Office of Naval Research Young Investigator Program (YIP) Award. He served as an Associate Editor for the IEEE PHOTONICS TECHNOLOGY LETTERS and the IEEE TRANSACTIONS ON COMMUNICATIONS. He was a Guest Editor for the IEEE JOURNAL OF LIGHTWAVE TECHNOLOGY Special Issue in Photonic Packet Switching Systems, Technologies, and Techniques, published in December 1998. He also served as Program Chair and Technical Program Committee Member on numerous conferences. He is a Member of the Optical Society of America.

II. Vertical-Cavity Surface-Emitting Lasers

Vertical-cavity surface-emitting lasers with lateral carrier confinement

D.D. Lofgreen, Y.-C. Chang and L.A. Coldren

A novel method to reduce threshold currents in vertical-cavity surface-emitting lasers (VCSELs) is proposed. By using selective quantum well intermixing, lateral heterobarriers are created that prevent carriers from diffusing away from the optical modes. Our devices show 40% reduction of threshold currents with the implementation of lateral carrier confinement.

Introduction: Optics is a viable solution to address the limitations of copper-based electronics in short-distance interconnects [1]. In these compact systems, devices must meet the stringent requirements imposed by the power budget and the thermal restriction. Recently, VCSELs have received considerable interest for board and chip level interconnects owing to their small footprints, ease of fabrication in arrays, and high-speed operation at low power dissipation. Smaller VCSELs are even more favourable in terms of speed and power consumption. However, as the dimension of VCSELs scales down, threshold currents do not scale accordingly owing to optical diffraction loss [2], current spreading [3], and carrier diffusion [4]. Optical diffraction loss can be reduced using tapered oxide aperture [2], and current spreading can be eliminated by placing the aperture close to the active region. Once carriers enter the quantum wells (QWs), the large lateral concentration gradient drives carriers to diffuse outwards and, consequently, a significant portion of the current does not provide useful gain to the optical modes and is dissipated as heat. To alleviate the problem, carriers must be confined laterally inside the QWs. In this Letter, we report a new VCSEL-compatible quantum well intermixing (QWI) process to achieve lateral carrier confinement. Using a sacrificial silicon-doped InGaP layer, we were able to selectively intermix InGaAs QWs for 980 nm VCSELs and our smallest 1 μm diameter device shows 40% reduction of threshold with the implementation of lateral carrier confinement.

Device structure and fabrication: The sample was grown on an *n*-type GaAs (100) substrate by molecular beam epitaxy (MBE). The bottom mirror consists of a 19-period silicon-doped GaAs/AlGaAs distributed Bragg reflector (DBR), followed by a 113 nm $Al_{0.3}Ga_{0.7}As$ separate confinement heterostructure (SCH). The active region consists of three InGaAs/GaAs QWs. On top of the QWs is a 36 nm $Al_{0.3}Ga_{0.7}As$ SCH, followed by a 50 nm GaAs layer for aluminum-free regrowth. A 300 nm sacrificial InGaP layer was then grown for intermixing purpose with the top 200 nm heavily doped with silicon to enhance QWI [5].

The intermixing process began by depositing and patterning SiO_2 on top of the sample and then subjecting the sample to reactive ion etch (RIE) with CF_4/O_2 gases to fluorinate the surface. It was then capped with another layer of SiO_2 and annealed at 850°C for 8 min using rapid thermal annealing (RTA). During the RTA, gallium atoms outdiffused into the SiO_2 and left vacancies at the surfaces in direct contact with SiO_2. Sequentially, these vacancies diffused down into the QWs and promoted the intermixing process [6]. On the other hand, fluorine bound with gallium and indium atoms to create gallium and indium fluorides during the RIE step on the surfaces without SiO_2, and these fluorides were reported to be thermally stable [7]. Because vacancies were not created, the intermixing process was suppressed. After RTA, the SiO_2 and InGaP layers were stripped off using buffered HF and diluted HCl, respectively, and the sample was loaded into MBE for regrowth.

A 10 nm GaAs layer was grown on top of the regrowth layer, followed by a 60 nm $Al_{0.8}Ga_{0.2}As$ and a 10 nm AlAs to form the tapered oxide aperture. The top mirror consists of a 32-period carbon-doped GaAs/AlGaAs DBR, followed by a highly doped *p*-contact layer. The device fabrication began by etching cylindrical mesas and forming the aperture using wet oxidation. Ti/Pt/Au and AuGe/Ni/Au were evaporated for *p*- and *n*-contacts, respectively. Finally, an antireflection coating was deposited to reduce the backside reflection.

Results and discussion: Fig. 1 shows the secondary ion mass spectrometry (SIMS) results for the non-intermixed and the intermixed areas on a test sample. In Fig. 1*a*, three indium peaks corresponding to three InGaAs QWs are clearly seen, which indicates that surface fluorination did help to preserve the layer structure during the RTA. The only noticeable difference from the as-grown sample (not shown) is that silicon atoms on the top 200 nm InGaP layer diffuse towards the active region. On the other hand, the indium profile of the QWs is completely washed out for the intermixed areas, as shown in Fig. 1*b*. Aluminum also diffused into the QWs, which is necessary to get enough bandgap shift for effective carrier confinement. Silicon atoms also diffused into the QWs at the non-intermixed areas and will introduce free carrier absorption loss, as will be seen in the device results.

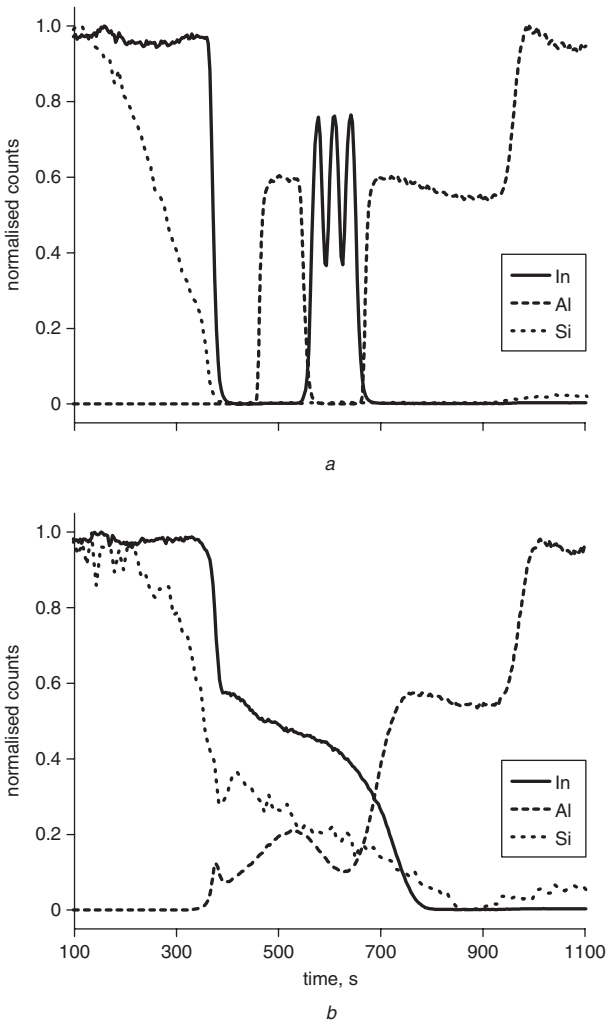

Fig. 1 *SIMS results showing aluminum, indium and silicon profiles*
a On non-intermixed area
b On intermixed area

Fig. 2 shows the threshold currents and differential quantum efficiencies for intermixed and non-intermixed VCSELs. There is significant scatter in the data owing to the roughness of the *p*-DBR regrowth interface, causing random amounts of loss for each device. However, the general trend is obvious. The devices where QWs have been selectively intermixed clearly show reduced threshold currents compared with the samples where QWs have not been intermixed. The reason that the VCSELs show higher thresholds overall can be explained by extra added loss at the regrowth interface since the differential quantum efficiencies are also statistically lower, as seen in Fig. 2*b*. For those that have been selectively intermixed, differential quantum efficiencies drop slightly for devices smaller than 4 μm. This indicates a size-dependent loss mechanism that is only present for the intermixed devices. Most likely, this loss comes from silicon diffusion into the QWs during the intermixing process and is more severe for smaller devices. To get a better measure of the amount of intermixing, the thresholds are fitted to a model to estimate the barrier height. The data lies partially on the 200 meV barrier curve for larger devices and partially on the 100 meV curve for smaller devices. Owing to the

size-dependent loss, the barrier is more likely to be closer to 200 meV, which is enough to provide lateral carrier confinement in VCSELs.

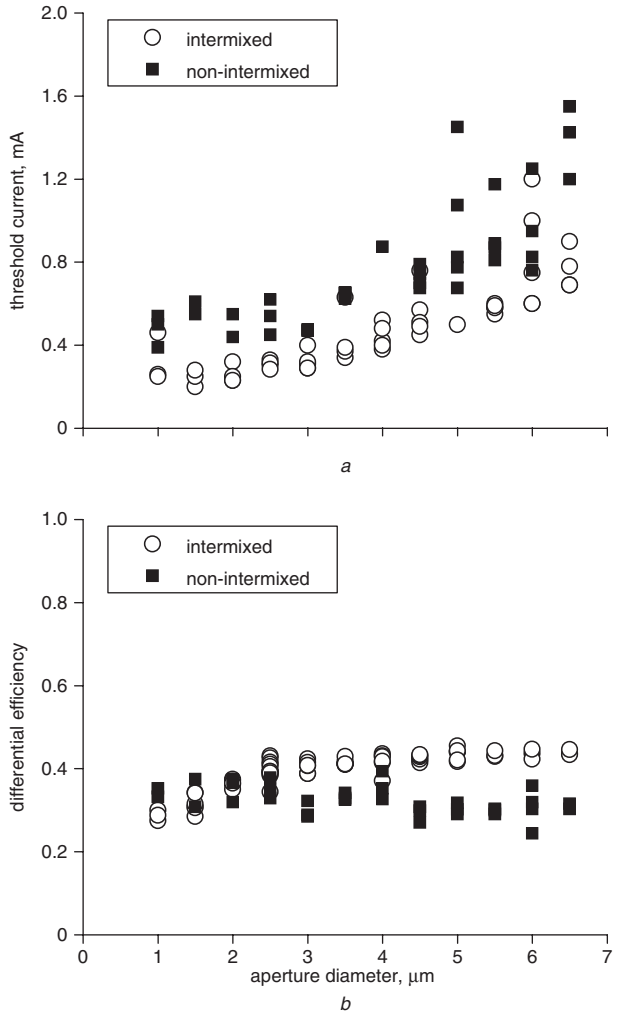

Fig. 2 *Threshold currents for different diameter devices, and differential quantum efficiencies for different diameter devices*

a Threshold currents
b Differential quantum efficiencies

Conclusions: We have developed a new VCSEL-compatible QWI process to achieve lateral carrier confinement in VCSELs and our results show that threshold currents are indeed reduced with lateral carrier confinement.

14 December 2006
Electronics Letters online no: 20073844
doi: 10.1049/el:20073844

D.D. Lofgreen, Y.-C. Chang and L.A. Coldren (*Department of Electrical and Computer Engineering, University of California, Santa Barbara, CA 93106-9560, USA*)

E-mail: yuchia@engineering.ucsb.edu

D.D. Lofgreen: Now with Raytheon Vision Systems, Goleta, CA 93117, USA

References

1 Miller, D.A.B.: 'Physical reasons for optical interconnection', *Int. J. Optoelectron.*, 1997, **11**, pp. 155–168
2 Hegblom, E.R., Babic, D.I., Thibeault, B.J., and Coldren, L.A.: 'Scattering losses from dielectric apertures in vertical-cavity lasers', *IEEE J. Sel. Top. Quantum Electron.*, 1997, **3**, pp. 379–389
3 Hegblom, E.R., Margalit, N.M., Thibeault, B.J., Coldren, L.A., and Bowers, J.E.: 'Current spreading in apertured vertical cavity lasers'. Proc. SPIE Photonics West, 1997, pp. 176–180
4 Naone, R.L., Floyd, P.D., Young, D.B., Hegblom, E.R., Strand, T.A., and Coldren, L.A.: 'Interdiffused quantum wells for lateral carrier confinement in VCSEL's', *IEEE J. Sel. Top. Quantum Electron.*, 1998, **4**, pp. 706–714
5 Deppe, D.G., and Holonyak Jr., N.: 'Atom diffusion and impurity-induced layer disordering in quantum well III-V semiconductor heterostructures', *J. Appl. Phys.*, 1988, **64**, pp. 93–113
6 Deppe, D.G., Guido, L.J., Holonyak Jr., N., Hsieh, K.C., Burnham, R.D., Thornton, R.L., and Paoli, T.L.: 'Stripe-geometry quantum well heterostructure $Al_xGa_{1-x}As$-GaAs lasers defined by defect diffusion', *Appl. Phys. Lett.*, 1986, **49**, pp. 510–512
7 Williston, L.R., Bello, I., and Lau, W.M.: 'X-ray photoelectron spectroscopic study of the interactions of CF^+ ions with gallium arsenide', *J. Vac. Sci. Technol. A*, 1993, **11**, pp. 1242–1247

Small-dimension power-efficient high-speed vertical-cavity surface-emitting lasers

Y.-C. Chang, C.S. Wang and L.A. Coldren

Small-dimension power-efficient high-speed oxide-confined 980 nm vertical-cavity surface-emitting lasers (VCSELs) with record-high bandwidth/power-dissipation ratio of 12.5 GHz/mW have been demonstrated. The devices show a modulation bandwidth of 15 GHz at a bias current 0.9 mA, corresponding to only 1.2 mW power dissipation.

Introduction: Recently, VCSELs have received considerable interest for short-distance optical interconnects owing to their small footprint, natural occurrence in arrays and, most importantly, cost effectiveness. Two of the main challenges for the devices to be used in board-to-board and chip-to-chip interconnects are speed and power dissipation. For directly modulated lasers, higher speed can be achieved with higher bias current at the expense of higher power dissipation. High power dissipation can be fatal in these compact systems with limited power budgets and stringent thermal restrictions. Most of the high-speed VCSELs have diameters from 6 to 8 μm and have threshold currents of 0.3 mA or above [1–3]. For these devices, 15 GHz bandwidth, which should enable 20 Gbit/s operation, was achieved at a current of at least 1.5 mA, but usually a much higher current was required owing to their high threshold currents and large mode volumes. Smaller devices are potentially faster and require less power, and thus are more suitable for optical interconnects. One of the obstacles for small devices to have high speed is the parasitics. By implementing deep oxidation layers [4] and optimising the doping schemes, we were able to reduce the parasitics to enable high-speed operation for smaller devices. Our 3 μm diameter device shows 15 GHz bandwidth at a bias current of 0.9 mA, corresponding to only 1.2 mW power dissipation. A bandwidth/power-dissipation ratio of 12.5 GHz/mW is achieved for 15 GHz, the highest ever reported.

Device structure and fabrication: Fig. 1*a* shows a schematic cross-section of the VCSEL. The layer structure is similar to our previous device [4] except that the following modifications were made to address the issues with parasitics. First, the number of deep oxidation layers was increased from two to five to further reduce the parasitic capacitance. Secondly, the overall *p*-doping concentration was increased to reduce the series resistance, especially in the first several periods of the DBRs above the active region, which account for most of the resistance. Fig. 1*b* shows a top view scanning electron micrograph (SEM) of a fabricated VCSEL. The devices were fabricated using the process given in [4] with the following improvements. After the *p*- and *n*-contact metals were deposited, the *n*-GaAs contact layer (RF ground) beneath the *p*-pad metal (RF signal) was first etched away using citric acid/hydrogen peroxide to eliminate the pad capacitance. The benzocyclobutene (BCB) between the *n*-pad metal and the *n*-metal was removed for better RF grounding and heat spreading. The dimension of the *p*-pad metal is also reduced to 40 × 70 μm. Before anti-reflection (AR) coating, the backside was lapped to remove residues accumulated throughout earlier processing steps.

Results: Figure 2 shows the voltage, output power and temperature rise against current (*L-I-V-T*) curves for a 3 μm diameter device, which is the smallest device and has the highest bandwidth/power-dissipation ratio. The device has a differential quantum efficiency of 53%, which is slightly lower than expected. This may have resulted from the lapping process, which roughens the output surface. The threshold current is only 0.155 mA, less than half the values for most high-speed VCSELs. The threshold current does not increase considerably from the higher doping concentration because the modes are better confined in the longitudinal direction and have less overlap with the highly doped DBRs. This is due to the increased number of the deep oxidation layers, which have higher aluminum fraction and larger index contrast in the region of the mode. The threshold voltage is 1.48 V, which is very low for such a small device, and it is only 220 meV larger than the quasi-Fermi level separation. The series resistance is ~220 Ω. The peak wall-plug efficiency is 30% at a current 1 mA. The thermal impedance of the device is 2.88°C/mW, calculated by measuring the wavelength shift at different stage temperature and at different bias [5]. The maximum output power is 3.6 mW at a bias current of 8.6 mA, corresponding to a temperature rise of 77°C.

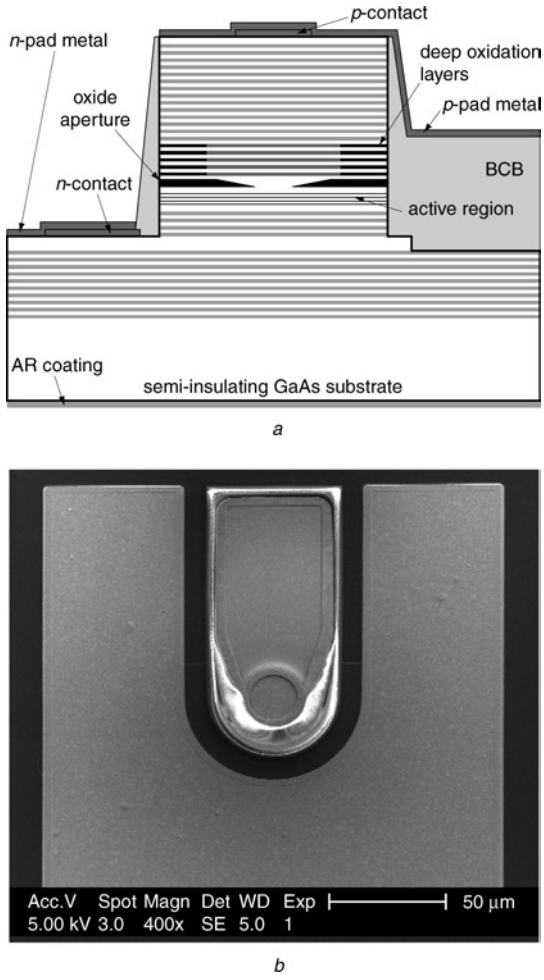

Fig. 1 *Schematic cross-section of VCSEL, and top view SEM of VCSEL*
a Cross-section of VCSEL
b SEM of VCSEL

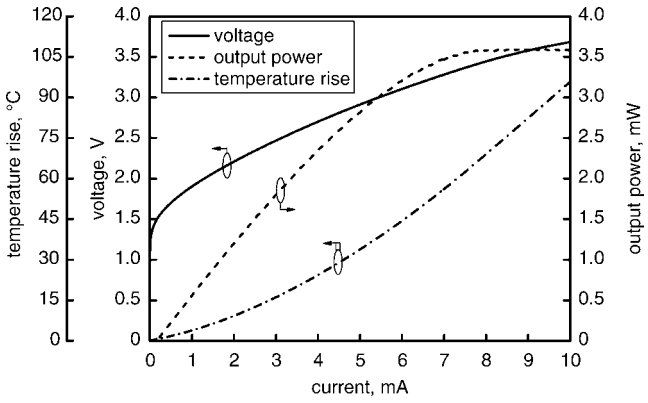

Fig. 2 *L-I-V-T curves for 3 μm diameter device at stage temperature 20°C*

Small-signal modulation responses were measured on-wafer using an RF probe and a calibrated Agilent PNA network analyser E8364A. Output power was collected by a 50/125 multimode fibre and measured using a New Focus 25 GHz photodetector coupled to a New Focus 20 GHz amplifier. The frequency responses for the 3 μm diameter device under different bias currents are shown in Fig. 3. An electrical −3 dB bandwidth of 15 GHz is achieved at a bias current 0.9 mA, corresponding to 1.6 mW input power and 1.2 mW dissipated power. Methods have been proposed to reduce the thermal impedance and alleviate the thermal degradation [3, 6]. With 1.2 mW power

dissipation, the temperature rise is only 3.5°C and should have negligible thermal impacts on the device performances. The modulation current efficiency factor (MCEF) for the device is 16.8 GHz/$\sqrt{}$mA, equal to the highest previously reported value [7]. The high MCEF is mainly due to the stronger mode confinement in both lateral and longitudinal directions.

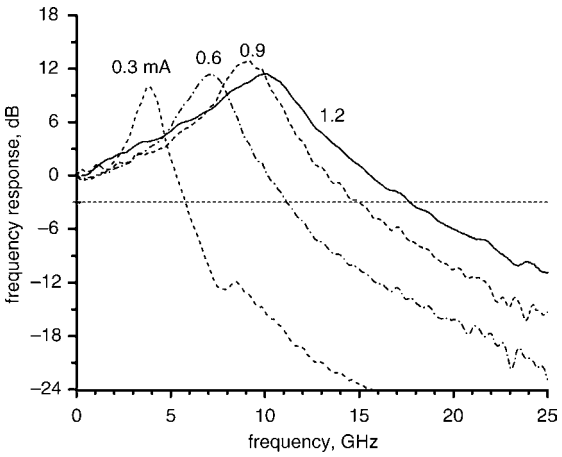

Fig. 3 *Small-signal modulation responses for 3 μm diameter device under different bias currents at stage temperature 20°C*

The modulation responses at higher bias currents were measured, and although they extended to higher frequencies, they also showed sharp drops at low frequency, usually below 0.5 GHz. This may be caused by mode partition inside the device and spatial mode filtering from our measurement setup. This supposition is supported by the fact that the photocurrent from the photodetector was relatively noisy at high VCSEL bias currents. By better controlling the higher order modes or by collecting all of the light, for example with a backside microlens [8], a usable bandwidth >20 GHz should be attainable.

Conclusions: Small-dimension, power-efficient high-speed VCSELs with 12.5 GHz/mW bandwidth/power-dissipation ratio have been demonstrated. 15 GHz bandwidth is achieved at 0.9 mA for 1.2 mW power dissipation. This high bandwidth with reduced power dissipation makes these devices more suitable for optical interconnect applications than previous designs.

Acknowledgments: The authors thank J.E. Bowers, L.A. Johansson and Y.-H. Kuo at University of California, Santa Barbara, for helping with the RF test setup.

20 January 2007
Electronics Letters online no: 20070195
doi: 10.1049/el:20070195

Y.-C. Chang, C.S. Wang and L.A. Coldren (*Department of Electrical and Computer Engineering, University of California, Santa Barbara, CA 93106-9560, USA*)

E-mail: yuchia@engineering.ucsb.edu

References

1 Kuchta, D.M., Pepeljugoski, P., and Kwark, Y.: 'VCSEL modulation at 20 Gbit/s over 200 m of multimode fiber using a 3.3 v SiGe laser driver IC'. Tech. Dig. LEOS Summer Topical Meeting, 2001, pp. 49–50
2 Suzuki, N., Hatakeyama, H., Fukatsu, K., Anan, T., Yashiki, K., and Tsuji, M.: '25-Gbps operation of 1.1-μm-range InGaAs VCSELs for high-speed optical interconnections'. Optical Fiber Communications Conf., Tech. Dig, 2006, paper no. OFA4
3 AL-Omari, A.N., Carey, G.P., Hallstein, S., Watson, J.P., Dang, G., and Lear, K.L.: 'Low thermal resistance, low current density, high-speed 980 and 850 nm VCSELs'. Int. Semiconductor Laser Conf., 2006, pp. 127–128
4 Chang, Y.-C., Wang, C.S., Johansson, L.A., and Coldren, L.A.: 'High-efficiency, high-speed VCSELs with deep oxidation layers', *Electron. Lett.*, 2006, **42**, (22), pp. 1281–1282
5 Young, D.B., Scott, J.W., Peters, F.H., Peters, M.G., Majewski, M.L., Thibeault, B.J., Corzine, S.W., and Coldren, L.A.: 'Enhanced performance of offset-gain high-barrier vertical-cavity surface-emitting lasers', *IEEE J. Quantum Electron.*, 1993, **29**, pp. 2013–2022
6 Mathine, D.L., Nejad, H., Allee, D.R., Droopad, R., and Maracas, G.N.: 'Reduction of the thermal impedance of vertical-cavity surface-emitting lasers after integration with copper substrates', *Appl. Phys. Lett.*, 1996, **69**, pp. 463–464
7 Strzelecka, E.M., Robinson, G.D., Coldren, L.A., and Hu, E.L.: 'Fabrication of refractive microlenses in semiconductors by mask shape transfer in reactive ion etching', *Microelectron. Eng.*, 1997, **35**, pp. 385–388
8 Lear, K.L., Mar, A., Choquette, K.D., Kilcoyne, S.P., Schneider, R.P., C.Y.Suen, Jr.and Geib, K.M.: 'High-frequency modulation of oxide-confined vertical cavity surface emitting lasers', *Electron. Lett.*, 1996, **32**, (9), pp. 457–458

High-efficiency, high-speed VCSELs with 35 Gbit/s error-free operation

Y.-C. Chang, C.S. Wang and L.A. Coldren

High-efficiency, high-speed, tapered-oxide-apertured 980 nm vertical-cavity surface-emitting lasers (VCSELs) with 35 Gbit/s error-free operation have been demonstrated. This is the highest data rate reported for directly modulated VCSELs to date. The devices are also highly efficient, showing a record-high data-rate/power-dissipation ratio of 3.5 Gps/mW.

Introduction: Recently, vertical-cavity surface-emitting lasers (VCSELs) have received considerable interest for their potential application in optical interconnects [1]. VCSELs are very attractive for short-distance optical interconnects owing to their small footprint, natural occurrence in arrays and, most importantly, cost effectiveness. To meet the bandwidth requirements for future datacom applications, researchers have been trying to improve the data rate of VCSELs [2–4]. VCSELs with data rate up to 30 Gbit/s and 3 dB bandwidth of 24 GHz at 1.1 µm have been demonstrated [4]. However, these devices use buried tunnel junctions and regrowth is required, which complicates the fabrication process and adds extra costs. In this Letter, we report high-efficiency, high-speed, tapered-oxide-apertured 980 nm VCSELs that do not require ion implementation and/or regrowth and can be mass manufactured easily. These devices demonstrate 35 Gbit/s error-free operation at a bias current of 4.4 mA. To the best of the authors' knowledge, this represents the highest data rate reported for directly modulated VCSELs to date. These devices also show the highest data-rate/power-dissipation ratio of 3.5 Gps/mW at 35 Gbit/s operation.

Device structure: The structure used in this work is *n*-intracavity, bottom-emitting, tapered-oxide-apertured 980 nm VCSELs, as shown in Fig. 1. Details of the device structure and fabrication process can be found in [5]. To achieve high-speed operation at low power dissipation, the mode volume needs to be reduced. This is accomplished by: (*a*) placing the *n*-contact layer five periods away from the active region to reduce the loss and provide better longitudinal mode confinement; and (*b*) using an optimised tapered oxide aperture with a 4 µm taper length and a thickness of $(1/2)\lambda$ to simultaneously achieve low scattering loss and better mode confinement.

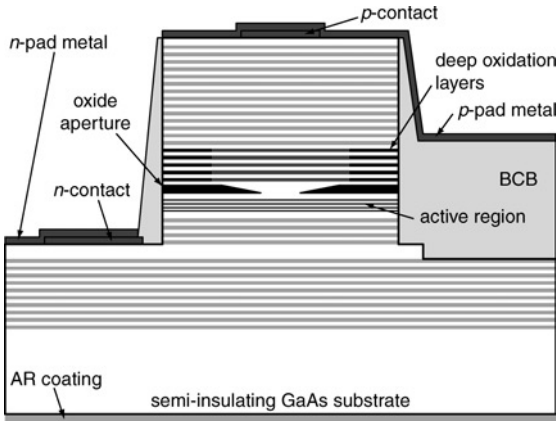

Fig. 1 *Schematic cross-section of VCSEL*

In addition to the improvements for the intrinsic laser properties, the extrinsic parasitic needs to be reduced. The series resistance is lowered by using an optimised *p*-doping scheme in the top mirror to balance the loss and resistance. The thicker oxide aperture, $(1/2)\lambda$ instead of the standard $(1/4)\lambda$ thick, and the employment of the deep oxidation layers [6] help to reduce the oxide capacitance, one of the main limiting factors of bandwidth. Another benefit of the high Al-content deep oxidation layers is that they also provide better mode confinement longitudinally owing to higher index contrast. The pad capacitance is further reduced by: (*a*) removing the *n*-contact layer (RF ground) beneath the *p*-pad (RF signal), (*b*) applying benzocyclobutene (BCB) between these two layers, and (*c*) shrinking the pad dimensions to 40×70 µm.

Results: Fig. 2 shows the voltage and output power against current (*L–I–V*) curves for a 3 µm-diameter device. The lasing wavelength is around 993 nm. The device has a differential quantum efficiency of 54% and a threshold current of 0.144 mA, relatively low for high-speed VCSELs previously reported. The threshold voltage is 1.47 V, which is very low for such a small device, as it is only 220 meV larger than the quasi-Fermi level separation for transparency. The series resistance is approximately 250 Ω at a bias current of 4.4 mA, where the large-signal modulation experiments are performed. The peak wallplug efficiency is 31%. The maximum output power is 3.1 mW at a bias current of 7 mA.

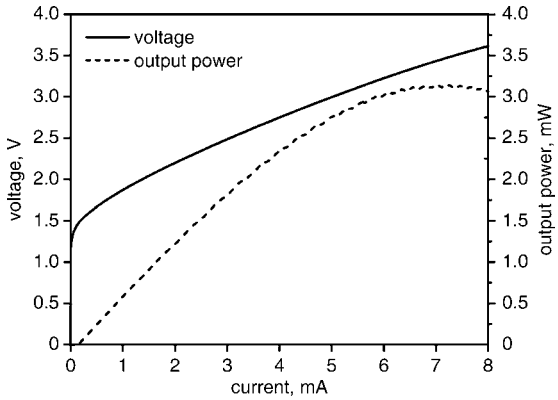

Fig. 2 *L–I–V curves for 3 µm diameter device at 20°C*

Fig. 3 shows the test setup for large-signal modulation experiments. The non-return-to-zero (NRZ) signal with $2^7 - 1$ word length from the pattern generator was amplified using a 38 GHz SHF 806E amplifier with 26 dB gain and then attenuated 6 dB using a fixed attenuator to reduce the voltage swing to $\sim 0.84\ V_{p\text{-}p}$. The RF signal was combined with the DC bias through a 65 GHz Anritsu V255 bias tee and fed to the device using a 67 GHz ground–signal–ground RF probe. The output power was collected into a 9/125 singlemode fibre using a dual-lens focuser. The eye diagrams were measured using an Agilent 86109A oscilloscope with an internal 30 GHz photodiode. To measure the bit error rate (BER), the optical signal was fed to a 25 GHz New Focus 1414 photodiode coupled with a 40 GHz SHF 810 amplifier and sent to the error analyser.

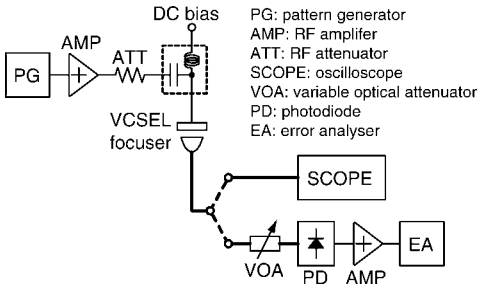

Fig. 3 *Experiment setup for BER and eye diagram measurements*
Thicker lines denote the optical fibre. Eye diagram is measured through upper path to oscilloscope and BER is measured through lower path to error analyser

Fig. 4 shows the BER curve at 35 Gbit/s for a 3 µm device at 20°C. The bias current is 4.4 mA and the voltage swing is $\sim 0.84\ V_{p\text{-}p}$. The 3 dB bandwidth at this bias current exceeds 20 GHz. The inset of the Figure shows the optical eye diagram at 35 Gbit/s and the eye is clearly open with an extinction ratio of 5.4 dB. In the BER curve, all the data points except the lowest one were taken with a variable optical attenuator (VOA). Owing to the ~3 dB insertion loss of the VOA, the BER in the range of 10^{-4} to 10^{-7} could not be measured. Thus, the lowest data point at a received power of −4.7 dBm was taken without the VOA. The BER is 9.2×10^{-12}, gated for 30 min with a total of 583 errors to ensure the accuracy of the measurement. In fact, the BER was $\sim 2 \times 10^{-12}$ for the first 10 min and increased slowly with time, possibly owing to fibre drift. This is statistically evident of error-free operation at 35 Gbit/s. To the best of the authors' knowledge, this represents the highest data rate for directly modulated VCSELs. At a

bias current of 4.4 mA, the power consumption and dissipation, excluding the RF driver circuitry, are only 12.5 and 10 mW, respectively. This corresponds to a data-rate/power-dissipation ratio of 3.5 Gps/mW, also the highest value ever reported.

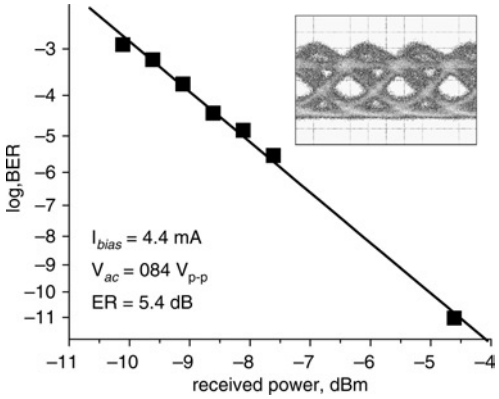

Fig. 4 *BER measurement at 35 Gbit/s at 20°C*

Bias current 4.4 mA and voltage swing $\sim$0.84 V_{p-p}. Lowest data point, taken without VOA, gated for 30 min to ensure measurement accuracy.
Inset: corresponding optical eye diagram with extinction ratio of 5.4 dB

Conclusions: High-efficiency, high-speed, tapered-oxide-apertured 980 nm VCSELs with 35 Gbit/s error-free operation have been demonstrated. This represents the highest data rate achieved for directly modulated VCSELs. In addition, the devices show a record high data-rate/power-dissipation ratio of 3.5 Gps/mW, making these devices suitable for interconnect applications.

Acknowledgments: The authors thank Prof. D.J. Blumenthal, H.N. Poulsen and L.A. Johansson at University of California, Santa Barbara, for helping with the RF test setup. This work was supported by a UC-MICRO with IBM and gift funds from Agilent.

14 July 2007
Electronics Letters online no: 20072074
doi: 10.1049/el:20072074

Y.-C. Chang, C.S. Wang and L.A. Coldren (*Department of Electrical and Computer Engineering, University of California, Santa Barbara, CA 93106-9560, USA*)

E-mail: yuchia@engineering.ucsb.edu

References

1 Schares, L., *et al*.: 'Terabus: terabit/second-class card-level optical interconnect technologies', *IEEE J. Sel. Top. Quantum Electron*., 2006, **12**, pp. 1032–1034
2 Kuchta, D.M., Pepeljugoski, P., and Kwark, Y.: 'VCSEL modulation at 20 Gb/s over 200 m of multimode fiber using a 3.3 v SiGe laser driver IC'. Tech. Dig. LEOS Summer Topical Meeting, 2001, pp. 49–50
3 Suzuki, N., Hatakeyama, H., Fukatsu, K., Anan, T., Yashiki, K., and Tsuji, M.: '25-Gbps operation of 1.1-μm-range InGaAs VCSELs for high-speed optical interconnections'. Proc. Optical Fiber Communications Conf., 2006, Paper OFA4
4 Yashiki, K., Suzuki, N., Fukatsu, K., Anan, T., Hatakeyama, H., and Tsuji, M.: '1.1-μm-range tunnel junction VCSELs with 27-GHz relaxation oscillation frequency'. Proc. Optical Fiber Communications Conf., 2007, Paper OMK1
5 Chang, Y.-C., Wang, C.S., and Coldren, L.A.: 'Small-dimension power-efficient high-speed vertical-cavity surface-emitting lasers', *Electron. Lett*., 2007, **43**, pp. 396–397
6 Chang, Y.-C., Wang, C.S., Johansson, L.A., and Coldren, L.A.: 'High-efficiency, high-speed VCSELs with deep oxidation layers', *Electron. Lett*., 2006, **42**, pp. 1281–1282

High-speed tapered-oxide-apertured 980 nm VCSELs supporting data rates up to 30 Gb/s

Yu-Chia Chang, Chad S. Wang, and Larry A. Coldren
ECE Dept. University of California, Santa Barbara, CA 93106

Phone: (805) 893-7065, Fax: (805) 893-4500, E-mail: yuchia@engineering.ucsb.edu

Abstract: High-speed 980 nm VCSELs with tapered oxide apertures were designed and fabricated. The devices show >20 GHz bandwidths for bias currents between 2 and 4 mA. Open eyes up to 30 Gb/s are also demonstrated.

1. INTRODUCTION

Recently, vertical-cavity surface-emitting lasers (VCSELs) have received considerable interest for their potential applications in optical interconnects [1]. VCSELs are very attractive for short-distance interconnects due to their small footprint, ease of fabrication in arrays, and high-speed operation at low power consumption. Although the fastest VCSELs have shown 30 Gb/s operation and bandwidths of 24 GHz at a 1.1 μm wavelength [2], these devices use buried tunnel-junctions and require regrowth. This not only reduces the manufacturability but also adds extra costs. Here we report high-speed, tapered-oxide-apertured 980 nm VCSELs which can be easily fabricated. The taper angle is increased to reduce the mode volume and improve the high-speed performance. The devices show > 20 GHz bandwidth for bias currents between 2 and 4 mA and open eye diagrams up to 30 Gb/s.

2. DEVICE

The structure used in this work is *n*-intracavity, bottom-emitting, tapered-oxide-apertured 980 nm VCSEL as shown in Fig. 1(a). The bottom mirror is an 18-period AlGaAs/GaAs distributed Bragg reflector (DBR). The 5/4λ thick *n*-contact layer is placed at the 5th period to reduce the loss and provide better longitudinal mode confinement. The top mirror has a 30-period AlGaAs/GaAs DBR. The Aluminum fraction of the first 5 periods DBR is increased from 85% to 93% to form deep oxidation layers for reducing capacitance [3]. Tapered oxide aperture with a 4 μm taper length and a thickness of 1/2λ is used to simultaneously achieve better mode confinement and low optical scattering loss. The doping scheme of the *p*-mirror is also optimized to reduce the series resistance without introducing too much loss. The pad capacitance is reduced by (a) removing the *n*-contact layer (RF ground) beneath the *p*-pad metal (RF signal), (b) applying Benzpcyclobutene (BCB) between these two layers, and (c) shrinking the pad dimension to 40×70 μm as shown in Fig. 1(b). Details of the device structure and process can be found in [4].

3. RESULTS

Figure 2(a) shows the voltage, output power against current (L-I-V) curves for a 3 μm diameter device. The device has a very low threshold current of 0.155 mA and a differential quantum efficiency of 53 %. The threshold voltage is only 1.48 V, 220 meV larger than the quasi-Fermi level separation. This low threshold voltage is the consequence of the optimized doping scheme and the low threshold current. The series resistance is approximately 220 Ω and the peak wall-plug efficiency is 30%. The maximum output power achieved is 3.6 mW.

The frequency responses of a 3 μm diameter device are shown in Fig. 2(b). An electrical –3 dB frequnecy of 20

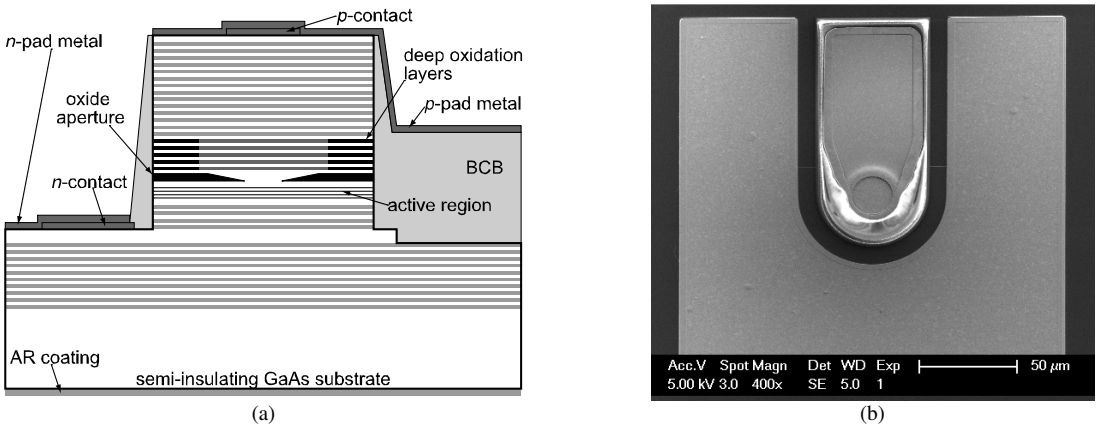

(a) (b)

FIGURE 1. (a) Schematic cross-section of VCSEL, and (b) top view scanning electron micrograph (SEM).

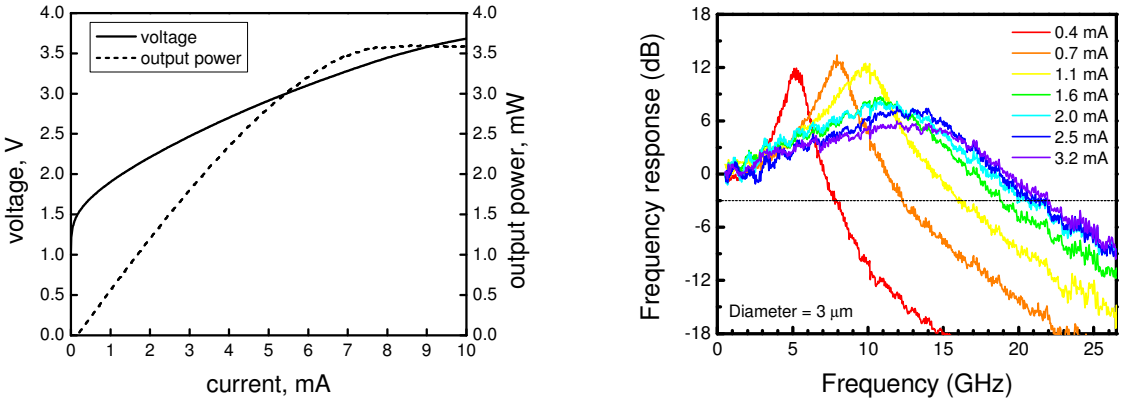

FIGURE 2. (a) L-I-V curves, and (b) frequency responses for a 3 µm diameter device. The estimated Gaussian 1/e mode diameter is 2.8 µm.

GHz is achieved at a bias current of 2 mA. The maximum modulation bandwidth is ~21.5 GHz at a bias current of 3.2 mA. The modulation current effeciency factor (MCEF) of this device is 16.8 GHz/√mA and ties with the highest reported value for QW VCSELs [5]. This high MCEF is the consquence of the low threshold current and the strong mode confinement.

Large signal modulation was also performed to evaluate the feasibility of these devices for optical interconnect applications. The NRZ signal (PRBS 2^{31}-1) from the pattern generator was amplified using a SHF 806E amplifier with 26 dB gain and combined with the DC bias through a 65 GHz bias tee. The combined signal was then attenuated using a 6 dB attenuator and fed to the devices. The optical signals were measured using Agilent 86109A oscilloscope with an internal 30 GHz photodiode. The measured eye diagrams at 20, 25, and 30 Gb/s are shown in Fig. 3. The estimated bias currents for these eyes are 4~5 mA. As shown in the figures, eye diagrams at 20 and 25 Gb/s are clearly open, and eye diagram at 30 Gb/s is still open with some limitation on the time window. Bit error rate (BER) measurement was performed and error-free operation up to 15 Gb/s was achieved, mainly limited by the bandwidth of the photoreceiver used.

4. CONCLUSION

High-speed, tapered-oxide-apertured 980 nm VCSELs were designed and fabricated. These devices show decent DC performance and achieve >20 GHz modulation bandwidth at bias current 2~4 mA. Open eyes up to 30 Gb/s is demonstrated and operation at this data rate can be expected with a better receiver.

5. REFERENCES

[1] L. Schares, et al., "Terabus: Terabit/Second-Class Card-Level Optical Interconnect Technologies," *IEEE J. of Sel. Topics in Quant. Electron.*, vol. 12, no. 5, pp. 1032-1034, 2006.

[2] K. Yashiki, N. Suzuki, K. Fukatsu, T. Anan, H. Hatakeyama, and M. Tsuji, "1.1-µm-Range Tunnel Junction VCSELs with 27-GHz Relaxation Oscillation Frequency," *Proc. Optical Fiber Communications Conf.*, paper no. OMK1, 2007.

[3] Y.-C. Chang, C.S. Wang, and L.A.Coldren, "High-efficiency, high-speed VCSELs with deep oxidation layers," *Electron. Lett.*, vol. 42, no. 22, pp. 1281–1282, 2006

[4] Y.-C. Chang, C.S. Wang, L.A. Coldren, "Small-dimension power-efficient high-speed vertical-cavity surface-emitting lasers," *Electron. Lett.*, vol 43, no 7, pp. 396–397, 2007

[5] K.L Lear, A. Mar, K.D. Choquette, S.P. Kilcoyne, R.P. Schneider Jr., and K.M. Geib, "High-frequency modulation of oxide-confined vertical cavity surface emitting lasers," *Electron. Lett.*, vol 32, no. 5, pp. 457–458, 1996

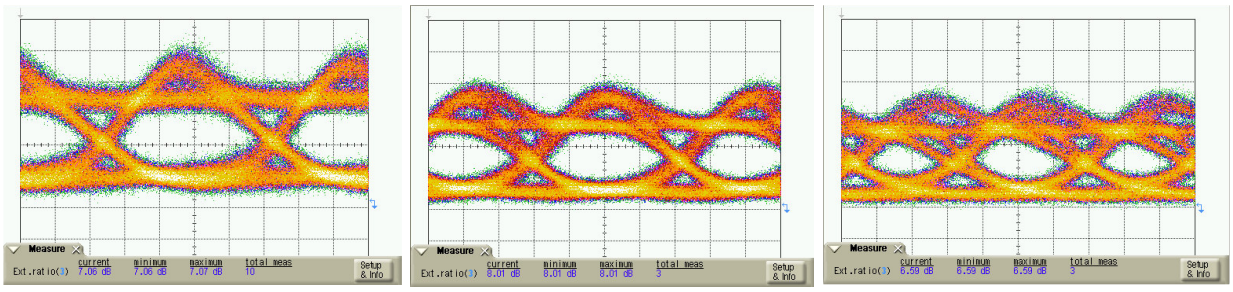

(a) 20 Gb/s, extinction ratio=7 dB (b) 25 Gb/s, extinction ratio=8 dB (c) 30 Gb/s, extinction ratio=6.6 dB

FIGURE 3. Optical eye diagrams measured by Agilent 86109A with a 30 GHz internal photodiode. The bias currents are estimated to be 4~5 mA. The time scale is 10 ps/Div.

High-Speed Datacom VCSELs at 1310 and 980 nm

Larry A. Coldren
ECE and Materials Departments
University of California, Santa Barbara, CA 93106
coldren@ece.ucsb.edu

Abstract:

Recent progress on VCSELs for datacom applications within the author's group at UCSB will be reviewed. Efforts on 'all-epitaxial, long-wavelength' InP-based devices as well as efficient, small-cavity-volume GaAs-based VCSELs will be included. InGaAlAs/InGaAsSb/InP all-epitaxial wafers processed in a conventional manner are found to provide viable VCSELs across the entire 1300-1600 nm wavelength band, and InGaAs/GaAlAs/GaAs structures with low-loss tapered-oxide apertures have demonstrated low-current, high-data-rate modulation up to 35 Gb/s.

1. Introduction

Although work on novel structures for high-efficiency, high-speed VCSELs began well over a decade ago for such applications as chip-to-chip, board-to-board and computer interconnection[1,2], the commercial world has largely ignored these technologies in favor of simple proton-implanted structures for such applications as multi-mode fiber links and, more recently, mice for computers. However, in the past year or two the chip and computer makers are now clearly acknowledging the need for a more power and space efficient way to transmit 20+ Gb/s data over relatively short distances. Thus, interconnect applications within and between high-end computers are emerging for high-speed, high-efficiency VCSELs. If a universal standard is not required, as in active cables or intra-box applications, 980 nm would appear to be more attractive because of its inherent efficiency and speed potential[3].

For somewhat more conventional data links over distances > 300 m or so, the longer wavelengths in the 1300—1600 nm band are preferred. Here manufacturable VCSELs with characteristics suitable for such applications as FTTH or pico-cell wireless distribution are desired. Recent results show that the entire 1300 – 1600 nm wavelength range can be covered in a common InGaAlAs/InGaAsSb/InP epitaxial VCSEL technology[4]. However, competition from edge-emitters manufactured in well-established factories can only be overcome in very high volume applications where the VCSEL can hope to be a lower cost solution. Obtaining edge-emitter-like characteristics is still a major concern.

2. High-speed, high-efficiency 980 nm VCSELs

Figure 1 illustrates a cross section of the GaAs-based VCSEL design along with its small-signal frequency response. The active region contains three strained InGaAs quantum-wells resulting in emission at 980 nm. Substrate emission is facilitated enabling flip-chip mounting as well as backside integrated microlenses as has been shown in prior work[5]. The strained InGaAs active region provides higher differential gain for higher resonance frequency, higher temperature operation (due to a higher T_0), and potentially higher reliability.

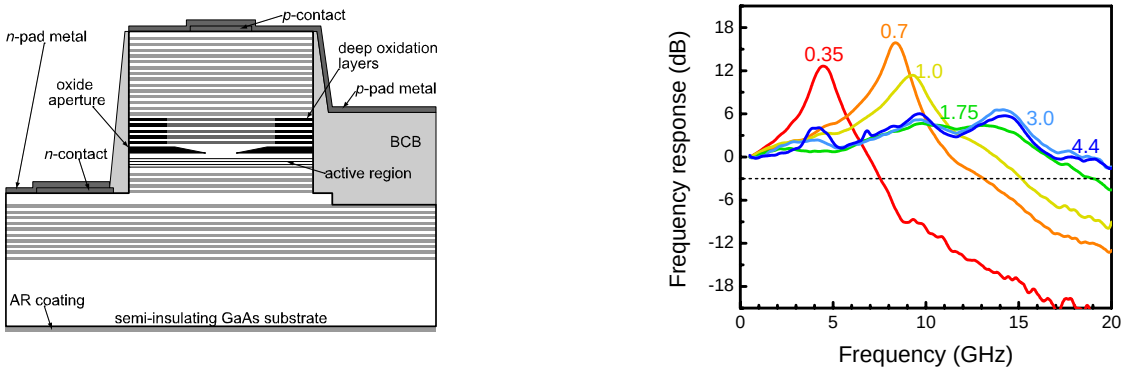

Figure 1. Schematic of tapered oxide VCSEL and frequency response for 3 μm aperture at various bias currents. Maximum cw output power @ 6.8 mA = 3.1 mW; power @ 4.4 mA = 2.6 mW; η_d = 54%.

Figure 1 also illustrates the use of a tapered oxide aperture[6]. This design acts more like an ideal intra-cavity lens and greatly reduces the optical loss, thereby enabling the use of much smaller cavity volumes. The aperture's tapered point also greatly reduces the stress that tends to exist at the tips of oxide apertures with blunt ends. This also should aid in improved reliability, especially with InGaAs quantum-well actives which inhibit defect clustering. The current VCSEL results have primarily been the result of reducing the cavity volume without adding noticeably to the optical mode loss. Resistance and capacitance have also been improved, but multimode operation is probably the primary limiting issue at present. Nevertheless, the frequency response shows a low current bandwidth/root-current figure-of-merit of MCEF = 16.8 GHz/mA$^{1/2}$, about as high as ever obtained in larger area, higher power dissipation devices[7].

Figure 2 shows the eye diagram and Bit-Error-Rate at 35 Gb/s, which indicates error-free operation at 10^{-11} BER. This is the highest error-free data rate and highest data-rata per mW of power dissipation ever obtained from any VCSEL[8]. If the issues identified above, e.g., multimode operation, can be addressed, data rates exceeding 40 Gb/s may be possible.

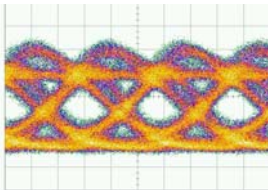

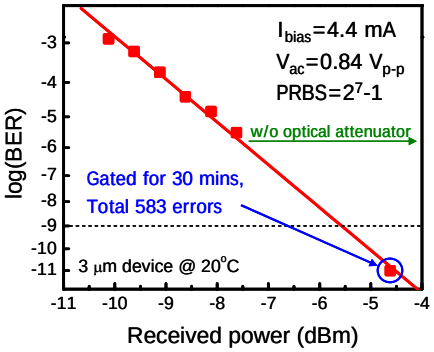

Figure 2. Eye diagram and Bit-Error-Rate at 35 Gb/s. Power dissipation @ 4.4 mA = 10 mW, or 3.5 Gbs/mW.

3. All-epitaxial 1310 nm results

Figure 3 shows a cross section of the 1310 nm InP-based device along with its cw light-current characteristics for a 6.5 μm aperture[4]. About double this cw power was obtained with larger apertures. Similar 1550 nm devices were demonstrated several years ago using the same basic technology platform[9]. As illustrated the device uses two n-type InP intra-cavity contacts for low thermal and electrical resistance with a thin (35 nm) n^+/p^+ tunnel junction placed at a null of the standing wave above the half-wavelength, 5-QW active region. The tunnel junction layers are selectively etched to form a thin aperture for lateral current and photon confinement. The epitaxially-grown DBR mirrors consist of undoped, lattice-matched InGaAsSb layers, which have an index contrast comparable to the AlGaAs layers used in many 850 nm VCSELs. This configuration provides relatively low internal optical losses (~ 7 cm^{-1}). The observed 20°C differential quantum efficiency is higher than 60% for aperture diameters larger than 6 μm. The 3dB small signal bandwidth was measured to be 4.5 GHz at 20°C, dropping to 3.5 GHz at 60°C [10].

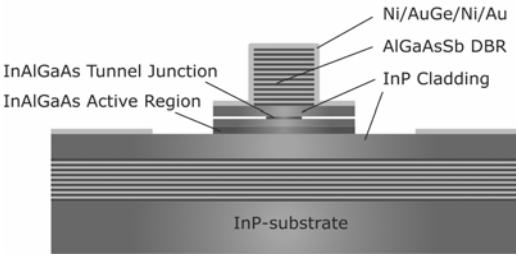

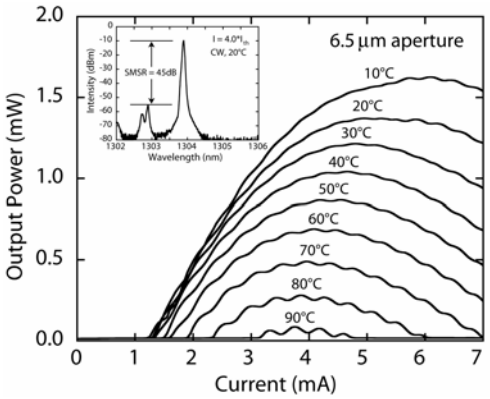

Figure 3. Schematic and L-I characteristics for InP-based 1310 nm VCSEL.

Figure 4 gives the eye diagrams and BER from 20 to 60°C. Open eye diagrams were obtained up to 60°C. The extinction ratios remained > 8dB for operation up to 60°C with a peak-to-peak drive voltage of only 800mV. The results illustrate viable operation at data rates of at least 3.125 Gb/s. Relatively straight-forward modifications to reduce parasitics and mode volume should provide ~ 10 Gb/s.

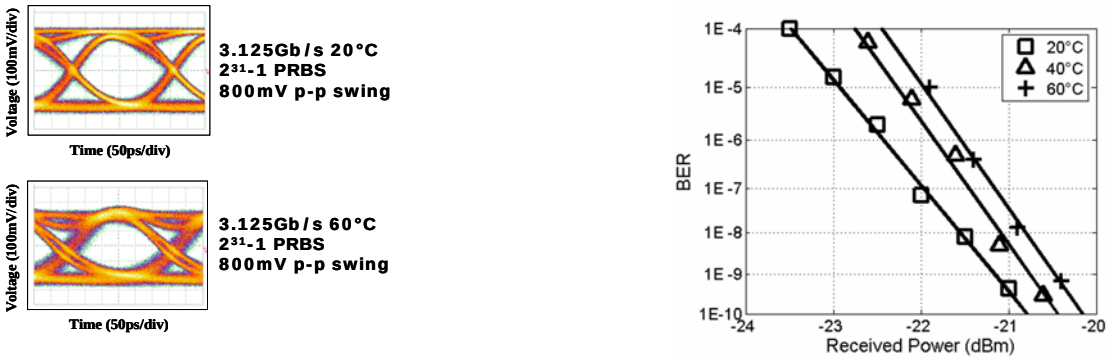

Figure 4. Eyes and BER for 1310 nm VCSEL at 3.125 Gb/s[10].

References

[1] J. W. Scott, B. J. Thibeault, D. B. Young, L. A. Coldren and F. H. Peters, *IEEE Photonics Tech. Letts.*, **6** (6), 678-680, June 1994.

[2] J. W. Scott, D. B. Young, B. J. Thibeault, M. G. Peters and L. A. Coldren, *IEEE J. Selected Topics in Quantum Electron*. **1** (2) 638-648, June 1995

[3] I. Suemune, L. A. Coldren, M. Yamanishi, and Y. Kan, *Appl. Phys. Letts.*, **53** (15) 1378-1381, Oct. 1988.

[4] D. Feezell, D.A. Buell, D. Lofgreen, M. Mehta, L.A. Coldren, *IEEE J. Quantum Electron.*, **42** (5) 494-499, May, 2006.

[5] E.M. Strzelecka, G.D. Robinson, M.G. Peters, F.H. Peters, and L.A. Coldren, *Electron. Letts.*,**31** (9),724-725,Apr. 1995.

[6] B. J. Thibeault, E. R. Hegblom, P. D. Floyd, Y. Akulova, R. L. Naone, and L. A. Coldren, *LEOS '95*, PD 2.1, San Francisco, Oct. 1995; also, E.R. Hegblom, D. I. Babic, B.J. Thibeault, and L.A. Coldren, *CLEO'96*, JTuH3, June, 1996.

[7] Y-C Chang, C. S. Wang, and L. A. Coldren, *LEOS'07*, paper WR3, Buena Vista, FL, Oct., 2007

[8] Y-C Chang, C. S. Wang, and L. A. Coldren, *Electron. Letts.*, **43** (19) 1022-1023, Sept., 2007

[9] S. Nakagawa, E. Hall, G. Almuneau, J.K. Kim, D.A. Buell, H. Kroemer, and L.A. Coldren, *Appl. Phys. Lett*, **78**, 1337-1339, 2001.

[10] D. Feezell, L. A. Johansson, D. A. Buell, and L. A. Coldren, *IEEE Photon. Tech. Letts.*. **17** (11) 2253-2255, Nov, 2005.

Larry A. Coldren is the Fred Kavli Professor of Optoelectronics and Sensors at the University of California, Santa Barbara, CA. He received the Ph.D. degree in Electrical Engineering from Stanford University in 1972. After 13 years in the research area at Bell Laboratories, he joined UC-Santa Barbara in 1984 where he now holds appointments in Materials and Electrical & Computer Engineering, and is Director of the Optoelectronics Technology Center. In 1990 he co-founded Optical Concepts, later acquired as Gore Photonics, to develop novel VCSEL technology; and in 1998 he co-founded Agility Communications, later acquired by JDSU, to develop widely-tunable integrated transmitters.

At Bell Labs Coldren initially worked on surface-acoustic-wave devices and then later on tunable coupled-cavity lasers using new reactive-ion etching (RIE) technology that he created for the then emerging InP-based materials. At UCSB he has worked on novel multiple-section tunable lasers, a variety of related photonic ICs, and high-efficiency vertical-cavity surface-emitting lasers (VCSELs), both at short and long wavelengths. His work has always involved developing new materials growth techniques (by MBE and MOCVD) as well as the necessary fabrication technology.

Professor Coldren has authored or co-authored over 800 papers, 5 book chapters, 1 textbook, and has been issued 61 patents. He has presented dozens of invited and plenary talks at major conferences; he is a Fellow of the IEEE, OSA, and IEE, the recipient of the 2004 John Tyndall Award, and a member of the National Academy of Engineering.

III. Cavity QED, Single-Photon Emitters, and Spin Physics

Cavity QED with quantum dots in semiconductor microcavities

M. T. Rakher*, S. Strauf, Y. Choi, N.G. Stolz, K.J. Hennessey, H. Kim, A. Badolato, L.A. Coldren, E.L. Hu, P.M. Petroff, D. Bouwmeester
University of California Santa Barbara, Santa Barbara, CA, USA 93106;

ABSTRACT

Cavity quantum electrodynamic (QED) effects are studied in semiconductor microcavities embedded with InGaAs quantum dots. Evidence of weak coupling in the form of lifetime enhancement (the Purcell effect) and inhibition is found in both oxide-apertured micropillars and photonic crystals. In addition, high-efficiency, low-threshold lasing is observed in the photonic crystal cavities where only 2-4 quantum dots exist within the cavity mode volume and are not in general spectrally resonant. The transition to lasing in these soft turn-on devices is explored in a series of nanocavities by observing the change in photon statistics of the cavity mode with increasing pump power near the threshold.

Keywords: quantum dot, photonic crystal, micropillar, microcavity, low threshold laser, cavity QED, photon statistics

1. INTRODUCTION

Many proposed implementations of quantum communication and computation in condensed matter systems rely on having a strong interaction between a localized two-level system and a high quality cavity mode [1, 2]. If the coupling strength (which is inversely proportional to the square root of the mode volume) between the two oscillators is weak compared to the lifetime of either the emitter or the cavity mode, then the coupling is said to be in the weak coupling regime. In this regime, the primary effect of the cavity mode is to enhance the lifetime of the emitter and this is called the Purcell effect [3]. This Purcell enhancement factor is proportional to the ratio of the quality factor (Q) of the cavity mode to the effective mode volume (V_{eff}). In addition, if the emitters can provide enough gain to compensate for the cavity decay rate, then lasing may be observed. In the case of semiconductor microcavities embedded with quantum dots (QDs), both of these interesting phenomena can be studied.

2. DEVICE GROWTH AND FABRICATION

2.1 InGaAs Quantum Dots embedded in Oxide-Apertured Micropillar Cavities

A low-density, single layer of InGaAs, self-assembled quantum dots is grown by molecular beam epitaxy in the Stranski-Krastanow growth mode. InGaAs islands are partially covered with GaAs and then annealed before completely capping with GaAs. This process shifts the emission spectrum of the QDs to the blue (near 930 nm) where Silicon-based single photon counting detectors work more efficiently. A low density of these QDs acts as the active region between two high quality AlGaAs/GaAs distributed Bragg reflector (DBR) mirrors. Just above the QD active region an oxide aperture is introduced [4]. This aperture is created by oxidizing a thin layer of pure AlAs, forming Al_xO_y. This oxidation is allowed to proceed until a small aperture of roughly 2 μm is created in the center. The Al_xO_y has a lower index of refraction than the surrounding material so the aperture acts as a lens and confines the mode to the center of the pillar. This has a two-fold effect; it keeps the field away from the sidewalls, which limits the Q of most micropillars, and it reduces the mode volume. In total, it serves to increase the Purcell factor. The pillars are defined by optical lithography and reactive ion etch and a SEM image of one is shown in Fig 1. An array of devices is created with varying total pillar diameter to achieve the optimum Purcell factor and account for small errors in oxidation time.

*rakher@physics.ucsb.edu

2.2 InGaAs QDs embedded in Photonic Crystal Membrane Cavities

Using a similar low density QD sample, photonic crystal (PC) cavities are formed by defining a triangular lattice of air holes by electron beam lithography. Then, holes are created along with the membrane by chemical etching in HF. Line defect cavities are formed by selective removal of 3, 7 or 11 holes (L3, L7, and L11 cavities) to create a defect region. An example of a SEM image of an L3 cavity is shown in Fig. 1. Strong optical confinement in the plane is provided by the 2-D photonic crystal while out of plane confinement is provided by the GaAs air interface at the top and bottom of the membrane. Device parameters such as hole radius, lattice spacing, and membrane thickness are optimized to provide the highest Q while keeping the mode volume as small as possible.

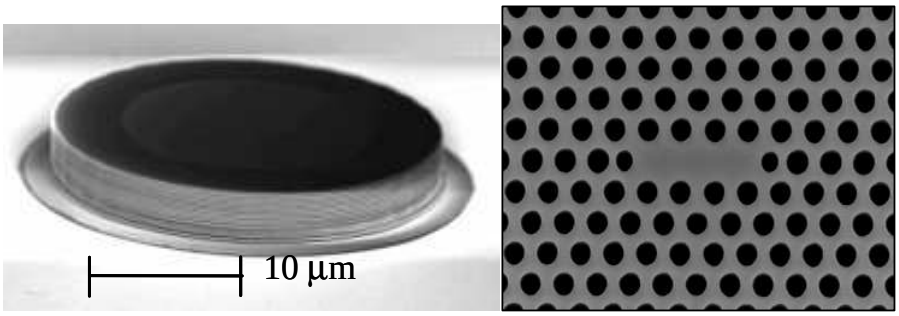

Fig. 1. Scanning electron microscope (SEM) images of an oxide-apertured micropillar (left) and an L3 PC cavity (right).

3. EXPERIMENTAL SETUP

3.1 QD and Device Spectroscopy

The QDs and the devices are primarily studied using micro-photoluminescence spectroscopy. The samples are kept in a He-flow cryostat operated at 4.2 K with a heater capable of increasing the temperature to 300 K. Carriers are excited in the samples by a pulsed 82 MHz Ti:Sa laser with approximately 100 fs pulse width. This laser is primarily operated at 850 nm to excite carriers resonantly into the wetting layer. Additionally, continuous wave lasers operating at 780 nm and 632.8 nm can be used for above-bandgap excitation. These sources are focused through a 50X objective with NA = 0.55 onto the sample surface as shown in Fig. 2. Emission is imaged through the same objective where it is picked off by a beamsplitter (BS) and directed into a 1.25 m spectrometer with a liquid nitrogen cooled CCD array, yielding a 30 μeV spectral resolution at 900 nm.

3.2 Lifetime and Hanbury-Brown and Twiss Measurements

Lifetime measurements of single QDs are performed with pulsed excitation using a single photon counting avalanche photodiode in conjunction with a time-to-amplitude converter card. Before detection, single QD spectral lines are chosen and spectrally filtered with a 0.5 nm bandpass filter as shown in Fig. 2. Hanbury-Brown and Twiss measurements are performed by incorporating a beamsplitter and another single photon detector as shown in Fig 2. This measures the second-order coherence of the emitted light and can be used to determine information about the photon statistics of the emitted light field.

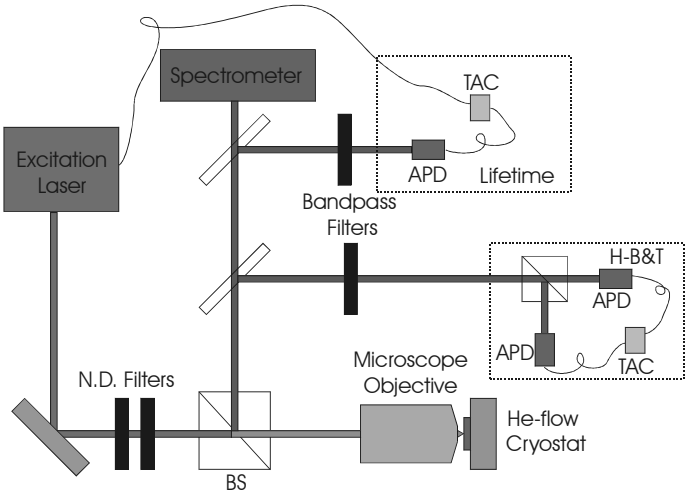

Fig. 2. A schematic of the experimental setup. The excitation laser is directed though an objective onto the sample surface. The collected photoluminescence can then be directed into the spectrometer, the lifetime setup, or the Hanbury-Brown and Twiss setup.

4. RESULTS

4.1 Cavity mode spectra

As shown in Fig. 3, the fabrication processes described in the previous section display high Q cavity modes in the spectral region of QD s-shell transitions. The spectra from the micropillar (Fig. 3) can be analyzed to determine the Q and values greater than 30000 (the resolution limit of the spectrometer) have been measured [5]. Comparing the mode spacing to values predicted from simulations, the mode volume can be determined to be approximately 51 $(\lambda/n)^3$. This yields an expected Purcell factor of around 72. The photonic crystal spectra can be analyzed to determine the Q and values nominally around 12000 are obtained. Mode volume calculations have been carried out by finite-difference time-domain simulations and typical values for the lowest order mode are around 0.68 $(\lambda/n)^3$.

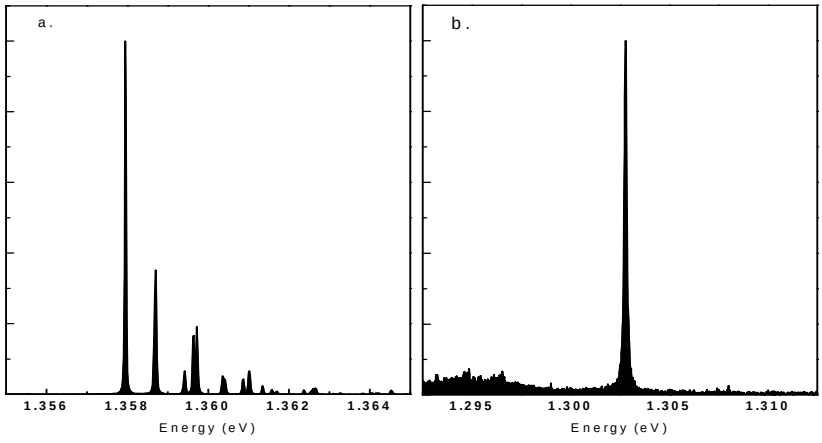

Fig. 3. Micro-photoluminescence spectra of cavity modes in the micropillar structure (a.) and the L3 photonic crystal cavity (b.). Both measurements were done at 4.2 K with the pump power high enough to saturate the QD transitions.

4.2 QD lifetime measurements

Measurements of single QD lifetimes on and off resonance with the cavity mode have also been carried out. Lifetimes for dots on resonance with micropillar cavity modes have been shown to be as small as 200 ps (our measurement resolution), corresponding to a Purcell factor of more than 6. As shown in Fig 4a, the lifetime decreases as the dot is brought into resonance with the cavity mode as expected by the Purcell effect. Measurements of QDs in photonic crystal cavities have shown lifetimes as long as 10 ns as shown in Fig 4b. This suggests that while the QD may be in spectral resonance with the cavity mode, its lifetime is inhibited due to spatial displacement from the cavity field maximum. Enhanced lifetimes are much harder to obtain experimentally due to the small probability of a dot being both spatially and spectrally on resonance with the cavity mode.

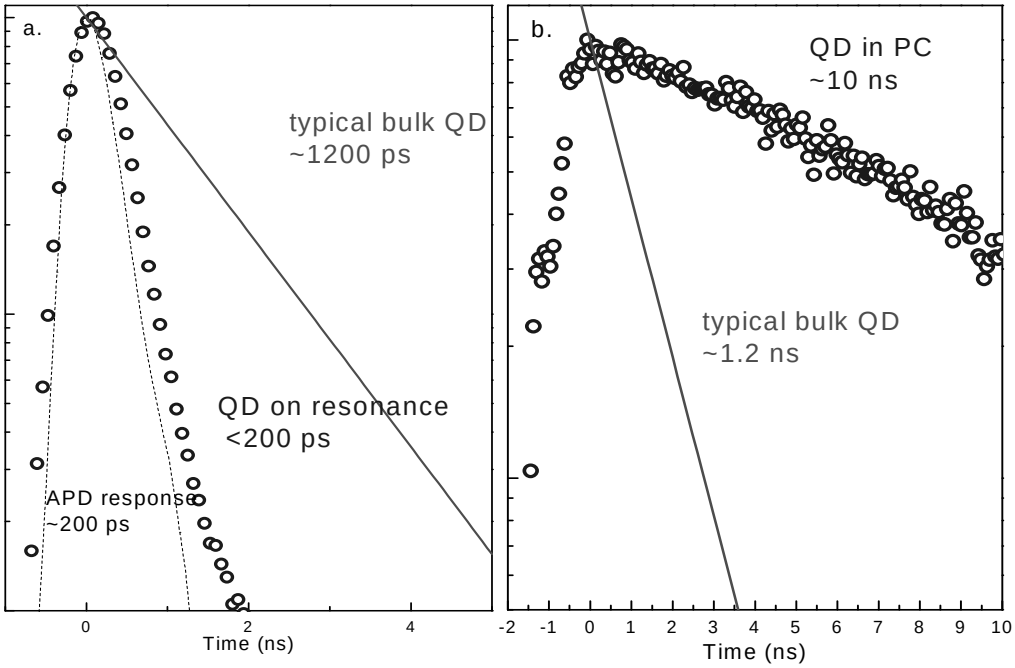

Fig. 4. a). A plot of the lifetime of a single QD on resonance with a micropillar cavity mode. The lifetime measurement is limited by the APD response (shown as the segmented line) of 200 ps. For comparison, a line showing a typical bulk QD lifetime of 1200 ps is shown. b). A plot of a QD inside a photonic crystal structure demonstrating a lifetime around 10 ns. This strong inhibition of the lifetime suggests the dot is spatially displaced from the maximum of the field. A typical bulk QD lifetime is shown for comparison.

4.3 Lasing in PC cavities

Analysis of the intensity and linewidth of PC cavity modes as a function of input pump power reveals lasing behavior in these devices as shown in Figure 5. The soft-turn on and low-threshold characteristics of these cavities demonstrates a high coupling of spontaneous emission into the mode, called the β factor, of around 0.85 [6]. Lasing was unexpected due to the extraordinarily low QD density as well as the fact that the sharp transition lines of the QDs are not spectrally resonant with cavity mode. Because of the high β factor, the onset of lasing action is hard to distinguish from other sources of nonlinear output behavior.

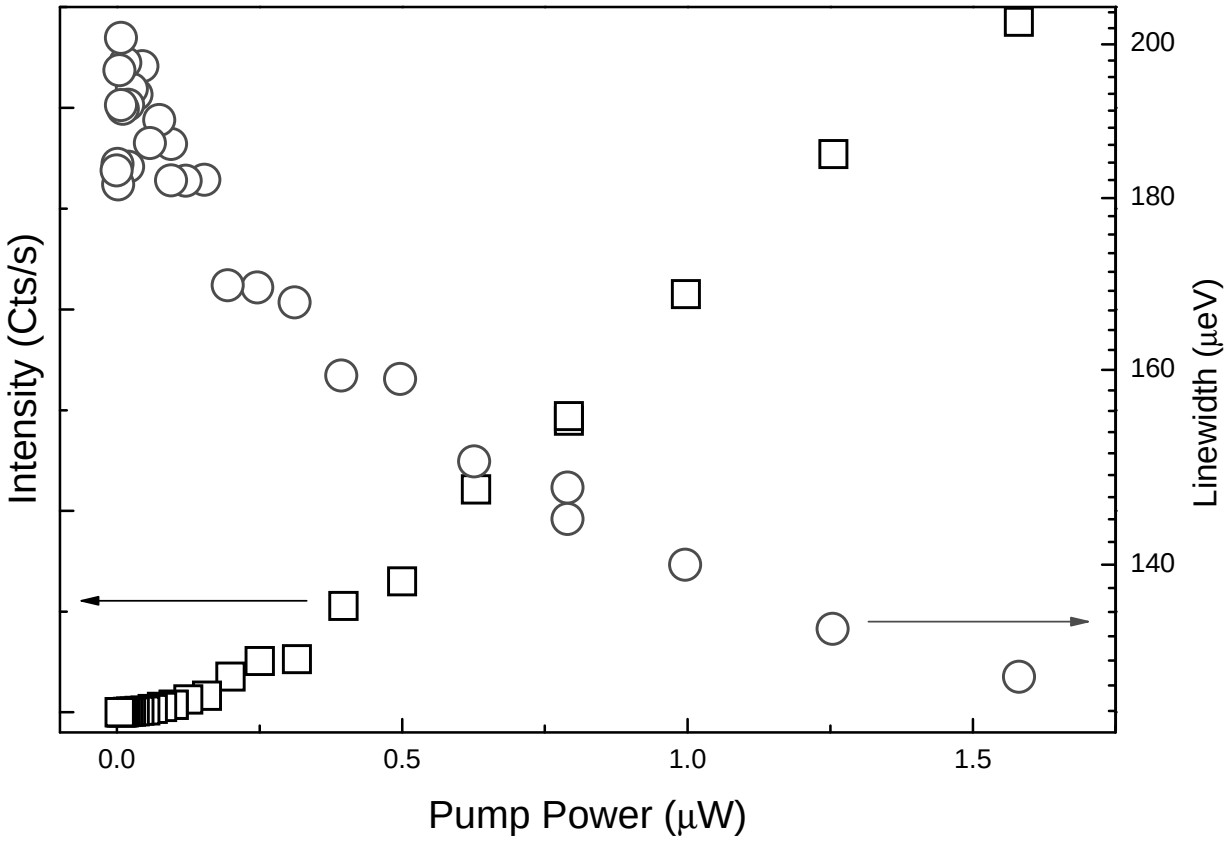

Fig. 5. Output count rate and linewidth of an L3 cavity mode vs. input power from a continuous wave 780 nm source.

4.4 Second-order correlation measurements for PC lasers

To validate the onset of lasing in the PC cavity devices, second order intensity correlation measurements were performed at pump powers near the lasing threshold. As shown in Figure 6, $g^{(2)}(0)$ increases to a value near 2 and then subsequently diminishes to 1 as the pump power is increased. Theoretically, one expects the photon statistics of a cavity mode below the laser threshold to behave like a thermal light source, corresponding to $g^{(2)}(0) = 2$. Once lasing is established, the photon statistics are described by a coherent state with Poissonian statistics, corresponding to $g^{(2)}(0) =1$. The results in Figure 6 demonstrate exactly that aside from the initial increase. This initial increase is attributed to the transition from the uncorrelated spontaneous emission regime to the stimulated emission regime. If the mode is comprised of uncorrelated spontaneous emission events, $g^{(2)}(0) =1$. Once stimulated emission sets in, $g^{(2)}(0)$ tends toward the thermal value of 2.

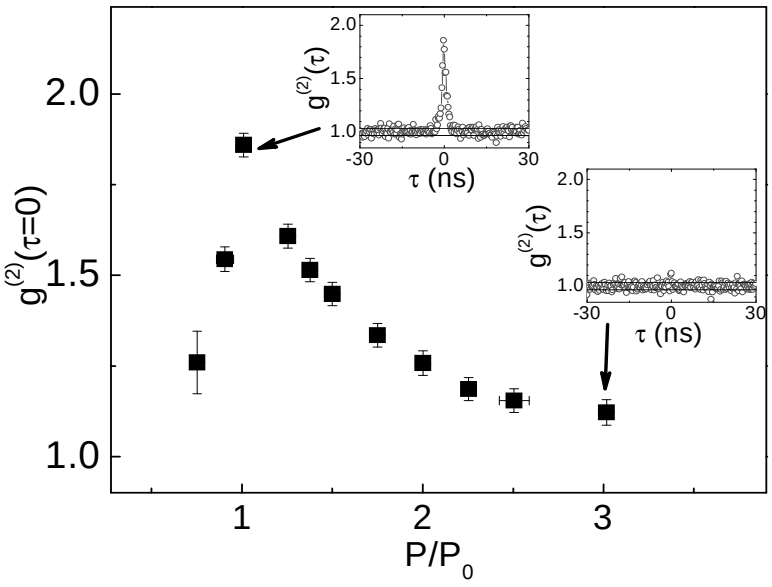

Fig. 6. $g^{(2)}(0)$ vs. threshold normalized pump power for an L11 laser. The insets show the corresponding $g^{(2)}(\tau)$ at two of the measured pump powers.

5. CONCLUSIONS

In conclusion, a wide variety of phenomena associated with cavity QED have been investigated using InGaAs quantum dots embedded in two different semiconductor nanocavity structures. Weak coupling in the form of the Purcell spontaneous emission enhancement has been experimentally found for QDs interacting with oxide-apertured micropillar cavity modes and strong inhibition has been demonstrated for QDs inside photonic crystal defect cavities. While a strong enhancement has not been found for PC cavities, advances in active QD positioning will enable future experiments in both the weak and strong coupling regimes [7].

Surprisingly, the photonic crystal cavities demonstrated the onset of lasing with increasing pump power. This was unexpected considering the low QD density along with the spectral mismatch of the sharp s-shell transitions and the cavity mode. Subsequent measurements of the photon statistics as a function of pump power near the lasing threshold validate the claim of lasing and are an important addition to the standard input-output and linewidth measurements. They are an essential measurement because of the soft turn-on nature of these high β, low threshold lasers, which can make identification of lasing action difficult [6].

REFERENCES

1. A. Imamoglu, et. al, "Quantum Information Processing Using Quantum Dot Spins and Cavity QED," *Phys. Rev. Lett.* **83**, 4204 (1999).
2. P. Michler, et. al, "A Quantum Dot Single-Photon Turnstile Device," *Science* **290** 2282 (2000).
3. K. J. Vahala, "Optical Microcavities," *Nature* **424,** 839 (2003).
4. N.G. Stolz, et. al, "Quantum Dot Spontaneous Emission Lifetime Modification in Optical Microcavities using Oxide Apertured Micropillars," *Proc. SPIE* **6101,** 61010W (2006).
5. N.G. Stolz, et. al, "High quality factor optical microcavities using oxide apertured micropillars," *App. Phys. Lett.* **87**, 031105 (2005).
6. S. Strauf, et. al, "Self-tuned quantum dot gain in photonic crystal lasers," *Phys. Rev. Lett.* **96**, 127404 (2006).
7. A. Badolato, et. al, "Deterministic Coupling of single quantum dots to single nanocavity modes," *Science* **308**, 1158 (2005).

Efficient Source of Single Photons from Charge-Tunable Quantum Dots in a Micropillar Cavity

M. T. Rakher[1], S. Strauf[1,2], N. G. Stolz[3], L. A. Coldren[3], P.M. Petroff[3], D. Bouwmeester[1]
1Department of Physics, University of California at Santa Barbara, CA 93106, USA
2 Physics Department, Stevens Institute of Technology, Hoboken, NJ 07030, USA
3 Materials Department, University of California at Santa Barbara, CA 93106, USA
rakher@physics.ucsb.edu

Abstract: A single photon source is demonstrated using a novel oxide-apertured micropillar cavity embedded with InGaAs quantum dots. A bright 80 MHz count rate is enabled by the Purcell effect and charge-tuning of the quantum dots.

OCIS codes: (300.6470) Spectroscopy, Semiconductors; (230.6080) Sources

Introduction

Single photon sources (SPS) are a vital component in many quantum cryptography and computation schemes [1]. To date, most SPS are limited due to small emission rates and rapid saturation. Up to date the highest single photon rates of 0.2 MHz have been observed from self-assembled quantum dots (QDs) embedded in etched micropillar structures [2,3], which largely outperform approaches based on photonic crystal cavities [4]. However, submicrosecond memory effects due to trapping of individual charges and dark excitons inside the QDs strongly limits the efficiency of those SPS devices [3]. Here, we overcome these difficulties by coupling a charged QD to a high quality cavity mode, enabling a single photon source with a count rate of 80 MHz.

Methods

The quantum dots are grown by molecular beam epitaxy in the Stranski-Krastanow growth mode using the partially covered island technique to shift the emission to around 930nm. AlGaAs/GaAs micropillar structures are fabricated using a low density of QDs embedded between two DBR stacks. The fifth DBR layer from the QDs is n-doped and acts as a top contact. Electrons can tunnel into the QDs from a Si delta doped layer 25 nm below the QDs. Each of these doped layers is contacted by etching down from the top of the sample. Then, trenches are etched away as shown in Fig. 1, leaving a roughly 20 um diameter pillar which is still connected via bridges to the surrounding material. Finally, an oxide aperture is introduced to decrease the mode volume while keeping the cavity mode away from the rough sidewalls, thereby increasing the quality factor (Q) [5].

We study these systems by performing timing-resolved micro-photoluminescence spectroscopy. The sample rests in vacuum at 4.2 K in a variable temperature He-flow cryostat and is connected to a voltage sourcemeter. The photoluminescence is directed into one of two measurement apparatuses; a 1.25 m spectrometer with a nitrogen-cooled CCD camera or a Hanbury-Brown and Twiss (H-B&T) setup. The combination of these instruments allows the determination of the electrical, spectral, and temporal properties as well as the photon statistics of the emitted light field.

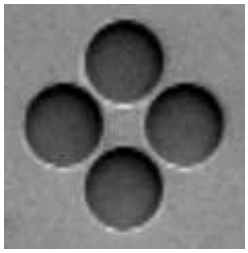

Figure 1. A SEM image of a trench micropillar cavity.

Results

We tune the QD into resonance with a cavity mode (Q ~ 40,000) and perform a time-correlated photon counting measurement to determine the excitonic lifetime. We obtain a value of 400 ps from a fit to a single exponential, thus demonstrating a Purcell effect of 2 to 3. In addition, the single exponential behavior of the decay signifies a reduction in the population of excitonic dark states, meaning the quantum dot is likely charged. Also, we measure the second-order intensity correlation function using the H-B&T setup and extract $g^{(2)}(0)$ to obtain information about the photon statistics. This is done as a function of the input pump power and is show in Fig. 2. Up to a collected count rate of 12 MHz (see Fig. 2 inset for a spectra), $g^{(2)}(0)$ remains less than 0.5, proving the single photon nature of the emitted light field. Once experimental losses are accounted for, 12 MHz of collected photons corresponds to an actual single photon rate of 80 MHz, which is a 400 times improvement over the best prior report [3].

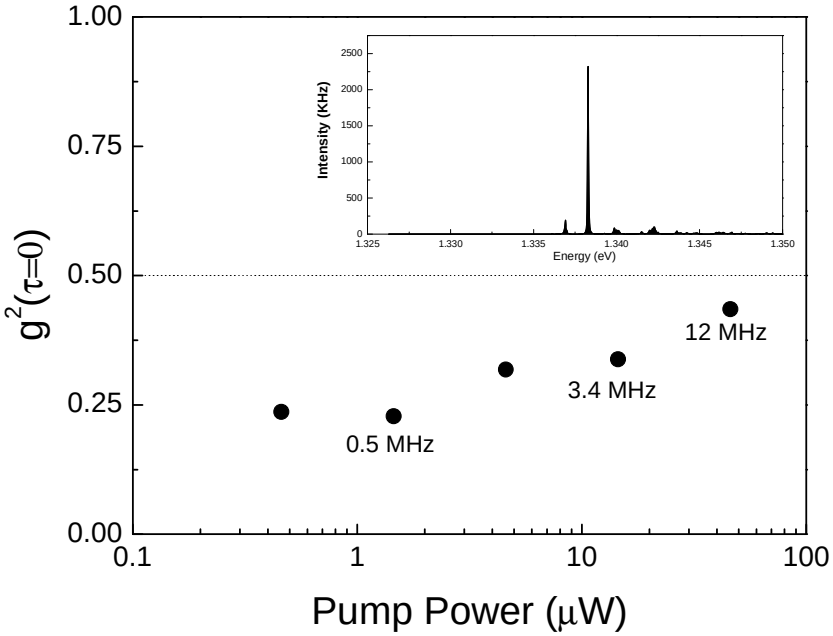

Figure 2. A plot of $g^{(2)}(0)$ for a quantum dot on resonance with a cavity mode as a function of pump power. Note that $g^{(2)}(0) < 0.5$, proving the emitted field is comprised of single photons. Inset: The spectra of the dot on resonance with a cavity mode.

Conclusions

We have demonstrated the highest count rate for a single photon source and have proven it is indeed comprised of single photons by measuring the second order intensity correlation function. The combination of the enhanced spontaneous emission rate due to the Purcell factor as well as removal of dark states by charge tuning enabled this drastic increase over prior reports. This combination of factors can only be realized in a novel device structure such as our trench design where a high quality, small volume cavity mode and electrical-gating are integrated in one device.

[1] E. Knill, R. Laflamme, G.J Milburn, "A Scheme for Efficient Quantum Computation with Linear Optics," Nature **46,** 409 (2001).
[2] M. Pelton, et. al, "Efficient Source of Single Photons: A Single Quantum Dot in a Micropost Microcavity," Phys. Rev. Lett. **89**, 233602 (2002).
[3] C. Santori, et. al, "Submicrosecond correlations in photoluminescence from InAs quantum dots," Phys. Rev. B 69 205324 (2004).
[4] D. Englund, et. al, "Controlling the Spontaneous Emission Rate of Single Quantum Dots in a Two-Dimensional Photonic Crystal," Phys. Rev. Lett. **95** 013904 (2005).
[5] N. G. Stolz, "High-quality factor optical microcavities using oxide apertured micropillars," App. Phys. Lett. **87** 031105 (2005)

High-frequency single-photon source with polarization control

STEFAN STRAUF[1,2]*, NICK G. STOLTZ[3], MATTHEW T. RAKHER[1], LARRY A. COLDREN[3,4], PIERRE M. PETROFF[3,4] AND DIRK BOUWMEESTER[1,5]

[1]Department of Physics, University of California, Santa Barbara, California 93106, USA
[2]Department of Physics and Engineering Physics, Stevens Institute of Technology, Hoboken, New Jersey 07030, USA
[3]Materials Department, University of California, Santa Barbara, California 93106, USA
[4]ECE Department, University of California, Santa Barbara, California 93106, USA
[5]Huygens Laboratory, Leiden University, PO Box 9504, 2300 RA Leiden, The Netherlands
*e-mail: strauf@stevens.edu

Published online: 18 November 2007; doi:10.1038/nphoton.2007.227

Optoelectronic devices that provide non-classical light states on demand have a broad range of applications in quantum information science[1], including quantum-key-distribution systems[2], quantum lithography[3] and quantum computing[4]. Single-photon sources[5,6] in particular have been demonstrated to outperform key distribution based on attenuated classical laser pulses[7]. Implementations based on individual molecules[8], nitrogen vacancy centres[9] or dopant atoms[10] are rather inefficient owing to low emission rates, rapid saturation and the lack of mature cavity technology. Promising single-photon-source designs combine high-quality microcavities[11] with quantum dots as active emitters[12]. So far, the highest measured single-photon rates are ∼200 kHz using etched micropillars[13,14]. Here, we demonstrate a quantum-dot-based single-photon source with a measured single-photon emission rate of 4.0 MHz (31 MHz into the first lens, with an extraction efficiency of 38%) due to the suppression of exciton dark states. Furthermore, our microcavity design provides mechanical stability, and voltage-controlled tuning of the emitter/mode resonance and of the polarization state.

Excitons inside semiconductor quantum dots (QDs) interact efficiently with light, making them attractive as an optically active material for single-photon sources (SPS)[5,6,12–18], LEDs (ref. 19), low-threshold lasers[20] and solar cells[21]. Under optical excitation or electrical-carrier injection, electrons and holes are created in higher energy states and subsequently relax into localized QD states. Random carrier capture leads to both geminate and non-geminate loading of the QD, causing limitations in device efficiency[22]. When a QD is loaded with a neutral exciton (X0), it can be either in a bright-state configuration with angular momentum $L_z = \pm 1$ or in a dark state with $L_z = \pm 2$. Although the bright-state configuration is dipole allowed with a typical spontaneous emission (SE) lifetime of 1 ns, the dark-state configuration is dipole forbidden and thus a long-lived state. If a QD is loaded into a dark state, a spin-flip must occur, for example involving the Fermi sea of an adjacent back gate[23], or it can be pumped through the biexciton (XX) to the bright state. Thus if a QD is triggered to emit single photons (SPs) at a high repetition rate, it occupies on average more time in dark-state configurations, which limits the maximal achievable emission rate

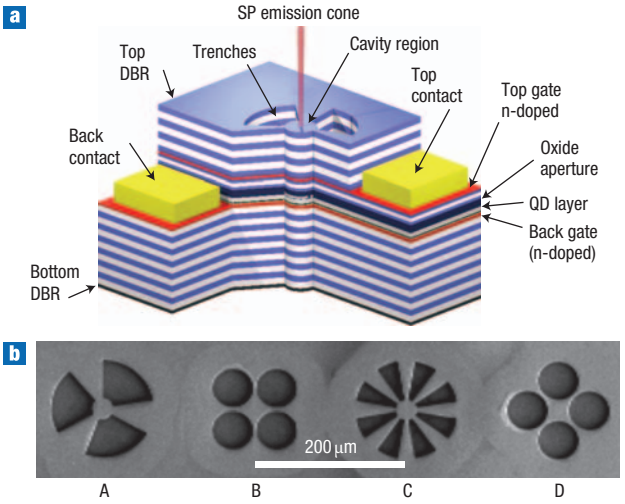

Figure 1 SPS device design. a, Schematic three-dimensional view of the SPS containing a λ-cavity region embedded between a 32-period bottom AlGaAs/GaAs DBR and a 23-period top DBR (white/blue layers). The cavity contains a single layer of InAs QDs (grey) and a mode-confining tapered AlO_x region (dark blue). Selective countersink etching allows separate global contacting (yellow) of the n-doped top and bottom gate layers (red). **b**, Scanning electron micrograph of various geometries of the trench design (top view). The inner lateral cavity area has a diameter of ∼20 μm. The remaining small bars provide lateral electrical contacts.

(see Supplementary Information). Additionally, the capture of single carriers leads to submicrosecond correlation effects[14], which act in effect as dark states.

To eliminate dark-state configurations we aimed to load a QD embedded in a microcavity with a single electron. Subsequent electron–hole pair capturing owing to optical (or electrical) excitation would create predominantly charged excitons (X−) in a singlet configuration. In such a case, recombination is always expected to be bright and an SPS can continuously fire SPs with

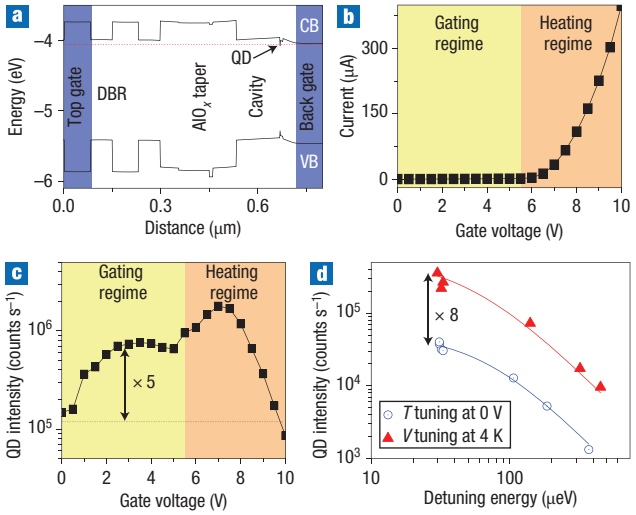

Figure 2 Influence of gate voltage on SPS performance. a, Schematic energy band diagram. The tunnel barrier width between the back gate and the QD is 25 nm. CB, conduction band; VB, valence band. **b**, Current–voltage characteristic of the entire SPS array recorded at 4 K. **c**, Single QD intensity as a function of gate voltage for a type B (from Fig. 1b) device under 780 nm excitation. **d**, Comparison of SPS intensity as a function of QD/mode detuning energy using the cryostat heater at zero gate voltage (*T* tuning, blue circles) and for fixed cryostat temperature (4 K) and gate voltages between 5 and 9 V (*V* tuning, red triangles). Detuning energies are taken from lorentzian line-shape analysis.

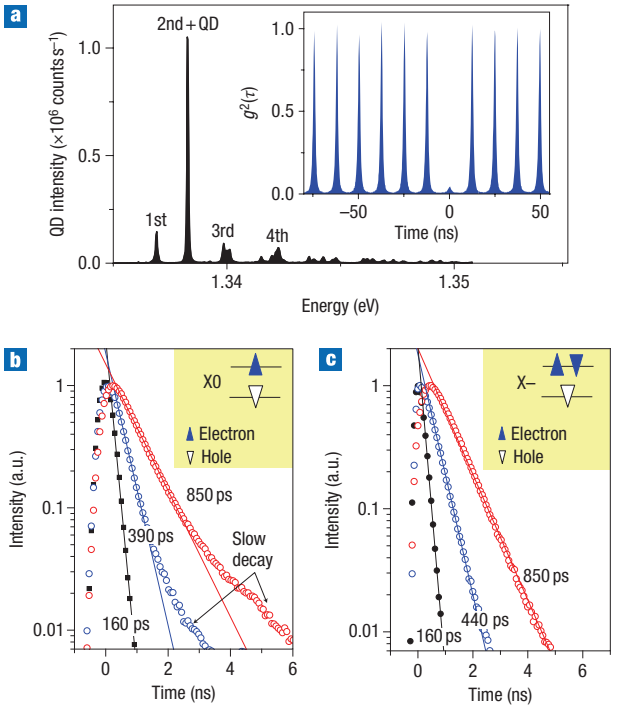

Figure 3 Single QD characterizations. a, Cavity mode spectrum with a neutral QD coupled to a second-order mode at 7.3 V bias. Inset: Second-order correlation function $g^2(\tau)$ recorded with 10 nW pump power. Note that submicrosecond correlation effects[14] are absent under biased conditions for both QD charge states even at lowest pump powers. **b**, Lifetime measurements for QD loaded with X0 under off-resonance (red circles) and on-resonance (blue circles) conditions. Black data points indicate scattered laser light corresponding to 160-ps system resolution. **c**, Comparable lifetime measurements for a QD loaded with X−. Note the mono-exponential decay in contrast to the bi-exponential decay of X0.

rates approaching the SE lifetime limit. Additional electrons can either be injected through electrical gates or provided by doping QDs or their surroundings or both.

Although controlled loading of single QDs has been demonstrated[23,24], implementation of electrical gates into high-*Q* cavities has not yet been achieved. To this end we have developed oxide-tapered high-*Q* microcavities based on a rugged trench design. Figure 1a shows a device schematic. A layer of QDs inside a wavelength-lang cavity (λ-cavity) is sandwiched between two distributed Bragg reflectors (DBR). A top electrical gate and a tunnel back gate with 25-nm barrier are formed adjacent to the QDs (see Methods for details). These n-doped layers provide an embedded electrical gating structure to control the QD loading process and local current heating within the cavity. Air-etched GaAs micropillars are typically fabricated with submicrometre diameters to confine the mode volume[11,13]. To avoid difficulties associated with micrometre-scale electrical contacts, we use trenches with various geometries etched down into the bottom DBR (Fig. 1b). These trenches are used to define an AlO_x oxidation front, providing high-quality factors up to 50,000 and simultaneously optical-mode confinement[15]. This design provides good mechanical stability, the possibility of controlling the mode degeneracy, and it allows global contacting by countersink etching two contacts to an entire SPS array.

Figure 2a shows a schematic of the band structure including top and back gates (blue areas). The bottom gate is grounded and voltage is applied to the top gate. Optical emission is probed under non-resonant laser excitation into the GaAs. At negative bias voltages below −2 V the QD emission completely quenches, in analogy to gated structures without a cavity[24]. For voltages above about 5.5 V, carriers overspill and create a current breakthrough, as shown in the current–voltage (*I*–*V*) curve in Fig. 2b. This creates two useful regimes for SPS operation. For voltages below breakthrough, one can manipulate the QD loading process as shown in the following. Above breakthrough, the electrical current causes localized heating (on-chip heater), which can be used to fine-tune the QD/mode resonance (Fig. 2c,d).

Interestingly, a strong fivefold increase in QD emission is observed for voltages of 2–5 V (Fig. 2c). In this regime, no spectral shift of the QD exciton occurs. This excludes both QD charging (X− formation) and spectral QD/mode detuning (Purcell effect[6]) as an explanation. Controlled QD/mode tuning can either be achieved at zero gate voltage using the cryostat heater (method A) or at a fixed base temperature (4 K) and increasing the gate voltage above 5 V (method B), as shown in Fig. 2d. For method A, the QD transition has a 40-fold intensity enhancement if tuned into resonance (blue circles). Method B creates an additional eightfold enhancement for all detuning conditions (red triangles). Simultaneously, the X0 transition displays a Purcell factor of two (see Fig. 3b), independent of the tuning method. Thus the intensity enhancement is independent of the actual SE rate, suggesting a relation to the QD loading process[25]. These findings suggest that the voltage-induced enhancement (Fig. 2c,d) is related to field-enhanced carrier capture processes. Indeed, if single QDs are optically pumped into SE saturation, the voltage-induced intensity enhancement also saturates (not shown). However, practically, SPSs are not operated at saturation because of degraded SP purity. Therefore,

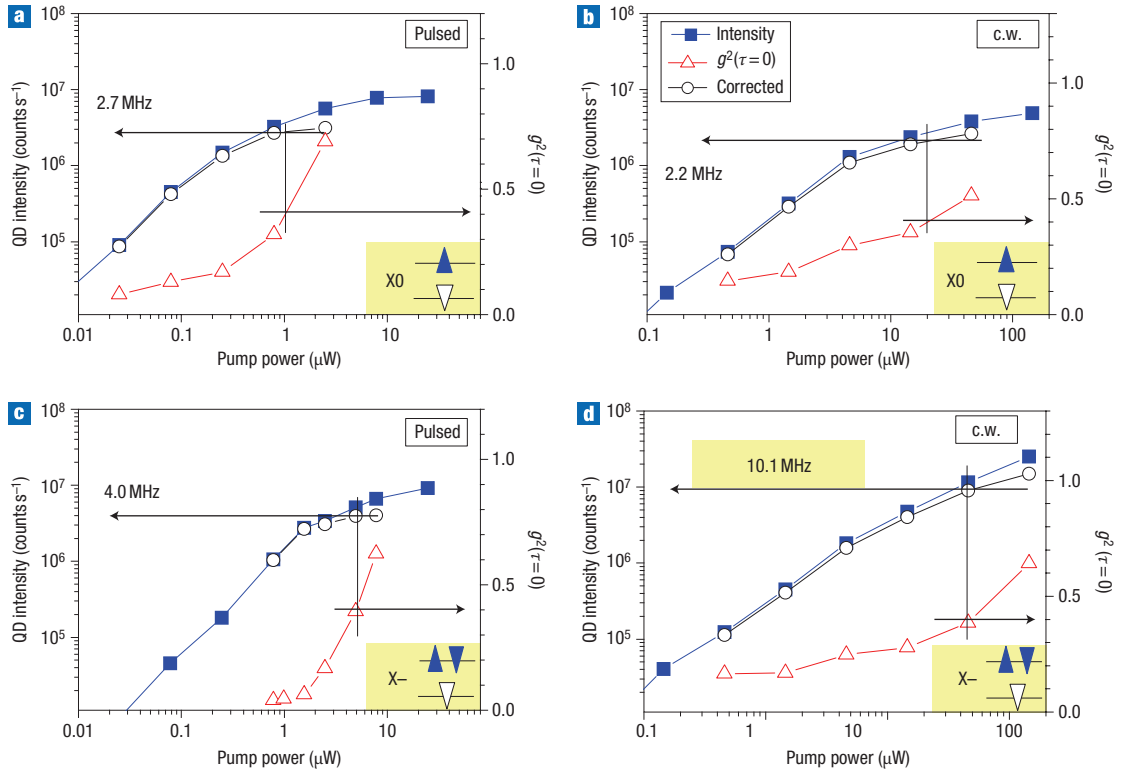

Figure 4 Impact of QD charging on SPS performance. a–d, QD intensity (blue squares, left *y* axis) and corresponding $g^2(\tau = 0)$ values from coincidence measurements (open red triangles, right *y* axis). Intensity data are corrected for background emission (open black dots; see Methods). Two devices are compared: one with X0 (**a**, **b**) and one with X– on resonance (**c**, **d**). For each charging state we compare pulsed laser excitation at 780 nm (**a**, **c**) and c.w. laser excitation at 630 nm (**b**, **d**). Arrows indicate SP intensities at $g^2(\tau = 0) = 0.4$, close to QD saturation. Note the noticeably improved count rates for charged QDs under c.w. excitation.

the achieved voltage-controlled enhancement is of high practical importance as it allows higher SP rates at a comparable injection level while minimizing background contributions that otherwise compromise the SP purity.

Single-photon sources are characterized by strong photon antibunching signatures[5,6]. Figure 3a shows a spectrum of a single QD loaded with X– and tuned in resonance with a degenerate cavity mode. The inset shows the corresponding second-order correlation function, $g^2(\tau)$, displaying a zero delay time peak area of 4%. This corresponds to a 25-fold decrease in unwanted multiphoton emission events compared with attenuated coherent light sources. Devices typically display a 40-fold enhanced SP emission rate if sharp exciton lines are tuned into spectral resonance (Fig. 2d). These results were achieved for QDs with an SE lifetime of about 1 ns, similar to QDs in bulk GaAs. They are thus spectrally, but not spatially, on resonance. In such a case intensity enhancement is entirely caused by enhanced geometrical collection efficiency and not related to the Purcell effect. In about a third of devices, the QDs under consideration are spatially on resonance and display a Purcell factor of from two to four if tuned spectrally into resonance. To separate effects related to random positioning of QDs from effects caused by charging and applied voltages, we concentrate on devices with a Purcell factor of approximately two (Fig. 3b,c).

To show that X– is better suited for an SPS than X0, we first have to identify the X0 and X– transitions of individual QDs. In high-Q cavities, clear identification based on spectral signatures, that is, the typical 5–6 meV Coulomb charging separation[24], is rather difficult because spectra are largely altered by the underlying mode distribution and stop band. However, as has been demonstrated[23], time-resolved measurements of QDs in gated structures display a mono-exponential decay for the X– transition and a pronounced bi-exponential decay for X0. Figure 3b,c shows lifetime measurements for single QDs located in two different devices, clearly distinguishing between bi-exponential (Fig. 3b) and mono-exponential (Fig. 3c) decay for both off-resonance (red circles) and on-resonance (blue circles) conditions with a degenerate mode, supporting our assignment of X0 and X–.

We investigated the SPS device performance by recording both intensity and antibunching signatures as a function of pump power (Fig. 4a–d). With increasing pump power, antibunching signatures bleach out owing to QD saturation and SE coupling from other QDs at higher pump powers[20], limiting the maximal achievable SP rates. To compare devices pumped under pulsed and continuous-wave (c.w.) excitation conditions we chose a working point close to QD saturation, where $g^2(\tau = 0) = 0.4$, that is, when the SPS still performs 2.5 times better than an attenuated laser source. Before comparison, the measured intensity data had been corrected for the multiphoton background to extract the bare SP rate (see Methods). Two devices with degenerate modes were chosen for comparison, one with X0 on resonance (Fig. 4a,b) and one with X– on resonance (Fig. 4c,d). Under pulsed excitation, measured SP rates are 2.7 MHz for the X0 and 4.0 MHz for the X– transition, respectively. If corrected for the 13% detection efficiency, these devices emit into the first lens

with a record high SP rate of 21 MHz for X0 and 31 MHz for X−. From these data and the given repetition rate (82 MHz) one can estimate an SP extraction efficiency η of 26% for X0 and 38% for X−. If a higher purity of SP is required[26], one can, for example, operate the X− devices at 1 μW pump power (Fig. 4c) leading to $g^2(0) = 0.05$, an SP rate of 21 MHz and $\eta = 25\%$.

If one drives the two-level system even faster than with an 82 MHz repetition rate, one would expect even higher SP rates of about 870 MHz up to the SE lifetime limit (This limit is estimated using the measured (Purcell enhanced) exciton lifetime of 440 ps (2.3 GHz) modified by the cavity-mode collection efficiency of 38%.) Pumping the single QD under c.w. excitation thus probes for the ultimate limit. We performed the same SPS characterization under c.w. excitation at 632 nm (Fig. 4b,d). Surprisingly, for QDs loaded with X0, maximal achievable SP rates saturate at about 2.2 MHz, which is comparable to the pulsed excitation experiment (Fig. 4b). This demonstrates that the emission rate of X0 is severely limited by dark states. Most strikingly, c.w. excitation of an SPS with X− on resonance yields an SP rate of 10.1 MHz (Fig. 4c), corresponding to 78 MHz if corrected for detection efficiency, which is a threefold improvement over the X0 case (see Methods). In contrast to the case of X0, the SP rate for X− saturates slowly and one can estimate 116 MHz at the highest pump powers near 150 μW. At lower pump powers the X−/X0 ratio is close to unity. These findings are in quantitative agreement with a rate-equation model (see Supplementary Information). At low pump rates there is enough time for a spin-flip to occur between excitation events, and X0 dark states can become bright again, leading to a ratio of unity. At higher pump rates the XX creates a path back into the bright state for X0. In a cavity the XX is inhibited if X is on resonance, which limits the X0 recovery time out of dark states compared with the Purcell enhanced recombination rate of the X− transition, which is always bright. Although these c.w. experiments clearly demonstrate that a threefold improvement can be achieved by using X−, the nature of c.w. excitation does not in principle allow for on-demand operation. Thus the highest achieved count rate for on-demand operation of our SPS devices is 31 MHz ($\eta = 38\%$), constituting a fivefold improvement compared with other SPSs (refs 5–18; see Methods), which makes them very attractive for quantum light applications.

In addition to high SP rates, a practical device for quantum communication can provide on-chip selection of the emitted polarization state. Non-degenerate cavity modes allow the generation of an SPS emitting either horizontal (H) or vertical (V) polarized SPs, as shown earlier[27,28]. To actively switch between polarization states on the chip, one must tune the QD emission either to the energy of the H- or V-polarized mode. To this end, we explored several types of trenches (Fig. 1b). Mode separation increases with decreasing aperture opening and/or longer oxidation time[15]. Depending on trench geometry and oxidization times, the cavity modes are either degenerate (type B, Fig. 5a) or non-degenerate (type D, Fig. 5b), with splitting energies of about 300 μeV and a contrast ratio of 57:1 between H- and V-polarized modes. For comparison to the results of Figs 2–4, we chose a type D device containing X0. Method A (cryostat heater) was used to achieve QD/mode resonance (Fig. 5c). Coupling of a single QD to either the H or V mode is manifested by a Purcell factor of 2.7, which is comparable to the type B devices. The measured intensity enhancement is about twofold lower compared with the type B devices, as expected if only one QD polarization state is coupled out using a non-degenerate mode. The ability to control the polarization state on the chip will thus reduce the overall SPS device efficiencies by a factor of two. The switching speed using temperature is

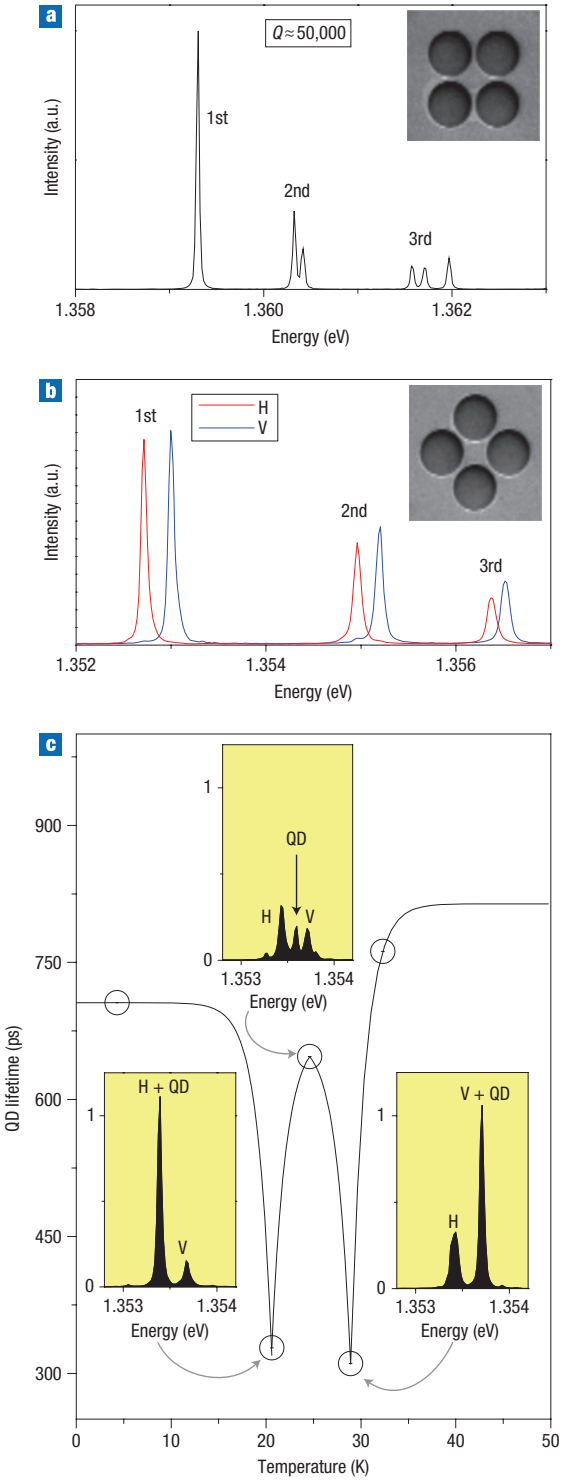

Figure 5 Demonstration of polarization control. a, Cavity mode spectrum for a type B device (depicted in the inset) showing polarization-degenerate modes (*Q* factors up to 50,000). **b**, Polarization-resolved spectra of a type D device (depicted in the inset) showing linear polarization splitting of 270 μeV for the first-order cavity mode (1st). H indicates horizontal polarization and V vertical polarization. **c**, Temperature tuning of a single QD exciton transition through the non-degenerate cavity modes. Coupling to either of the H- or V-modes is manifested by an enhanced lifetime from about 800 ps off resonance to 300 ps on resonance (*y* axis). Insets show spectra taken for different QD/mode detuning conditions.

nevertheless very limited. To overcome these limitations Stark-shift tuning[29] in an applied electrical field can be used. Our rugged cavity trench design offers possibilities to integrate additional lateral gates; this will be the subject of another study.

Ultrahigh SP rates are a combination of several effects. First, large geometrical extraction efficiency is provided by the cavity design. Second, the observed single QD Purcell effect contributes a factor of from two to four. Third, the positive bias voltage creates a fivefold intensity enhancement at comparable optical injection levels, reducing background contributions that otherwise compromise SP purity. Finally, QDs loaded with X– effectively reduce dark states, which further increase the SPS efficiency by a factor of three. Together, these effects contribute to the observed record high rates of SPs on demand up to 31 MHz, and promise rates above 116 MHz as investigated by the c.w. experiments. Nevertheless, devices still do not approach the SE lifetime limit of about 870 MHz (ref. 27). One reason for this is that non-geminate-carrier capture allows for a single-hole capture directly after the X– state has decayed into the single electron state. This leads to formation of X0 rather than X–, and dark-state configurations are again possible.

In conclusion, we fabricated an SPS by integrating high-Q (50,000) GaAs/AlGaAs microcavities with embedded oxide-tapered apertures, a rugged trench design, as well as buried electrical gates allowing controlled loading and Purcell tuning of individual InAs QDs. We observed single photons at record high rates up to 31 MHz, and SP extraction efficiencies up to 38% if negatively charged excitons were used. Additionally, we demonstrated tunability of the spectral mode degeneracy and also controlled coupling of single QDs to either H- or V-polarized cavity modes. This type of SPS is of direct interest for applications in quantum information science.

METHODS

SAMPLE PREPARATION

Devices are grown by molecular beam epitaxy on a semi-insulating GaAs (100) substrate with a 0.1-μm buffer layer. There are four sections in the structure, the bottom mirror, the active region, the oxide-aperture region and the top mirror as described in more detail in our previous study[15]. The optical GaAs cavity is Si n-doped up to 25 nm below the single layer of InAs QDs, providing a tunnel back gate. The fifth GaAs DBR period above the aperture region is Si n-doped, providing a top gate. Two etch windows with selective countersink depth are created using reactive-ion etching in Cl_2 plasma away from the SPS devices and contacted using a Ti/Pt/Au metallization. Cavity trenches were formed by optical lithography and reactive-ion etching to penetrate approximately five mirror periods into the bottom DBR. This etches small trenches in the surface that are used to define the AlO_x oxidation front. Tapered AlO_x apertures are formed laterally during steam oxidation within the cavity area, creating inner openings of 0.5–2 μm, effectively confining the mode volume[15].

OPTICAL CHARACTERIZATION

Micro-photoluminescence (micro-PL) measurements were performed using a microscope objective with numerical aperture NA = 0.4. Photon coincidences were recorded as a histogram of start–stop events and provide a measure of the second-order correlation function $g^2(\tau) = \langle I(t)I(t+\tau)\rangle / \langle I(t)\rangle\langle I(t)\rangle$, where $\langle I(t)\rangle$ is the expectation value of the photon intensity at time t. Additional details can be found in refs 15 and 20. Time-resolved single QD measurements have been performed under pulsed TiSa-laser excitation (150 fs pulsewidth) at a repetition rate of 82 MHz. The single QD PL signal was spectrally filtered with a 1-nm bandpass and coupled into a single-photon detector with about 130 ps timing jitter.

DATA ANALYSIS

Measured SP count rates were corrected for multiphoton emission events by multiplying by $(1 - g^2(\tau = 0))^{0.5}$ as introduced in ref. 13. A detection efficiency of 13% was estimated by measuring losses of all optical components at 920 nm and by using the detector efficiency. The total amount of single photons emitted into the first lens is 7.7 times the value shown on the y axis in Fig. 4. Aperture losses at the first lens can be neglected because our high-Q cavity emits into a far-field angle of only 10°, in contrast with earlier work[13,14] with low-Q cavities where 78% of the light was lost at the first lens. With these corrections, our highest SP rate with on-demand character is 31 MHz. Highest measured SP rates of 200 kHz were reported in ref. 14 under resonant excitation. For comparison with our experiments the off-resonance value of 50 kHz should be used, but no detection efficiency was given in ref. 14. We have thus used the stated SPS collection efficiency from ref. 14 of 8% multiplied by the repetition rate, yielding 6 MHz. From this number we estimate a fivefold improvement compared with former works.

X–/X0 ENHANCEMENT FACTOR

The bare X–/X0 ratio from the c.w. experiments is 4.6 (10.1 MHz/2.2 MHz). Because it is difficult to control the charging state and simultaneously also the QD/mode resonance within the same device, we compared two very similar devices, one loaded with X0 and tuned into resonance and one with X–. Thus, it is necessary to correct for the difference between the devices, which can be taken from the pulsed experiments close to saturation (4.0 MHz/2.7 MHz), leading to a corrected improvement factor of 3.1. (See Supplementary Information for a theoretical foundation in a rate-equation analysis.)

Received 7 June 2007; accepted 16 October 2007;
published 18 November 2007.

References

1. Bouwmeester, D., Ekert, A. K. & Zeilinger A. *The Physics of Quantum Information* (Springer, Berlin, 2000).
2. Gisin, N., Ribordy, G., Tittel, W. & Zbinden, H. Quantum cryptography. *Rev. Mod. Phys.* **74,** 145–195 (2002).
3. Boto, A. N. *et al.* Quantum interferometric optical lithography: exploiting entanglement to beat the diffraction limit. *Phys. Rev. Lett.* **85,** 2733–2736 (2000).
4. Knill, E., Laflamme, R. & Milburn, G. J. A scheme for efficient quantum computation with linear optics. *Nature* **409,** 46–52 (2001).
5. Lounis, B. & Orrit, M. Single-photon sources. *Rep. Prog. Phys.* **68,** 1129–1179 (2005).
6. Shields, A. J. Semiconductor quantum light sources. *Nature Photon.* **1,** 215–223 (2007).
7. Waks, E. *et al.* Quantum cryptography with a photon turnstile. *Nature* **420,** 762 (2002).
8. Lee, T.-H. *et al.* Oriented semiconducting polymer nanostructures as on-demand room-temperature single-photon source. *Appl. Phys. Lett.* **85,** 100–102 (2004).
9. Kurtsiefer, C., Mayer, S., Zarda, P. & Weinfurter, H. Stable solid-state source of single photons. *Phys. Rev. Lett.* **85,** 290–293 (2000).
10. Strauf, S. *et al.* Quantum optical studies on individual acceptor bound excitons in a semiconductor. *Phys. Rev. Lett.* **89,** 177403 (2002).
11. Vahala, K. Optical microcavities. *Nature* **424,** 839–846 (2003).
12. Michler, P. *et al.* A quantum dot single-photon turnstile device. *Science* **290,** 2282–2285 (2000).
13. Pelton, M. *et al.* Efficient source of single photons: A single quantum dot in a micropost microcavity. *Phys. Rev. Lett.* **89,** 233602 (2002).
14. Santori, C. *et al.* Submicrosecond correlations in photoluminescence from InAs quantum dots. *Phys. Rev. B* **69,** 205324 (2004).
15. Stoltz, N. G. *et al.* High-quality factor optical microcavity using oxide apertured micropillars. *Appl. Phys. Lett.* **87,** 031105 (2005).
16. Yuan, Z. *et al.* Electrically driven single-photon source. *Science* **295,** 102–105 (2002).
17. Chang, W.-H. *et al.* Efficient single-photon sources based on low-density quantum dots in photonic-crystal nanocavities. *Phys. Rev. Lett.* **96,** 117401 (2006).
18. Takemoto, K. *et al.* An optical horn structure for single-photon source using quantum dots at telecommunication wavelength *J. Appl. Phys.* **101,** 081720 (2007).
19. Colvin, V., Schlamp, M. & Alivisatos, A. P. Light-emitting diodes made from cadmium selenide nanocrystals and semiconducting polymer. *Nature* **370,** 354–357 (1994).
20. Strauf, S. *et al.* Self-tuned quantum dot gain in photonic crystal lasers. *Phys. Rev. Lett.* **96,** 127404 (2006).
21. Gur, I., Fromer, M. A., Geier, M. L. & Alivisatos, A. P. Air-stable all inorganic nanocrystal solar cell processed from solution. *Science* **310,** 462–465 (2005).
22. Urayama, J., Norris, T. B., Singh, J. & Bhattacharya, P. Observation of phonon bottleneck in quantum dot electronic relaxation. *Phys. Rev. Lett.* **86,** 4930–4933 (2001).
23. Smith, J. M. *et al.* Voltage control of the spin dynamics of an exciton in a semiconductor quantum dot. *Phys. Rev. Lett.* **94,** 197402 (2005).
24. Warburton, R. *et al.* Optical emission from a charge-tunable quantum ring. *Nature* **405,** 926–929 (2000).
25. Holtz, P. O. *et al.* Enhanced luminescence from InAs/GaAs quantum dots. *Proc. SPIE* **6401,** 64010I (2006).
26. Waks, E., Santori, C. & Yamamoto, Y. Security aspect of quantum key distribution with sub-Poissonian light. *Phys. Rev. A* **66,** 042315 (2002).
27. Moreau, E. *et al.* Single-mode solid-state single photon source based on isolated quantum dots in pillar microcavities. *Appl. Phys. Lett.* **79,** 2865–2867 (2001).
28. Unitt, D. C., Bennett, A. J., Atkinson, P., Ritchie, D. A. & Shields, A. J. Polarization control of quantum dot single-photon sources by means of dipole-dependent Purcell effect. *Phys. Rev. B* **72,** 033318 (2006).
29. Zrenner, A. *et al.* Coherent properties of a two-level system based on a quantum-dot photodiode. *Nature* **418,** 612–614 (2002).

Acknowledgements

We would like to thank D. Cohen for fruitful discussions. This work was supported through DARPA, NSF and ARO grants.
Correspondence and requests for materials should be addressed to S.S.
Supplementary Information accompanies this paper on www.nature.com/naturephotonics.

Optically detected coherent spin dynamics of a single electron in a quantum dot

M. H. MIKKELSEN, J. BEREZOVSKY, N. G. STOLTZ, L. A. COLDREN AND D. D. AWSCHALOM*

Center for Spintronics and Quantum Computation, University of California, Santa Barbara, California 93106, USA

*e-mail: awsch@physics.ucsb.edu

Published online: 7 October 2007; doi:10.1038/nphys736

The ability to sequentially initialize, manipulate and read out the state of a qubit, such as an electron spin in a quantum dot (QD), is a requirement in virtually any scheme for quantum information processing[1–3]. However, previous optical measurements of a single electron spin have focused on time-averaged detection, with the spin being initialized and read out continuously[4–8]. Here, we monitor the coherent evolution of an electron spin in a single QD. We use time-resolved Kerr rotation (KR) spectroscopy, an all-optical, non-destructive technique that enables us to monitor the precession of the spin in a superposition of Zeeman-split sublevels with nanosecond time resolution. The data show an exponential decay of the spin polarization with time, and directly reveal the *g*-factor and spin lifetime of the electron in the QD. Furthermore, the observed spin dynamics provide a sensitive probe of the local nuclear spin environment.

The magneto-optical Kerr effect results in a rotation of the plane of polarization of linearly polarized light on reflection off the sample, analogous to the Faraday effect for transmitted light. For a probe laser energy E, the KR angle, θ_K, is proportional to the difference of the dynamic dielectric response functions for left and right (σ^+ and σ^-) circularly polarized light[9], which are proportional to the modulus squared of the interband momentum matrix elements $P^{\sigma^\pm}_{c,v} = \langle\psi_c|\hat{p}_x \pm i\hat{p}_y|\psi_v\rangle$, where $|\psi_c\rangle$ ($|\psi_v\rangle$) is a conduction (valence) band state and $\hat{p}_{x,y}$ are momentum operators. For a single conduction band energy level in a QD containing a spin-up electron in a state $|\psi_\uparrow\rangle$, optical transitions to the spin-up state are forbidden by the Pauli exclusion principle. Considering only the transitions from a single twofold-degenerate valence-band level $|\psi_{v_0}\rangle$, θ_K is given by

$$\theta_K(E) = CE\left(\left|P^{\sigma^+}_{\downarrow,v_0}\right|^2 - \left|P^{\sigma^-}_{\downarrow,v_0}\right|^2\right)\frac{E - E_{0,v_0}}{(E - E_{0,v_0})^2 + \Gamma^2_{0,v_0}}, \qquad (1)$$

where E_{0,v_0} is the energy of the transition, Γ_{0,v_0} is the linewidth of the transition and C is a material-dependent constant. In a QD containing a single conduction-band electron, the lowest-energy interband transition is to the negatively charged exciton state, X^-, with an energy E_{X^-}. Thus, as has recently been demonstrated[4,5], a single electron spin produces a feature in the KR spectrum with the odd-lorentzian lineshape given by equation (1), centred at the energy E_{X^-}.

In the present work, the electron is confined to a single QD formed by monolayer fluctuations at the interfaces of a gallium arsenide (GaAs) quantum well. The QD is embedded within a diode structure, enabling controllable charging of the dot with a bias voltage[10]. Also, the QD is centred within an integrated optical cavity to enhance the small, single-spin KR signal[4]. With

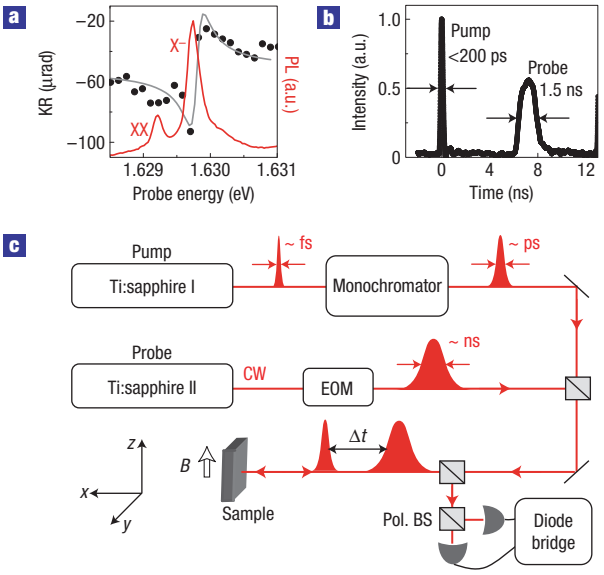

Figure 1 Experimental set-up for single-spin detection. a, X^- and biexciton (XX) PL lines from a QD and the corresponding KR spectrum measured with continuous-wave pump and probe, $B = 0$ G. The grey line is an odd-lorentzian fit centred at the X^- energy, demonstrating single-electron spin detection. **b**, The profiles of the pump and probe pulses as detected with a photodiode. The measured width of the pump pulse is limited by the 2 GHz bandwidth of the photodiode. **c**, Schematic diagram of the experimental set-up (EOM, electro-optic modulator; Pol. BS, polarizing beam-splitter).

circularly polarized excitation, spin-polarized electrons and holes are pumped into the quantum well, according to the selection rules governing interband transitions in GaAs (ref. 11). One or more electrons and/or holes then relax into the QD. By measuring the subsequent single-QD photoluminescence (PL), we determine the equilibrium charge state of the QD as well as the energies of various interband optical transitions as a function of bias voltage[4,12]. The measurements described below are made at a bias voltage where the QD is nominally uncharged, and the optical excitation injects one or more electrons or holes. In this regime, the QD may contain a single spin-polarized electron through the capture of an optically injected electron, or spin-dependent X^- decay[4]. Knowing the transition energy E_{X^-} from the PL measurements, we use the spectroscopic dependence of the Kerr effect to isolate the dynamics

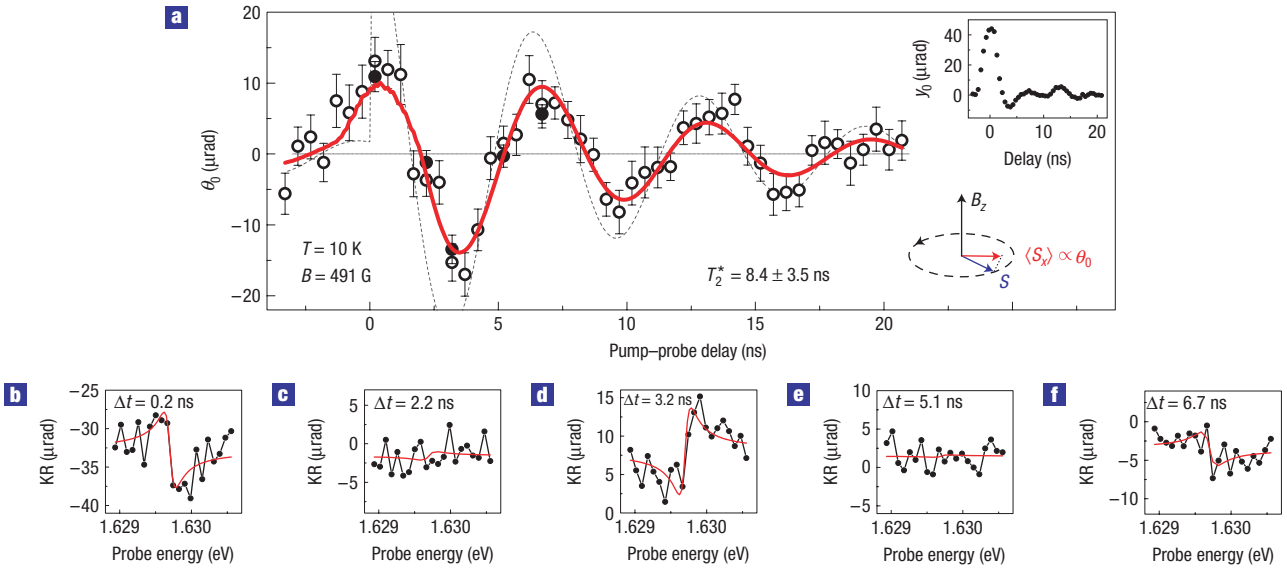

Figure 2 Coherent evolution of a single electron spin. a, Single-spin KR amplitude, θ_0, as a function of time, with 3-ns-duration probe pulses and $B = 491$ G. The solid line is a fit to equation (2) and the dashed line shows the solution of equation (2) without the probe-pulse convolution for the same fit parameters. The inset shows the offset, y_0. Error bars indicate the standard error as obtained from the least-squares fit to the KR spectra. The solid circles indicate the values of θ_0 obtained from the fits shown in **b–f**. **b–f**, KR angle as a function of probe energy at five different delays; solid lines are fits to equation (1), with a constant offset, y_0.

of the single electron spin from that of multiparticle complexes, such as charged or neutral excitons. Figure 1a shows the X^- and biexciton PL lines from a QD, along with the corresponding KR spectrum measured with a continuous-wave pump and probe. The odd-lorentzian feature centred at the X^- energy demonstrates the time-averaged measurement of a single electron spin.

In previous work, only the steady-state spin polarization was measured, concealing information about the evolution of the spin state in time. Here, we use time-delayed pump and probe pulses, shown schematically in Fig. 1c, to map out the coherent dynamics of the spin in the QD. The pump and probe pulses, as detected by a fast photodiode, are shown in Fig. 1b. Details of the experimental set-up are given in the Methods section.

For a fixed delay between the pump and the probe, θ_K is measured as a function of probe energy. At each point, the pump excitation is switched between σ^+ and σ^- polarization at a rate $1/t_{switch}$, and the spin-dependent signal is obtained from the difference in θ_K at the two helicities. The resulting KR spectrum is fitted to equation (1) plus a constant vertical offset, y_0. The amplitude, $\theta_0 = CE(|P^{\sigma^+}_{\downarrow,v_0}|^2 - |P^{\sigma^-}_{\downarrow,v_0}|^2)\Gamma^{-1}_{0,v_0}$, of the odd lorentzian is proportional to the projection of the spin in the QD along the measurement axis. The origin of the vertical offset, y_0, is unknown, but might be due to the broad KR feature from free electron spins in the quantum well, as discussed below. By repeating this measurement at various pump–probe delays, the evolution of the spin state can be mapped out.

When a magnetic field is applied along the z axis, transverse to the injected spin (the Voigt geometry), the spin is quantized into eigenstates $|\uparrow\rangle$ and $|\downarrow\rangle$, with eigenvalues $S_z = \pm\hbar/2$. The pump pulse initializes the spin at time $t = 0$ into the superposition $|\psi(t=0)\rangle = (|\uparrow\rangle \pm |\downarrow\rangle)/\sqrt{2}$, for $\sigma^\pm$ polarized excitation. If isolated from its environment, the spin state then coherently evolves according to $|\psi(t)\rangle = (e^{-i\Omega t/2}|\uparrow\rangle \pm e^{i\Omega t/2}|\downarrow\rangle)/\sqrt{2}$, where $\hbar\Omega = g\mu_B B_z$ is the Zeeman splitting. When the probe arrives at time $t = \Delta t$, the spin state is projected onto the x axis, resulting in an average measured spin polarization of $\langle S_x(\Delta t)\rangle = \pm(\hbar/2)\cos(\Omega \cdot \Delta t)$. This picture has not included the various environmental effects that cause spin decoherence and dephasing, inevitably leading to a reduction of the measured spin polarization with time.

The single-spin KR amplitude as a function of delay, measured with a 3-ns-duration probe pulse and a magnetic field $B = 491$ G, is shown in Fig. 2a, showing the expected oscillations due to the coherent evolution described above. Figure 2b–f shows a sequence of KR spectra at several delays, and the fits from which the data in Fig. 2a are obtained. In the inset of Fig. 2a the offset y_0 is shown, which oscillates with the same frequency as the single-spin KR but decays with a shorter lifetime. This behaviour may be consistent with that of free-electron spins in the quantum well, previously investigated in time-averaged measurements[13].

In the simplest case, the evolution of the measured KR amplitude can be described by an exponentially decaying cosine,

$$\theta(\Delta t) = A \cdot \Theta(\Delta t) \cdot \exp\left(\frac{-\Delta t}{T_2^*}\right)\cos(\Omega \cdot \Delta t),$$

where A is the overall amplitude, $\Theta(\Delta t)$ is the Heaviside step function and T_2^* is the effective transverse spin lifetime (though this measurement eliminates ensemble averaging, the observed spin lifetime may be reduced from the transverse spin lifetime, T_2, by inhomogeneities that vary in time). To model our data, we sum over the contributions from each pump pulse separated by the repetition period T_r, and convolve (denoted '$*$') with the measured probe-pulse shape, $p(t)$,

$$\theta_0(\Delta t) = p * \left[\sum_n \theta(\Delta t - nT_r)\right]. \qquad (2)$$

The solid line in Fig. 2a is a fit to equation (2), yielding $\Omega = 0.98 \pm 0.02$ GHz and $T_2^* = 8.4 \pm 3.5$ ns. The dashed line shows equation (2) without the probe pulse convolution, plotted with the same parameters for comparison.

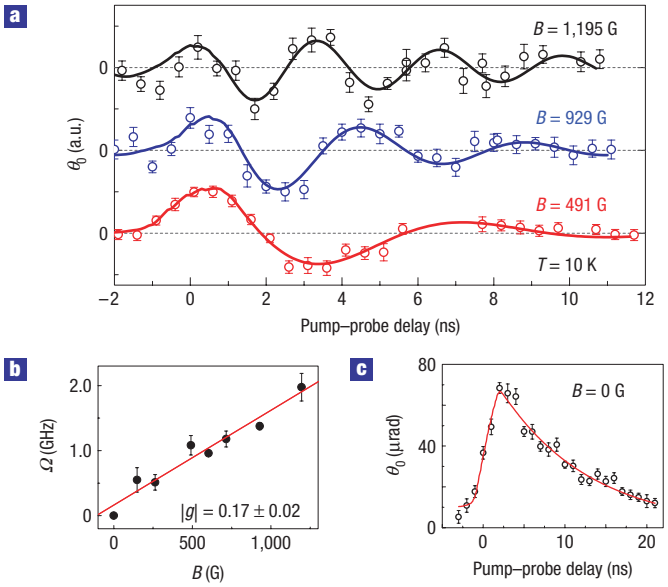

Figure 3 Magnetic-field dependence. a, Single-spin KR amplitude, θ_0, as a function of delay at three different magnetic fields. The probe-pulse duration is 1.5, 1.5 and 2 ns from top to bottom. Solid lines are fits to equation (2) and the error bars indicate the standard error as obtained from the least-squares fit to the KR spectra. The data are vertically offset for clarity. **b**, Precession frequency, Ω, of the electron spin as a function of applied magnetic field, as obtained from fits to the data. Each data point is the average of several delay scans and the error bars indicate the root-mean-squared deviation of the measured frequencies. From a linear fit to the data (solid line) a g-factor of 0.17 ± 0.02 is obtained. **c**, θ_0 as a function of delay at zero applied magnetic field, with 3 ns probe-pulse duration, and a fit to equation (2) yielding $T_2^* = 10.9 \pm 0.5$ ns. Error bars indicate the standard error as obtained from the least-squares fit to the KR spectra.

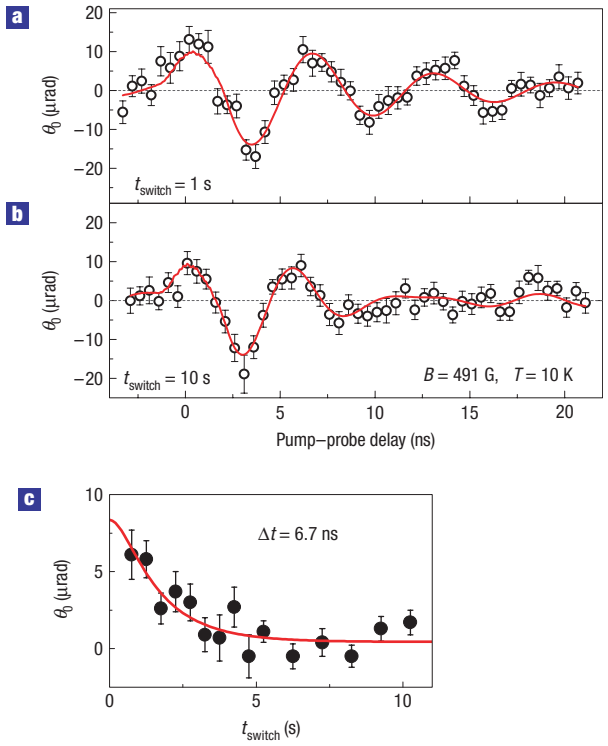

Figure 4 Probing the nuclear-spin environment. a,**b**, Single-spin KR amplitude, θ_0, as a function of delay where the excitation helicity is switched between σ^+ and σ^- polarization every 1 s ($t_{switch} = 1$ s) (**a**) and every 10 s ($t_{switch} = 10$ s) (**b**). The solid lines are fits to equation (3) convolved with the probe pulse, yielding a frequency shift due to the effective nuclear field of $\delta = 0 \pm 0.04$ GHz for $t_{switch} = 1$ s and $\delta = 0.14 \pm 0.02$ GHz for $t_{switch} = 10$ s. Increased nuclear polarization is clearly seen as frequency beating when $t_{switch} = 10$ s. **c**, KR amplitude as a function of t_{switch} for a fixed pump–probe delay, Δt, of 6.7 ns, revealing a DNP saturation time of 1.5 s. Error bars indicate the standard error as obtained from the least-squares fit to the KR spectra.

In Fig. 3a the precession of the spin is shown at three different magnetic fields. As expected, the precession frequency increases with increasing field. The solid lines in Fig. 3a are fits to equation (2), and the frequency Ω obtained from such fits is shown in Fig. 3b as a function of magnetic field. A linear fit to these data yields an electron g-factor of $|g| = 0.17 \pm 0.02$, consistent with the range of g-factors for these quantum dots found in previous ensemble or time-averaged measurements[6,14]. At zero magnetic field, as shown in Fig. 3c, the spin lifetime is found to be $T_2^* = 10.9 \pm 0.5$ ns. This value agrees with previous time-averaged[6] and ensemble[13,14] measurements where the relevant decay mechanism is often suggested to be dephasing due to slow fluctuations in the nuclear spin polarization. However, these polarization fluctuations are not expected to result in a single-exponential decay of the electron spin[15,16]. Using these non-Markovian models to fit our data results in an increase of χ^2 to 24.3 from 3.8 for the fit with a single-exponential decay, suggesting that other decay mechanisms than nuclear spin fluctuations might also be relevant in this case. In these QDs, the electronic level spacing of ~1 meV (ref. 17) is of the same order as $k_B T$ for this temperature range. Therefore, thermally activated or phonon-mediated processes[18–21] which yield an exponential decay might be significant in this regime.

This measurement technique is also sensitive to small nuclear spin polarizations. Ideally, there should be no induced steady-state nuclear polarization in this experimental geometry. Since the magnetic field is applied perpendicular to the direction of the spin, nuclear spins that are polarized by the electron spins precess around the applied field, resulting in zero steady-state polarization. However, for any misalignment of the pump laser from the perpendicular, there is a projection of the spin along the magnetic field, and right (left) circularly polarized light induces a small dynamic nuclear polarization (DNP) parallel (antiparallel) to the applied magnetic field[11,22]. Due to the hyperfine interaction this acts on the electron spin as an effective magnetic field, increasing (decreasing) the total magnetic field, resulting in a different precession frequency for right and left circularly polarized pump excitation. Since each data point is the difference of the KR signal with σ^+ and σ^- polarized excitation, a small deviation from perpendicular between the magnetic field and the electron spin yields a measured KR signal

$$\theta(\Delta t) = A \cdot \Theta(\Delta t) \cdot \exp\left(\frac{-\Delta t}{T_2^*}\right) \times [\cos((\Omega + \delta)\Delta t) + \cos((\Omega - \delta)\Delta t)], \quad (3)$$

where $\delta = g\mu_B \overline{B_{nuc}}/\hbar$ is the frequency shift due to the steady-state effective nuclear field, $\overline{B_{nuc}}$.

In order to investigate the effects of nuclear polarization on the electron spin, we have varied the rate $1/t_{switch}$ at which the pump helicity is switched. Figure 4a, b shows the single-spin KR signal as a function of time with $t_{switch} = 1$ s (as in Fig. 2a), and $t_{switch} = 10$ s,

respectively, with otherwise identical conditions. With larger t_{switch}, the nuclear polarization has time to build, as is shown in Fig. 4b by the visible beating, as expected from equation (3). A fit of the data in Fig. 4a ($t_{switch} = 1$ s) to equation (3) convolved with the probe pulse yields $\delta = 0 \pm 0.04$ GHz and $T_2^* = 8.4$ ns, whereas for the data in Fig. 4b ($t_{switch} = 10$ s) $\delta = 0.14 \pm 0.02$ GHz and $T_2^* = 8.3$ ns, with a χ^2 of 2.3. For comparison, a single-frequency fit of the data in Fig. 4b to equation (2) yields a slightly larger χ^2 of 2.8, and a significantly shorter T_2^* of 5.7 ns. It is unlikely that t_{switch} would have such an effect on the spin lifetime; moreover, nuclear polarization is the only effect in this system known to act on the spin with timescales on the order of seconds. Figure 4c shows the KR amplitude as a function of t_{switch} for a fixed pump–probe delay. A fit of the data to equation (3) with δ saturating exponentially in t_{switch} reveals a DNP saturation time of 1.5 s, similar to what has previously been found in these QDs[23]. The nuclear polarization seen in Fig. 4b corresponds to an effective magnetic field of 100 G, or an electron spin splitting of 100 neV. For comparison, when the magnetic field and the electron spin are parallel, hyperfine spin splittings ~1,000 times larger have been observed[23]. Given the typical size of these QDs[17], the electron interacts with $\sim 10^5$ nuclear spins. Since the hyperfine splitting here is smaller by a factor of 1,000 than the maximum observed splitting, the data shown in Fig. 4b represent the detection of at most $\sim 10^5/10^3 = 100$ polarized nuclear spins.

These measurements constitute a non-invasive optical probe of the coherent evolution of a single-electron spin state with nanosecond temporal resolution, which is a key ingredient for many spin/photon-based quantum-information proposals[24,25]. Furthermore, this technique provides a sensitive probe of the dynamics of the spin, revealing information about the spin coherence time and g-factor. Future work may exploit this ability to further explore the relevant decoherence mechanisms and the electron–nuclear spin interactions, and to observe the coherent manipulation of single spins in real time.

METHODS

A mode-locked Ti:sapphire laser provides pump pulses with energy $E_{pump} = 1.653$ eV and duration ~150 fs at a repetition period $T_r = 13.1$ ns. The bandwidth of the spectrally broad pump pulses is narrowed to ~1 meV by passing the pump beam through a monochromator. The probe pulses are derived from a wavelength-tunable continuous-wave Ti:sapphire laser passing through an EOM, allowing for electrical control of the pulse duration from continuous wave down to 1.5 ns. This technique yields short pulses while maintaining the narrow linewidth and wavelength tunability of the probe laser. Also, it enables us to adjust the pulse duration so as to maintain enough average power to achieve good signal-to-noise, while keeping the instantaneous power low enough to avoid unwanted nonlinear effects. The EOM is driven by an electrical pulse generator triggered by the pump laser, allowing for electrical control of the time delay between the pump and the probe pulses with picosecond precision. Additionally, in measurements with pump–probe delay $\Delta t > 13$ ns the pump beam has also been passed through an electro-optic pulse picker to increase the repetition period of the pulse train to $T_r = 26.2$ ns.

The sample is mounted on the cold finger of a He-flow cryostat at the focus of a microscope objective, at a temperature $T = 10$ K. The pump and probe beams are focused and spatially overlapped on the sample with a spot size of ~1 μm. The reflected light is collected through the same objective and the rotation of the probe polarization is detected by a balanced photodiode bridge. By chopping the pump beam at 4.1 kHz and the probe beam at 20 Hz, two lock-in amplifiers in series serve to isolate the KR signal induced by the pump. The pump polarization is switched between σ^+ and σ^- with a liquid crystal retarder at a rate $1/t_{switch}$, and a measurement of the rotation angle is taken at each helicity, with several seconds of averaging for noise reduction (that is, the spin is initialized and probed repeatedly for each measurement). The spin-dependent signal is then obtained by subtracting the measurements at each helicity. Typical time-averaged pump and probe intensities incident on the sample are 20 W cm^{-2} and 200 W cm^{-2}, respectively.

The sample is grown by molecular beam epitaxy and consists of a single 4.2 nm GaAs quantum well in the centre of a planar $Al_{0.3}Ga_{0.7}As$ λ-cavity. A 2 min growth interruption at each quantum well interface enables large (~100-nm-diameter[17]) monolayer thickness fluctuations to develop that act as QDs[26,27]. The front and back cavity mirrors are distributed Bragg reflectors composed of five and 28 pairs of $AlAs/Al_{0.3}Ga_{0.7}As$ $\lambda/4$ layers, respectively. This asymmetrical design enables light to be injected into and emitted from the cavity on the same side. The cavity resonance is centred at 1.624 eV at 10 K and has a quality factor of 120. We expect the KR at the peak of the resonance to be enhanced by a factor of ~15 (refs 28,29).

Received 29 May 2007; accepted 6 September 2007; published 7 October 2007.

References

1. Loss, D. & DiVincenzo, D. P. Quantum computation with quantum dots. *Phys. Rev. A* **57**, 120–126 (1998).
2. Awschalom, D. D., Loss, D. & Samarth, N. (eds) *Semiconductor Spintronics and Quantum Computation* (Springer, Berlin, 2002).
3. Hanson, R., Kouwenhoven, L. P., Petta, J. R., Tarucha, S. & Vandersypen, L. M. K. Spins in few-electron quantum dots. *Rev. Mod. Phys.* (in the press); preprint at <http://arxiv.org/abs/cond-mat/0610433> (2006).
4. Berezovsky, J. *et al.* Nondestructive optical measurements of a single electron spin in a quantum dot. *Science* **314**, 1916–1920 (2006).
5. Atatüre, M., Dreiser, J., Badolato, A. & Imamoglu, A. Observation of Faraday rotation from a single confined spin. *Nature Phys.* **3**, 101–105 (2007).
6. Bracker, A. S. *et al.* Optical pumping of the electronic and nuclear spin of single charge-tunable quantum dots. *Phys. Rev. Lett.* **94**, 047402 (2005).
7. Ebbens, A. *et al.* Optical orientation and control of spin memory in individual InGaAs quantum dots. *Phys. Rev. B* **72**, 073307 (2005).
8. Högele, A. *et al.* Spin-selective optical absorption of singly charged excitons in a quantum dot. *Appl. Phys. Lett.* **86**, 221905 (2005).
9. Meier, F. & Awschalom, D. D. Faraday rotation spectroscopy of quantum-dot quantum wells. *Phys. Rev. B* **71**, 205315 (2005).
10. Warburton, R. J. *et al.* Optical emission from a charge-tunable quantum ring. *Nature* **405**, 926–929 (2000).
11. Meier, F. & Zakharchenya, B. P. (eds) *Optical Orientation: Modern Problems in Condensed Matter Sciences* (North Holland, Amsterdam, 1984).
12. Bracker, A. S. *et al.* Binding energies of positive and negative trions: From quantum wells to quantum dots. *Phys. Rev. B* **72**, 035332 (2005).
13. Dzhioev, R. I. *et al.* Optical orientation and the Hanle effect of neutral and negatively charged excitons in $GaAs/Al_xGa_{1-x}As$ quantum wells. *Phys. Rev. B* **66**, 153409 (2002).
14. Dutt, M. V. G. *et al.* Stimulated and spontaneous optical generation of electron spin coherence in charged GaAs quantum dots. *Phys. Rev. Lett.* **94**, 227403 (2005).
15. Khaetskii, A. V., Loss, D. & Glazman, L. Electron spin decoherence in quantum dots due to interaction with nuclei. *Phys. Rev. Lett.* **88**, 186802 (2002).
16. Merkulov, I. A., Efros, Al. L. & Rosen, M. Electron spin relaxation by nuclei in semiconductor quantum dots. *Phys. Rev. B* **65**, 205309 (2002).
17. Gammon, D., Snow, E. S., Shanabrook, B. V., Katzer, D. S. & Park, D. Fine structure splitting in the optical spectra of single GaAs quantum dots. *Phys. Rev. Lett.* **76**, 3005–3008 (1996).
18. Semenov, Y. G. & Kim, K. W. Phonon-mediated electron-spin phase diffusion in a quantum dot. *Phys. Rev. Lett.* **92**, 026601 (2004).
19. Golovach, V. N., Khaetskii, A. & Loss, D. Phonon-induced decay of the electron spin in quantum dots. *Phys. Rev. Lett.* **93**, 016601 (2004).
20. Khaetskii, A. V. & Nazarov, Y. V. Spin-flip transitions between Zeeman sublevels in semiconductor quantum dots. *Phys. Rev. B* **64**, 125316 (2001).
21. Erlingsson, S. I., Nazarov, Y. V. & Fal'ko, V. I. Nucleus-mediated spin-flip transitions in GaAs quantum dots. *Phys. Rev. B* **64**, 195306 (2001).
22. Salis, G., Awschalom, D. D., Ohno, Y. & Ohno, H. Origin of enhanced dynamic nuclear polarization and all-optical nuclear magnetic resonance in GaAs quantum wells. *Phys. Rev. B* **64**, 195304 (2001).
23. Gammon, D. *et al.* Electron and nuclear spin interactions in the optical spectra of single GaAs quantum dots. *Phys. Rev. Lett.* **86**, 5176–5179 (2001).
24. Meier, F. & Awschalom, D. D. Spin-photon dynamics of quantum dots in two-mode cavities. *Phys. Rev. B* **70**, 205329 (2004).
25. Leuenberger, M. N. Fault-tolerant quantum computing with coded spins using the conditional Faraday rotation in quantum dots. *Phys. Rev. B* **73**, 075312 (2006).
26. Zrenner, A. *et al.* Quantum dots formed by interface fluctuations in a AlAs/GaAs coupled quantum well structures. *Phys. Rev. Lett.* **72**, 3382 (1994).
27. Gammon, D., Snow, E. S., Shanabrook, B. V., Katzer, D. S. & Park, D. Homogeneous linewidths in the optical spectrum of a single gallium arsenide quantum dot. *Science* **273**, 87–90 (1996).
28. Salis, G. & Moser, M. Faraday-rotation spectrum of electron spins in a microcavity-embedded GaAs quantum wells. *Phys. Rev. B* **72**, 115325 (2005).
29. Li, Y. Q. *et al.* Cavity enhanced Faraday rotation of semiconductor quantum dots. *Appl. Phys. Lett.* **88**, 193126 (2006).

Acknowledgements

We acknowledge support from NSF and the Air Force Office of Scientific Research.
Correspondence and requests for materials should be addressed to D.D.A.